α-“$NaLuF_4$”: a Structure with Sixfold Twinning, Modulation and Diffuse Scattering. Structure Determination and Disorder Modelling

Dissertation

zur

Erlangung der naturwissenschaftlichen Doktorwürde

(Dr. sc. Nat.)

vorgelegt der

Mathematisch-naturwissenschaftlichen Fakultät

der

Universität Zürich

von

Partha Pratim Das
aus Indien

Promotionskomitee:

Prof. Dr. Jay S. Siegel (Vorsitz)

Dr. Anthony Linden

Prof. Dr. Greta Patzke

Prof. Dr. Hans-Beat Bürgi

Zürich, 2011

To my family

Abstract

Hexagonal β-NaLnF$_4$ compounds are a family of light up-conversion materials which emit visible light upon IR excitation e.g. β-NaLnF$_4$ shows green and blue emission for Er^{3+}, Yb^{3+} and Tm^{3+}, Yb^{3+} doping, respectively. Understanding of the properties of these technologically important materials requires knowledge of their structure at an atomic level. The theme of this doctoral thesis is the modelling of disorder in the single crystal structure of α-NaLuF$_4$ obtained from the melt with a likely composition of Na$_5$Lu$_9$F$_{32}$. Two different phases of α-NaLuF$_4$ have been identified and all studied in this doctoral thesis. The motivation of this study is to reveal the complex structure within the crystals and to make a systematic investigation of the complex disorder by exploiting the available methods and consequently to understand the driving force for the formation and stability of the material and to find a relationship between the up-conversion properties and the structure. In this work the complex Bragg diffraction is analysed, whereas a quantitative analysis of the disorder diffuse scattering is beyond the scope of this thesis.

Phase I shows strong Bragg scattering, commensurate satellite reflections and significant diffuse scattering. The strong main reflections in the apparently “cubic” reciprocal lattice rows are not collinear and split at high diffraction angles. This suggests the crystal is a multiple twin of lower symmetry with near overlap of reflections. If the satellite reflections are treated as Bragg peaks then a fivefold orthorhombic supercell and six fold twinning follow with a likely space group of *Cmmm*.

Phase II of the sample which comes from another part of the same ampoule crystalized from the melt shows strong Bragg scattering and significant diffuse scattering but no satellite reflections. The nature of the diffuse scattering is different in the two phases. In Phase II, the main reflections with apparent “cubic” symmetry have a similar nature to those of Phase I and the structure can also be described as a sixfold orthorhombic twin.

The main reflections vary in size and position from low diffraction angle to high angle. To account for this variation an increased mask size was used to integrate the main reflections. To avoid problems arising from the different peak profiles of main and satellite reflections, the latter were integrated with a non-crystallographic absence

condition that eliminates the main reflections during the data integration procedure. These non-trivial data integration procedures play a key role for optimal intensity extraction, which is essential for being able to correctly model and refine the structure.

The first step of the structure determination was to establish the average structural model based on the main reflections and ignoring the supercell. The initial model was derived from the structure of CaF_2. Considering only the positions of the heavy atoms in the asymmetric unit of the small unit cell, the average structure may be described about equally well in two different ways for both the phases. The two possible descriptions of the structure can be understood from the eigensymmetries of the heavy metal atom positions. The presence of residual electron density in the difference Fourier map of both models was interpreted in terms of disordered fluorine atoms. Their positions are chemically more meaningful for one of the two heavy atom models.

For the Phase I structure, the phases of the superstructure reflections were determined by band flipping implemented in the program SUPERFLIP. The reconstructed difference electron densities shows two distinct commensurately modulated parallel columns of cations: one with varying Na^+/Lu^{3+} occupancy and one with additional positional displacement of the ions from the average structure positions. Interestingly, two different solutions result from band flipping of superstructure reflections with equal probability. These two solutions differ only in the details of the positional and occupational modulation. As the main and satellite reflections could not be refined simultaneously due to the twinning, the refinement was performed only using the superstructure reflections. Although the two distinct solutions refine well, bond valence calculations suggest one solution to be chemically more meaningful than the other. Refinement based solely on the superstructure reflections and the information from difference electron density maps were successfully tested for the first time.

The diffuse scattering in the structure may be a result of the strain in the twin boundaries and possible further occupational and positional disorder which may correlate with the up-conversion properties of the crystal. In this study it was shown that non-trivial data integration methods and use of non-crystallographic absence conditions play a crucial role for optimal intensity extraction in case of rare sixfold pseudomerohedral twinning.

It was also shown in this study that bond valence calculations are important when structural refinement does not converge to a unique solution.

Zusammenfassung

Hexagonale β-NaLnF$_4$ Verbindungen sind eine Familie von Licht aufkonvertierenden (up-conversion) Materialien, welche bei IR Anregung sichtbares Licht abgeben. So zeigt z.B. β-NaLnF4 grüne und blaue Emission für Er^{3+}, Yb^{3+} beziehungsweise Tm^{3+}, Yb^{3+} Dotierung. Um die Eigenschaften dieser technologisch wichtigen Materialen zu verstehen, sind Kenntnisse von deren Struktur im atomaren Massstab nötig. Das Thema dieser Doktorarbeit ist die Modellierung von Fehlordnung in der Ein-Kristall Struktur von α-NaLnF$_4$, erhalten aus der Schmelze mit der wahrscheinlichen Zusammensetzung Na$_5$Lu$_9$F$_{32}$. Zwei unterschiedliche Phasen von α-NaLnF$_4$ wurden in dieser Arbeit gefunden und untersucht. Der Beweggrund für diese Untersuchung ist es, die komplexe Struktur innerhalb des Kristalls zu entschlüsseln durch systematische Erforschung der komplexen Fehlordnung und unter Nutzung der verfügbaren Methoden, um somit die treibende Kraft, welche dieses Material formt und stabilisiert, zu verstehen und eine Beziehung zwischen ‚up-conversions' Eigenschaften und der Struktur zu finden. In dieser Arbeit wird die *Bragg*-Streuung analysiert; die quantitative Analyse der diffusen Streuung verursacht durch Fehlordnung liegt ausserhalb des Rahmens dieser Dissertation.

Phase I zeigt starke *Bragg*-Streuung, kommensurable Satellitenreflexe und ausgeprägte diffuse Streuung. Die starken Hauptreflexe in den scheinbar kubisch reziproken Gitterreihen sind nicht kollinear oder bei hohen Beugungswinkeln auf gespaltet. Dies deutet an, dass der Kristall ein mehrfacher Zwilling mit tiefer Symmetrie ist und die meisten Reflexe überlappen. Werden die Satellitenreflexe als *Bragg*-Peaks behandelt, dann ergibt sich eine fünffache orthorhombische Überstruktur und sechsfache Zwillingsbildung mit der wahrscheinlichen Raumgruppe *Cmmm*.

Phase II der Probe, welche in einem anderen Teil derselben Ampulle aus der Schmelze kristallisierte, zeigte starke *Bragg*-Streuung und ausgeprägte diffuse Streuung aber keine Satellitenreflexe. Die Art der diffusen Streuung ist bei den beiden Phasen verschieden. In Phase II sind die Hauptreflexe mit offensichtlicher kubischer Symmetrie ähnlich denen in Phase I und die Struktur kann ebenfalls als sechsfacher orthorhombischer Zwilling beschreiben werden.

Die Hauptreflexe variieren in Grösse und Position von niedrigen zu hohen Streuwinkeln. Um diese Variationen zu berücksichtigen, wurde zur Integration der Hauptreflexe eine vergrösserte Maske benutzt. Um Probleme zu verhindern, welche

aus den unterschiedlichen Peak Profilen von Haupt- und Satellitenreflexen entstehen, wurden letztere mit einer nicht-kristallographischer Auslöschungsbedingung integriert, dies eliminierte die Hauptreflexe während des Vorganges der Datenintegration. Dieses ungewöhnliche Vorgehen bei der Datenintegration spielt eine Schlüsselrolle zur optimalen Bestimmung der Reflexintensitäten, welche unabdingbar sind um die Struktur korrekt darzustellen und zu verfeinern.

Der erste Schritt der Strukturbestimmung diente dem Aufbau des durchschnittlichen Strukturmodells, basierend auf den Hauptreflexen und ohne die Superzelle zu berücksichtigen. Das anfängliche Modell wurde aus der Struktur von CaF_2 abgeleitet. Betrachtet man nur die Positionen der Schweratome in der asymmetrischen Einheit der kleinen Einheitszelle, kann für beide Phasen die durchschnittliche Struktur auf zwei unterschiedliche Arten etwa gleich gut beschrieben werden. Beide möglichen Beschreibungen der Struktur können aus der Eigensymmetrie der Lage der Schwermetallatome verstanden werden. Die restliche Elektronendichte in den verschiedenen *Fourier*-Karten beider Modelle, wurde in Form von ungeordneten Fluoratomen interpretiert. Deren Positionen sind chemisch sinnvoller für eines der beiden Schweratom Modelle.

Für die Phase I Struktur wurden die Phasen der Überstruktur-Reflexe durch ‚band flipping‘ bestimmt, welches im Programm SUPERFLIP eingebaut ist. Die rekonstruierten Differenz-Elektronendichten zeigen zwei unterschiedliche kommensurabel modulierte parallele Kolonnen von Kationen: eine mit unterschiedlicher Na^+/Lu^{3+} Belegung, die andere mit zusätzlichen Lageverschiebungen der Ionen von den durchschnittlichen Strukturpositionen. Interessanterweise resultierten auch aus dem ‚band flipping‘ der Überstruktur-Reflexe zwei verschiedene Modelle mit gleicher Wahrscheinlichkeit. Die zwei Lösungen unterscheiden sich nur in Details der Lage- und Belegungs-Modulation. Da die Haupt- und Überstruktur-Reflexe nicht gleichzeitig verfeinert werden konnten, wurde die Verfeinerung nur mit den Überstruktur-Reflexen ausgeführt. Obwohl beide besprochenen Lösungen gut verfeinern, deuten Bindungs-Valenz Berechnungen an, dass die eine sinnvoller ist als die andere. Verfeinerungen, basierend einzig auf Überstruktur-Reflexen und den Informationen aus der Differenz-Elektronendichte Karte, wurden das erste Mal erfolgreich getestet.

Die diffuse Streuung in der Struktur könnte durch Spannungen an den Zwillingsgrenzen und möglicher weiterer Belegungs- und Lage-Fehlordnung entstehen, welche in Beziehung zu den ‚up-conversion‘ Eigenschaften des Kristalls stehen können. In dieser Arbeit wurde gezeigt, dass besondere Datenintegrations-Methoden und der Gebrauch von nicht-kristallographischen Auslöschungsbedingungen, eine entscheidende Rolle spielen bei der optimalen Bestimmung der Reflexionsintensitäten im Falle der seltenen sechsfach pseudomerohedralen Zwillinge.

Auch wurde in dieser Arbeit gezeigt, dass Bindungsvalenz Berechnungen wichtig sind, wenn die Strukturverfeinerung nicht zu einer eindeutigen Lösung findet.

Definition of Terms

The terms used in different chapters of this thesis have been summarized below.

1) Chemical Terms

Bond Valence: The bond valence method is a method to estimate the oxidation state of atoms in coordination chemistry. In bond valence method the valence V of an atom is the sum of the individual bond valences v_i surrounding the atom

$$V = \sum_{i=1}^{n} v_i$$

The individual bond valences in turn are calculated from the observed bond lengths

$$v_i = \exp\left(\frac{R_0 - R_i}{b}\right)$$

R_i is the observed bond length, R_0 is a tabulated parameter in the bond valence parameter tables, expressing the ideal bond length when the element i has exactly valence 1, and b is an empirical constant, typically 0.37 Å.

Classical Bond Valence Parameter Tables:

Brese, N. E. & O'Keeffe, M.; Acta Cryst. B47 (1991) 192-197.

Brown, I. D. & Altermatt, D.; Acta Cryst. B41 (1985) 244-247.

Brown, I. D.; in Structure and Bonding in Crystals, edited by M. O'Keeffe & A. Navrotsky,Vol. II, pp. 1-30. New York; Academic Press (1981).

2) Crystallographic Terms

These definitions have been taken from the IUCR Online Dictionary of Crystallography.

s.u. (σ): Standard uncertainty of a parameter.

F_{obs} : Observed structure factor.

F_{calc} : Calculated structure factor.

R_{int}: It defines the agreement between the symmetry equivalent reflections which is given by the following equation:

$$R_{\text{int}} = \frac{\sum_{all} \left| I - \bar{I} \right|}{\sum_{all} I}$$

The summation is performed over all the measured reflections including the symmetry equivalent reflections.

***R* Factor:** The term *R* factor is commonly taken to refer to the 'conventional' *R* factor given by the following equation:

$$R = \frac{\sum \left\| F_{obs} \right| - \left| F_{calc} \right\|}{\sum \left| F_{obs} \right|}$$

The sum extends over all the reflections measured and their calculated counterparts respectively. This is a measure of agreement between the amplitudes of the structure factors from a crystallographic model (F_{calc}) and those from the original X-ray diffraction data (F_{obs}). The R factor is calculated during each cycle of least-square refinement to assess the progress. The final *R* factor is one of the measures of model quality. The structure factor *F* is closely related to the intensity of the reflection it describes:

$$I_{hkl} \propto \left| F_{hkl} \right|^2$$

There are two possible ways to mention *R* Factor, if the refinement is performed against all the measured reflections it is called R_{all} and if the refinement is performed only against those reflections which are above a certain σ(I), then it is called R_{obs}. The criteria used for observed reflections in the current refinements in Jana2006 are I > 3σ(I).

Weighted *R* Factor: In practice, weighted *R* factors are more often used to track least square-refinement, since the functions minimized are weighted according to estimates of the precession of the measured quantity $Y : \sum (Y_{obs} - Y_{calc})^2$ Where Y being F, F^2 or I.

The general term for a weighted residual is given by the following equation:

$$wR = \left(\frac{\sum \left| w \left| Y_{obs} - Y_{calc} \right|^2 \right|}{\sum \left| w Y_{obs}{}^2 \right|} \right)^{1/2}$$

The sum is usually computed over all reflections measured in the experiment and it is called wR_{all} and if the sum is computed over those reflections which are above a certain σ(I), then it is called wR_{obs}. All the refinements performed in this work are based on F and the weighting is based on measured σ's.

$$w = 1 \big/ \sigma^2(F) + kF^2$$

The factor k determined empirically.

Goodness-of-fit (*GOF*): The other important parameter during the least squares refinement is goodness of fit (GOF), which is defined by the equation:

$$GOF = \left(\frac{\sum \left| w \left| Y_{obs} - Y_{calc} \right|^2 \ \right|}{N_{ref} - N_{param}} \right)^{1/2}$$

Where N_{ref} defines the number of reflections and N_{param} defines the number of parameters used during the least square refinement. If the least square refinement is performed against all the measured reflections then it is called GOF_{all} and if the refinement is performed against the reflections which are above a certain criteria of σ(I), then it is called GOF_{obs}.

***F*(000)** is the structure factor for the (0,0,0) reflection and theoretically it is the total number of electrons in one unit cell.

$\Delta_{\mathrm{max}}/\sigma$ is the largest ratio of the final least-squares parameter shift (Δ_{max}) to the final standard uncertainty (σ).

Δρ(max, min) is the largest and smallest values in e $Å^{-3}$ of the final difference electron density.

Site multiplicity of a special position is the site symmetry of the general position divided by the site symmetry of the special position.

Contents

Chapter 1 Introduction and Disorder in Crystal Structures

Chapter 2 Up-conversion and Materials for Up-conversion

Chapter 3 The Interpretation of the Diffraction Patterns and Data Integration

Chapter 4 Understanding of the Phase II Structure

Chapter 5 Understanding the Phase I Structure

Chapter 1: Introduction and Disorder in Crystal Structures

1.1 Routine Crystallography and its Shortcomings

Crystals have long been admired for their regularity and symmetry, but they were not investigated scientifically until the 17th century. Johannes Kepler hypothesized in his work *Strena seu de Nive Sexangula* (1661) that the hexagonal symmetry of snowflake crystals was due to a regular packing of spherical water molecules. At the same time crystal symmetry was investigated experimentally by Nicolas Steno (1669), who showed that the angles between specific faces are the same in every crystal of a particular compound. In 1772 Romé de I′Isle published his book *Essai de Cristallographie* (Romé de l'Isle, 1772) on the classification of his own mineral collection and *Cristallographie* (Romé de l'Isle, 1783) in 1783, in which he demonstrated that minerals could be classified and identified by the constancy of the dihedral angles between the faces of the crystals of the same mineral species. The law of constancy of the angles is attributed to him. Some years later René Just Haüy proposed in his books *Essai d′une théorie sur la structure des crystaux* (Haüy, 1784) and *Traité de minéralogie* (Haüy, 1801), that crystals are made of microscopic building blocks (the unit cell), that the shape of the macroscopic crystal is isomorphic with the shape of the building block and that these building blocks, the *molécules intégrantes*, are small parallelepipeds. Haüy also discovered that every face of a crystal can be described by simple stacking patterns of blocks of the same shape and size. Hence, William Hallowes Miller in 1839 was able to give each face a unique label of three small integers, the Miller indices which are still used for identifying crystal faces. Haüy's study led to the correct idea that crystals are built up of a periodic array of those fundamental structural units in all dimensions, *i.e.* crystals have not only a three dimensional periodic arrangement of the unit cells with its characteristic translational symmetry, but also a three-dimensional periodic arrangement of the motif, the contents of the unit cell (the atomic constituents like atoms, molecules and ions)! This three dimensional periodicity was then believed for almost the next 200 years to be one of the most fundamental principles underlying crystalline architecture.

As a consequence of this periodicity, only a finite number of symmetry arrangements (with respect to rotation, reflection, rotation combined with inversion and translation) of the atomic building blocks are possible in three-dimensional space such that the symmetry continues uninterrupted throughout the crystal. The translational symmetry imposes limitations on the rotational symmetries: only one, two, three, four, and sixfold rotations are allowed, while fivefold and higher than sixfold rotational symmetries are forbidden. These symmetry operations (rotation, reflection and rotation combined with inversion) result in 32 crystal classes (crystallographic point groups) and these point groups combined with translational symmetry make 230 space groups which are tabulated in the *International Tables for Crystallography, Volume A-Space Group Symmetry* (2005). Each space group represents one possible combination of the symmetry operations and therefore the spatial arrangement of the motifs. The smallest motif from which the symmetry builds the structure is known as asymmetric unit.

The interaction between light and matter can be formulated as the interaction between an oscillating electric field and the electrons of atoms and molecules. The oscillating electric field forces the electrons and nuclei to oscillate about their equilibrium positions and thereby to emit secondary waves themselves. The secondary waves from electrons and nuclei have opposite phases due to their opposite charges. Since a proton is 1836 times heavier than an electron, the amplitude of oscillation of the electron and of its emitted wave is 1836 times larger than that of proton. For this reason the scattering of the heavy nuclei is neglected in analysing X-ray scattering. For ideal crystals which have perfect periodicity the scattering leads to the constructive interference of the secondary waves only when Bragg's Law is fullfilled, complete destructive interference elsewhere. The sharp and discrete diffraction maxima form a three dimensional reciprocal lattice. The distances between these sharp Bragg peaks represent, inversely the periodicity in the crystal because a reciprocal relationship exists between diffraction space and direct space. If the repeat unit is large in direct space then the Bragg reflections are more closely spaced. This concept of periodicity and symmetry is a powerful tool for structural studies and is at the origin of the successful investigation of crystals by optics and diffraction.

With the development of modern day diffractometers with area detectors and advancements of the structure solution and refinement programs, it has become very easy to solve and refine a routine crystal structure on a daily basis. However, in the real world, crystals are not ideal. This leads to complexity in the crystal and in the structure. There are two main source of complexity. The first is when the crystal does not grow as a single domain of uniformly oriented unit cells, but as many domains related by some symmetry element or rotation. This is known as twinning. In the second case some instantaneous breakdown of crystal symmetry occurs because of motion and many cases show a permanent breakdown. Such breakdown is known as disorder. Disorder may take one or more forms: thermal, occupational, compositional, orientational or translational and manifests itself in diffraction experiments in terms of diffuse scattering. In the case of alloys and ionic crystals, there is a predominance of substitutional and positional disorder. In molecular crystals, the molecules often break crystal symmetry by assuming different orientations or conformations in different unit cells. In the case of instantaneous disorder, the diffuse scattering is called thermal diffuse scattering, while permanent breakdown of order leads to static disorder diffuse scattering.

In a routine crystal structure determination, one generally considers only the Bragg scattering when determining the average structure, and ignores the weak diffuse scattering intensities, if present at all. But in the case of severe disorder, the diffuse scattering intensity may become comparable with the Bragg scattering intensity and it then becomes essential to take account of the diffuse scattering along with Bragg scattering intensity for a proper description of the crystal structure. The probability of successfully developing a full picture of a crystal structure decreases as the degree of structural disorder increases, because the structural information tends to be transferred from the sharp Bragg scattering to the diffuse scattering.

It is not infrequent that the crystal structures of materials which show scientifically interesting and potentially useful technological properties are frustratingly disordered. In such cases, the elucidation of their structure is not straightforward, but nonetheless crucial to the understanding of the properties of the compound. The concepts of twinning and disorder will be discussed in the subsequent sections of this chapter.

1.2 Twinning

One of the commonly occurring deviations from an ideal crystal comes in terms of twinning. Twins are regular aggregates consisting of individual crystallites with the same structure joined together in some definite mutual orientation. Crystal twinning is a problem that adds difficulties to the whole procedure of structure determination, from selection of crystals to the refinement and the interpretation of results. Based on the diffraction pattern, twinned crystals may be grouped into four general classes.

1.2.1 Merohedral Twins

These types of twins have domains whose diffraction patterns are completely overlapped. In these cases, the twin element is not a symmetry of the crystal class but is an element of the crystal system. This leads to the complete overlap of the direct and reciprocal lattices making the diffraction pattern from the crystal appear as if it comes from a single domain. If the volumes of the different twin domains are nearly equal then the additional symmetry element often leads to the selection of an incorrect higher symmetry space group. It is sometimes possible to solve and refine the structure in the higher symmetry space group, and obtain a false average of the true structure. When a model appears to require extensive disorder, the structure should be checked to ascertain that it is not twinned, because it may be possible that the structure has been interpreted incorrectly. Merohedral twins frequently occur when a phase transition takes a high temperature form of high symmetry to a low temperature form of lower crystal class (Kleemann *et al.*, 1987). One type of merohedral twinning is inversion twinning (Herbst-Irmer & Sheldrick, 1998).

1.2.2 Pseudomerohedral Twins

These types of twins have lattice parameters that suggest higher Laue symmetry than the symmetry appropriate for the point group of the sample and have a twin element that emulates the additional symmetry. For example, consider a monoclinic structure with β very close to 90°. In such a case, a twin plane on (100) will cause symmetry-unrelated pairs of reflections to lie too close to be distinguishable. If the volumes of the two domains are nearly equal, the intensities will appear to have *mmm* symmetry instead of *2/m*, and the structure will not be readily solvable. Once the nature of the twinning is recognized and included in the model, the structure refinement usually proceeds without further problems (Partik *et al.*, 1996).

1.2.3 Non-Merohedral Twins

This type of twin has two or more crystalline domains with reciprocal lattices that either do not overlap or are only partially overlapped. In non-merohedral twinning the twin element is neither an element of the crystal class nor of the crystal system. The sets of reflections that are not overlapping are used to discover the twin law. It may then be possible to measure only those reflections that corresponds to a single component, correcting the intensities of those to which the other twin domains make a contribution, and to solve and refine the structure based on only one set of reflections (Jiang *et al.*, 2007). The intensities of the overlapping reflections must be accounted for properly in order to obtain a good result. Where reflections are nearly overlapped, data integration becomes very challenging. Modern data integration software can integrate non-overlapping reflections which originate from different twin domains by using more than one orientation matrices and the overlapping reflections can be scaled according to the relative intensities of the non-overlapped reflections. The combined data set can then be used to refine the structure.

In special occasions if by chance the unit cell parameters are such that every second, third or n^{th} layer of the reciprocal lattices of two components overlaps exactly they are termed as partial merohedral twinning.

1.3 Modulation

Second type of deviation from an ideal crystal may come up when atoms, groups of atoms or even whole molecules are shifted or rotated with respect to their neighbours or occupation of the atomic sites varies such that the three dimensional translational symmetry, often considered as the characteristic of a crystal structure, is modified, this is commonly known as modulated crystal structure. These shifts and rotations in modulated structures follow distinct rules and within these distortions there is additional periodicity which can be mathematically described by a so called atomic modulation function (AMF). AMFs can be harmonic (continuous) and therefore may be expressed by sine/cosine series or they may be discontinuous, in which case crenel or sawtooth functions are needed (Petrícek *et al.*, 1995). Based on the periodicity of the modulation wave, a modulated structure can be of two types: commensurately modulated structures (Lam *et al.*, 1995) where periodicity matches an integral number of lattice translations of the basic cell and incommensurately modulated structures (Wolff *et al.*, 1981) where periodicity does not match an integral number of lattice translation of the basic cell.

Due to the periodic nature of the modulation, additional sharp peaks appear in the diffraction pattern, just as the Bragg reflections (main reflections) produced by a three dimensional crystal are a result of the periodicity in the structure. These additional peaks are referred to as satellite reflections and usually are weaker than the main reflections. In reciprocal space, satellite reflections can lie parallel to one of the reciprocal axes belonging to the main reflections, but they can extend in any arbitrary direction depending on the direction of modulation. The modulation can occur in two ways in a broader sense: one is occupational modulation when the occupational part in the crystal structure is affected and the other one is positional modulation where the atomic positions in the crystal structure are affected by the distortion. For positional modulation, the number of satellite reflections that can be observed depends on the amplitude of distortion (modulation). With stronger modulation in the structure, the intensities of the satellite reflections increase and at the same time the number of satellite reflections with measurable intensity increases. It should be emphasized that the modulated structures are not completely disordered but have long-range order which is reflected in terms of discrete additional satellite reflections.

1.3.1 Understanding the Diffraction Pattern

For a better understanding of the modulation in a crystal structure it is essential to describe the diffraction pattern obtained from the experiment. The diffraction pattern can be approached in three general ways.

1.3.1.1 Basic Unit Cell and Average Structure

In this method the weak satellite reflections are ignored. The main reflections are used for indexing and refinement and this sort of structure is commonly referred to as the average structure. In these sorts of structures, atoms might have large anisotropic displacement parameters as well as chemically unrealistic bond lengths and angles between mean atomic positions.

1.3.1.2 Supercell and Superstructure

In this method, the distinction between the satellite and main reflections is removed, all the reflections are considered as “main” reflections. Combining the satellite reflections with the main reflections we get a larger unit cell in direct space that is commonly referred to as a supercell. The resulting crystal structure is called a superstructure which will have a larger number of independent molecules in the asymmetric unit. For commensurate structures (the periodicity matches an integral number of lattice translation of the basic cell) the superstructure description is a valid approach (Hao *et al.*, 2005) but for incommensurate cases (the periodicity does not match with an integral number of lattice translations), problems may arise like poor agreement factors, large standard uncertainties of the refined parameters, large atomic displacement parameters of the atoms or poor geometry(Schmid & Wagner, 2005).

1.3.1.3 Superspace Approach

This discussion is primarily taken from Wagner & Schönleber, 2009. In this approach the distinction between the main and satellite reflections is maintained. At first, a reciprocal unit cell is established using the main reflections only. In the next step, additional vectors $\mathbf{q}_i$, so-called modulation wave vectors, are defined, which relate the satellite reflections to their parent main reflections. Then each satellite peak can be uniquely identified as being $n.\mathbf{q}$ (n = ±1, ±2, ±3, ±4…) away from its main reflection, and one speaks of the n^{th} order satellite reflection of this main reflection, as shown in Fig. 1.1. In three dimensional periodic structures three reciprocal vectors $\mathbf{a}^*$, $\mathbf{b}^*$, $\mathbf{c}^*$ describe the basic reciprocal unit cell, the modulation vector $\mathbf{q}$ can then be expressed with the help of fractional components: $\mathbf{q} = \alpha\mathbf{a}^* + \beta\mathbf{b}^* + \gamma\mathbf{c}^*$. Depending on the rationality of α, β, γ a modulated structure can be described as commensurate or incommensurate, for commensurate cases all the components (α, β, γ) are rational, but for incommensurate cases at least one of the components of α, β, γ is irrational (Wagner & Schönleber, 2009).

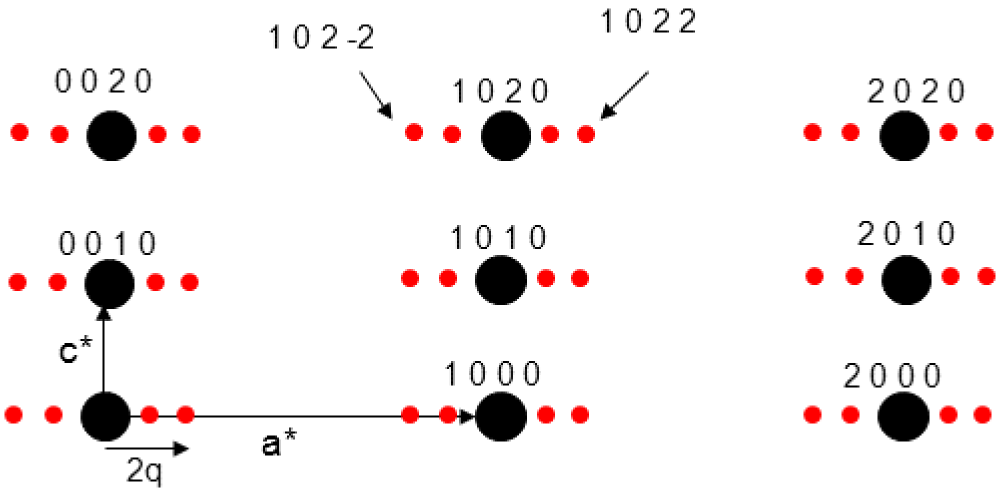

Fig. 1.1: Four dimensionally indexed diffraction pattern of a hypothetical one dimensionally modulated structure, where the vectors a* and c* define the basic reciprocal unit cell based on the main reflections. The additional vector q, reaching from the main reflection to the satellite can be expressed as q = 0.125a* + 0b* + 0c*.Taken from Fig. 6 of Wagner & Schönleber (2009).

1.3.2 Reciprocal Space and Direct Space in Aperiodic Crystals

The relationship between a diffraction pattern in reciprocal space and reciprocal superspace and between main and satellite reflections is illustrated in Fig. 1.2. A hypothetical four dimensional modulated structure is created by main and satellite reflections along **R***, where the reciprocal lattice vector $\mathbf{R}^* = h\mathbf{a}^* + k\mathbf{b}^* + l\mathbf{c}^*$ (h, k, l are integers between $-\infty$ to $+\infty$ and **a***, **b***, **c*** are reciprocal unit cell vectors). Here **q** is chosen in such a way that it is parallel to **a*** in Fig. 1.2, where **a*** is a reciprocal lattice (three dimensional) vector. The additional fourth dimension is defined by the unit vector $\mathbf{e}_4^*$, which is perpendicular to **a***. The linear combination of $\mathbf{e}_4^*$ and **q** defines the fourth reciprocal lattice vector $\mathbf{a}_{s4}^*$. Extending this vector $\mathbf{a}_{s4}^*$ illustrates that every satellite reflection along the three dimensional lattice vector **a*** can now be understood as a projection of a reflection along the reciprocal superspace vector $\mathbf{a}_{s4}^*$.

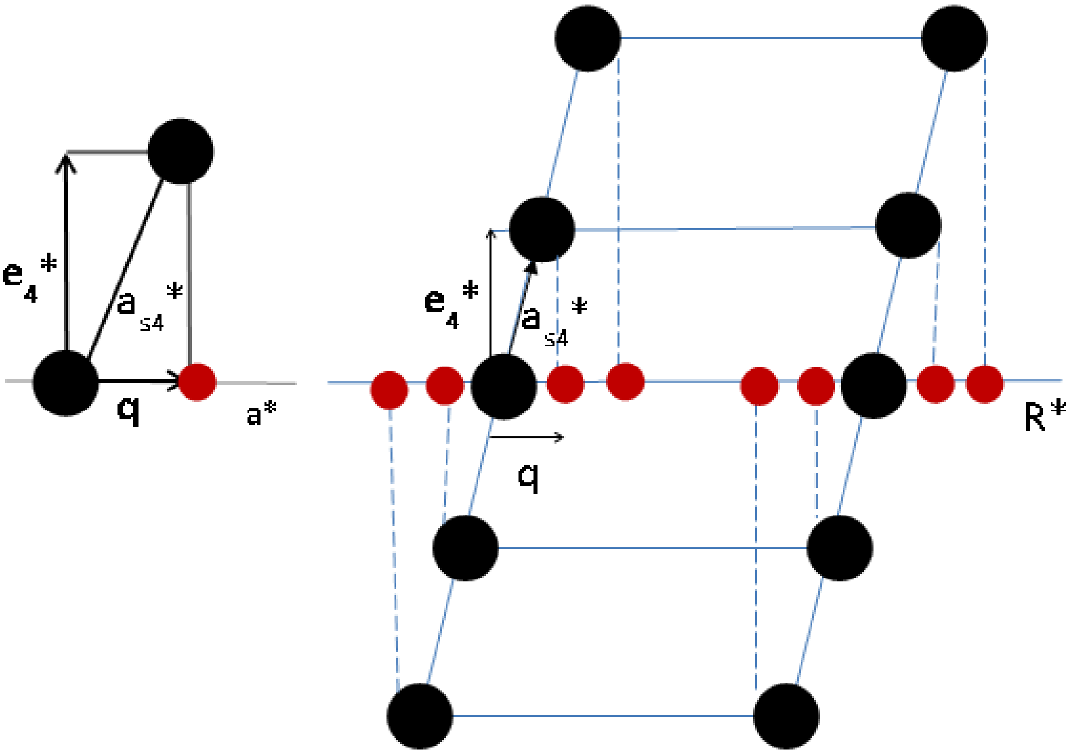

Fig. 1.2: The diffraction pattern of a one dimensionally modulated crystal. The reciprocal space is created by main and satellite reflections along R. The reflections along a_{s4}* are projected as satellite reflections onto the one dimensional space R*.Taken from Fig. 6. of Wagner & Schönleber (2009).*

The relationship between reciprocal space (diffraction) and direct space (crystal structure) has many similarities in aperiodic and periodic crystals (van Smaalen, 2004). In both cases, the diffraction is a result of the interference of the waves scattered by atoms. The lack of translational symmetry for aperiodic crystals complicates the computation of scattered waves for these materials, but the physics of scattering is the same as for the periodic crystals. The consequence is that geometrical correction factors, like Lorentz and polarization factors and absorption and extinction corrections, equally apply well to periodic and aperiodic crystals, provided that the true scattering vectors (Eq. 1.1) and scattering angles are employed in the formulas describing these effects. In periodic crystals, each reflection is indexed by three integers with respect to the reciprocal lattice of the translationally symmetric structure. The Bragg reflections for the aperiodic structures can then be indexed by integers, if instead of three; one can use additional vectors, according to Eq. 1.1

$$\mathbf{H} = \sum_{k=1}^{3+d} h_k \mathbf{a}^*_K \qquad \text{[Eq. 1.1]}$$

where **H** is the scattering vector (Welberry *et al.*, 1998) of the Bragg reflection in (3+d) reciprocal space, d is the number of additional periodicities, h_k are integers, and $\mathbf{a}^*_\mathbf{K}$ are reciprocal lattice vectors,

Once we have the scattering vector **H** for the aperiodic crystal one can use a Fourier transformation to get the electron density which is in 3D real space. The electron density of an aperiodic crystal in 3D space is given by the Fourier synthesis of the structure factors (Eq. 1.2):

$$\rho(\mathbf{r}) = \sum_{h_1}^{h_{3+d}} F(H) \exp[-2\Pi i \mathbf{H}.\mathbf{r}] \qquad \text{[Eq. 1.2]}$$

where the summation is over all observed Bragg reflections, $\rho(\mathbf{r})$ is the electron density in the 3D real space.

By similar logic, one can move in superspace, where reciprocal lattice vector will be according to Eq. 1.3,

$$\mathbf{H}_s = \sum_{k=1}^{3+d} h_k \mathbf{a}^*_{s,k} \qquad \text{[Eq. 1.3]}$$

where $\mathbf{H_s}$ is the vector in (3+d) D superspace. Now the Bragg reflections (Eq. 1.1) can be considered as the projections of the nodes of a reciprocal lattice in (3+d) D space, so called superspace. The reciprocal basis vectors $\mathbf{a^*_k}$ are the projections of the basis vectors $\mathbf{a^*_{s,k}}$ of a reciprocal lattice in (3+d) D superspace. The direct lattice of this reciprocal lattice then defines a periodic atomic structure in superspace. Now after establishing the relationships between the measured scattering vectors of the Bragg reflections (**H**) and the reciprocal lattice vectors in (3+d) D space ($\mathbf{H_s}$) described in Fig. 1.2, we can perform crystallography in superspace by assigning the observed intensities of the Bragg reflections to the corresponding reciprocal lattice vectors in superspace. The superspace electron density ($\rho_s(\mathbf{r}_s)$) is then derived from the Fourier transformation in superspace (Eq. 1.4):

$$\rho_s(\mathbf{r}_s) = \sum_{h_1}^{h_{3+d}} F(H_s)\exp[-2\Pi i\mathbf{H}_s.\mathbf{r}_s] \qquad \text{[Eq. 1.4]}$$

where the summation is all over all observed reflections, and $\mathbf{r_s}$ are the position vectors in superspace.

The only difference between a periodic and an aperiodic crystal is that $\rho(\mathbf{r})$ is a periodic function for the former type of crystals, while it is not periodic for aperiodic crystals. It has been shown in Fig. 1.2 that the experimental scattering vectors of Bragg reflections of aperiodic crystals are obtained as projections of the reciprocal lattice vectors in the (3+d) D superspace. Furthermore, the superspace electron density ($\rho_s(\mathbf{r}_s)$) can be defined as the inverse Fourier transformations of the structure factors in (3+d) D superspace. It is a mathematical property of Fourier transformation that a projection in reciprocal space is a section in direct space. Accordingly, non-periodic electron density in 3D can be obtained as a section perpendicular to the additional dimensions of the (3+d) periodic superspace electron density, which has been described schematically in Fig. 1.3.

$$\begin{tikzcd}
\rho_s(r_s) \arrow[r, shift right, "(3+d)\text{D FT}"'] \arrow[d, "\text{Intersection}"] & F(H_s) \arrow[l, shift right, "(3+d)\text{D inverse FT}"'] \arrow[d, "\text{Projection}"] \\
\rho(r) \arrow[r, shift right, "3\text{D FT}"'] & F(H) \arrow[l, shift right, "3\text{D inverse FT}"']
\end{tikzcd}$$

Fig. 1.3: The relationship between the electron density and the structure factors is given by the Fourier transformations (FT). 3D space is obtained from superspace by an intersection in direct space and by the projections of the reciprocal lattice points onto the reflection positions in reciprocal space. Taken from Fig. 6 of van Smaalen et al. (2004).

1.4 Disorder in 3D Periodic Crystals and Diffuse Scattering

In a crystal, molecules always try to pack in such a way that the free energy of the system is minimal, but it may be possible that due to conformational flexibility, the molecules can assume different conformations with similar energy and at local levels these molecules with different conformations or ions may not be able to arrange in a consistent way for chemical, steric or geometric reasons and this leads to disorder in the crystal as well. Disorder may change the periodicity in very specific ways or be completely random. If the periodicity changes in a very specific way that leads to additional Bragg peaks in the diffraction space. If the disorder causes the true repeat unit to become very large, the Bragg reflections occur very closer together. In the extreme of complete breakdown of periodicity in one direction, the Bragg reflections would become continuous streaks of diffuse scattering. If the breakdown of periodicity is two dimensional then it will form planes of diffuse scattering. A three dimensional breakdown of periodicity will result in diffuse clouds. It is also possible that the breakdown is only affecting one component of the chemical entity, and then periodicity is retained in the rest of the entity, so the Bragg reflections remain, and the diffuse detail is telling us about the “disordered” part. While conventional crystallography provides information about the average crystal structure (atomic coordinates, site occupancies or mean square atomic displacements which are all properties of single atom sites), diffuse scattering contains information about the deviation from the average structure. It gives structural information on a scale that extends beyond that of the average unit cell, over a range of 10-1000 Å. In many important materials, it is this extended range of structural information that is crucial in determining the unique or novel properties of the material, and not the structure averaged onto one unit cell. Rather than describing the single-site properties of the average structure, diffuse scattering contains information about pairs of sites and is thus a rich source of information on how atoms and molecules interact.

Disorder is nothing but variations in the average structure. It should be emphasized that when modulated structure (discussed in the previous section) loses its long range order and the orders only become short range, diffuse scattering arises. The variations in the average structure caused by various types of disorder are described in the following section.

1.4.1 Site Occupancy Disorder

When it is possible to describe a disordered structure completely in terms of variation in the occupation of the atom sites in the unit cell, some of these sites may be occupied randomly by different types of atoms (Yvon *et al.*, 1977). This is a very common situation in mineral structures, where a site is occupied statistically by an array of two or more atoms or ion types of similar size or may be vacant.

1.4.2 Positional and Orientational Disorder

Positional disorder occurs when one or more atoms or an entire molecule is distributed over two or more positions. Orientational disorder implies that a molecule or a part thereof is distributed over two orientations (Bürgi *et al.*, 1992).

1.4.3 Dynamic and Static Disorder

This discussion is primarily taken from Cowley (1995). So far it has been assumed that a disordered group is statistically distributed over two or more “rest” positions about which they vibrate. But with sufficient thermal energy, it is also possible for an atom or group of atoms to pass back and forth between the alternative positions, giving a dynamic equilibrium. In such cases, the model for a structure will exhibit large, possibly highly anisotropic atomic displacement parameters. X-rays cannot distinguish between dynamic and static disorder (Boese *et al.*, 1998). It may be possible, by carrying out investigations at different temperatures and especially at very lower temperatures, to observe changes in atomic displacement parameters which might be indicative of the types of disorder. By this means, it may be possible to observe a free rotating group freeze into a single position. On the other hand, a dynamic situation may pass smoothly over into a static disorder, and there will be no significant change in the diffraction. To differentiate dynamic and static disorder other physical methods, like thermal analysis combined with single crystal X-ray diffraction may provide useful information.

Diffuse scattering can be elastic (Marshall, 1968), quasielastic (Hlinka *et al.*, 2003) and inelastic (Vanbodegom *et al.*, 1981) in nature. In the case of elastic scattering, the incident beam does not change its energy during the scattering process. This is the case for diffuse scattering from static disorder phenomena. Quasi-elastic and inelastic scattering occur when the energy of the beam changes during the scattering process. This type of diffuse scattering is due to dynamic disorder. A diffuse scattering measurement in which no energy discrimination is used effectively integrates over all intensities, i.e. the distinction between elastic and inelastic scattering is lost. The observed intensity is then a time average of the instantaneous intensities. This time averaging can be considered equivalent to an averaging over space (Cowley, 1995). Usually the region of a homogeneous sample, which reflects coherently, is limited in size to be very much smaller than the total illuminated size. The reason for this behaviour is on the one hand due to the size of the mosaic grains of the crystals and on the other hand due to the limitations on the coherence of the incident beam. The lateral coherence of the beam is on the order of several hundred angstroms and is limited by the divergence of the beam. The coherence of the beam in the direction of the propagation is limited by the monochromaticity and is typically on the order of about one micron for X-rays from a sealed tube source. Thus, the total diffracted intensity corresponds to the incoherent summation of the scattering intensities from a large number of independent but statistically equivalent regions. This is the same as the incoherent summation of the scattering intensities from any one region at different times. In time any one region may take all the possible configurations of the atoms present and for a large number of independent regions, all possible configurations are present at any time.

Provided that kinematical theory of diffraction applies, the diffraction pattern of any object is the Fourier transformation of the pair-correlation function. Information on multi-site interactions between atoms or arrangements of atoms does not directly contribute to the diffraction patterns (Welberry, 1986). However, their effects are felt indirectly, for example in the constraints that are imposed on the two sites interactions and the way in which these decay with distance. Two-site and multi-site interactions are not independent since the need to densely fill the space with atoms restricts the possible atomic arrangements. Multi-site occupational correlations can result distinctive diffraction effects when additional relaxation displacements are considered. However, if a system has properties that stem from multi-site interactions, there is no simple way in which these can be related to the observed intensities. The diffuse scattering from such a system arises from pair correlations, which are indirectly generated from the fundamental multi-site interaction (Welberry, 2004).

Developments in the analysis of diffuse scattering are quite limited. One of the main reasons for this slow progress is that diffuse scattering intensities are very weak in comparison to Bragg peaks, making the experimental observation more demanding and time consuming. Only with the increasing availability of synchrotron radiation has this obstacle been, if not removed, substantially diminished. Secondly, the sheer diversity of different types of disorder and their effect on the diffraction pattern made it difficult to formulate a solution strategy that would work for all problems (Welberry, 1985).

With recent advancements in computing power (processor speeds, memory and storage) it is becoming possible to perform computer simulations taking account the chemical knowledge of the model system. This has emerged as a general method by which the diffuse scattering problem may be tackled in a systematic manner (Welberry & Goossens, 2008). The bottleneck is that there is no readily accessible software for the users, which can be used to model and interpret the diffuse scattering in a routine manner.

1.4.4 Modelling Techniques

It is becoming increasingly common for scientists to adopt computer simulation methods to investigate crystalline systems. It is often not possible to apply established theoretical descriptions to disordered systems analytically, and it quickly becomes a complex task to rigorously describe the interactions between the atoms as the material becomes increasingly disordered and the formula unit becomes larger. Nevertheless, computer simulations can be used to bridge the gap between theory and experiment. This is completely true in the case of structural disorder where a more complete picture may be obtained from computer simulations than from an analytical treatment that relies on a number of possibly inappropriate approximations. Nowadays, a model system can be simulated that closely represent the physical system of interest (Weber & Bürgi, 2002).

The analysis of diffuse scattering using model calculations of disordered structures involves the comparison of calculated diffuse scattering from the model structure with the experimental diffuse scattering. This approach does not give a unique solution of the problem. However, with the incorporation of chemical knowledge into the construction of a disordered structure model, both chemically and physically meaningful solutions can be found.

1.5 Organization of the Thesis

We are studying the "cubic" phase of $NaLuF_4$, which shows light up-conversion properties when doped with rare earth ions. The diffraction pattern from crystals of this compound shows strong satellite reflections (indicative of modulation) around the main reflections, strong diffuse scattering (indicative of disorder) and split high angle main reflections (indicative of twinning). Understanding of the structural complexity may give a better insight of physical properties of the material. In the remaining chapters of this thesis, the origin of this observed complex diffraction pattern in terms of the structural model will be discussed.

The thesis is divided into 6 parts. **Chapter 1** has introduced the concept of periodicity in crystals and the consequences of breakdown of periodicity, caused by structural complexity, on the diffraction pattern.

Chapter 2 contains an elementary discussion of the light up-conversion processes and the exploitation of up-conversion in the field of materials science. In this chapter, we will also discuss materials that have been used for light up-conversion processes and the importance of understanding the local structure in order to be able to improve the up-conversion properties. Properly understanding the true structure will also show that sometimes the average structure from Bragg reflections may contradict the properties of a material determined by some other method. A synthetic route for the synthesis of "cubic" $NaLuF_4$ will also be given in this chapter.

Chapter 3 describes the diffraction studies of the different phases of “cubic” $NaLuF_4$ obtained from its melt. Mainly two types of diffraction pattern were obtained from the different phases: one diffraction pattern has satellite reflections around the main reflections and strong diffuse scattering. These data will be termed the satellite data set, another diffraction pattern contains only main reflections with strong diffuse scattering; it will be termed as the non-satellite data set. This chapter also discusses the sixfold twinning present in both data sets.

Chapter 4 contains the detailed description of the derivation and refinement of the model for the average structure of the phase that produces the non-satellite data set and a qualitative description of the disorder present in the structure.

Chapter 5 contains the detailed description of the derivation and refinement of the model for the average structure of the phase that produces the satellite data set and a description of the modulation present in the superstructure. A qualitative description of the disorder present in the structure will also be discussed.

Chapter 6 describes the importance of understanding the local structure beyond the average structure and how the above study can be used as a start point for modelling the possible disorder quantitatively from the diffuse scattering.

1.6 References

Boese, R., Antipin, M. Y., Blaser, D. & Lyssenko, K. A. (1998). *J. Phys. Chem. B* **102**, 8654-8660.

Bürgi, H. B., Blanc, E., Schwarzenbach, D., Liu, S. Z., Lu, Y. J., Kappes, M. M. & Ibers, J. A. (1992). *Angew. Chem. Int. Ed. Engl.* **31**, 640-643.

Cowley, J. M. (1995). *Diffraction Physics*, 3rd edition ed. Amsterdam:North-Holland.

Hao, X., Parkin, S. & Brock, C. P. (2005). *Acta Cryst. B***61**, 675-688.

Haüy, R. J. (1784). *Essai d'une théorie sur la structure des crystaux : appliquée a plusieurs genres de substances crystallisées*. Gogué & Née, Paris.

Haüy, R. J. (1801). *Traité de minéralogie*. Louis, Paris.

Herbst-Irmer, R. & Sheldrick, G. M. (1998). *Acta Cryst. B***54**, 443-449.

Hlinka, J., Kamba, S., Petzelt, J., Kulda, J., Randall, C. A. & Zhang, S. J. (2003). *J. Phys. Condens. Matter* **15**, 4249-4257.

Jiang, J. Y., Kaafarani, B. R., Kirschbaum, K., Hu, Y. & Neckers, D. C. (2007). *Acta Cryst. E***63**, O3760-U2601.

Kleemann, W., Schafer, F. J. & Chaves, A. S. (1987). *Solid State Commun.* **64**, 1001-1004.

Lam, E. J. W., Beurskens, P. T., Smits, J. M. M., Smaalen, S. v., Deboer, J. L. & Fan, H. F. (1995). *Acta Cryst. B* **51**, 779-789.

Marshall, W. (1968). *J. Phys. C: Solid State Phys.* **1**, 88-101.

Partik, M., Kringe, C. & Lutz, H. D. (1996). *Z. Kristallogr.* **211**, 304-312.

Petrícek, V., Vanderlee, A. & Evain, M. (1995). *Acta Cryst. A***51**, 529-535.

Romé de l'Isle, J. B. L. d. (1772). *Essai de Cristallographie*. Didot Knapen and Delaguette, Paris.

Romé de l'Isle, J. B. L. d. (1783). *Cristallographie*. Imprimerie de Monsieur, Paris.

Schmid, S. & Wagner, T. (2005). *Acta Cryst. B***61**, 361-366.

van Smaalen, S. (2004). *Z. Kristallogr.* **219**, 681-691.

Vanbodegom, B., Larson, B. C. & Mook, H. A. (1981). *Phys. Rev. B***24**, 1520-1523.

Wagner, T. & Schönleber, A. (2009). *Acta Cryst. B***65**, 249-268.

Weber, T. & Bürgi, H. B. (2002). *Acta Cryst. A***58**, 526-540.

Welberry, T. R. (1985). *Rep Prog Phys* **48**, 1543-1593.

Welberry, T. R. (1986). *J. Appl. Cryst.* **19**, 382-389.

Welberry, T. R. (2004). *Diffuse X-Ray Scattering and Models of Disorder. IUCr Monographs on Crystallography*. Oxford University Press, UK.

Welberry, T. R. & Goossens, D. J. (2008). *Acta Cryst. A***64**, 23-32.

Welberry, T. R., Proffen, T. & Bown, M. (1998). *Acta Cryst. A***54**, 661-674.

Wolff, P. M. de, Janssen, T. & Janner, A. (1981). *Acta Cryst. A***37**, 625-636.

Yvon, K., Paoli, A., Flukiger, R. & Chevrel, R. (1977). *Acta Cryst. B***33**, 3066-3072.

Chapter 2: Light Up-conversion and Material for Up-conversion

The physical properties of a material are closely related to its structure. A better understanding of the structure may give more control of the physical properties of the material. One such property which is related with the family of lanthanide-halides is up-conversion properties. In this chapter we will give a brief introduction of the concept of light up-conversion. Then we will discuss how the understanding of a structure may give a better understanding of up-conversion.

2.1 Up-Conversion and its Application

This discussion is primarily taken from Ronda (2007). Up-Conversion (UC) phosphors are capable of absorbing photons of a certain energy E_1 and emitting photons with another energy E_2, such that $E_2 > E_1$ (Auzel, 2004). Depending on the physical mechanism, these up-conversion phosphors can be divided into two types: single photon process up-conversion or multi-photon process up-conversion. The most famous single-photon conversion process is anti-Stokes emission, where one photon is absorbed and subsequently emitted at higher energy. The additional energy is usually provided by the lattice in the form of the annihilation of one or more phonons, which makes it less efficient. In the multi-photon processes, two or more incident photons are converted into one photon of substantially higher energy.

The mechanism of conversion of long-wavelength excitation light into short-wavelength emission light may occur in several ways. Some of the most important ones are summarized here (Ronda, 2007). Fig. 2.1(a) describes an often-used, though rather inefficient, process: anti-Stokes Raman emission. Here, a vibronic excited state of the ground state is the initial state. After absorption of a photon, emission occurs from a virtual excited state down to the real ground state. As a result, the emission energy lies at a somewhat higher level than the excitation energy, and the energy difference depends on the phonon spectrum of the material.

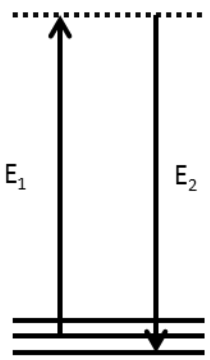

Fig. 2.1(a): Anti–Stokes Raman emission. The dotted horizontal line indicates a virtual state, an upward arrow indicates excitation and a downward arrow indicates emission.

Fig. 2.1(b) schematically indicates the process of two photon absorption (TPA). In this case the intermediate state is still a virtual one, but now both the ground state and the excited state are real. TPA occurs when a single excitation photon cannot bridge the gap between the ground state and the excited state, but two excitation photons can.

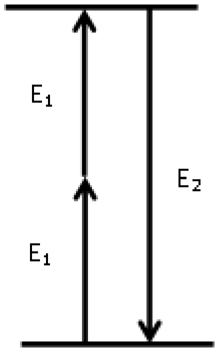

Fig. 2.1(b): Two photon absorption. An upward arrow indicates excitation and a downward arrow indicates emission.

Fig 2.1(c) illustrates second harmonic generation (SHG) as may occur in e.g., the green 532 nm emission observed from $KNbO_3$ crystals under 1064 nm excitation. Here, only the ground state is real, both the intermediate and the excited states are virtual. This implies that the two excitation photons must coincide and must also be coherent.

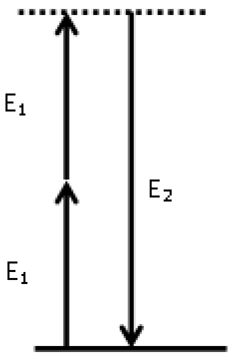

Fig. 2.1(c): Second harmonic generation. The dotted horizontal line indicates a virtual state, an upward arrow indicates excitation and a downward arrow indicates emission.

Fig. 2.1(d) shows the up-conversion fluorescence process shown by $NaLnF_4$ (Ln = Y, La-Lu) when Ln is replaced in any ratio by other rare-earth ions, where the wavelength of the emitted light is shorter than that of the excited light (Lucy, 1972). One kind of mechanism for this up-conversion process, as illustrated in Fig. 2.1(d), is sequential absorption of pump photons by excited-state absorption. A first absorption process leads to some metastable excited level, from where further absorption can take the ion to even higher levels. Such a process requires high pump intensities, but not necessarily high doping concentration.

Another type of mechanism involves energy transfer process between ions of different species. Here, e.g. two different ions in a metastable intermediate level interact to excite one ion into a higher state while the other one becomes de-excited (cooperative up-conversion). High doping densities are usually required in order to make such energy transfers possible (Scheps, 1996).

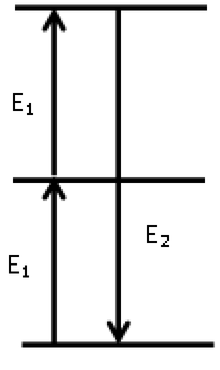

Fig. 2.1(d): Up-conversion fluorescence. An upward arrow indicates excitation, and a downward arrow indicates emission.

Fig. 2.1(e) shows the cooperative luminescence process. Here, two excitation photons are sequentially absorbed by two different active ions, bringing both of them into their excited states. Next, both excited ions simultaneously decay to their ground states with emission of a single photon that contains the combined energy of both ions.

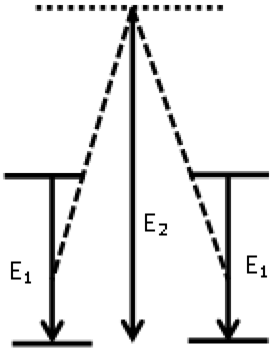

Fig. 2.1(e): Cooperative luminescence. A dotted horizontal line indicates virtual state and a downward arrow indicates emission.

Fig. 2.1(f) shows cooperative sensitization, a process that is quite similar to the cooperative luminescence process. In this process, again two excitation photons are sequentially absorbed by two different active ions, bringing both of them into their excited states. However, now the energy of the two excited ions is transferred to another ion, bringing it from its ground state into an excited state at an energy resonant with the sum of the two excitation energies. As the final state is a real one, in contrast with the case of cooperative luminescence, the cooperative sensitization is more efficient than cooperative luminescence.

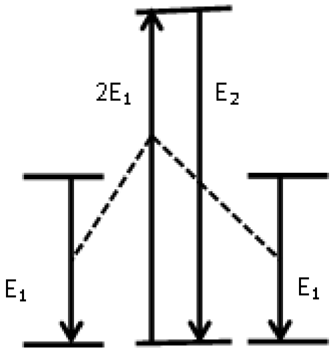

Fig. 2.1(f): Cooperative sensitization. An upward arrow indicates excitation and a downward arrow indicates emission.

The other three photon up-conversion processes are excited state absorption, energy transfer up-conversion, and sensitized energy transfer up-conversion. Such up-conversions may involve a single ion or may involve two types of ion depending on the mechanism. Up-conversion involves four main processes which have been schematically depicted in Fig. 2.2(a)-(d). The first and second processes involve excitation of a material from its ground state or from an excited state, respectively, shown in Fig. 2.2 (a) and (b). When two ions are both in an excited state, energy transfer up-conversion can take place, as shown in Fig. 2.2 (c). As a result of this process, one ion is de-excited to a lower energy state, while the second is excited to a higher energy state. The fourth process, cross-relaxation, is the reverse of energy transfer up-conversion: one is excited to a higher-energy state, while the second is de-excited to a lower-energy state. This process is shown in Fig. 2.2(d). The distinction between these last two processes lies in the highest excited state: if, after the process, one of the ions is in a higher excited state than either of the ions before the process, one speaks of energy transfer up-conversion. If this is not the case, one speaks of cross-relaxation. Usually for the up-converting phosphors, energy transfer up-conversion is a wanted process, while cross-relaxation is considered to be undesirable.

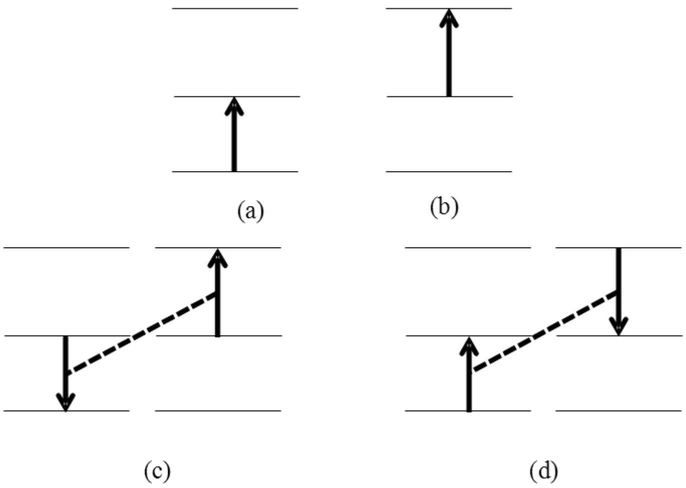

Fig. 2.2: The four main energy transfer processes that are important for up-conversion (a) ground-state absorption (b) excited state absorption (c) energy transfer up-conversion (d) cross-relaxation

Such up-conversion phosphors have attracted considerable interest in the fields of lighting and display technology since the development of IR laser diodes (Phillips *et al.*, 2000). In recent times, up-conversion phosphors have been applied in immunoassays (Niedbala *et al.*, 2001).

2.2 Materials for Up-Conversion

Solid trivalent lanthanide halides when doped with other rare earth ions, convert near- infrared (NIR) radiation into visible light by the method of up-conversion. This was first studied more than 30 years ago (Kano *et al.*, 1972). Hexagonal $NaYF_4$ is an efficient host material for green and blue phosphors (Krämer *et al.*, 2004). In the case of hexagonal $NaYF_4$, Y^{3+} can be replaced in any ratio by any rare earth ion, e.g., by Yb^{3+} and Er^{3+} or by Yb^{3+} and Tm^{3+} for green or blue UC phosphors, respectively. But it is an open question as to why the UC efficiency in this host material is superior to other upconverters like transition metal upconverters (Moncorge *et al.*, 1985), mixed rare earth/transition metal systems (Ovsyanki.Vv & Feofilov, 1966) and nanocrystalline upconverters (Capobianco *et al.*, 2000). So to understand the method of up-conversion, as well as to improve the properties of such materials, it is important to understand the local solid-state structure of this family of lanthanides.

Thoma *et al.* reported the quasi binary phase diagrams (Fig. 2.3) of $NaF\text{-}LnF_3$ with Ln = Y, La-Lu (Thoma *et al.*, 1966). Two equilibrium compounds of the formula $NaF.LnF_3$ and $5NaF.9LnF_3$ were observed within each of the $NaF\text{-}LnF_3$ systems from $NaF\text{-}PrF_3$ to $NaF\text{-}LuF_3$.The hexagonal $NaF.LnF_3$ ($\beta\text{-}NaLnF_4$) is stable at temperatures below approximately 600 to 700 ^{o}C for the whole series of lanthanides and yttrium. On heating, they decompose in a variety of phase reactions, which differ sufficiently from each other in character and properties to enable one $NaF\text{-}LnF_3$ system to be distinguished from another. In the systems of $NaF\text{-}LaF_3$ and $NaF\text{-}CeF_3$ the hexagonal phase melts incongruently to an NaF enriched melt and cubic LaF_3, while $NaF\text{-}TbF_3$ to $NaF\text{-}GdF_3$ melt incongruently to an NaF enriched melt and cubic $NaF.LnF_3$. In the systems $NaF\text{-}TbF_3$ to $NaF\text{-}LuF_3$ a disordered cubic phase of variable composition appears depending on size of the Ln^{3+} cation. The cubic solid solution phases are unstable below temperatures varying from 800-530 ^{o}C. On cooling, they transform into to a variety of products depending on the composition of the decomposing phases. At equi-molar $NaF\text{-}LnF_3$ compositions, partial ordering occurs and the hexagonal $NaF.LnF_3$ phase forms. At the $5NaF.9LnF_3$ phase boundary, the cubic phases of $NaF\text{-}PrF_3$ to $NaF\text{-}TbF_3$ decompose on cooling to hexagonal $NaF.LnF_3$ and LnF_3. In the systems $NaF\text{-}DyF_3$ to $NaF\text{-}LuF_3$ the cubic phase again becomes partially ordered on cooling and transforms into an orthorhombic form of the compound which, except for 5NaF.9LuF$_3$, is also unstable at lower temperatures with respect to NaF.LnF$_3$ and LnF$_3$.

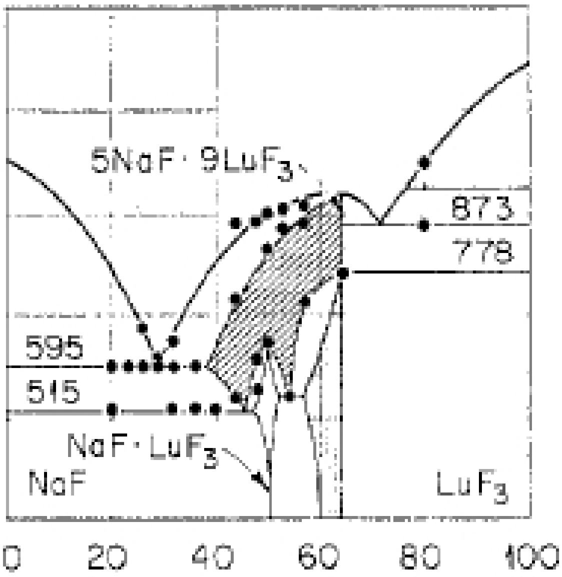

Fig. 2.3: The equilibrium phase diagram of the NaF-LuF$_3$ system. Diagonally hatched areas indicate cubic solid solution phases and dotted areas indicate orthorhombic phases. Taken from Fig. 1 of Thoma et al. (1966).

Most of the reported spectroscopic studies on doped *β*-NaLnF$_4$ (Ln = Y, La-Lu) have been done using powder samples (Suyver *et al.*, 2005). However there was not little progress in correlating the up-conversion properties with the structures of lanthanide host materials. The crystal structure of the hexagonal phase was determined by Burns for NaNdF$_4$ (Burns, 1965). The disordered structure was described with an average structure in space group *P*-6. Sobolev et al. Sobolev *et al.*(1963) related the structure of *β*-NaLnF$_4$ to gargarinite, NaCaLaF$_6$, with space group *P*6$_3$/*m*. They agree on the positions of 6 F$^-$ anions per unit cell, but there are differences about the cation sites and distribution.

Aebischer *et al.* (2006) reported the first polarized absorption spectra from single crystals of *β*-NaGdF$_4$ doped with Er^{3+}. They interpreted the spectra on the basis of a microscopic model of the structural disorder as derived from diffuse scattering experiments and showed that standard single-crystal X-ray diffraction methods produce misleading results. X-ray data indicate an average structure with two different, but C_{3h} symmetric Ln^{3+} sites, whereas the spectroscopic data indicate only one such site and another one lacking C_{3h} symmetry.

The average structure (Fig. 2.4) of *β*-$NaLnF_4$ compounds shows three different columns of cations. Site A at (2/3, 1/3, 1/2), as well as site B at (0, 0, 0), are coordinated by nine F^- ions forming tricapped trigonal prisms with crystallographic C_{3h} symmetry. Site B is fully occupied by Ln^{3+}, whereas site A shows occupational disorder involving a 1:1 ratio of Na^+ and Ln^{3+}. The third cation site, with irregular octahedral coordination, is half vacant and half occupied by Na^+.

Disorder in the structure of *β*-$NaLaF_4$ was characterized from a diffuse scattering experiment and from reconstructions of the undistorted planes of the reciprocal space from the raw diffraction data of *β*-$NaLaF_4$. The main characteristic features present in **a***, **b*** planes at l = (2n + 1)/2. The main features in these planes are: diffuse scattering is sharp along the **c*** direction (Fig. 2.5), a honeycomb pattern within the planes with webs at h and/or k = (2n + 1)/2, different modulation of the honeycomb pattern (Fig. 2.6) in the consecutive planes like (*hk*-1.5) and (*hk*-2.5).

The sharpness of the honeycomb layers along c* implies a real structure with translational order along **c**, that is, within the column of site A the Na2 and Ln2 alternate with a repeat distance **c'** = 2**c** corresponding to a reciprocal repeat distance **c*'** = **c***/2 (Fig. 2.5). The continuous honeycomb pattern in the **a***, **b*** plane requires a disordered arrangement of adjacent ordered Na2/Ln2 columns along a and b; from the diffuse scattering pattern it can be predicated that Na2…Ln2 columns tend to be next to Ln2…Na2 columns. If Na2…Ln2 columns tend to be next to Na2…Ln2 columns, which will be an ordered structure and it would produce broad maxima at integer values of h and l which are not observed experimentally (Fig. 2.6). After the alignment of Na2…Ln2 and Ln2…Na2 columns of metal ions in an antiparallel way, third column will be a frustrated one because it has two possible orientations, Na2…Ln2 and Ln2…Na2, give the same energy. This will cause disorder in the structure and hence diffuse scattering will be observed in the diffraction pattern of the compound. Because of strict alternation of Ln2 and Na2 in the Ln2…Na2 columns and due to columbic interactions, fluorine atoms shift from $Na2^+$ towards $Ln2^{3+}$. Such a displacement enhances the intensity of the diffuse signal in a ring of six hexagons around the origin in the (*hk*-1.5) layer (Fig. 2.6) and of the central hexagon in the (*hk*-2.5) layer (Fig. 2.6).

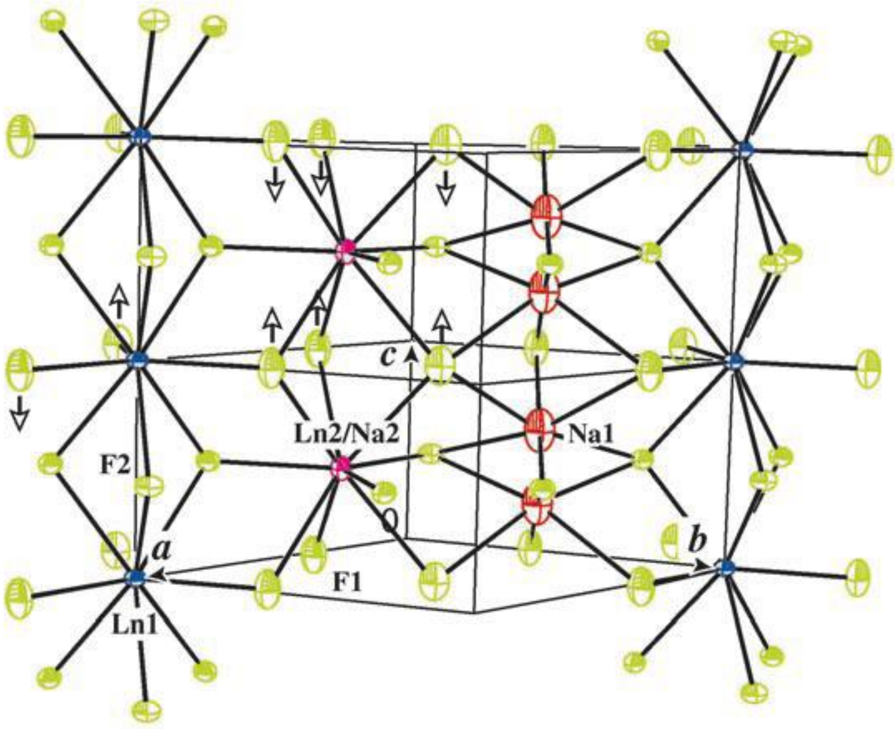

Fig. 2.4: The average structure of β-NaLnF$_4$ (Ln = Y, La-Lu) showing three different columns of metal sites running parallel to the c axis: site A with a 1:1 mixture of Na, Ln (pink colour), Site B with Ln1 (blue), both with C$_{3h}$ symmetric, trigonal tricapped prismatic coordination, and the Na1 site (red) with C$_3$ symmetric, distorted octahedral coordination. Local distortions of the F atoms are shown by arrows. Taken from Fig. 1 of Aebischer et al. (2006).

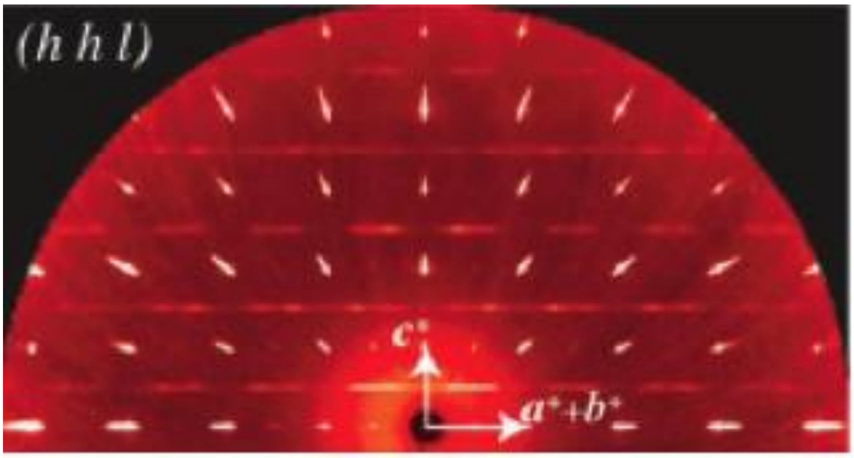

Fig. 2.5: The (hhl) reciprocal layer showing the traces of the planes of diffuse scattering parallel to a* + b* at l = (2n + 1)/2 between a regular array of Bragg reflections at integer l. The diffuse planes are sharp along c* but diffuse intensities are weaker than the Bragg intensities. Taken from Fig. 1 of Aebischer et al. (2006).

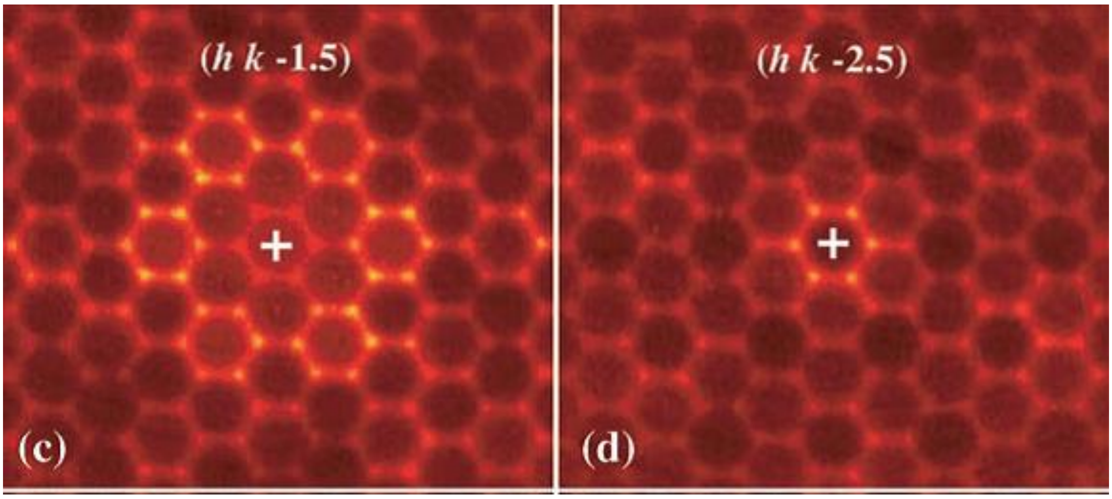

Fig. 2.6: Reciprocal layers (hk-1.5, hk-2.5) showing the honeycomb pattern in the a*b* plane. Taken from Fig. 2 of Aebischer et al. (2006).

The six F1 atoms forming the trigonal prism around site A (Na2/Ln2 columns) are displaced in unison towards Ln2 and away from Na2, implying that site A preserves local C_{3h} symmetry. But for site B (Ln2 columns), the local symmetry is reduced to C_3 or C_1 from C_{3h} depending upon the number of displacement directions of the fluorine atoms (Fig. 2.4). With this interpretation of the disorder from diffuse scattering it was straightforward to assign the crystallographic sites A and B to the spectroscopic sets A and B, respectively which were assigned by site-selective excitation experiments by Aebischer *et al.* (2006). The spectroscopic intensity ratio A/B of about 0.5, is in agreement with the structural site occupancies by Ln of 0.5 and 1, respectively. The study showed that where disorder is present in a structure, the average structure, as obtained from an analysis of only the Bragg reflections may be inconsistent with the data obtained from other physical methods.

The above observations clearly indicate that it is essential to understand the local structure instead of the average structure for a better understanding of the physical properties of the material. The cubic phase of the NaF-LuF$_3$ system α-NaLuF$_4$ is a disordered fluorite related phase with two orders of magnitude less UC efficiency than the β-phase. We believe that the structural analysis of this phase may give a better insight into these weaker UC properties and this study forms the body of the work reported in this thesis.

2.3 Preparation of $Na_5Lu_9F_{32}$ (“cubic” phase of $NaLuF_4$) Samples

Powder samples were prepared from rare-earth oxide of lutetium (Lu_2O_3) of 5N (0.99999) or 6N (0.999999) purity, Na_2CO_3, and 65% HNO_3 and 40% HF acids in H_2O according to the method described by Krämer *et al.* (2004). Batches are typically calculated in such a way that the product amount is about five grams. Lu_2O_3 was dissolved in a small amount of HNO_3 in a Teflon beaker, evaporated to dryness, dissolved in water, and LuF_3 precipitated with HF. The liquid was evaporated and HF was added again. An amount of Na_2CO_3 to obtain a 5:9 ratio of Na:Lu was dissolved in water in a separate beaker and slowly added to the mixture. Care has been taken to avoid spilling due to the CO_2 evolution. The product was dried, and the addition of HF and drying were repeated. The solid, which consists of a mixture of LuF_3 and NaF according to powder X-ray diffraction, was ground up in a mortar, transferred to a glassy carbon boat, and heated to 550 °C in a HF/Ar gas stream for twenty hours. In this step, the reaction toward the sodium lutetium fluoride phase took place. The HF gas stream removed traces of oxygen. For the crystal growth, the resulting powder was transferred into a glassy carbon ampoule, evacuated and purged with argon, heated to 950 °C and cooled slowly to room temperature in a temperature gradient in a Bridgman furnace over about 4 weeks (Cox & Fong, 1973).

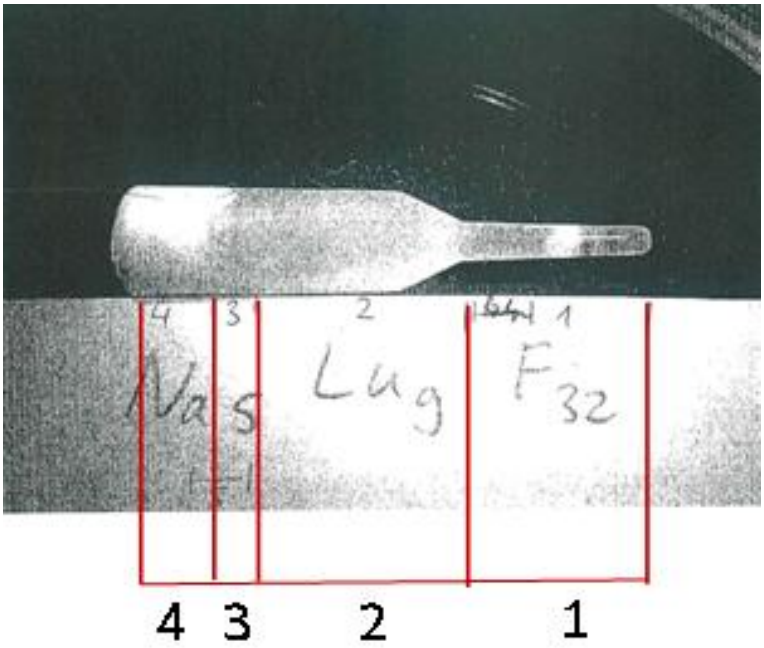

Fig. 2.7: Sample of α-$NaLuF_4$ obtained from its melt. Zones marked with 1, 2, 3, 4 indicate different parts of the sample and samples from zone 1, 2 and 3 were used for the diffraction experiment.

The extreme right part of the sample in Fig. 2.7 was cooled down first and was first crystallized from the melt. The crystallization proceeds from the right to left direction as the cooling direction is from left to right in the Bridgman furnace. The extreme left part in the Fig. 2.7 was cooled down at the end in the Bridgman furnace and is not crystalline. This extreme left part of the sample was marked as Zone 4 and this part is called eutectic. The remaining part of the sample in the glassy carbon ampule is crystalline in nature. The crystalline part of the sample was divided into 3 parts named, Zone 1, Zone 2 and Zone 3. The boundary between zones 1, 2 and 3 was selected randomly. A sample from each Zone 1, 2 and 3 was selected for the diffraction experiment to find out the similarities as well as dissimilarities. The composition of the entire crystalline part is $Na_5Lu_9F_{32}$. The composition of the sample was confirmed by Energy-Dispersive X-ray spectroscopy (EDX) analysis on the samples from the different zones of 1, 2 and 3. The EDX analysis was performed by Dr. Karl Krämer from University of Bern.

2.4 References

Aebischer, A., Hostettler, M., Haüser, J., Krämer, K., Weber, T., Güdel, H. U. & Bürgi, H. B. (2006). *Angew. Chem. Int. Ed.* **45**, 2802-2806.

Auzel, F. (2004). *Chem. Rev.* **104**, 139-173.

Burns, J. H. (1965). *Inorg. Chem.* **4**, 881-886.

Capobianco, J. A., Vetrone, F., D'Alesio, T., Tessari, G., Speghini, A. & Bettinelli, M. (2000). *Phys. Chem. Chem. Phys.* **2**, 3203-3207.

Cox, D. E. & Fong, F. K. (1973). *J. Cryst. Growth* **20**, 233-238.

Kano, T., Otomo, Y. & Yamamoto, H. (1972). *J. Electrochem. Soc.* **119**, 1561-1564.

Krämer, K. W., Biner, D., Frei, G., Güdel, H. U., Hehlen, M. P. & Luthi, S. R. (2004). *Chem. Mater.* **16**, 1244-1251.

Lucy, R. F. (1972). *Appl. Optics* **11**, 1329-1336.

Moncorge, R., Auzel, F. & Breteau, J. M. (1985). *Philos Mag B* **51**, 489-499.

Niedbala, R. S., Feindt, H., Kardos, K., Vail, T., Burton, J., Bielska, B., Li, S., Milunic, D., Bourdelle, P. & Vallejo, R. (2001). *Anal. Biochem.* **293**, 22-30.

Ovsyankin,V. V. & Feofilov, P. P. (1966). *JETP Lett* **3**, 322-323.

Phillips, M. L. F., Hehlen, M. P., Nguyen, K., Sheldon, J. M. & Cockroft, N. J. (2000). Physics and Chemistry of Luminescent Materials: Proceedings of the Eighth International Symposium.

Ronda, C. (2007). *Luminescence from theory to applications*. Weinheim: Wiley-Vch.

Scheps, R. (1996). *Prog. Quant. Electron.* **20**, 271-358.

Sobolev, B. P., Mineev, D. A. & Pashutin, V. P. (1963). *Dokl Akad Nauk Sssr* **150**, 791-794.

Suyver, J. F., Grimm, J., Krämer, K. W. & Güdel, H. U. (2005). *J. Lumin.* **114**, 53-59.

Thoma, R. E., Insley, H. & Hebert, G. M. (1966). *Inorg. Chem.* **5**, 1222-&.

Chapter 3: The Interpretation of the Diffraction Patterns and Data Integration

The first step in the determination of any crystal structure from its single-crystal diffraction data is to record and analyse the diffraction pattern itself. This chapter describes (1) the considerations behind choosing the optimal experimental conditions necessary to collect the desired diffraction data from the α-NaLuF$_4$ samples, whose diffraction patterns are far from routine, (2) the details of the experiments themselves, and (3) the analysis and interpretation of the obtained diffraction patterns from the points of view of initial visual observations, understanding what the diffraction patterns telling us and the integration of the data in preparation for structure solution, modelling and model refinement. The complexity of the diffraction patterns required non-trivial data reduction methods and extensive trials in order to extract optimal and correct intensities.

3.1 Experimental Considerations

In planning to collect diffraction data from a crystalline sample, one has to consider several aspects of the experimental setup. These include the intensity of the X-ray beam, the desired wavelength, the desired resolution of the data, the detector type and the goniometer type. For any given crystalline material, one needs to tailor the experiment in order to achieve the best data and to achieve the aims of the experiment. Sometimes optimizing one aspect of an experiment might have a detrimental effect on another parameter, so a balance often has to be found. The following items need to be considered.

3.1.1 X-ray Source

The diffractometer available in our laboratory is a Nonius KappaCCD fitted with Mo Kα radiation (λ = 0.71073 Å) from a sealed tube source. Such a wavelength is appropriate for obtaining data to a high resolution of 0.7 Å or better, provided the sample diffracts well. The disadvantages are that the wavelength is fixed and the intensity of the X-ray beam is limited.

Another source of X-rays is synchrotron radiation. A synchrotron provides very high intensity X-ray beams several orders of magnitude more intense than standard sealed-tube X-ray sources. The wavelength is also tuneable. We have access to the Swiss Norwegian Beam Lines (SNBL-01A) of the European Synchrotron Radiation

Facility (ESRF) in Grenoble. The beam from the SNBL is 1000 times more intense than a sealed tube source and the wavelength can be tuned within the range of 0.5 - 1.5 Å.

3.1.2 Wavelength

One of the most important considerations affecting the choice of wavelength is the absorption properties of the sample. If a sample is very strongly absorbing, one needs to look at the variation of the linear absorption coefficient of the material with change of energy or wavelength of the radiation. The linear absorption coefficient (μ) describes the fraction of a beam of X-rays that is absorbed per unit thickness of the absorber. Since the linear absorption coefficient is dependent on the density of the material, the mass attenuation coefficient (μ/ρ) is often reported for convenience. To convert a linear absorption coefficient to a mass attenuation coefficient, simply divide it by the density (ρ) of the material. This constant has units of cm^2/gm. The graphs of the mass attenuation coefficients versus energy for the elements Lu and Y are available at the National Institute of Standards and Technology website (Fig. 3.1 and Fig. 3.2). The plots cover the energies of photons from 1 keV to 20 keV. From the plots one can see that the mass attenuation coefficient decreases with higher energy (shorter wavelength). At the same time we need to avoid the absorption edges during the measurement shown by the vertical discontinuities in the graph (Fig. 3.1 and Fig. 3.2). The characteristic absorption edge of Y is at 17.0384 keV (0.7277 Å) and for Lu they are at 63.3138 keV (0.1958 Å), 10.8704 keV (1.1406 Å), 10.3486 keV (1.1981Å) and 9.2441 keV (1.3412 Å) if we consider energies less than 6 keV (2 Å) as given in http://skuld.bmsc.washington.edu/scatter/AS_periodic.html. So in terms of wavelength, a wavelength slightly shorter or longer than 0.7277 Å would be a choice which is within the range of accessible wavelength in SNBL. The longer wavelength will give better separation between the reflections on the detector but at the cost of higher absorption. Shorter wavelength will allow access to more high order reflections and will reduce the absorption. During our first synchrotron experiment we were also interested in the diffuse scattering of α-$NaYF_4$ and the material did not exhibit any observable diffuse scattering, so it was not considered further.

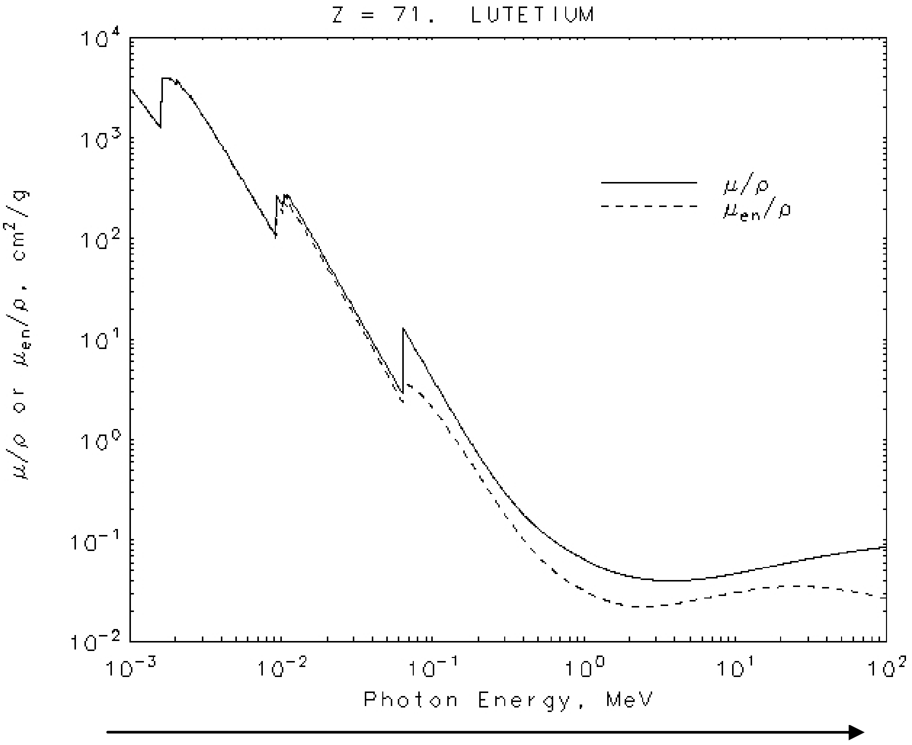

Shorter Wavelength (Å)

Fig. 3.1: Plot of mass attenuation coefficient (μ/ρ) with energy (MeV) for Lutetium.

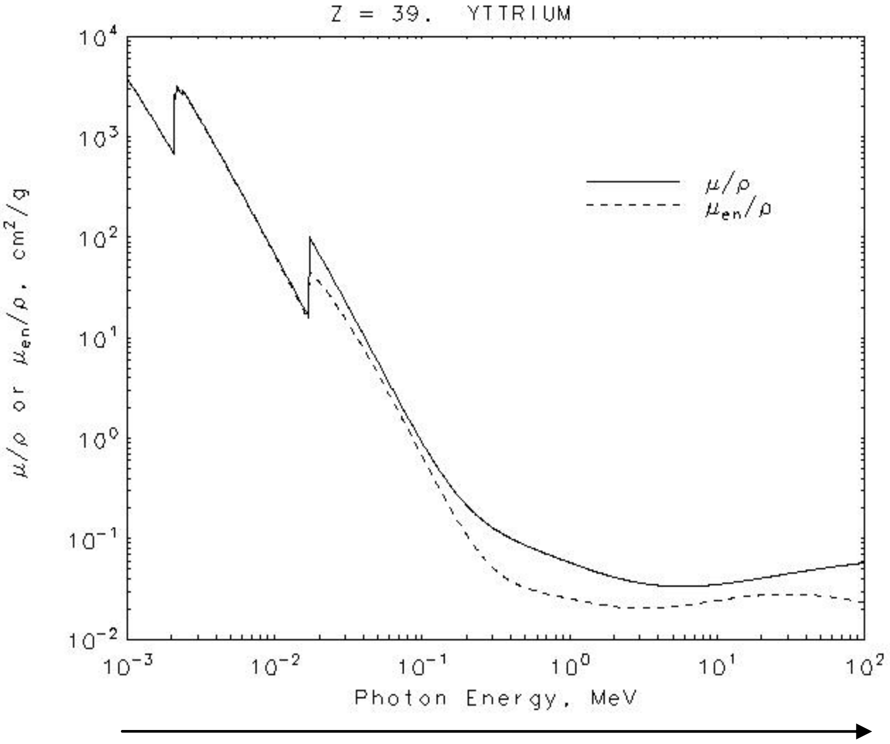

Shorter Wavelength (Å)

Fig. 3.2: Plot of mass attenuation coefficient (μ/ρ) with energy (MeV) for Yttrium.

3.1.3 Extent of the Data

In routine X-ray crystal structure determination, the recommended minimum resolution is 0.84 Å ($\sin\theta/\lambda \geq 0.6$ Å^{-1}, or $\theta_{\max} = 25°$ with Mo Kα radiation). Resolution to 0.7 Å or better is helpful if a crystal diffracts adequately as this will improve the reflection/parameter ratio in the refinement which usually helps improve the precision of the refined parameters. If the unit cell of the material being studied is quite small, for example only 5-6 Å, in each dimension the maximum *h*, *k* or *l* indices of the reflections may be quite limited, with the result that there are relatively few reciprocal lattice layers that can be examined. This might then limit one's ability to analyse the patterns of reflections. In such cases, data collection to a higher $\theta_{\max}$ is desirable so that more high order reflections are obtained.

3.1.4 Detectors

Two main types of detectors in common use for collecting single crystal diffractions data are image plates (IPs) and Charge Coupled Device (CCD) detectors and each has been used in experiments to record large 3D volumes of scattering data. The two detector types have different properties, which can be an important consideration when planning an experiment. The pixels of CCD detectors 'bloom' or 'bleed' into surrounding pixels if they become saturated, as might occur when a strong Bragg reflection is over-exposed (Campbell *et al.*, 2004). For CCDs such artifacts are associated with the overflow of electric charge from one CCD pixel to another. An IP detector does not suffer from bleeding. A CCD detector has one great advantage over an IP detector in that the recorded data from an individual frame can be read out in about 1 second, rather than the 1 - 2 minutes required for reading out an IP. In the case of IPs, the main artifacts appear to be a 'ghosting' of strong Bragg peaks resulting from the fact that strongly overexposed IP pixels are not completely erased on read-out so that the peak persists on subsequent frames (Weber *et al.*, 2001). In the case of CCD detectors, electronic noise builds up continuously and can become significant for long exposures. This effect increases the background and can make it very hard to distinguish weak diffuse scattering signals from background. The chip in CCD detectors is normally cooled to -40 °C or -60 °C, but even then the electronic noise cannot be suppressed entirely. IP detectors are noise free and thus the better choice for measuring weak diffuse signals. The available detector in our laboratory is a Nonius CCD detector and the SNBL at the ESRF in Grenoble is equipped with a Titan CCD and a MAR345 IP detector.

3.1.5 Goniometer Type

The four-circle goniometer is the goniometer of choice. This readily allows all regions of reciprocal space to be sampled and a $\theta_{\max}$ of up to 60-65° is usually achievable, thereby permitting very high resolution to be attained with wavelengths less than about 1.0 Å, and routine resolution with Cu Kα radiation. The goniometer available in our laboratory is Nonius KappaCCD diffractometer and the SNBL has even a six-circle goniometer, but this necessitates the use of a CCD detector. The second goniometer at the SNBL is an one-circle device allowing rotation about ϕ only (crystal mounting axis). This goniometer has to be used if one wishes to record the data using the Mar345 IP detector. The disadvantage of such a goniometer is that with one mounting of the crystal, it might not be possible to access all of the reflections in the Ewald sphere. Such an arrangement of goniometer will not be able to access many of the reflections of type $h00$, $0k0$ or $00l$ if the goniometer axis coincides with the crystal axis **a**, **b** or **c** respectively. In addition, the detector is mounted at $\theta = 0°$ and the obtainable resolution is thus dependent on the crystal-to-detector distance and the wavelength employed.

3.1.6 Diffuse Scattering Experiments

Diffuse scattering is typically 10^3 – 10^4 times weaker than Bragg scattering (Welberry *et al.*, 2005). The measurement of such features usually requires very intense X-ray beams and/or very long exposures. It is also important to be able to distinguish weak diffuse signals from other sources of noise on the detector, so that, ideally, the latter should be minimised as far as possible. Therefore, an IP detector is a better choice than a CCD detector for diffuse scattering experiments as described above. Coupled with the need for a very intense X-ray beam, the SNBL seems the ideal experimental station at which to record the data for the study presented in this work.

3.2 Planning the Experiment for α-NaLuF$_4$

In planning the optimal experiment, one needs to consider what is known about the material and what information one wishes to extract from the data. As indicated in § 2, the structure of β-$NaLnF_4$ (Ln = Y, La-Lu) has been described (Aebischer *et al.*, 2006) and the diffuse scattering explained in terms of a frustrated structure. The work being presented here concerns the lower temperature α-phase of the NaF-LnF_3 (Ln = Pr-Lu) family of compounds, specifically the Lu member. As with the β modification, diffuse scattering is anticipated, so the experiment needs to be able to record reliably both accurate Bragg scattering intensities and very weak diffuse scattering. Very fine slicing of the images (small rotations of the crystal per frame) is desirable in order to clearly see and separate any finely spaced features in the diffuse scattering signals, e.g. is a diffuse rod really a smooth rod or a sequence of closely spaced peaks of intensity.

So what is already known about α-$NaLuF_4$? Thoma *et al.* (1966) described the α-phase of the NaF-LnF_3 (Ln = Pr-Lu) family of compounds as having a “cubic” unit cell with dimensions of approximately 5.4-5.7 Å. Thus the expected unit cell for α-$NaLuF_4$ is quite small. Thoma *et al.* also suggested there may be an orthorhombic modification of the “cubic” structure for Ln = Lu, but the orthorhombic unit cell still has its shortest axis of ≈ 5.5 Å. As indicated above, with short unit cell axes, it is desirable to collect data to quite higher diffraction angles (large $\theta_{\max}$), so as to ensure there are enough high order reflections representing the shortest axis. As mentioned in 3.1.2, absorption of α-$NaLuF_4$ is significant. The linear absorption coefficient is 36.907 mm^{-1} (based on an actual stoichiometry of $Na_5Lu_9F_{32}$ as described in §2.3) at a wavelength of 0.7355 Å and Lu is the greatest contributor to the absorption.

The above information now needs to be considered together in order to decide the best experimental setup for this study. As it will be a diffuse scattering study, an image plate is the better choice and intense synchrotron radiation is desirable for the observation of the weak diffuse signals. Therefore, the plan was to conduct the main experiment at the SNBL station 01A using the Mar345 detector.

This immediately has the disadvantage of the single circle goniometer and fixed detector setting ($\theta = 0°$), which could limit data completeness. The crystal-to-detector distance is variable, but while a shorter distance improves the number of high angle reflections that can be accessed, a longer distance is better if one wishes to resolve fine detail in the diffuse scattering, or partially overlapping reflections (a feature of the material under investigation which was discovered and will be discussed later on). During our first experiment we were interested in the diffuse scattering of $NaYF_4$ and

$NaLuF_4$. So taking account of the absorption edges of Lu and Y and considering the desired resolution, a wavelength slightly longer than 0.7277 Å was selected for the experiments.

Two experiments were planned for each sample. One, faster experiment accurately recorded the Bragg intensities while trying to ensure that no reflection saturated the detector. In this experiment, the diffuse scattering was not important. The aim of the experiment was to obtain accurate Bragg intensities for the determination of the average structure. In order to obtain sufficient high-angle reflections a high θmax was desirable. The crystal-to-detector distance could be relatively short for this purpose, although later on reflection splitting was detected, which meant in one experiment a longer distance was more desirable in order to try to resolve this feature. The second experiment was conducted more slowly with longer exposure times for each frame. The aim of this experiment was to obtain good intensities for the diffuse scattering. It did not matter if the Bragg peaks were saturated (as long as they did not remain as ghost peaks on subsequent images). In this case, high-angle features were not important, so a longer crystal-to-detector could be used in order to resolve fine detail in the scattering pattern.

3.3 Selecting the Samples

Before any synchrotron experiments could be done, it was necessary to select suitable crystals from the sample that had been synthesized according to the procedure described in § 2.3. The selected crystals then needed to be tested on the laboratory Nonius KappaCCD diffractometer in order to learn something about their diffraction patterns and to ensure that the chosen crystals were indeed proper single crystals.

As the compound is very hard, the ampoule obtained from the melt had to be carefully smashed. This resulted in many small fragments which were often irregular in shape and which often proved to be cracked, leading to misoriented domains and a complex diffraction pattern which was useless for the purpose of the study. In order to have as uniform absorption profile as possible, the crystal fragments needed to be as isotropic in shape as possible as well, which was not always so easy to achieve.

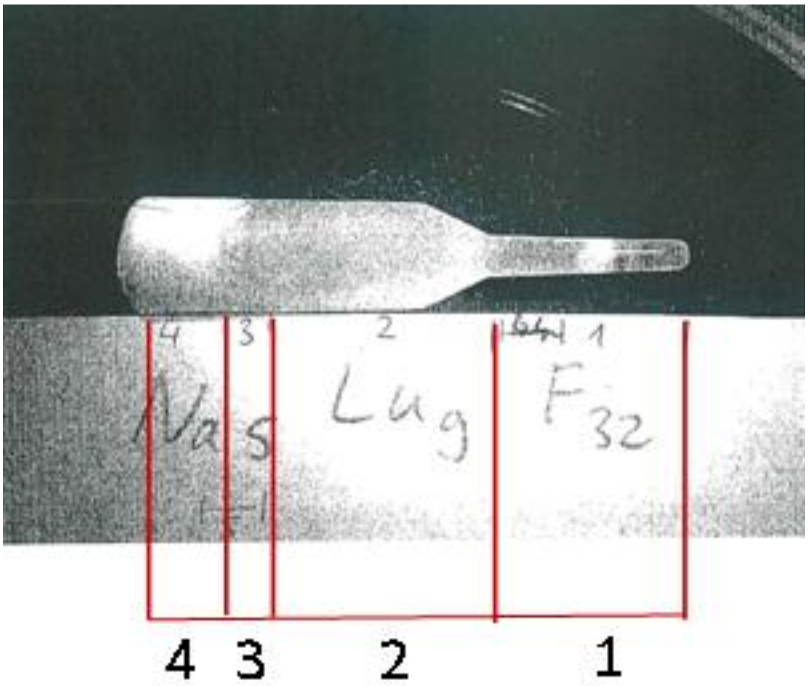

Fig. 3.3: Sample of α-NaLuF$_4$ obtained from its melt. Zones marked with 1, 2, 3, 4 indicate different parts of the sample and samples from zone 1, 2 and 3 were used for the diffraction experiment.

Crystals were carefully selected from zones 1, 2 and 3 of the ampoule (see Fig. 3.3). With the exception of crystals taken from near the boundary between zones 1 and 2, all crystals showed similar diffraction images on the laboratory diffractometer. This will be described as the Phase I diffraction pattern. Fig. 3.4 shows such an image. The main features in this image are the sharp, strong and large Bragg peaks that stand out and seem to be spaced on a "square" grid. In the subsequent discussion, these strong reflections will be called "main" reflections. The automatic unit cell indexing routine of the diffractometer produced a “cubic” unit cell based on these reflections of dimension $\mathbf{a} \approx 5.47$ Å. Closer inspection of the image shows that each main reflection appears to be surrounded by two, three or four weaker and sharper reflections forming a sort of "X" around each main reflection. These additional reflections will be called "satellite" reflections from now on. There are also a few additional reflections that might be additional satellites or other features, plus, if one looks very closely, a suggestion of lines of weak diffuse scattering, which appear to form "boxes" or "arrow heads" around groups of main reflections and their satellites.

This is about all one can see from the laboratory diffraction data, but as will be shown later on, the synchrotron data reveals much more detail.

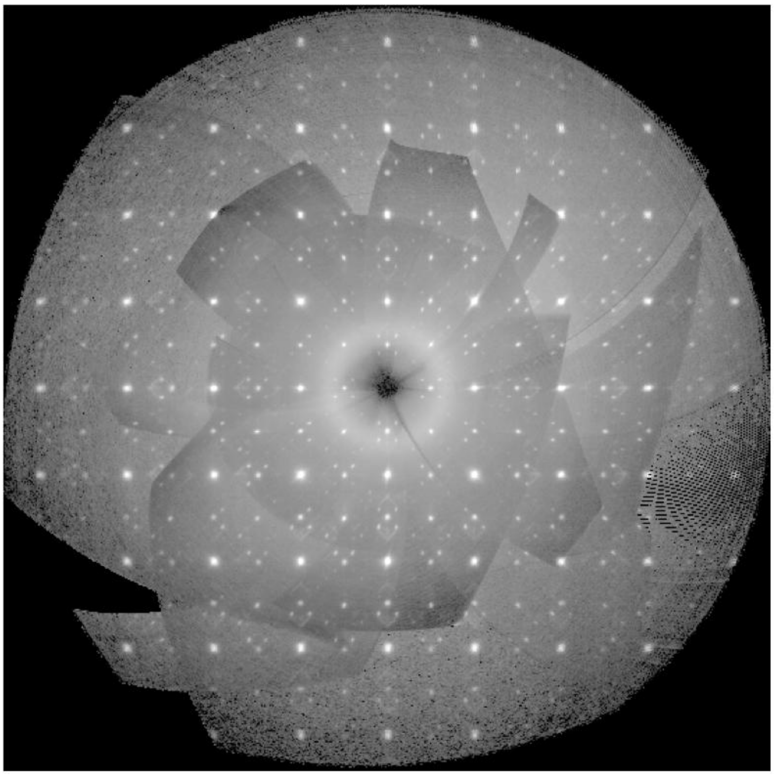

Fig. 3.4: The h0l layer for Phase I collected on the Nonius KappaCCD diffractometer.

Crystals taken from near the boundary between zones 1 and 2 exhibited a different diffraction pattern (Fig. 3.5), so these crystals have been designated as Phase II of α-$NaLuF_4$. The main feature in Fig. 3.5 is the sharp Bragg peaks that seem to be spaced on a "square" grid, much like those in Phase I. The automatic cell indexing routine of the diffractometer also produced a “cubic” unit cell of dimension 5.471 Å. Each Bragg reflection appears to be surrounded by a faint cloud of diffuse scattering, which has the appearance of "flowers". The diffuse scattering here is clearly different from that observed with Phase I. There is no evidence of satellite reflections surrounding each of the main reflections.

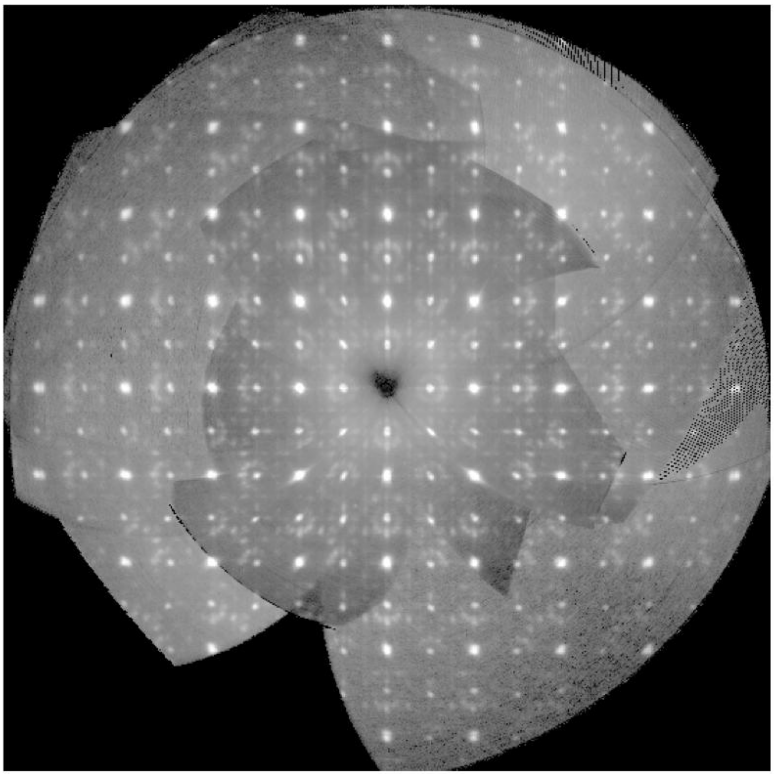

Fig. 3.5: The h0l layer for Phase II collected on the NoniusKappaCCD diffractometer.

Interestingly, Zones 1 and 2 of the sample are not stable. Crystals from these parts collapse to powders after a couple of months. Zone 3 is stable; it does not degrade with time. However it is unclear why this behaviour occurs.

With this information and suitable crystals in hand, the synchrotron experiments were planned.

3.4 Recording of Diffraction Data

All data sets were collected on a MAR345 image plate (detector size 345mm in diameter, pixel size 150 microns and usable detector area 93.480 mm^2) at the SNBL of the ESRF. MAR345 software from MarResearch (2000) was used for diffractometer control and data acquisition. The goniometer for the data collection was a 1-circle goniometer with rotation of ϕ only. For each phase of the samples two types of data sets were collected. In each case the data collection covered a hemisphere of reciprocal space. Three visits to the SNBL were made and a slightly different wavelength was used at each visit. At the beginning of each experiment, test frames were recorded to ascertain the best exposure time needed to just avoid having any reflections of the class being measured (mains or satellites) saturate the detector. The dose for the chosen exposure time of that frame was then used to collect the subsequent frames. This dose mode was used to ensure constant exposures despite the slow decay (or refilling) of the synchrotron beam during the measurement time.

A short exposure time, together with a Cu attenuator, a short crystal-to-detector distance and a rotation of $\phi = 1$ degree/frame was used for an accurate measurement of the intensities of the strong main reflections.

After measuring the strong features, a longer exposure time and/or removal of the attenuator with a rotation of $\phi = 0.5$ degree/frame was used to collect the intensities of the weaker features like satellite reflections and diffuse scattering. A longer crystal-to-detector distance was used to collect these data sets.

The details of the experiment are tabulated below (see Table 3.1 and Table 3.2)

Experiment	**Phase I**		**Phase II**	
	Mains	**Satellites and Diffuse scattering**	**Mains**	**Diffuse Scattering**
Temperature	293 K	293 K	293 K	293 K
Exposure time/Frame	Approximately 10 sec	Approximately 6 sec	Approximately 4 sec	Approximately 20 sec
Filter used	50 micron Cu	No filter	50 micron Cu	No filter
Distance $_{\text{Crystal-Detector}}$	110 mm	130 mm	110 mm	150 mm
No of frames	180 frames	360 frames	180 frames	360 frames
Rotation/Frame	$\Delta\phi = 1.0^{\circ}$	$\Delta\phi = 0.5^{\circ}$	$\Delta\phi = 1.0^{\circ}$	$\Delta\phi = 0.5^{\circ}$
Wavelength	0.73550 Å	0.73550 Å	0.70826 Å	0.70826 Å
Crystal size (mm)	$0.1 \times 0.075 \times 0.05$		$0.1 \times 0.1 \times 0.1$	

Table 3.1: Experimental settings during the RT measurements using the MAR345 IP at the SNBL.

The Phase I main reflections were also measured at 200 K and 150 K and for Phase II main reflections were collected at 200 K, 150 K and 100 K as well. The goal of the low temperature data collections was to understand the behaviour of atomic displacement parameters (ADPs) of the heavy atoms present in the structure, to see if there was any phase change as the temperature of the sample was lowered, and to reduce the dynamic disorder in the crystal.

Experiment	Phase I	Phase II
	Mains	**Mains**
Temperature	100 K/200 K	100 K/150 K/200 K
Detector Type	MAR 345 IP	MAR 345 IP
Exposure time/Frame	Approximately 5 sec	Approximately 4 sec at all temperatures
Filter used	50 micron Cu	50 micron Cu
Distance $_{\text{Crystal-Detector}}$	110 mm	110 mm
No of frames	180 frames	180 frames
Rotation/Frame	$\Delta\phi = 1.0^{\circ}$	$\Delta\phi = 1.0^{\circ}$
Wavelength	0.70150 Å	0.70826 Å
Crystal size (mm)	$0.1 \times 0.1 \times 0.1$	$0.1 \times 0.1 \times 0.1$

Table 3.2: Experimental settings during the low temperature measurements using the MAR345 IP at the SNBL.

3.5 Data Treatment

3.5.1 Unit Cell Determination and Optimization

After measuring the intensities, the first step is to determine the orientation matrix which defines the orientation of the crystal axes relative to the instrument coordinate system and derive the unit cell parameters. The unit cell parameters are defined and refined via the spatial coordinates x, y, z of the peaks in the orthogonal diffraction coordinate system (goniometer system). To obtain these coordinates, a peak search over the measured raw MAR IP images was done with the standard diffractometer software packages, CryAlis PRO RED (*CrysAlis PRO*; Agilent, 2010). At first the orientation matrix for the unit cell was based only on the strong main reflections using a specific threshold of intensity so that the orientation matrix is not influenced by the satellite reflections. The “cubic” unit cell parameter for both Phase I and Phase II is ≈ 5.471 Å, which is consistent with the cell parameter obtained from our laboratory diffractometer measurements.

3.5.2 Diffraction Pattern

After obtaining the unit cell parameters, synthetic precession photographs were generated for both the Phase I and Phase II data based on the orientation matrices obtained from the strong main reflections. For Phase I and Phase II, the 0*kl, h*0*l, hk*0 layers were created initially (Figs. 3.6-3.9). The Phase I diffraction pattern contains strong main reflections, weak satellite reflections and strong diffuse scattering (Figs.

3.6-3.7). The satellite reflections appear to be running diagonal to the “cubic” cell which is aligned in Fig. 3.6 with the reciprocal cell axes horizontal and vertical directions. The Phase II type of diffraction pattern contains main reflections and strong diffuse scattering (Figs. 3.8-3.9). One can clearly see that, the patterns of diffuse scattering are entirely different in Phase I and Phase II.

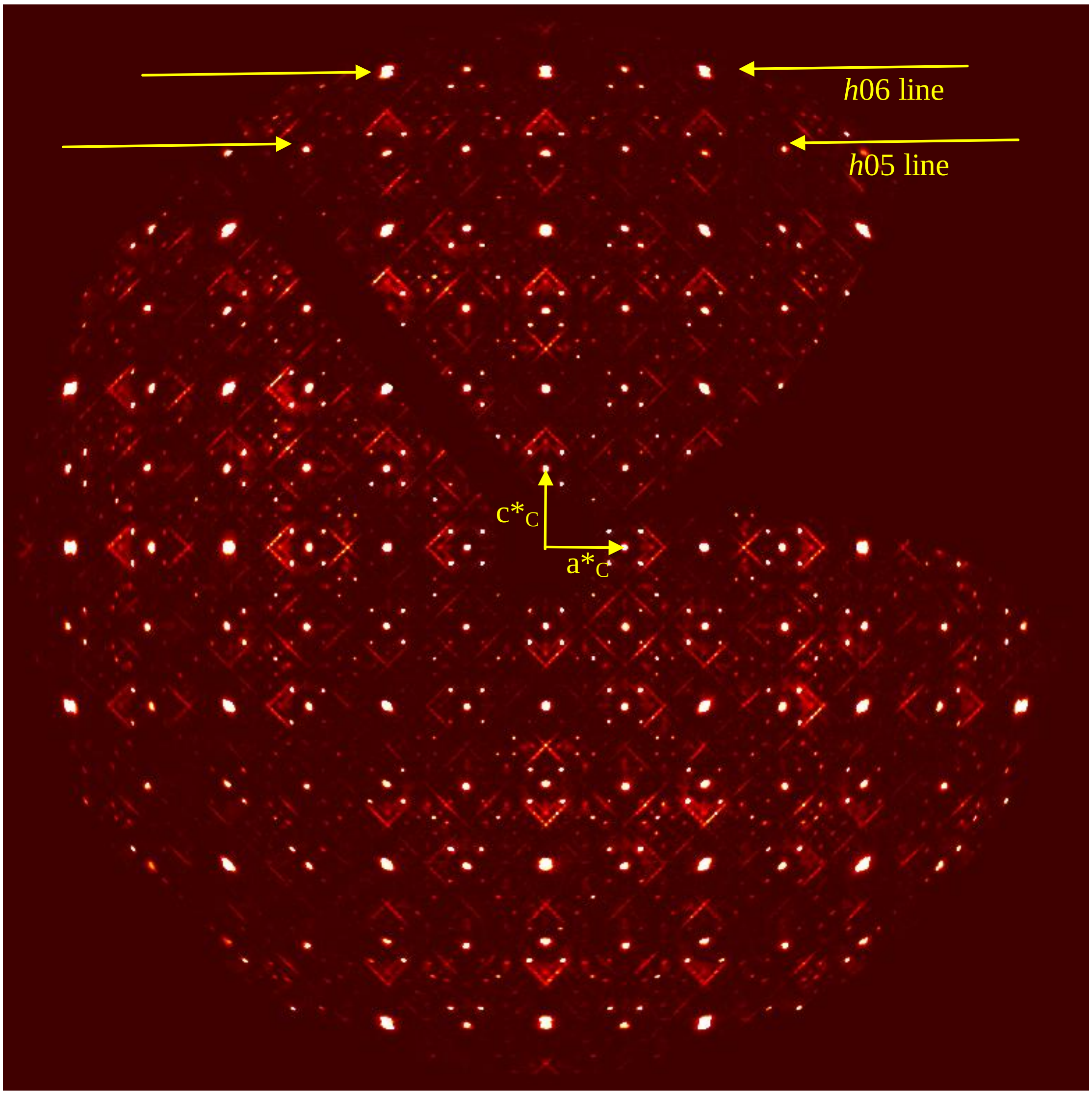

Fig. 3.6: A reconstruction of the h0l layer of Phase I based on the “cubic” orientation matrix. The direction and lengths of the reciprocal lattice vectors a*$_C$ and c*$_C$ have been shown at the origin of the reciprocal lattice layer. The splitting (line between the upper arrows) and non-linearity (line between the lower arrows) of the strong reflections will be discussed in § 3.5.3.

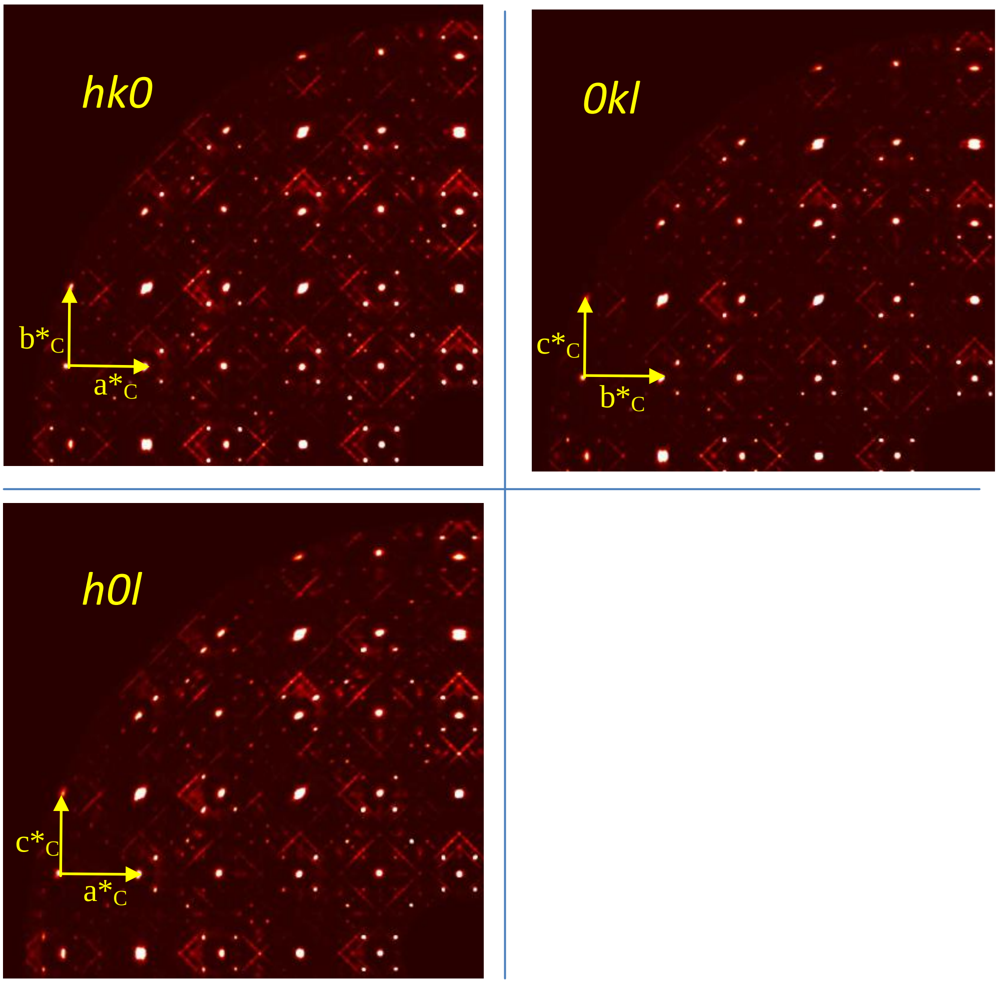

Fig. 3.7: Parts of the 0kl, h0l, hk0 layers of Phase I based on the “cubic” orientation matrix are shown for comparison and demonstrate the apparent “cubic” symmetry of the diffraction pattern. The direction and lengths of the reciprocal lattice vectors have been shown by a^*_C, b^*_C ***and*** c^*_C ***and they are not at the origin of the respective reciprocal lattice layer.***

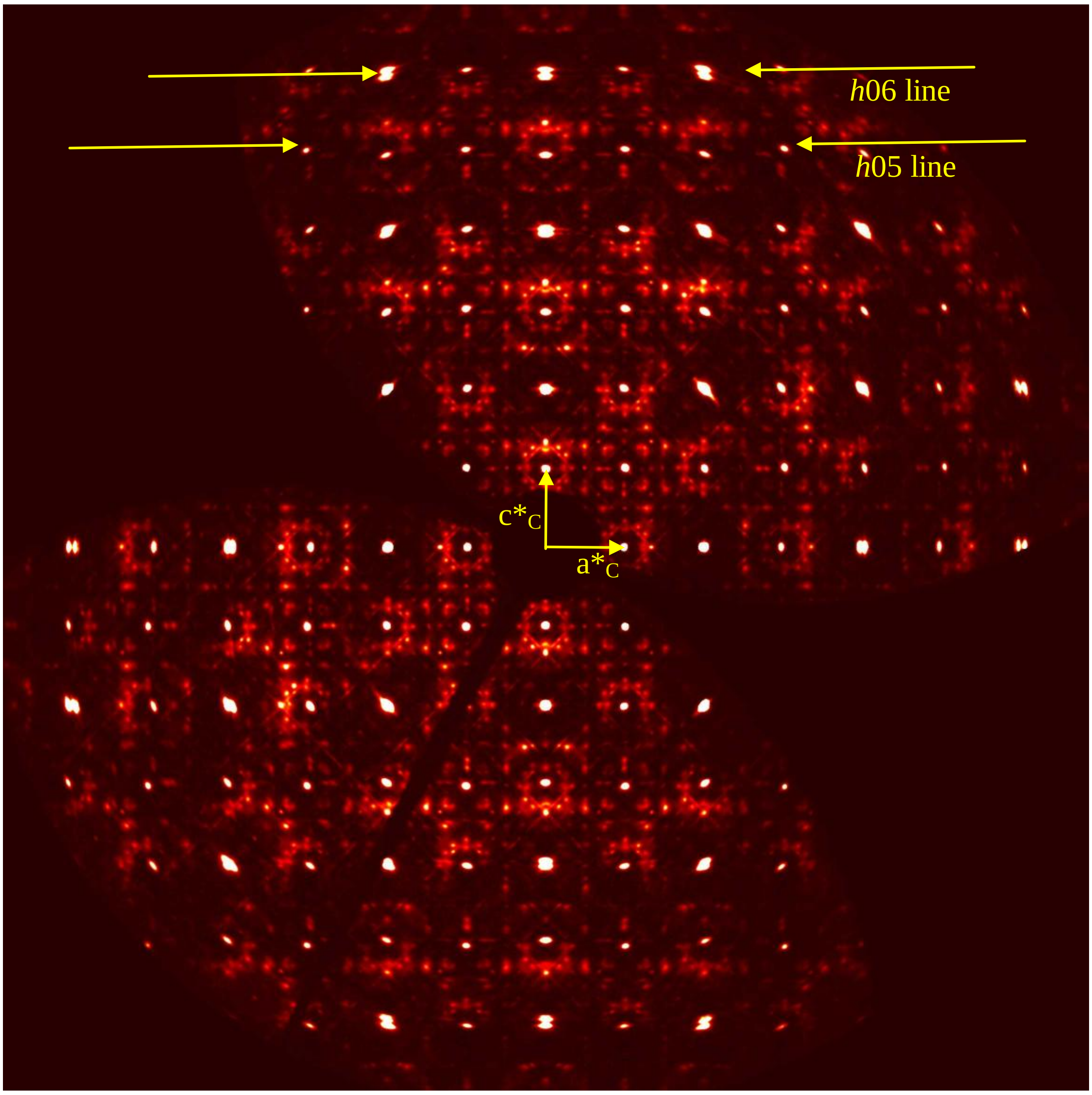

Fig. 3.8: A reconstruction of the h0l layer of Phase II based on the "cubic" orientation matrix. The direction and the length of the reciprocal "cubic" lattice vectors a*$_C$ and c*$_C$ have been shown at the origin.

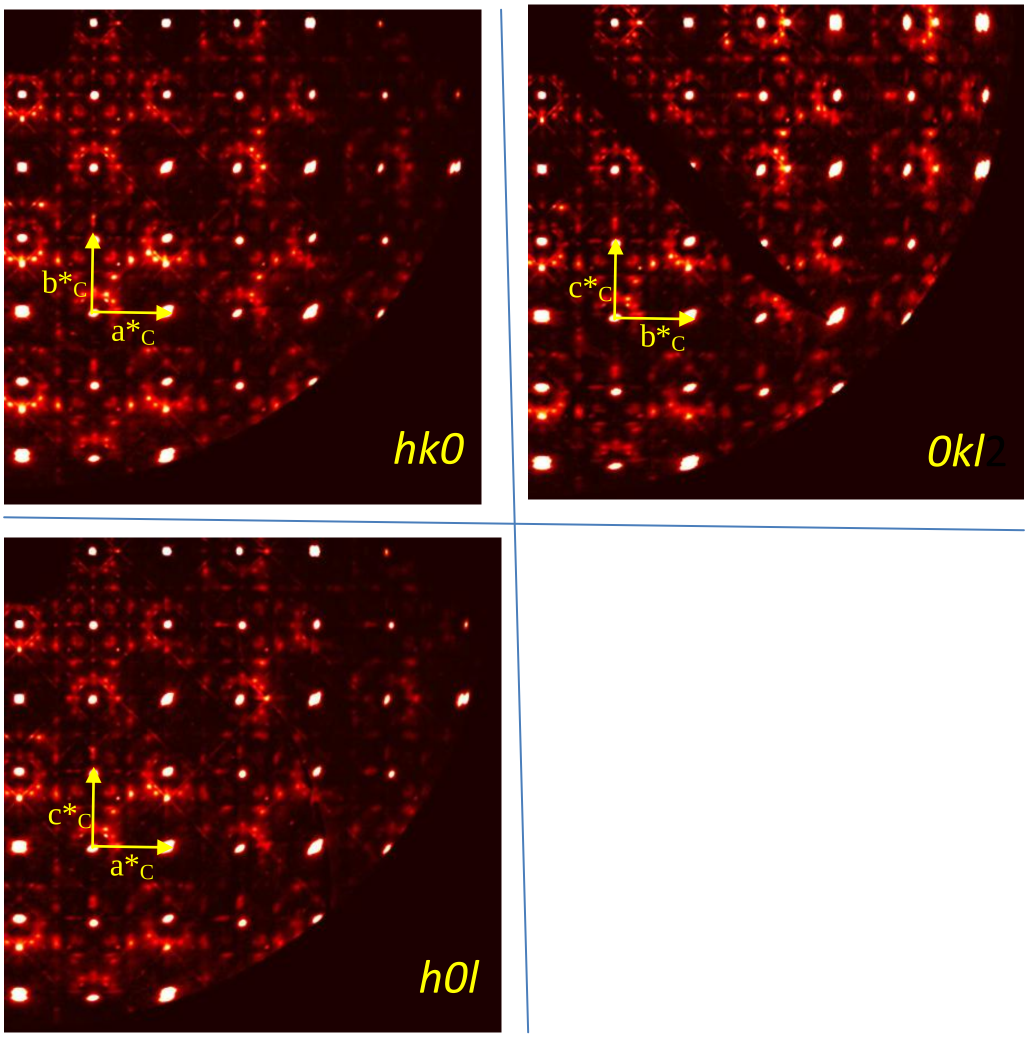

Fig. 3.9: Parts of the 0kl, h0l, hk0 layers of Phase II based on the "cubic" orientation matrix are shown for comparison and demonstrate the apparent "cubic" symmetry of the diffraction pattern. The direction and lengths of the reciprocal "cubic" lattice vectors have been shown by a^*_C, b^*_C and c^*_C and they are not at the origin of the respective reciprocal lattice layer.

3.5.3 Analysis of the Phase I Diffraction Pattern

At first glance, the reciprocal lattice layers *h*0*l*, 0*kl* and *hk*0 in the diffraction pattern of Phase I suggest the presence of primitive "cubic" symmetry with a unit cell constant **a** ≈ 5.471(4) Å and $m\bar{3}m$ Laue symmetry. This is consistent with the "cubic" unit cell parameters from the "cubic" phase of the NaF-LnF$_3$ (Ln = Pr-Lu) systems as observed by Thoma *et al.* (1966). However, a close look at the high angle reflections reveals that there is slight splitting, as shown in Fig. 3.6, at the same time high angle reflections of a reciprocal lattice line are not collinear e.g. the *h*05 reflections in Fig. 3.6. This suggests the presence of more than one lattice orientation in the crystal and that the true lattice is not "cubic". The splitting is visible in all directions, namely the *h*0*l*, 0*kl*, *hk*0 layers (Figs. 3.6 and 3.7). The non-linearity of rows of high angle reflections and their splitting in all directions ($\mathbf{a^*_{Cubic}}$, $\mathbf{b^*_{Cubic}}$, $\mathbf{c^*_{Cubic}}$) can be interpreted in-terms of threefold tetragonal twinning if the tetragonal axes are defined as coincident with the "cubic" axes, where the tetragonal c axis is just slightly longer than the "cubic" c axis.

There are previous reports by Federov *et al.* (1996) and Thoma *et al.* (1966) on the possibility of an orthorhombic modification of α-NaLuF$_4$. For the orthorhombic modification of α-NaLuF$_4$, Fedorov reported unit cell parameters of **a** = 11.016 Å (≈ 2 × $\mathbf{a_{Cubic}}$), **b** = 30.978 Å (≈ √2 × 4 × $\mathbf{a_{Cubic}}$), **c** = 77.16 (≈ √2 × 10 × $\mathbf{a_{Cubic}}$). In 1999, Federov in his review article reported different unit cell parameters based on an electron diffraction study. The unit cell parameters are **a** ≅ 11 Å, **b** ≅ 31 Å, **c** ≅ 38.5 Å (√2 × 10 × $\mathbf{a_{Cubic}}$) (Fedorov, 1999). The power diffraction pattern collected by Federov *et al.* on a similar lanthanide system, NaF-YbF$_3$, shows splitting of the reflections as well (see Fig. 3.10) when indexed assuming tetragonal crystal system. According to Federov, the compound Na$_7$Yb$_{13}$F$_{46}$ gives a powder diffraction pattern very similar to that of the lutetium analogue. There was no report on the name of the compound marked as F in Fig. 3.10 in the original article. This is most probably the ideal *F*-centered powder pattern from fluorite without any distortion in the unit cell.

The powder diffraction data collected from material taken from Zone 1 of our α-NaLuF$_4$ ampoule (Phase I) by K. Krämer at the University of Bern shows a similar splitting of the reflections, especially for the 111, 200, 220 and 311 reflections (see Fig. 3.11). These reflections are the main reflections in the single crystal diffraction pattern indexed on the “cubic” unit cell. A point is to note that the *F*- centering in the structure is violated due to the presence of the reflections 100, 110, 210, 211, 300 and 310. The reflections in between the indexed peaks are most probably the satellite reflections seen in Phase I.

A powder pattern was extracted from the single crystal data for Phase I at RT (Fig. 3.12). Unlike for the experiment powder pattern in Fig 3.11, splitting of the peaks for the reflections 111, 200, 220 and 311 could not be discerned. This may be due to a non-optimized orientation matrix (as will be discussed later) so that information from the reflection triplets like 200, 020 and 002 is not simultaneously appearing in the expected powder pattern. The satellite peaks are not visible because this powder pattern has been extracted from the single crystal data set recorded with a short exposure time in order to accurately measure the Bragg intensities. In addition, the background appears to be quite high.

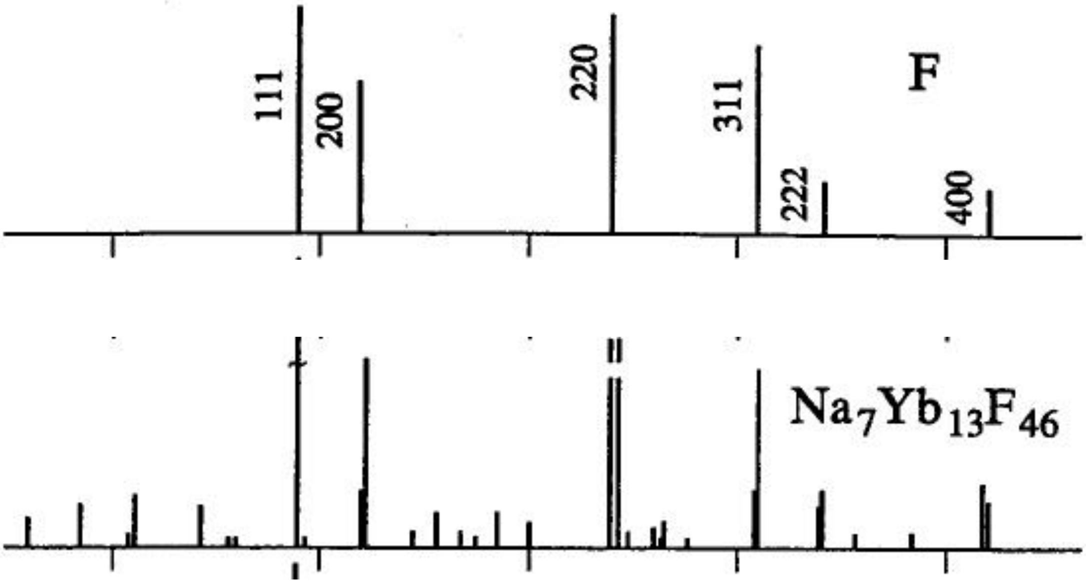

Fig. 3.10: X-ray powder diffraction pattern (Cu Kα radiation) of the orthorhombic phase of NaF-YbF$_3$ indexed assuming the tetragonal crystal system. Taken from Fig. 2 of Fedorov et al. (1996).

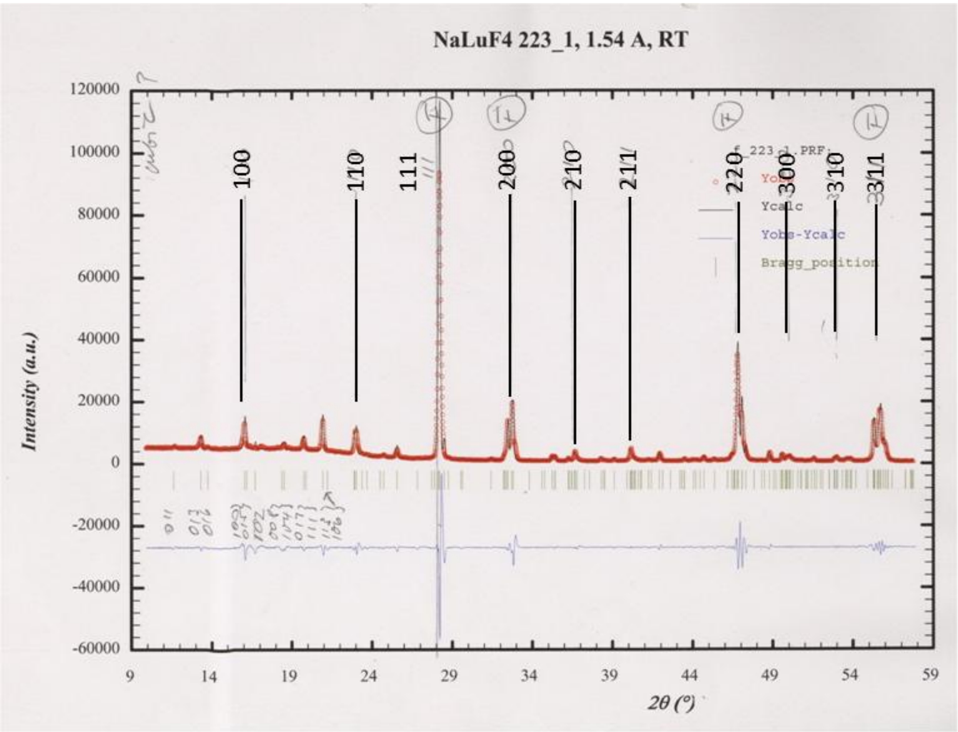

Fig. 3.11: X-ray powder diffraction pattern (Cu Kα radiation) of Phase I of α-NaLuF$_4$ recorded by Dr. Karl Krämer.

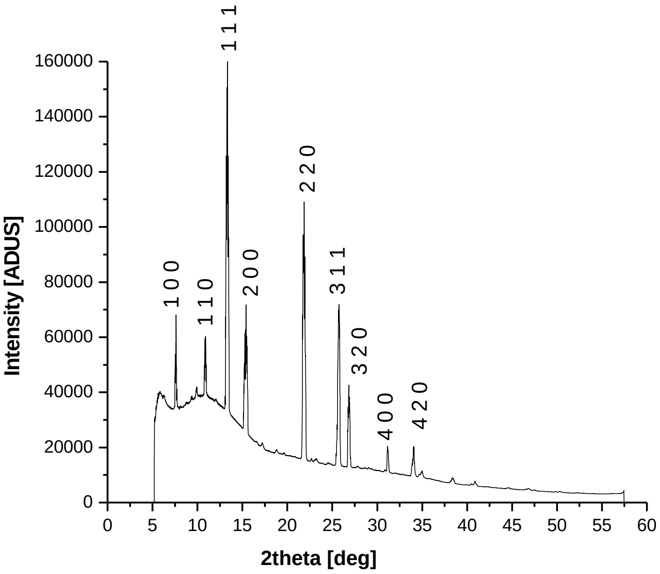

Fig. 3.12: The powder pattern extracted from the single crystal data at a wavelength 0.73550 Å for Phase I at RT using CrysAlis PRO. The index of each reflection is shown on the top of the intensity peaks.

Returning to the analysis of the Phase I diffraction pattern, there are satellite reflections present which run along the diagonals of the "cubic" lattice. It simplifies matters to transform the "cubic" unit cell to a *C*-centered tetragonal cell, as shown in the Fig. 3.13. This is convenient because the satellite reflections then run parallel to the unit cell axes, instead of diagonal to them. In reciprocal space, the transformation from "cubic" to tetragonal *C*-centered will be as follows:

$\mathbf{a^*_{Tetragonal} \cong 0.5\,(a^*_{Cubic} - b^*_{Cubic})}$

$\mathbf{b^*_{Tetragonal} \cong 0.5\,(a^*_{Cubic} + b^*_{Cubic})}$

$\mathbf{c^*_{Tetragonal} \lesssim c^*_{Cubic}}$

This transformation in reciprocal space corresponds in direct space to a transformation matrix, which can be approximated by the following transformation matrix of the form

$$\begin{pmatrix} 1 & -1 & 0 \\ 1 & 1 & 0 \\ 0 & 0 & 1 \end{pmatrix}$$

Though the initial simplified matrix transformation from the "cubic" unit cell to tetragonal unit is exact in direct space, but the new tetragonal unit cell will only be approximately equal to these values because of the distortion of the "cubic" unit cell parameters caused by the inexact orientation matrix resulting from the splitting/partially overlapping reflections. This new tetragonal unit cell will be a *C* centered as the reflection class hkl, $h + k = 2n + 1$ is absent in this setting of the unit cell. After this transformation, all the satellite reflections will be regularly distributed along the new tetragonal **a*** and **b*** reciprocal axes, between the so-called main reflections. If the satellite reflections can be indexed with the rational indices of the new tetragonal reciprocal lattice, the main and satellite reflections can be called substructure and superstructure reflections respectively and one can redefine the unit cell as a supercell such that the satellite reflections have integer indices. The satellite reflections will form a fivefold orthorhombic superstructure if the $\mathbf{a^*_T}$ or $\mathbf{b^*_T}$ can be divided in equal five unit cell lengths, where only every 2nd satellite is visible along $\mathbf{a^*_T}$ or $\mathbf{b^*_T}$. The transformation from the *C* centered tetragonal cell to a *C* centered orthorhombic cell will be of this form in reciprocal space:

$\mathbf{a^*_{Orthorhombic} = a^*_{Tetragonal} / 5}$

$\mathbf{b^*_{Orthorhombic} = b^*_{Tetragonal}}$

$\mathbf{c^*_{Orthorhombic} = c^*_{Tetragonal}}$

This orthorhombic cell is also *C*-centered as the reflection class *hkl*, $h + k = 2n + 1$ is still absent.

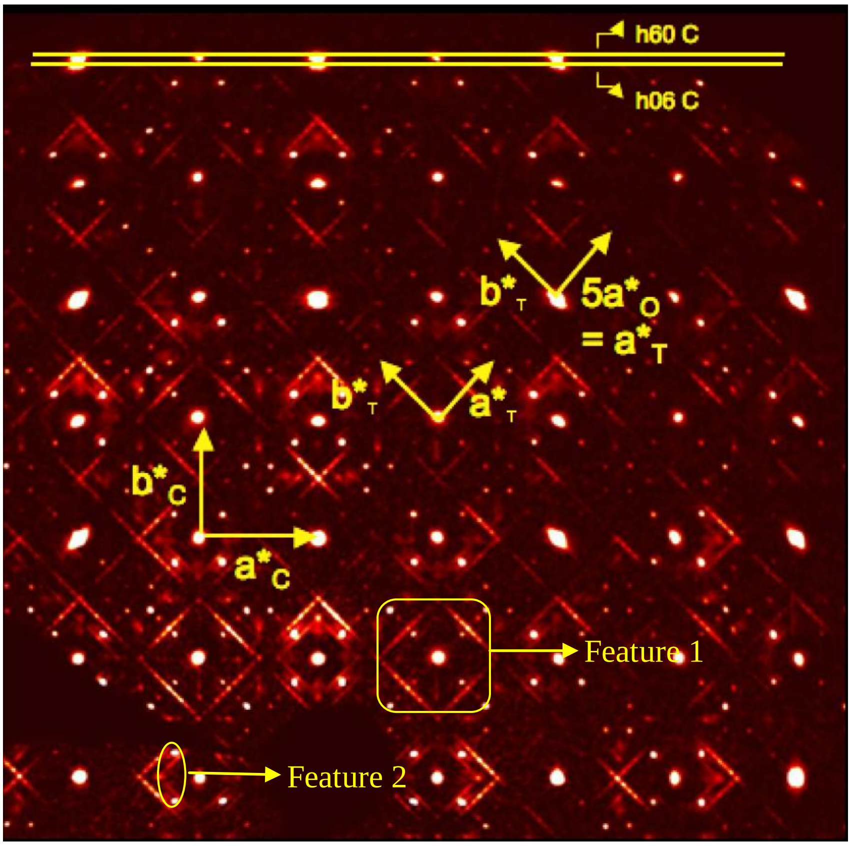

Fig. 3.13: Schematic diagram showing the "cubic" to tetragonal to orthorhombic transformation in a hk0 reciprocal lattice layer of Phase I based on "cubic" orientation matrix, where $a^*_C = a^*_{Cubic}$, $b^*_C = b^*_{Cubic}$, $a^*_T = a^*_{Tetragonal}$, $b^*_T = b^*_{Tetragonal}$, $a^*_O = a^*_{Orthorhombic}$. The h06 C set of reflections which are partiality separated from h60 C set of reflections in "cubic" indexing, are form the reflections of another twin component. Feature 1 and Feature 2 shown in the image will be discussed later.

If these satellite reflections are considered as Bragg peaks, this orthorhombic cell is consistent with the diffraction symmetries are *Cmmm*, *C*222 and *Cmm*2, or the other axial variants of *Cmm*2 because there are no systematic absence conditions other than those corresponding with the *C*-centered lattice. The unit cell parameters for this orthorhombic cell based on the integration of satellite reflections only are **a** =

38.628 (12) Å, **b** = 7.743 (5) Å, **c** = 5.513(4) Å which is consistent with the orthorhombic cell (**a** = 7.74, **b** = 38.5, **c** = 5.52) obtained in measurements of powder diffraction obtained by Thoma *et al.* (1966). The relationships among the cell constants lead to extensive, near-merohedral overlap of reflections as a consequence of the threefold tetragonal twinning mentioned earlier, which closely superimposes the reflections from the tetragonal **c*** axis over those each of the cubic reciprocal axis.

Now from the reconstructions of the reciprocal lattice layers *h0l, 0kl* and *hk0* (Figs. 3.6 and 3.7), one can schematically represent the smallest repeat unit of the main reflections in three dimensional reciprocal space in the form of a cube. If the main reflections are present at the eight corners of a cube, then satellite reflections are present along the six face diagonals of the cube, as shown in Fig. 3.14. Consequently, the structure can be best described in terms of sixfold orthorhombic twinning instead of threefold tetragonal twins. The six independent directions of the satellite reflections represent the orientations of the six twin components.

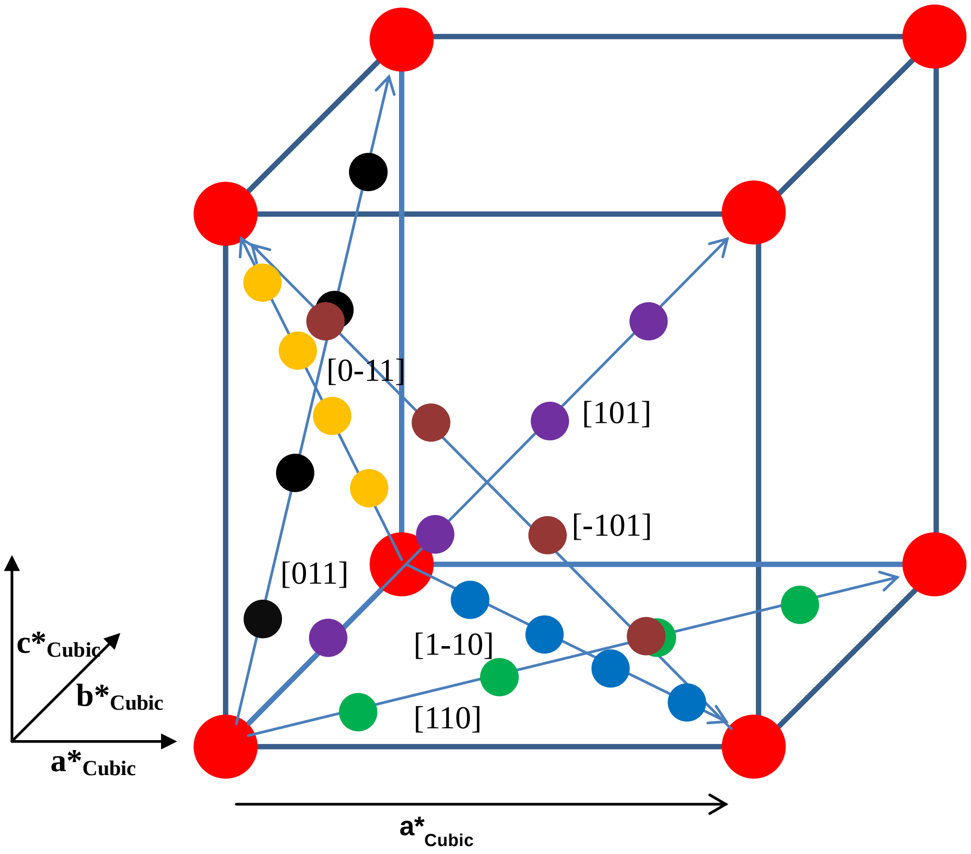

Fig. 3.14: Schematic diagram showing the positions of the satellite reflections in Phase I with respect to the main reflections (red colour). The directions of the reciprocal lattice vectors a*$_{Cubic}$, b*$_{Cubic}$ and c*$_{Cubic}$ are shown in the diagram.

Now we need to find the twin laws which will relate these 6 twin domains. There are two ways to find the twin laws: a) Find a relationship between the orientation matrices of the orthorhombic cells of different twin domains, or b) derive the approximate twin matrices theoretically on the basis of the directions of satellite reflections which are also the directions of the orthorhombic **a*** or **b*** axes. As these twin matrices are very approximate in nature, exact twin laws can be derived by data integration on the basis of these approximate twin matrices and finding a relationship between the orientation matrices obtained after the data reduction of each of the six twin domains. As the main reflections belonging to different twin domains are completely or partially overlapped with each other it is quite difficult to derive the exact unit cell parameters and orientation matrices of the six twin domains based on the main reflections, but the satellite reflections belonging to each of the six twin domains are completely separated, so on the basis of the directions of the orthorhombic **a*** and **b*** axes, one can derive the orientation matrices of the twin domains. Our task is to find transformation matrices for transforming one orthorhombic setting to the five other equivalent orthorhombic settings. Thus, we want to find a set of matrices $\mathbf{T}_i$, $i = 1\ldots6$ such that $\mathbf{a}_i = \mathbf{a}_1\mathbf{T}_i$ are the basis vectors of the six twin domains expressed interms of the first twin domain ($\mathbf{a}_1$). These basis vectors are row vectors and they have to be multiplied from the right by the transformation matrix. Now to find the set of matrices, we have to identify all of the symmetry operations of the “cubic” lattice that are not the symmetry operations of the orthorhombic lattice.

i=1: identity matrix

i=2: fourfold rotation around z:

$$M_2 = \begin{pmatrix} 0 & -1 & 0 \\ 1 & 0 & 0 \\ 0 & 0 & 1 \end{pmatrix}$$

i=3: a threefold rotation around one of the body diagonals of a cube (say [111]), to the next position in a positive sense:

$$M_3 = \begin{pmatrix} 0 & 0 & 1 \\ 1 & 0 & 0 \\ 0 & 1 & 0 \end{pmatrix}$$

i=4: a threefold rotation around one of the body diagonals of a cube (say [111]), to the next position in a negative sense:

$$M_4 = \begin{pmatrix} 0 & 1 & 0 \\ 0 & 0 & 1 \\ 1 & 0 & 0 \end{pmatrix}$$

i=5: a fourfold rotation around the x axis in a negative sense.

$$M_5 = \begin{pmatrix} 1 & 0 & 0 \\ 0 & 0 & 1 \\ 0 & -1 & 0 \end{pmatrix}$$

i=6: a threefold rotation around [-1-11] in a positive sense.

$$M_6 = \begin{pmatrix} 0 & 0 & -1 \\ 1 & 0 & 0 \\ 0 & -1 & 0 \end{pmatrix}$$

This set of matrices (M1 to M6) is applicable to the "cubic" coordinate system. All other combinations lead to either one of the matrices $\mathbf{M}_i$, or to a matrix that is symmetry related by a twofold axis or a mirror plane, which are symmetry operations of the orthorhombic lattice. The six independent matrices can be confirmed by applying them to the vector [110] in a "cubic" crystal system, which generates the six independent vectors [110], [-110], [011], [101], [10-1] and [0 1-1] that correspond with the six face diagonals of the cube, as shown in Fig. 3.14.

Now for the transformation of one orthorhombic setting into the other five settings we have to follow three steps a) transform the orthorhombic basis vector to the "cubic" basis vector b) transform the basis c) transform the new basis back to the orthorhombic setting. If the "cubic"-*P*-to-tetragonal-*C* transformation is denoted by Q, then we have $\mathbf{a}_i=\mathbf{a}_1\mathbf{Q}^{-1}\mathbf{M}_i\mathbf{Q}$

The Q matrix has the form

$$\begin{pmatrix} 1 & 1 & 0 \\ -1 & 1 & 0 \\ 0 & 0 & 1 \end{pmatrix}$$

Our tetragonal *C*-centered cell is diagonal to the "cubic" one. Thus:

$$Q^{-1} = \begin{pmatrix} 0.5 & -0.5 & 0 \\ 0.5 & 0.5 & 0 \\ 0 & 0 & 1 \end{pmatrix}$$

$\mathbf{a}_i = \mathbf{a}_1\mathbf{Q}^{-1}\mathbf{M}_i\mathbf{Q}$ **Eq. 3.1**

$\mathbf{a}_1\mathbf{T}_1 = \mathbf{a}_1\mathbf{Q}^{-1}\mathbf{M}_i\mathbf{Q}$ **Eq. 3.2**

$\mathbf{T}_1 = \mathbf{Q}^{-1}\mathbf{M}_i\mathbf{Q}$ **Eq. 3.3**

We can now directly calculate the six twin matrices. The result is

$$\mathrm{T1} = \begin{pmatrix} 1 & 0 & 0 \\ 0 & 1 & 0 \\ 0 & 0 & 1 \end{pmatrix}$$

$$\mathrm{T2} = \begin{pmatrix} 0 & -1 & 0 \\ 1 & 0 & 0 \\ 0 & 0 & 1 \end{pmatrix}$$

$$\mathrm{T3} = \begin{pmatrix} -0.5 & -0.5 & 0.5 \\ 0.5 & 0.5 & 0.5 \\ -1 & 1 & 0 \end{pmatrix}$$

$$\mathrm{T4} = \begin{pmatrix} -0.5 & 0.5 & -0.5 \\ -0.5 & 0.5 & 0.5 \\ 1 & 1 & 0 \end{pmatrix}$$

$$\mathrm{T5} = \begin{pmatrix} 0.5 & 0.5 & -0.5 \\ 0.5 & 0.5 & 0.5 \\ 1 & -1 & 0 \end{pmatrix}$$

$$\mathrm{T6} = \begin{pmatrix} -0.5 & -0.5 & -0.5 \\ 0.5 & 0.5 & -0.5 \\ 1 & -1 & 0 \end{pmatrix}$$

In CrysAlis PRO, a transformation of the cell parameter is considered as a multiplication of a column vector by a matrix from the left (**a_new = M · a_old**), where **a_old** is the cell parameter before applying the transformation matrix and **a_new** is the cell parameter after applying the transformation matrix and they are column vectors, **M** is the transformation matrix. In our derivation, the basis vectors are considered as row vectors, so we need to transpose these matrices to get them in the form directly usable in CrysAlis PRO.

So the usable form in CrysAlis PRO in the tetragonal coordinate system will be:

$$T1^T = \begin{pmatrix} 1 & 0 & 0 \\ 0 & 1 & 0 \\ 0 & 0 & 1 \end{pmatrix}$$

$$T2^T = \begin{pmatrix} 0 & 1 & 0 \\ -1 & 0 & 0 \\ 0 & 0 & 1 \end{pmatrix}$$

$$T3^T = \begin{pmatrix} -0.5 & 0.5 & -1 \\ -0.5 & 0.5 & 1 \\ 0.5 & 0.5 & 0 \end{pmatrix}$$

$$T4^T = \begin{pmatrix} -0.5 & -0.5 & 1 \\ 0.5 & 0.5 & 1 \\ -0.5 & 0.5 & 0 \end{pmatrix}$$

$$T5^T = \begin{pmatrix} 0.5 & 0.5 & 1 \\ 0.5 & 0.5 & -1 \\ -0.5 & 0.5 & 0 \end{pmatrix}$$

$$T6^T = \begin{pmatrix} -0.5 & 0.5 & 1 \\ -0.5 & 0.5 & -1 \\ -0.5 & -0.5 & 0 \end{pmatrix}$$

These matrices can be applied directly to the tetragonal basis vectors and then the following transformation matrix is applied to get the orthorhombic basis vectors:

$$\begin{pmatrix} 5 & 0 & 0 \\ 0 & 1 & 0 \\ 0 & 0 & 1 \end{pmatrix}$$

One can directly apply the orthorhombic twin matrices to the orthorhombic basis vectors instead of applying the twin matrices on the tetragonal basis vector and multiplying one of the axes by 5.

So the twin matrices in the orthorhombic coordinate system will be:

$$O1 = \begin{pmatrix} 1 & 0 & 0 \\ 0 & 1 & 0 \\ 0 & 0 & 1 \end{pmatrix}$$

$$O2 = \begin{pmatrix} 0 & 5 & 0 \\ -0.2 & 0 & 0 \\ 0 & 0 & 1 \end{pmatrix}$$

$$\mathrm{O3} = \begin{pmatrix} -0.5 & 2.5 & -5 \\ -0.1 & 0.5 & 1 \\ 0.1 & 0.5 & 0 \end{pmatrix}$$

$$\mathrm{O4} = \begin{pmatrix} -0.5 & -2.5 & 5 \\ 0.1 & 0.5 & 1 \\ -0.1 & 0.5 & 0 \end{pmatrix}$$

$$\mathrm{O5} = \begin{pmatrix} 0.5 & 2.5 & 5 \\ 0.1 & 0.5 & -1 \\ -0.1 & 0.5 & 0 \end{pmatrix}$$

$$\mathrm{O6} = \begin{pmatrix} -0.5 & 2.5 & 5 \\ -0.1 & 0.5 & -1 \\ -0.1 & -0.5 & 0 \end{pmatrix}$$

During our work, we have used the tetragonal twin matrices for the necessary transformation.

There are some additional features present in the diffraction pattern of Phase I. Diffuse streaks lie along the lines parallel to $\mathbf{a}^{*}_{\mathrm{T}}$ at l integer, $k = n + 0.5$, and parallel to $\mathbf{b}^{*}_{\mathrm{T}}$ at l integer, $h = n + 0.5$, where hkl belongs to the tetragonal unit cell. These prominent diffuse lines, apparently forming squares in the diffraction pattern are shown in Fig. 3.13 as Feature 1. A closer look at these diffuse lines shows that they have sharper more intense features within the diffuse signal suggesting the presence of some additional long range order in the structure or the features might be an artifact resulting from insufficiently fine slicing of reciprocal space during the recording of the diffraction images ($\Delta\phi = 0.5^{\circ}$/frame).

There is another prominent feature with diffuse streaks along the lines parallel to $\mathbf{a}^{*}_{\mathrm{T}}$ lying at l integer, $k = n \pm 1/3$, and parallel to $\mathbf{b}^{*}_{\mathrm{T}}$ at l integer, $h = n \pm 1/3$, shown in Fig. 3.13 as Feature 2, where hkl belongs to the tetragonal unit cell. Feature 2 is also visible in Phase II of the diffraction pattern. Satellite reflections are visible in the $hk0.2$, $hk0.4$, $hk0.6$ and $hk0.8$ layers. These satellite reflections are actually the fivefold superstructure reflections in directions rising out of the plane of the reconstructed reciprocal lattice layer. The diffraction pattern of the $hk0.2$ and $hk0.8$ layers are similar in nature while the $hk0.6$ and $hk0.8$ layers are also similar in nature, as shown in Figs. 3.15 and 3.16, the pattern is consistent with the expected positions of the satellite reflections.

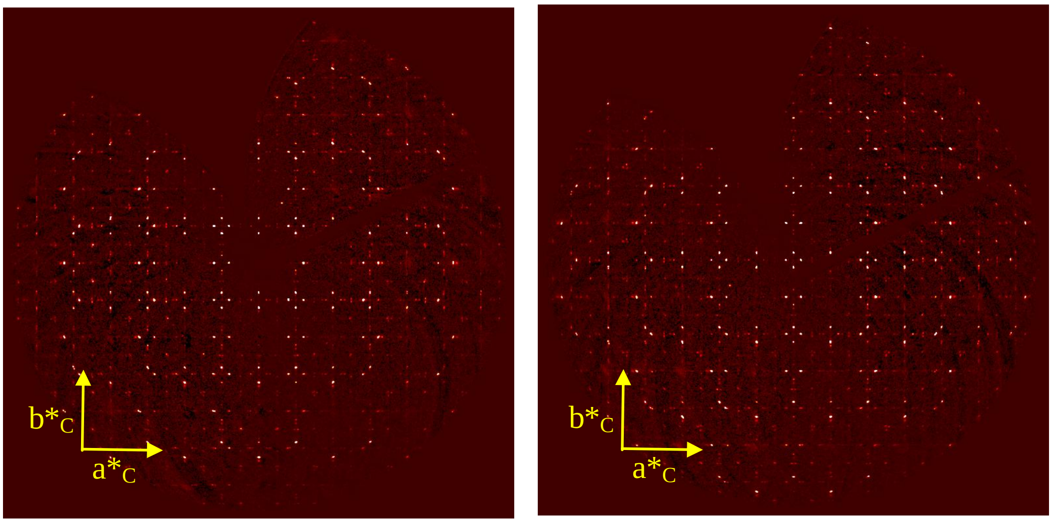

Fig. 3.15: Reconstructions of the hk0.2 and hk0.8 layers in Phase I based on the "cubic" orientation matrix showing the satellite reflections. The directions of a^*_C and b^*_C axes are shown in the diagram, but not placed at the origin.

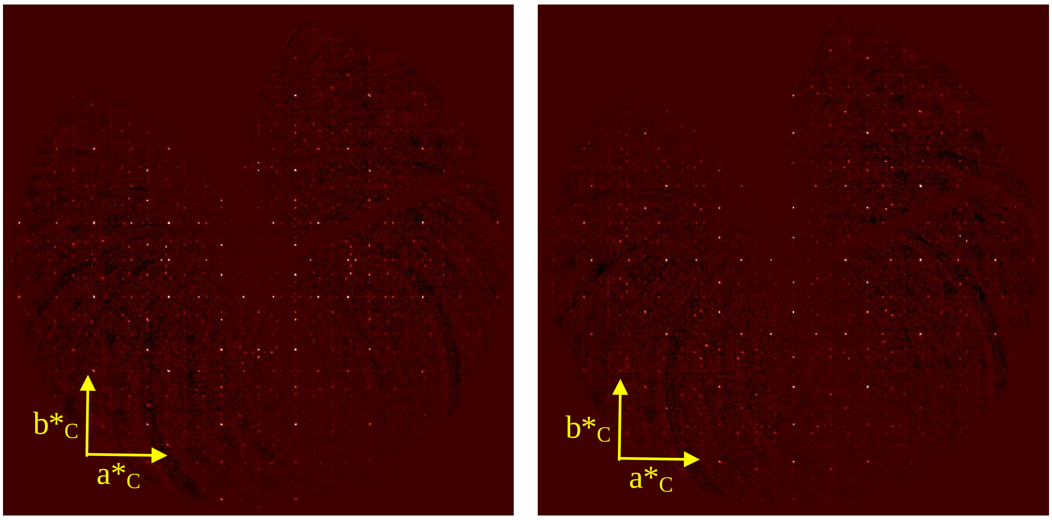

Fig. 3.16: Reconstructions of the hk0.4 and hk0.6 layers in Phase I based on the "cubic" orientation matrix showing the satellite reflections. The directions of a^*_C and b^*_C axes are shown in the diagram, but not placed at the origin.

Diffuse lines are also present parallel to the $\mathbf{a}^*_T$ at $l = n + 0.5$, $k = n + 0.25$ and parallel to the $\mathbf{a}^*_T$ at $l = n + 0.5$, $h = n + 0.25$, which is forming apparent square as shown in the Fig. 3.17.

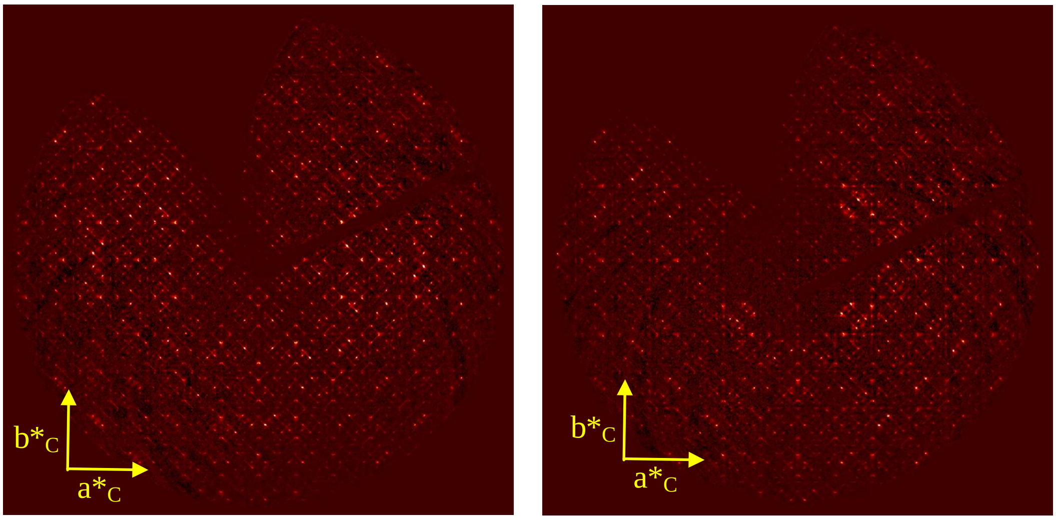

Fig. 3.17: Reconstructions of the hk0.5 and hk1.5 layers in Phase I based on the "cubic" orientation matrix showing the apparent square formed by diffuse lines. The directions of a^*_C and b^*_C axes are shown in the diagram, but are not placed at the origin.

3.5.4 Analysis of the Phase II diffraction Pattern

The diffraction pattern of the Phase II samples contains only main reflections and diffuse scattering. The reciprocal lattice layer reconstructions at 0*kl*, *hk*0, *h*0*l* confirm the "cubic" symmetry. The appearance of the main reflections is the same as in Phase I: the main reflections are splitted at high diffraction angles and the non-linearity of reciprocal lattice lines of main reflections (e.g. *h*06 in Fig. 3.8) becomes obvious at the higher angles. This again suggests the presence of more than one lattice in the crystal. The splitting of the main reflections is visible in all "cubic" reciprocal lattice directions, which can be confirmed from the reconstructions of the *0kl*, *hk0* and *h0l* layers (see Fig. 3.8 and 3.9). The diffraction pattern of Phase II does not contain any satellite reflections, so the Phase II of diffraction pattern can be explained in terms of threefold tetragonal twinning. However, as both Phase I and Phase II come from the same bulk crystal we can assume that the nature of the twinning is the same in both phases, so Phase II can also be considered as a sixfold orthorhombic twin.

As to be expected, no satellite reflections are observed in the reciprocal lattice layers *hk*0.2, *hk*0.4, *hk*0.5 and *hk*0.6. Instead, there are lines of diffuse scattering parallel to $\mathbf{a}^*_C$ with $l = n + 0.2$, h = integer and parallel to $\mathbf{b}^*_C$ with $l = n + 0.2$, k = integer which forms squares as shown in Fig. 3.18 for the *hk*0.2 and *hk*0.8 layers. This particular feature is also visible in the *hk*0.2 and *hk*0.8 layer of the Phase I diffraction pattern, but they are weak compared to those from Phase II. It may be important to point out that the square pattern is the result of intersecting perpendicular diffuse rods, running parallel to all “cubic” axes. Traces of the diffuse lines are also visible in the *hk*0.4 and *hk*0.6 layers but they are very weak in nature, as shown in Fig. 3.19.

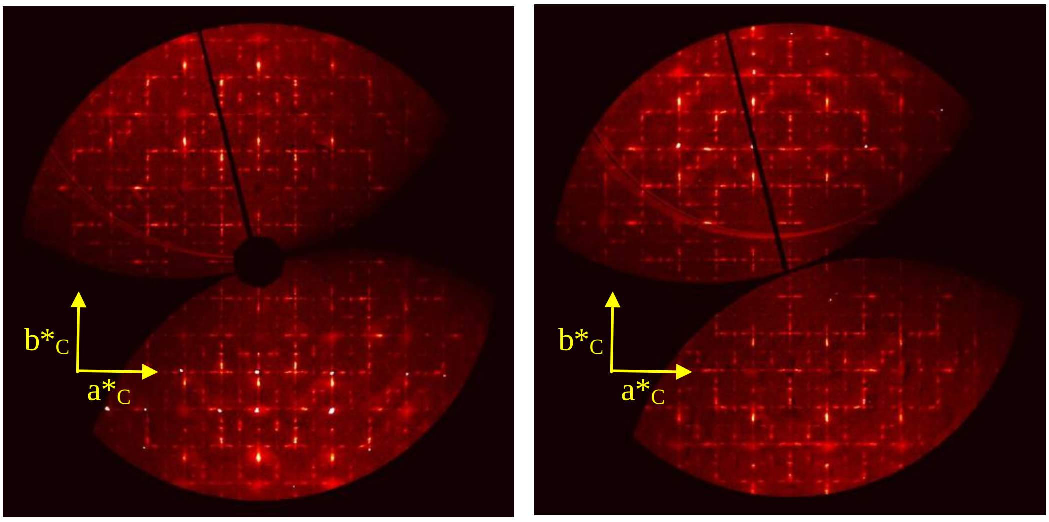

Fig. 3.18: Reconstructions of the hk0.2 and hk0.8 layers of Phase II based on the “cubic” orientation matrix showing the square pattern of diffuse scattering. The directions of a^*_C and b^*_C axes are shown in the diagram, which is not at the origin.

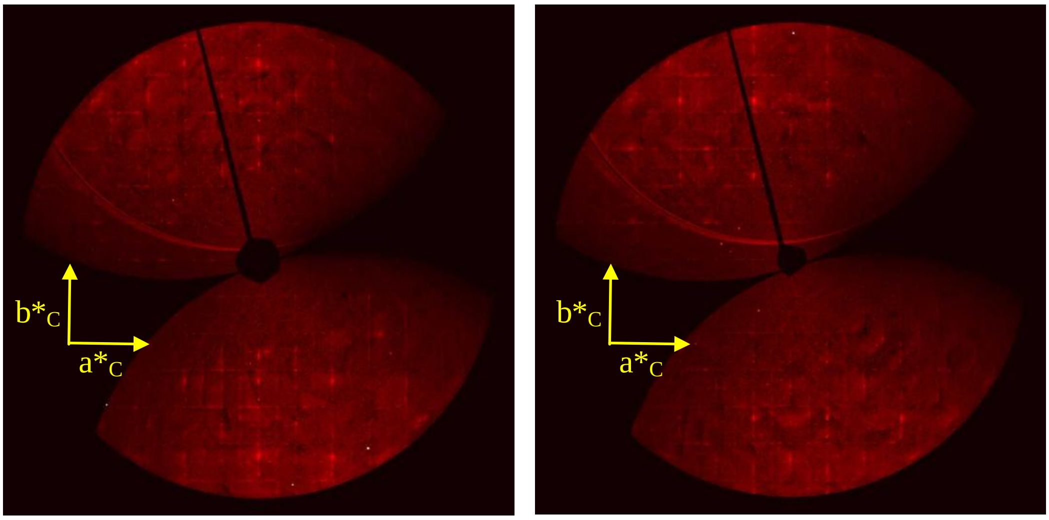

Fig. 3.19: Reconstructions of the hk0.4 and hk0.6 layers of Phase II based on the “cubic” orientation matrix showing the square pattern of diffuse scattering. The directions of a^*_C and b^*_C axes are shown in the diagram, but are not placed at the origin.

3.5.5 Derivation of Symmetry in the Diffraction Pattern

The diffraction patterns of both samples of Phase I and Phase II are a superposition of the diffraction patterns from several twin domains. This makes it difficult to find the true symmetry of the diffraction pattern of an individual twin. The derivation of the true symmetry is only possible if one can deconvolute the diffraction pattern to that of a single twin domain. If one considers the reconstructions of the reciprocal lattice layer *h*0*l* of Phase I (Fig 3.6) and Phase II (Fig 3.8) based on the "cubic" unit cell, one can see that in the reciprocal lattice line *h*06, reflections with even values of *h* (006 and 206 reflections in "cubic" indexing) are splitted and for the lattice line *h*05, reflections with even values of *h* (005 and 205 reflections in "cubic" indexing) are not collinear with the reflections of odd values of *h* (105 and 305 reflections in "cubic" indexing). This behaviour of the high angle reflections can only be explained if one considers a tetragonal unit cell where one of the reciprocal unit cell axes is slightly smaller than the other two axes. The splitting of the high angle reflections is visible in all three cubic lattice directions ($\mathbf{a}^*_c$, $\mathbf{b}^*_c$ and $\mathbf{c}^*_c$) of a reconstructed "cubic" reciprocal lattice layer and hence the twinning is at least threefold. The reciprocal lattice lines *h*06 and *h*05 where reflections from the different twin components are resolved, can be used to deconvolute the diffraction pattern with the help of the best estimated average "cubic" unit cell parameter (averaging of $\mathbf{a}^*_C$, $\mathbf{b}^*_C$ and $\mathbf{c}^*_C$) indexed from the main reflections and tetragonal unit cell parameter obtained from the data integration of just the satellite reflections (data integration of satellite reflections will be discussed later). The average reciprocal "cubic" unit cell parameter is 0.1828 Å^{-1}, the reciprocal tetragonal unit cell parameter $\mathbf{c}^*_T$ is 0.1814 Å^{-1} and $(\mathbf{a}^*_T + \mathbf{b}^*_T)/\sqrt{2}$ is 0.1829 Å^{-1}.

From the reciprocal unit cell constants as calculated above, the 600 reflection in the tetragonal indexing will be $6 \times 0.1829/0.1828 = 6.0033$ 0 0 in a "cubic" reconstruction. Similarly, the 006 reflection in tetragonal indexing will be $6\times0.1814/0.1828 = 5.954$ 0 0 in a "cubic" reconstruction. Thus, in terms of the "cubic" cell constants, the desired reconstructions will be the 6.0033*kl* [Fig. 3.20(a)] and the 5.9725*kl* [Fig. 3.20(b)] "cubic" reciprocal lattice layers. For each of the reconstructions, one quarter of the reciprocal lattice layers have been indexed with tetragonal reflection indices referring to the tetragonal reciprocal axes directions $\mathbf{a}^*_{\mathbf{Tori}}$, $\mathbf{b}^*_{\mathbf{Tori}}$ and $\mathbf{c}^*_{\mathbf{Tori}}$.

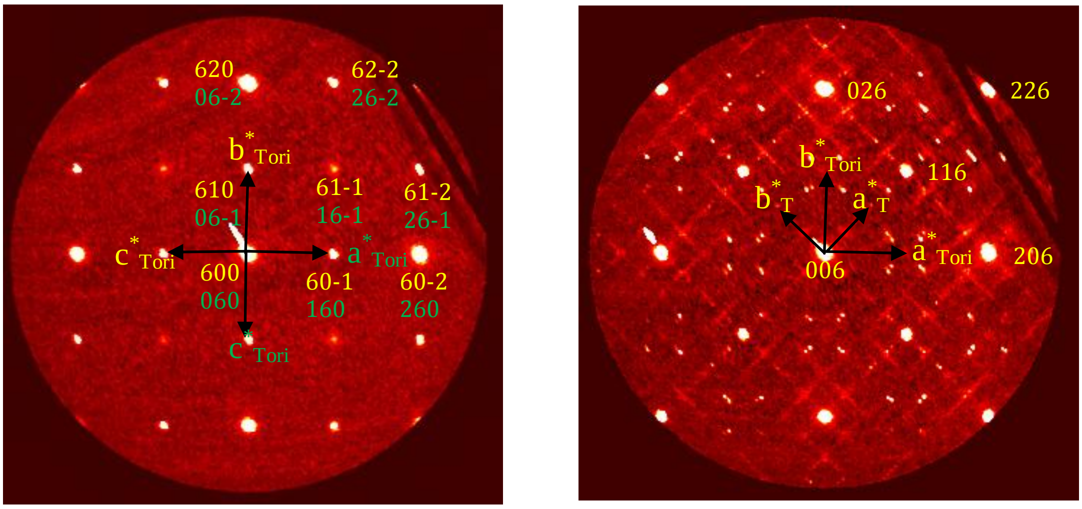

Fig. 3.20(a) Fig. 3.20(b)

Fig. 3.20: Reconstructions of the 6.0033kl [Fig. 3.20(a)] and 5.954kl [Fig. 3.20(b)] reciprocal lattice layers based on the "cubic" unit cell. The reflection indices shown are based on the tetragonal unit cell (a^*_{Tori}, b^*_{Tori} and c^*_{Tori}) and the colours correspond with those of the shown reciprocal axes.

By a similar consideration, the 500 and 005 reflections from the tetragonal lattice can be found in the 5.0027*kl* and 4.9617*kl* reciprocal lattice layer reconstructions based on the "cubic" cell [Fig. 3.21(a)-(b)]. All the reflections in the reciprocal lattice layer can be indexed similarly to the Fig. 3.20(a) and 3.20(b), but for clarity all the reflections have not been indexed here.

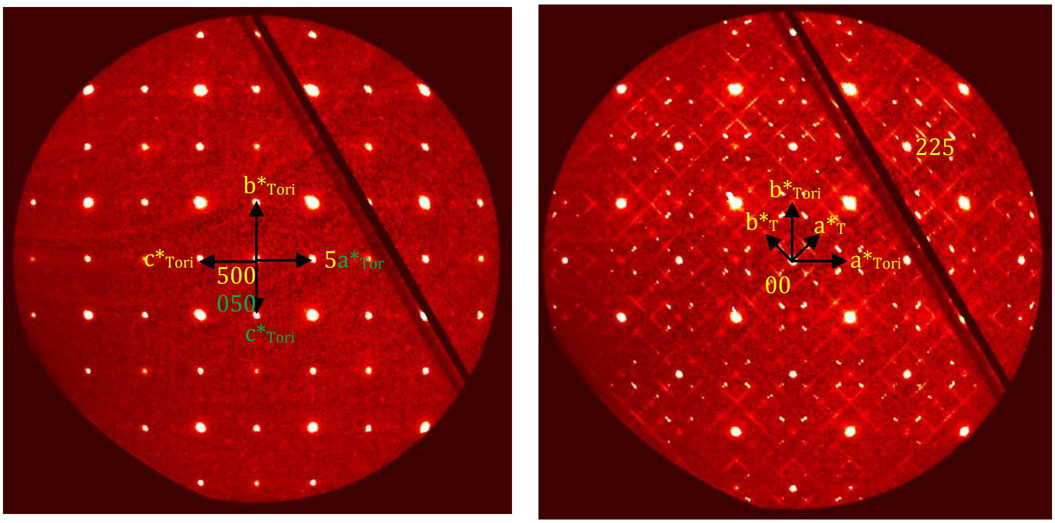

Fig. 3.21(a) Fig. 3.21(b)

Fig. 3.21: Reconstructions of the 5.0027kl [Fig. 3.21(a)] and 4.9617kl [Fig. 3.21(b)] reciprocal lattice layers based on the "cubic" unit cell. The reflection indices shown are based on the tetragonal unit cell (a^*_{Tori}, b^*_{Tori} and c^*_{Tori}) and the colours correspond with those of the shown reciprocal axes.

The reflections in the reconstructed reciprocal lattice layer 5.954*kl* (*hk*6 tetragonal layer) and 4.9617*kl* (*hk*5 tetragonal layer) are from a single twin domain and the reflections in the 6.0033*kl* and 5.0027*kl* reciprocal lattice layers are from two tetragonal twin domains, the reflection indices of these three twin domains have been given in Figs. 3.20(a)-(b).

The structure of $NaLuF_4$ is based on the fluorite type structure, which is *F* centered. But in the deconvoluted diffraction pattern of a single twin domain of $NaLuF_4$, the (116) reflection with tetragonal indices is visible in the tetragonal reciprocal lattice layer *hk*6, which is forbidden in an *F*-centered crystal lattice. The same thing is true for the *hk*5 tetragonal lattice layer where the (225) reflection will be forbidden in an *F*-centered lattice. The *F*-centering in the structure will only be recovered if we assume the reflections of the type (116) or (225) are absent. Interestingly, these reflections appear to be weaker than the other reflections in the *hk*6 and *hk*5 tetragonal lattice layers. The assumption of the fluorite structure is further supported because the positions of the difference densities in the difference density map obtained from the band flipping (part of SUPERFLIP program) of satellite reflections coincides with the positions of the metal atom in a fluorite structure, as will be discussed in detail in § 5.

The diffraction pattern of Phase I consists of strong main reflections and weak satellite reflections and for Phase II only of strong main reflections if one ignores the diffuse scattering intensities. The Laue symmetry of the diffraction pattern of a single twin domain considering only the strong main reflections is *4/mmm* and the possible space group will be *P*4*/mmm* with the reciprocal unit cell axes $\mathbf{a}^*_{\mathbf{Tori}}$, $\mathbf{b}^*_{\mathbf{Tori}}$ and $\mathbf{c}^*_{\mathbf{Tori}}$. Now the tetragonal cell can be reoriented by a transformation matrix 1 -1 0 1 1 0 0 0 1, so that the satellite reflections of Phase I are along the transformed tetragonal reciprocal axes as given in Fig. 3.13 and for the new orientation of the tetragonal cell the reflections of the type $h + k = 2n + 1$ will be absent and it will be a *C* centered cell. The possible space group will be the non-conventional *C*4*/mmm*. The reoriented tetragonal reciprocal lattice vectors ($\mathbf{a}^*_{\mathbf{T}}$ and $\mathbf{b}^*_{\mathbf{T}}$) are shown in Figs. 3.20(b) and 3.21(b). Now if one considers the weak satellite reflections in Phase I which are present along the $\mathbf{a}^*_{\mathbf{T}}$ or $\mathbf{b}^*_{\mathbf{T}}$ axes as shown in Fig. 3.13, one finds that there are satellite reflections only along those two direction in a $\mathbf{a}^*_{\mathbf{T}}$ $\mathbf{b}^*_{\mathbf{T}}$ reciprocal lattice layer, but not between. This suggests that these satellite reflections are from two different twin domains and hence the total diffraction pattern is from 6 twin domains, as there are six independent directions of the satellite reflections along the face diagonal of an imaginary cube (Fig. 3.14). The Laue symmetry of the diffraction pattern of a single twin domain is *mmm* and the possible space group will be *Cmmm*.

3.5.6 Data Integration of the Main Reflections of Phase I and Phase II

During the reconstruction of the reciprocal lattice layers we have seen that the high angle main reflections are splitted and the non-linearity of reciprocal lattice lines of main reflections become more obvious when one moves to high angle reflections. Due to this problem, the data integration procedure cannot optimize all peak positions from the initial orientation matrix. This makes the optimal intensity extraction quite challenging. One way to achieve this goal is to use a larger mask size. A larger mask allows the integration of pixels from a bigger area during the data integration procedure, which will take care of the splitting and nonlinearity of the main reflections. Using a larger mask size may pick up some noise, but it will more readily permit the optimal integration of high angle reflections. The effect of mask size on the consistency of the intensities of the main reflections of the Phase I and Phase II data sets was tested by integrating the main reflections with various mask sizes and comparing the values obtained for R_{int} (Described in Definition of Terms) from merging the symmetry-equivalent reflections (Table 3.3) after an empirical absorption correction in SADABS (Bruker, 2007). Note that these sizes are the relative sizes of the mask. No units are given for these mask sizes in the CrysAlis PRO user manual (Version 4). Absorption correction and scaling, including even and odd ordered spherical harmonics (8,5) were performed using SADABS (Blessing, 1995). Several combination of even and odd spherical harmonics (8,5; 6,1 and 2,0) were tested during the SADABS absorption correction, but the spherical harmonics with 8, 5 least R_{int} was obtained. An additional spherical correction was applied by using the μ*r value, which is dependent upon the size of the crystal, where μ is the linear absorption coefficient in mm^{-1} and r is the radius of the equivalent sphere in mm. It was not possible to do a numerical absorption correction as the data acquisition program in SNBL does not allow modelling the crystal faces which later can be transferred to the CrysAlis PRO for a numerical absorption correction, but a careful numerical absorption correction may improve the refinement results as the material have high linear absorption coefficient.

RT Data Integration of Mains	**Mask Size 2.5**	**Mask Size 2.0**	**Mask Size 1.5**	**Mask Size 1.0**	**Mask Size 0.5**
R_{int} **Phase I**	3.87%	3.98%	4.19%	4.29%	5.41%
R_{int} **Phase II**	4.56%	4.71%	4.90%	4.91%	6.99%

Table 3.3: The change of R_{int} with integration mask size during data reduction of main reflections after absorption correction.

Table 3.3 gives a clear indication that the maximal mask size possible is essential for an optimal intensity extraction. A clear decrease of R_{int} with increasing mask size during the data integration process suggests the importance of a larger mask size when integrating near-merohedray overlapped reflections.

3.5.7 Data Integration of the Satellite Reflections of Phase I

The Phase I diffraction pattern contains strong main reflections and satellite reflections. These classes of reflections have quite different peak profiles as the main reflections result from the close overlapping of 6 twin domains, but the satellite reflections are much sharper and completely separated because the satellite reflections from each twin domain run in quite distinct direction and they are free from overlaps. The substantially different peak profiles and the presence of overlapping and non-overlapping reflections make it difficult to extract the intensities of the satellite reflections if the main and satellite reflections are integrated simultaneously. Another problem is splitting of the high angle main reflections and the non-linearity of reciprocal lattice lines of the high angle main reflections, which leads to false estimations of the peak positions and makes it difficult to obtain accurate orientation matrices. The unreliability of the “cubic” orientation matrices makes the integration of the satellite reflections unreliable, because the integration boxes are then not coincides with the centers of these reflections and consequently some of the intensity is “missed” by the integration box. It is important to note that consecutive integration of the main and satellite reflections together will improve the orientation matrix, and thus reduces the amount of satellite intensity “missed” by the integration boxes, but still the intensities will contain errors as the main and satellite reflections have quite different peak sizes and centroids. So simultaneous integration of both main and satellite intensities and then manually removing the main reflections in the final reflection file may not give the correct intensities of the satellite reflections.

The best way to avoid the above-mentioned problem is to use a non-crystallographic absence condition so that during the data integration process the main reflections are not used in the integration and thus do not influence the peak profile fitting. In CrysAlis PRO, this can be done by adding custom extinction rules to the data reduction process using the command "dc extinct". By using this instruction, one can build not only crystallographic extinction conditions, but also non-crystallographic extinction rules. In our case, during the data integration, we wanted to exclude the main reflections when indexed on the orthorhombic supercell, these reflections have the indices *hkl* : 5*n*. Therefore, the CrysAlis PRO instruction used was:

dc extinct *hkl* 1 0 0 5 0 = 1**h* + 0**k* + 0**l* = 5**n* + 0

The improvement of the integration of the satellite reflections can be verified by looking the R_{int} values (Table 3.4). In the first case, the main and satellite reflections have been integrated simultaneously without any extinction condition and then an empirical absorption correction was applied to the satellite reflections after removing the main reflections from a reflection file of main and satellite reflections. Then R_{int} was calculated. In the second case, the satellite reflections alone were integrated using the above mentioned extinction condition and then an empirical absorption correction was applied and R_{int} was calculated. Although the change of R_{int} is insignificant but improvement in the intensity extraction can be verified by the refinement of the fivefold superstructure model (Discussed in § 5) based on the two types of satellite reflections data set integrated from the above mentioned methods. The data set where main and satellite reflections integrated simultaneously, ADPs of the few metal atoms become non positive definite during anisotropic refinement of the fivefold superstructure but it is not the case for the same structural model where the satellite reflections has been integrated alone. It suggests that in the first case, when the main and satellite reflections has been integrated simultaneously, all the symmetry equivalent satellite reflections have equal errors or "missed" intensity, which ultimately gives apparently low R_{int} value.

RT Data Integration of Satellites	R_{int}
Main and Satellite Integrated Simultaneously	4.84 %
Mains Excluded from the Integration Process	4.25 %

Table 3.4: The effect of including or excluding the main reflections on the value of R_{int} during the data reduction of satellite reflections for Phase I.

3.6 Conclusion

Accurate intensities of the Bragg reflections (mains and satellite reflections) and diffuse scattering were collected on a MAR345 detector at several temperatures to understand the dynamic and static disorder present in the structure for both the Phases of the sample. The diffraction pattern of Phase I sample contains main and satellite reflections, while the Phase II sample contains only main reflections. The nature of diffuse scattering in the both the phases are different. Data integration of the main and satellite reflections was a challenge because of the twinning, peak overlap and different peak profiles of the reflections, but this was optimized with a careful integration strategy for the main and satellite reflections. A point to note that Phase II diffraction pattern was observed only from the first preparation of the $NaLuF_4$ sample. The other three preparations of the same gives only Phase I diffraction pattern. This behaviour of the diffraction pattern is not understandable, which needs further investigation.

3.7 References

Aebischer, A., Hostettler, M., Haüser, J., Krämer, K., Weber, T., Güdel, H. U. & Bürgi, H. B. (2006). *Angew. Chem. Int. Ed.* **45**, 2802-2806.

Blessing, R. H. (1995). *Acta Cryst. A* **51**, 33-38.

Campbell, B. J., Welberry, T. R., Broach, R. W., Hong, H. W. & Cheetham, A. K. (2004). *J. Appl. Cryst.* **37**, 187-192.

Fedorov, P. P. (1999). *Russ. J. Inorg. Chem.* **44**, 1703-1727.

Thoma, R. E., Insley, H. & Hebert, G. M. (1966). *Inorg. Chem.* **5**, 1222-1229.

Weber, T., Estermann, M. A. & Burgi, H. B. (2001). *Acta Cryst. B* **57**, 579-590.

Welberry, T. R., Goossens, D. J., Heerdegen, A. P. & Lee, P. L. (2005). *Z. Kristallogr.* **220**, 1052-1058.

Chapter 4: Understanding of the Phase II Structure

With the integrated data sets for the Phase I and II structures in hand, the next task is to develop structural models that explain the observed diffraction patterns. The first step is to establish the average structures that explain the Bragg reflections, for which the current discussions are the "main" reflections from the Phase II crystal and the "main" plus "satellite" reflections for the Phase I crystal. Once the average structures have been established, one can proceed to extend the models to include the additional disorder that is responsible for the extensive diffuse scattering that has been observed. However, a quantitative analysis of the diffuse scattering is beyond the scope of this thesis and the remaining chapters will focus on developing just the models for the average structures of the two phases.

If the diffuse scattering is ignored, the only significant difference in the diffraction patterns of the two phases is the presence of additional satellite reflections in the Phase I diffraction pattern. As mentioned in § 3.5.3 and 3.5.4, the patterns of the main reflections for both phases have been interpreted as being indicative of a sixfold twinned structure in either a *C*-centred tetragonal unit cell (for convenience of conversion from the original apparently cubic metric) or a *C*-centred orthorhombic unit cell with a pseudo-tetragonal metric. Therefore, it is convenient to develop initially an average model for the phase II structure, and this work will be described in this chapter. Such an average model can also be build up for Phase I and then it can be used as the starting point for generating a model for the Phase I modulated structure in the five-times larger unit cell which takes the satellite reflections into account and that work will be described in § 5.

The basic structure of α-$NaLuF_4$ comes from the fluorite type structure; it is one of the common crystalline solid types found in nature. The structure of fluorite can be described as face centered cubic packing of cations, with anions in all the tetrahedral holes. It can also be described as simple cubic packing of anions with cations in half of the cubic (eight coordinate) holes. In a fluorite structure with space group *Fm-3m* the metal atom is at 0, 0, 0 and the fluorine atom is at 0.25, 0.25, 0.25. This is the ideal fluorine atom position if there is no distortion in the structure.

The average structure of α-$NaLuF_4$ can be described in the space group *Cmmm* settings with a pseudo tetragonal metric and unit cell parameters **a** = 7.726(2), **b** =

7.743(5), **c** = 5.513(4) Å. The space group can be determined in two possible ways. In the first method, the space group determination was done from the deconvoluted diffraction pattern of single twin domain as described in § 3.5.5. In the second method, the space group was determined by analysis of the difference electron density map by the band-flipping algorithm of the SUPERFLIP program (Palatinus & Chapuis, 2007) which was run using only the Phase I satellite reflections from the 5-times larger orthorhombic cell, and then transforming back to the smaller pseudo-tetragonal cell. This will be discussed in more detail in § 5. The five times larger orthorhombic cell is used for structure solution because the best possible estimate of the unit cell parameters can be achieved only from satellite reflections. Although the unit cell parameters will change with temperature, unfortunately the satellite dataset was collected only at room temperature. So the room temperature pseudo tetragonal unit cell parameters have been used for the refinement against all of the datasets from different temperatures (293 K, 200 K, 150 K and 100 K).

Interestingly the average structure can be described in two different ways, namely Type A and Type B, follows from the group/subgroup relations as described in § 3.5.6. As will be seen below, this has the consequences for the number and site symmetries of the unique atoms. Both the structural descriptions are based on the parent fluorite type structure, which has a cubic lattice. Details of the structural modelling of both types will be described in this chapter and at the same time how bond distance can be used to choose the correct solution. As the structure of α-$NaLuF_4$ has the composition $Na_5Lu_9F_{32}$ as described in § 2.3 and is based on the fluorite type structure, one can safely assume that all or some of the metal atom sites will be mixed with Lu^{3+}/Na^{+} and that there will be vacancy at some of the metal atom sites to fulfill the composition.

4.1 Refinement of the Type A Structure of Phase II

The fluorite structure is *F*-centered cubic with space group $Fm\bar{3}m$, but the α-$NaLuF_4$ structure was modeled using a pseudo tetragonal metric setting with the orthorhombic *Cmmm* space group symmetry. The transformation of the coordinates in direct space from a cubic *P*-centered lattice with space group symmetry $Pm\bar{3}m$ to *C*-centered tetragonal lattice (pseudo tetragonal) with symmetry *Cmmm* requires the transformation matrix 0.5 -0.5 0 0.5 0.5 0 0 0 1. After the necessary coordinate transformation the Type A structure contains three metal atom positions and two fluorine atom positions in the asymmetric unit of the structure. The heavy atom positions are

0, 0, 0 with site symmetry *mmm* and site multiplicity 8, consists of Lu1 and Na1 and vacancy;

0.25, 0.25, 0.50 with site symmetry ..2/*m* and site multiplicity 4, consists of Lu2 and Na2 and vacancy;

0, 0.50, 0 with site symmetry *mmm* and site multiplicity 8, consists of Lu3 and Na3 and vacancy.

At first it is assumed that all the sites are mixed with Lu^{3+}, Na^{+} and vacancy.

The fluorine atom positions are

0, y, z with site symmetry *m..* and site multiplicity 2, described as the position of atom F1 with y and z ~ 0.25

x, 0, z with site symmetry *.m.* and site multiplicity 2, described as the position of atom F2 with x and z ~ 0.25.

Data sets from the Phase II crystal were collected at four different temperatures 293 K, 200 K, 150 K, 100 K and the model was refined against the four different data sets to see the behaviour of the atomic displacement parameters of the metal atoms with temperature.

An isotropic model was developed in the first instance assuming that the fluorine atoms are ordered. All the refinements were performed in Jana2006 (Petricek *et al.*, 2006). All the parameters (scale factor, twin volume, occupation, atomic positions, ADPs) of the model have been refined together. Initially only compositional constraints were applied to the site occupation factors of the metal atoms. As described in § 2.3 the composition of the sample is $Na_5Lu_9F_{32}$. According to the composition, the pseudo tetragonal unit cell will have the formula of $Na_{2.5}Lu_{4.5}F_{16}$. There are sixteen formula units present in the unit cell; so each unit will have the formula of $Na_{0.15625}Lu_{0.28125}F$, such that

$$2.5 = \sum_i nmai[Na]$$

$$4.5 = \sum_i nmai[Lu]$$

where, ai[Lu] and ai[Na] are the site occupation factors of the Lu and Na atom at each of the three atomic sites (Lu1/Na1, Lu2/Na2 and Lu3/Na3 atomic sites) in the formula unit, *m* is the site multiplicity and *n* is the number of symmetry copies of a particular atomic site present in the unit cell. Thus the necessary constraints for the metal atoms in terms of the site occupation factor will be

ai[Lu2] = 0.28125 - ai[Lu1] - ai[Lu3] [Eq. 4.1]
ai[Na2] = 0.15625 - ai[Na1] - ai[Na3] [Eq. 4.2]

To obtain the physical occupation of a site one needs to account for the site multiplicity of that particular site with the site occupation factor of the metal atoms. During the initial refinements the total occupation of the metal atoms at some of the atomic sites exceeded the maximum possible physical occupation of one. This makes it necessary to add new constraints, so that the physical occupation at a particular atomic site does not exceed one (mai ≤ 1). So in the second set of refinements the Na3/Lu3 site was constrained in such a way that the occupation factor of that site does not exceed 0.125 which is the maximum allowed site occupation factor due to the site multiplicity. So the new constraints are:

ai[Lu2] = 0.28125 - ai[Lu1] - ai[Lu3] [Eq. 4.1]
ai[Na2] = 0.15625 - ai[Na1] - ai[Na3] [Eq. 4.2]
ai[Na3] = 0.125 - ai[Lu3] [Eq. 4.3]

In Eq. 4.3 the occupation factor of Na3 is a dependent variable, but in Eq. 4.2 the occupation factor of Na3 is an independent variable. Therefore substituting ai[Na3] in Eq. 4.2 gives

ai[Lu2] = 0.28125 - ai[Lu1] - ai[Lu3] [Eq. 4.1]
ai[Na2] = 0.03125 - ai[Na1] + ai[Lu3] [Eq. 4.2a]
ai[Na3] = 0.125 - ai[Lu3] [Eq. 4.3]

By using this new set of constraints refinement was performed again on the isotropic model of the metal and fluorine atoms.

Six twin volumes were refined during the structural refinement. For an ideal sixfold twin structure each twin volume will be 1/6 = 0.1667. After the refinement the twin volumes were close to 1/6 which is in agreement with the observation that there are six equally intense satellite reflection directions in the Phase I diffraction pattern. The twin volumes were also consistent across the different temperature datasets (Table 4.1). The values in the parenthesis given in Table are the standard uncertainty (s.u.) of the parameter concerned. The s.u.s of the twin volumes are high which suggests that the current isotropic model is not sufficient to describe the twin volumes reliably at this stage.

The values of R_{obs} and wR_{obs} for all the data sets collected at four different temperatures are also consistent (Table 4.1). *GOF* should be close to one for a well converged refinement, if the GOF is more than one it suggests that there are unexplained errors or inadequacies present in the current model. In the current stage of the refinement *GOF* is higher than one (Table 4.1) for all the refinements across different temperature. R_{int} is low and similar across all the temperatures (Table 4.1), suggesting that the integrated intensities are well estimated. Consistent R_{int} suggests that the same model at different temperatures will have similar R_{obs}. In the Lu1/Na1 site, the occupation of Lu atoms is consistent across different temperatures with high s.u.s and the occupation of Na in that site has very high s.u. compared with its occupation. It suggests that the occupation of the metal atoms in that site is not reliable in the current stage of the refinement. In the case of Lu2/Na2, the site occupation of Lu across different temperature is consistent with lower s.u. than the s.u. of the site occupation of Lu1 site but occupation of Na in Lu2/Na2 site have very s.u. compared to its occupation. In the case of Lu3/Na3 site occupation, Lu and Na is consistent across different temperature with low s.u. for both (Table 4.1). Lu being a heavier scatterer than Na and F, Lu site occupation is consistent in this stage of the model, so lower and consistent values of R_{obs} and wR_{obs} are expected in this stage of the refinement. We know that the atomic displacement parameters (ADPs) and site occupation factors of the atomic sites are highly correlated in a disordered structure (Trueblood *et al.*, 1996). The occupations of the heavy scatterer Lu are already consistent across different temperature and isotropic ADPs are consistent as well with the temperature at the current stage of the refinement, which suggests that the occupation of Na have little effect on the isotropic ADPs in the current model. Atomic displacement parameter reduces with lowering of temperature but during the current stage of the refinement the ADPs across different temperature have not been reduced with lowering of temperature (Table 4.1).

	100 K	**150 K**	**200 K**	**293 K**
Twin Volume1	0.17(6)	0.17(5)	0.17(5)	0.17(5)
Twin Volume2	0.17(2)	0.17(2)	0.167(19)	0.167(19)
Twin Volume3	0.16(3)	0.16(2)	0.16(2)	0.16(2)
Twin Volume4	0.18(2)	0.17(2)	0.17(2)	0.17(2)
Twin Volume5	0.17(2)	0.17(2)	0.17(2)	0.17(2)
Twin Volume6	0.16(3)	0.16(2)	0.16(2)	0.16(2)
R_{obs}	2.80 %	2.60 %	2.52 %	2.52 %
wR_{obs}	4.04 %	3.87 %	3.74 %	3.70 %
GOF	2.96	2.84	2.71	2.59
R_{int}	3.54 %	3.58 %	3.63 %	3.67 %
Lu1 Occupation	0.84(13)	0.83(13)	0.85(13)	0.91(12)
Na1 Occupation	0.3(9)	0.4(9)	0.3(9)	population goes slightly negative
Lu2 Occupation	0.61(6)	0.62(6)	0.60(6)	0.58(6)
Na2 Occupation	0.1(4)	0.0(4)	0.1(4)	0.3(4)
Lu3 Occupation	0.189(18)	0.190(19)	0.19(2)	0.18(2)
Na3 Occupation	0.811(18)	0.810(19)	0.81(2)	0.82(2)
Lu1/Na1 U_{iso} **(Å^2)**	0.0137(15)	0.0138(15)	0.0148(14)	0.0168(13)
Lu2/Na2 U_{iso} **(Å^2)**	0.020(2)	0.020(2)	0.020(2)	0.021(2)
Lu3/Na3 U_{iso} **(Å^2)**	0.014(6)	0.014(6)	0.015(6)	0.016(7)

Table 4.1: The refined twin volumes, agreement factors, site occupancies and isotropic displacement parameters of the metal atoms for the Type A structure of Phase II at four different temperatures.

Atomic site Lu1/Na1 has a maximum physically allowed occupation of one, but during the initial stage of the refinement the physical occupation has crossed that limit (Table 4.1). At the same time in the Lu1/Na1 site Na1 occupation has a high s.u. compared to its occupation. Lu is a heavy scatterer and it has a comparatively low s.u. compared to its occupation, one can safely assume that the Lu1/Na1 site is mostly occupied by Lu and may be the remaining content is the vacancy or very little amount of Na. This little amount of Na is not possible to refine based on the available dataset and according to the composition and on the basis of the first isotropic refinement there will be vacancies in the Lu1/Na1 site and Lu2/Na2 site. Based on the above information occupation of Na at Lu1/Na1 site was set to zero in the next set of refinements. The following set of constraints was used to refine the isotropic model again

ai[Lu2] = 0.28125 - ai[Lu1] - ai[Lu3] [Eq. 4.1], constraint used for restricting the amount of Lu in the formula unit according to the composition of $Na_{2.5}Lu_{4.5}F_{16}$.

ai[Na2] = 0.03125 + ai[Lu3] [Eq. 4.2b], constraint used for restricting the amount of Na in the formula unit according to the composition of $Na_{2.5}Lu_{4.5}F_{16}$.

ai[Na3] = 0.125 - ai[Lu3] [Eq. 4.3], constraint used for restricting amount of Lu and Na on Lu3/Na3 site. As Lu3/Na3 site contains only Lu and Na, the vacancies in the structure due to its composition will be distributed in the Lu2/Na2 and Lu1/Na1 site.

ai[Na1] = 0 [Eq. 4.4], constraint used to set the amount of Na to zero according to the previously mentioned argument.

The refined values have been tabulated in Table 4.2. The twin volumes are consistent across the four different temperatures (Table 4.2). There are no significant changes in the twin volumes from the previous refinement. Agreement factors also did not change from the previous refinement (Table 4.2). The distribution of Na and Lu at different atomic sites is more consistent across the temperatures than in the previous refinements after the addition of the constraints (Table 4.2). The isotropic ADPs remain consistent with the temperature after a consistent distribution of Na in different atomic sites at different temperatures. A point to note is that the isotropic ADPs do not decrease much when lowering the temperature (Table 4.2). There is no significant change of R_{obs} after adding the constraints. The isotropic fluorine atoms have larger ADPs which suggest a possible disorder in the fluorine atom positions, F1 atom has U_{iso} 0.018(5) and fluorine atom has U_{iso} 0.049(10) for the 100 K dataset.

	100 K	**150 K**	**200 K**	**293 K**
Twin Volume1	0.17(5)	0.17(5)	0.17(5)	0.17(5)
Twin Volume2	0.17(2)	0.17(2)	0.167(18)	0.167(19)
Twin Volume3	0.16(2)	0.16(2)	0.16(2)	0.16(2)
Twin Volume4	0.18(2)	0.17(2)	0.17(2)	0.17(2)
Twin Volume5	0.17(2)	0.17(2)	0.17(2)	0.17(2)
Twin Volume6	0.16(2)	0.16(2)	0.16(2)	0.16(2)
R_{obs}	2.81 %	2.61 %	2.52 %	2.54 %
wR_{obs}	4.05 %	3.88 %	3.75 %	3.71 %
GOF	2.96	2.84	2.71	2.59
Lu1 Occupation	0.882(18)	0.887(18)	0.891(19)	0.89 (2)
Na1 Occupation	0.000000	0.000000	0.000000	0.000000
Lu2 Occupation	0.590(13)	0.587(13)	0.586(14)	0.588(14)
Na2 Occupation	0.219((9)	0.219(9)	0.218(10)	0.215(10)
Lu3 Occupation	0.188(19)	0.188(19)	0.19(2)	0.18(2)
Na3 Occupation	0.812(19)	0.812(19)	0.81 (2)	0.82(2)
Lu1/Na1 U_{iso} (Å^2)	0.0144(10)	0.0147(10)	0.0153(10)	0.0167(11)
Lu2/Na2 U_{iso} (Å^2)	0.020(2)	0.020(2)	0.020(2)	0.021(2)
Lu3/Na3 U_{iso} (Å^2)	0.013(5)	0.014(5)	0.014(5)	0.016(5)

Table 4.2: The refined twin volumes, agreement factors, site occupancies and isotropic displacement parameters of the metal atoms for the Type A structure of Phase II at four different temperatures.

After isotropic modelling, difference Fourier maps (DF) were generated in the $0 \le x \le 1/2$, $0 \le y \le 1/2$ and $0 \le z \le 1/2$ section of the unit cell taking account of the necessary correction for the sixfold twining. Nine equally spaced slices were calculated along z. In the x and y directions a step size of 0.1 Å was used for the DF. The DF maps in xy sections were calculated through z = 0.00, 0.062, 0.125, 0.188, 0.250, 0.312, 0.375, 0.438 and 0.50. The DF maps were calculated for all the four different temperature datasets using a contour level of ± 0.1 e/Å^3. As all the DF maps look similar at all temperatures, only the maps for the 100 K data are presented here (Fig. 4.1).

The positions of high residual electron density have been identified and are mainly in the z = 0.5 and z = 0.125 layers. These high contour features have been marked with open red circles in the DF maps in Fig. 4.1. The coordinates of the high residual electron density peaks are

x = 0.184, y = 0.184, z = 0.128;

x = 0.5, y = 0.129, z = 0.5;

x = 0.131, y = 0.5, z = 0.5.

These positions are consistent across all the four temperatures. The high contour positions are broad as they appear in up to three of the calculated layers, as shown in Fig. 4.1, e.g. high electron density peaks at z = 0.125 appear also in the z = 0.062 and 0.188 layers. The metal atom positions have been marked with closed red dots in the DF map. The scale along the x and y directions have been shown for z = 0.050 layer in Fig. 4.1. Same scale has been used for all the DF sections. Continuous lines represent positive electron density and dotted lines represent negative electron density.

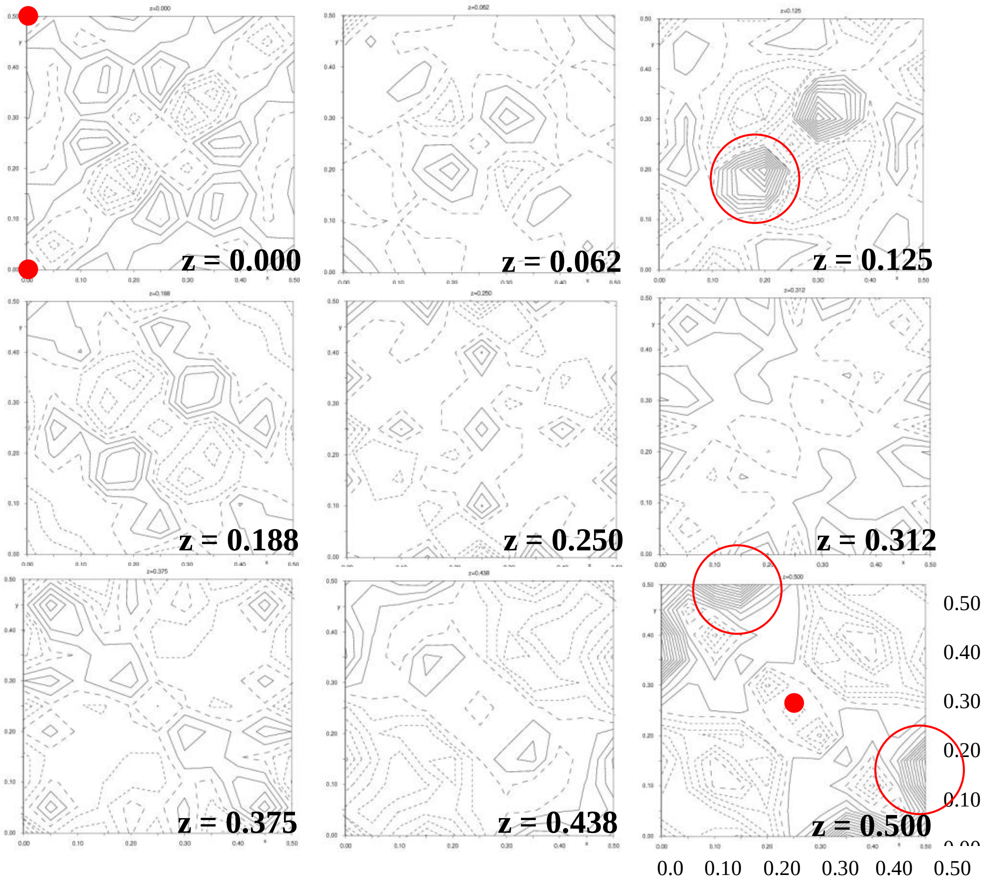

Fig. 4.1: Difference Fourier electron density maps for the 100 K dataset after isotropic modelling for the Type A structure of Phase II.

The positions of the high electron density peaks relative to those of the metal atoms closely resemble Metal-Fluorine distances, so first two peaks have been defined as the positions of disordered fluorine atoms, namely F3 and F4. The total occupancy of all the fluorine atoms (F1, F2, F3 and F4) was kept sixteen according to the composition during the refinement. A point is to note that the third peak (0.131, 0.5, 0.5) in the DF map has also been defined as a possible disordered fluorine atom position, but during the refinement occupation of this site becomes negative and so it was deleted in the subsequent refinement. After refining the occupancies of the disordered fluorine atoms, the sites of the metal atoms were refined anisotropically and further DF maps were calculated as before. The occupancies of the disordered fluorine atoms will be discussed later in this chapter.

Once we take account of the difference electron densities in the DF map in terms of disordered fluorine atoms and introduce anisotropy for the metal atom sites there is no significant electron density left in the model. The DF maps at this stage of the model are consistent across all the temperatures and only the map for 100 K is presented here (Fig. 4.2). The metal atom positions in the structure have been marked with red dots in the DF map. Introducing disorder in the fluorine atom positions from the DF map, the isotropic ADPs of the fluorine atoms become more reasonable (U_{iso} = 0.0276 for 100 K data set). All the fluorine atoms have been refined using the same isotropic ADPs. However, it was not possible to refine the fluorine atoms anisotropically, because the ADPs become non-positive definite during the refinement. At the same time it was also not possible to refine the isotropic ADPs of the fluorine atoms individually, as U_{iso} values of the low occupied fluorine atoms (F3, F4) become slightly negative.

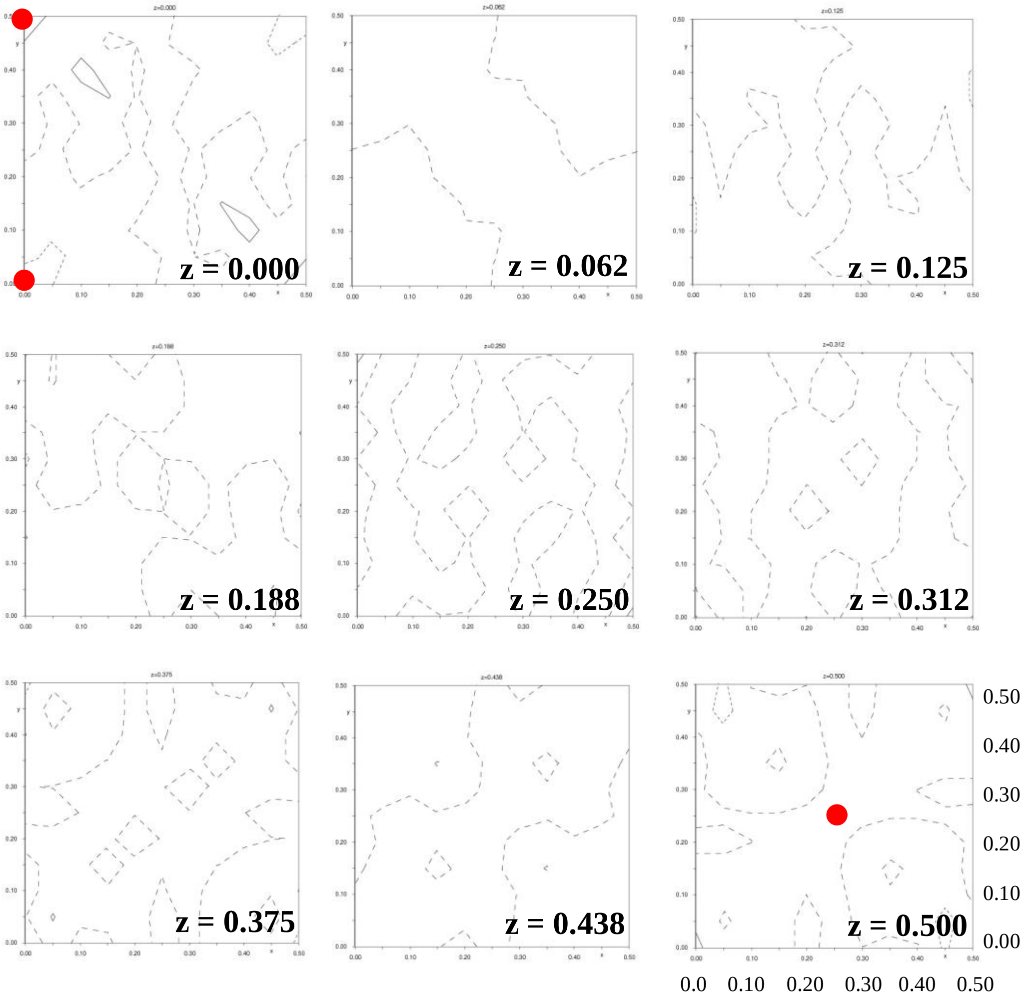

Fig. 4.2: Difference Fourier electron density maps for the 100 K dataset for anisotropic model for the Type A structure of Phase II.

The results of the latest refinement have been tabulated in Table 4.3. After the refinement, the six twin volumes are similar across all the four temperatures (Table 4.3). There were no significant changes in the twin volumes from the previous set of refinements, but the s.u.s of the twin volumes reduce after the anisotropic modelling. R_{obs}, wR_{obs} and *GOF* reduce significantly across all the temperatures once we take account of the disordered fluorine atoms (Table 4.3). The distributions of Lu and Na at the different atomic sites are consistent across all temperatures and have low s.u.s (Table 4.3). The anisotropic U_{11}, U_{22} and U_{33} values across the temperatures for different metal atom sites do not reduce with lowering the temperature. It is interesting to note that at all the temperatures U_{22} is always larger than U_{11} and U_{33} for all the atomic sites (Table 4.3). This suggests a possible disorder along the b axis of the tetragonal cell.

	100 K	**150 K**	**200 K**	**293 K**
Twin Volume1	0.168(8)	0.168(13)	0.168(10)	0.167(10)
Twin Volume2	0.167(2)	0.167(4)	0.166(3)	0.166(3)
Twin Volume3	0.168(4)	0.166(5)	0.169(4)	0.168(4)
Twin Volume4	0.161(5)	0.166(8)	0.159(6)	0.166(6)
Twin Volume5	0.169(3)	0.169(5)	0.170(4)	0.164(4)
Twin Volume6	0.167(4)	0.165(5)	0.168(4)	0.167(4)
R_{obs}	0.89 %	1.07 %	0.93 %	1.08 %
wR_{obs}	1.21 %	1.46 %	1.28 %	1.37 %
GOF	0.91	1.10	0.95	0.98
Lu1 Occupation	0.936(4)	0.961(5)	0.942(5)	0.941(8)
Na1 Occupation	0.0	0.0	0.0	0.0
Lu2 Occupation	0.495(6)	0.490(7)	0.502(7)	0.512(9)
Na2 Occupation	0.287(6)	0.280(7)	0.277(7)	0.267(9)
Lu3 Occupation	0.324(11)	0.309(14)	0.304(13)	0.284(17)
Na3 Occupation	0.676(11)	0.691(14)	0.696(13)	0.716(17)
Lu1/Na1 (U_{11}) **Lu2/Na2 (U_{11})** **Lu3/Na3 (U_{11})** **(Å^2)**	0.0076(5) 0.0044(9) 0.033(2)	0.0078(13) 0.005(3) 0.019(7)	0.0124(9) 0.0082(11) 0.021(2)	0.0126(11) 0.0093(13) 0.019(3)
Lu1/Na1 (U_{22}) **Lu2/Na2 (U_{22})** **Lu3/Na3 (U_{22})** **(Å^2)**	0.0303(12) 0.057(3) 0.067(6)	0.0214(14) 0.024(3) 0.019(5)	0.036(2) 0.054(4) 0.059(7)	0.039(3) 0.054(4) 0.060(8)
Lu1/Na1 (U_{33}) **Lu2/Na2 (U_{33})** **Lu3/Na3 (U_{33})** **(Å^2)**	0.0232(10) 0.0044(8) -0.0044(16)	0.0232(17) 0.027(5) 0.023(6)	0.0128(6) 0.0037(11) 0.013(2)	0.0134(5) 0.0054(10) 0.0139(18)

Table 4.3: The refined twin volumes, agreement factors, site occupancies and anisotropic atomic displacement parameters of the metal atoms for the Type A structure of Phase II at four different temperatures.

The anisotropic ADPs and their s.u.s of the metal atom sites are plotted against temperature in Fig. 4.3 for each of the independent metal atom sites. Changes of anisotropic displacement parameters with temperature are not significant, but the ADPs of the heavy atoms do not give a perfect slope with change of temperature. The source of this problem most probably is the occupational distribution of Lu and Na at different atomic sites. Though the distribution of Lu and Na are very similar across different temperatures within the 3σ but imperfect slope of anisotropic ADPs suggest that the occupations are very sensitive with the ADPs. A small change in the composition will influence the ADPs. In particular, the ADPs at 150 K do not behave well with changing temperature. Such ADP plots are helpful in finding the amount of static disorder present in a system by extrapolating the graph to absolute zero, which needs further investigation.

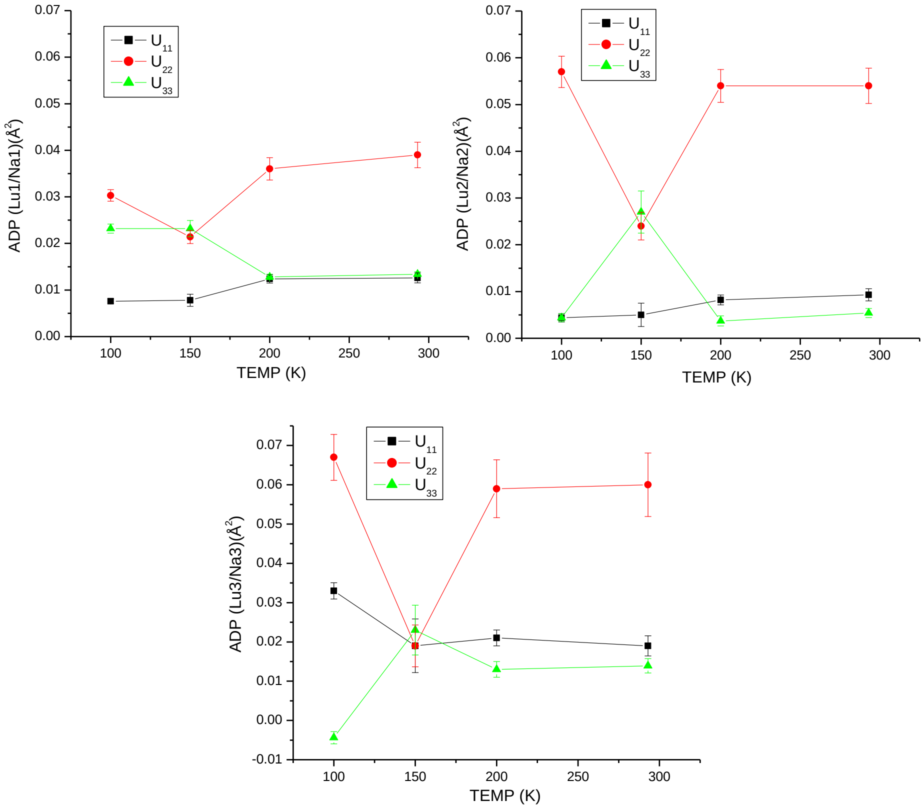

Fig. 4.3: Plot of ADPs (U$_{11}$, U$_{22}$ and U$_{33}$) and their s.u.s against temperature for the Type A structure of Phase II.

From the previous set of anisotropic refinements it was not possible to get a good estimate of the anisotropic ADPs to take an account of this behaviour of the ADPs the distribution of Na and Lu on each site has been averaged at all four temperatures for the different atomic sites and then this average value has been used in the anisotropic refinement at each of the temperatures. The average value used for the refinement has been tabulated in Table 4.4. Once we keep the composition constant there is no significant effect on the twin volumes or their s.u.s (Table 4.4).

The agreement factor (*R*-factor) increases slightly compared to the refinement where the occupation has been freely refined (Table 4.4). But interestingly the ADPs behave in a much better way across the temperatures (Table 4.4). There is no significant reduction of ADP with lowering of temperature. A point to note is that U_{22} for the heavy atoms is still greater than U_{11} and U_{33} in the anisotropic refinement after using the average composition for all temperatures. In Table 4.5, the numbers of measured reflections, numbers of symmetry independent reflections, numbers of reflections with $I > 3\sigma(I)$ used for final set of refinements and the highest and lowest electron density peak (e/Å^3) in the model across the different temperatures are tabulated.

	100 K	**150 K**	**200 K**	**293 K**
Twin Volume1	0.166(11)	0.166(12)	0.166(12)	0.167(10)
Twin Volume2	0.166(4)	0.167(4)	0.167(4)	0.165(3)
Twin Volume3	0.165(5)	0.164(5)	0.164(5)	0.168(4)
Twin Volume4	0.157(5)	0.158(5)	0.158(5)	0.172(6)
Twin Volume5	0.180(6)	0.180(6)	0.180 (6)	0.161(4)
Twin Volume6	0.165(5)	0.165(5)	0.164(5)	0.167(4)
R_{obs}	1.18 %	1.26 %	1.28 %	1.04 %
wR_{obs}	1.47 %	1.53 %	1.53 %	1.29 %
GOF	1.10	1.15	1.13	0.92
Lu1 Occupation	0.945	0.945	0.945	0.945
Na1 Occupation	0.0	0.0	0.0	0.0
Lu2 Occupation	0.500	0.500	0.500	0.500
Na2 Occupation	0.278	0.278	0.278	0.278
Lu3 Occupation	0.305	0.305	0.305	0.305
Na3 Occupation	0.695	0.695	0.695	0.695
Lu1/Na1 (U_{11}) **Lu2/Na2 (U_{11})** **Lu3/Na3 (U_{11})** **($Å^2$)**	0.0044(12) 0.0032(15) 0.006(3)	0.0043(12) 0.0019(14) 0.005(3)	0.0048(12) 0.0023(14) 0.001(2)	0.0133(11) 0.0077(13) 0.022(3)
Lu1/Na1 (U_{22}) **Lu2/Na2 (U_{22})** **Lu3/Na3 (U_{22})** **($Å^2$)**	0.0250(12) 0.0236(19) 0.035(4)	0.0261(13) 0.025(2) 0.035(4)	0.0265(12) 0.027(2) 0.034(4)	0.0403(14) 0.056(2) 0.063(5)
Lu1/Na1 (U_{33}) **Lu2/Na2 (U_{33})** **Lu3/Na3 (U_{33})** **($Å^2$)**	0.0251(17) 0.034(2) 0.028(4)	0.0258(18) 0.037(2) 0.032(4)	0.0263(17) 0.042(2) 0.032(3)	0.0128(6) 0.0061(10) 0.014(2)

Table 4.4: The refined twin volumes, agreement factors, average used site occupancies and anisotropic atomic displacement parameters of the metal atoms for the Type A structure of Phase II at four different temperatures.

	$2\theta_{(max)}$[°]	**Total reflections measured**	**Symmetry independent reflections**	**Reflections with I> σ(I)**	**Reflections used in the refinement**	**Δ_{max}/σ**	**$\Delta\rho$(max, min) e/Å^3**
100 K	55.88	1293	755	755	755	0.0033	0.20,-0.32
150 K	55.84	1308	755	755	755	0.0034	0.21,-0.35
200 K	55.8	1305	755	755	755	0.0035	0.23,-0.32
293 K	56.30	1322	791	791	791	0.0033	0.18,-0.23

Table 4.5: Parameters for the final set of refinements for the Type A structure of Phase II.

After the refinement keeping the composition equal at the four different temperatures, the refined ADPs of the metal atoms and their s.u.s were plotted in Fig. 4.4. The ADPs look more consistent across the temperatures, but the problem still exists for the 293 K dataset. Most probably the ADPs at 293 K are going to a false minimum which is very close to the right minimum.

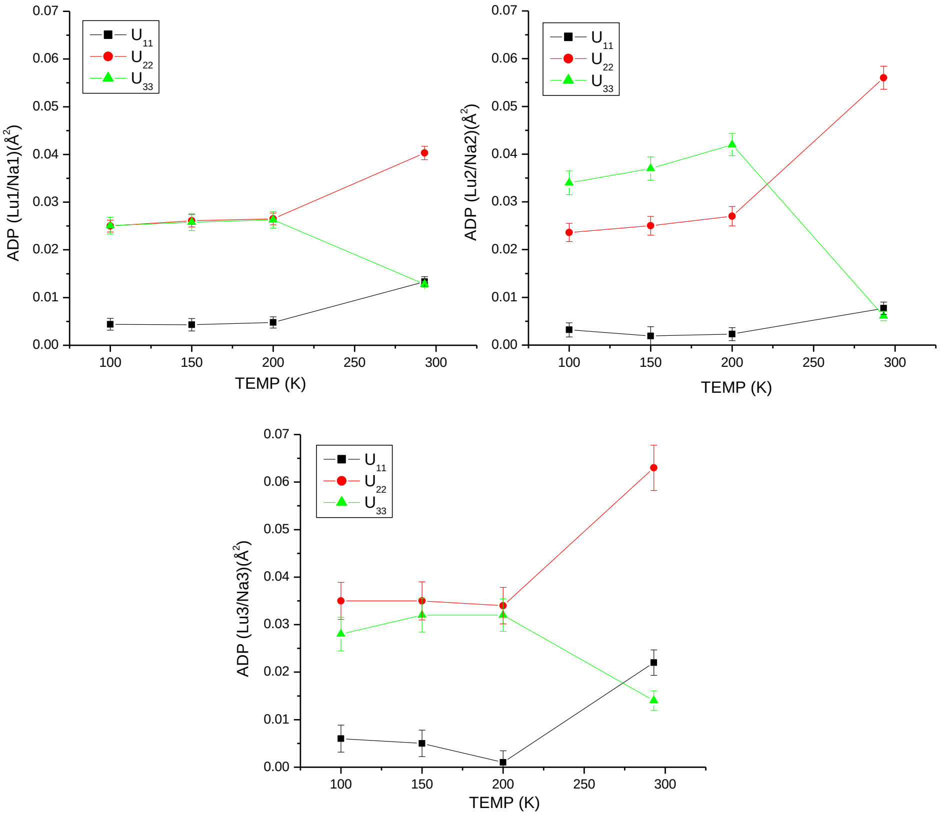

Fig. 4.4: Plot of ADPs (U_{11}, U_{22} and U_{33}) and their s.u.s against temperature of the Type A structure of Phase II after using uniform composition at different temperatures.

4.2 Refinement of the Type B Structure of Phase II

After the necessary transformation (0.5 -0.5 0 0.5 0.5 0 0 0 1) in direct space and a translation of 0, 0.25 , 0, from the parent cubic fluorite structure, the Type B structure consists of two metal atom positions and three fluorine atoms in the asymmetric unit. The structure was modeled in a pseudo tetragonal metric unit cell with the orthorhombic *Cmmm* space group symmetry. Heavy atom positions are

x, 0, 0.50 with site symmetry 2*mm* and site multiplicity 4, consists of Lu1, Na1 and vacancy, where x is ~ 0.25

0, y, 0 with site symmetry *m*2*m* and site multiplicity 4, consists of Lu2, Na2 and vacancy where y is ~ 0.25

And the fluorine atom positions are

0, 0, z where z is ~ 0.25 described as F1 atom with site symmetry *mm*2 and site multiplicity 4

0.5, 0, z where z is ~ 0.25 described as F2 atom with site symmetry *mm*2 and site multiplicity 4

0.25, 0.25, z where z is ~ 0.25 described as F3 atom with site symmetry ..2 and site multiplicity 2

First an isotropic model was built up and a compositional constraint was used for the refinement. As the composition of the formula unit is $Na_{0.15625}$ $Lu_{0.21825}$ F,

the compositional constraints for the metal atom sites will be

ai[Lu2] = 0.28125 - ai[Lu1] [Eq. 4.5]

ai[Na2] = 0.15625 - ai[Na1] [Eq. 4.6]

where ai[Na] and ai[Lu] are the site occupation factors of the Lu and Na atom at the various atomic sites in the formula unit. To obtain the physical occupation at a particular site one needs to take account the site multiplicity with the site occupancy factor.

Using the above constraints, isotropic refinement was performed with the ideal positions of the fluorine atoms included. All the parameters like scale factor, occupation of metal atoms, ADPs and the positions of the metal and fluorine atoms were refined at the same time. In the initial refinement twin volumes behaved well, have low s.u.s and they are consistent across the four temperatures (Table 4.6). R_{obs}, wR_{obs} and *GOF* are consistent across the temperatures (Table 4.6). The Lu population at different atomic sites is consistent and has low s.u. across the temperatures. The site occupation factors of Na1 have very high s.u.s. A point to note is that the site occupation factors of Na2 are close to zero or slightly negative (Table 4.6). This indicates that there is very little or no Na at that site. As there are only two metal atom sites in the formula unit of the structure, all the Na is present at the Lu1/Na1 site. On the basis of this observation the occupation factor of Na2 can be set to zero in the next stage of the refinement. The isotropic displacement parameters have low s.u.s and they do not change much with temperature (Table 4.6).

	100 K	**150 K**	**200 K**	**293 K**
Twin Volume1	0.17(2)	0.17(2)	0.17(2)	0.17(2)
Twin Volume2	0.167(8)	0.167(8)	0.167(8)	0.167(8)
Twin Volume3	0.167(10)	0.167(10)	0.167(10)	0.167(10)
Twin Volume4	0.177(10)	0.176(10)	0.176(10)	0.175(11)
Twin Volume5	0.156(9)	0.156(9)	0.156(9)	0.157(9)
Twin Volume6	0.168(10)	0.168(10)	0.168(10)	0.168(10)
R_{obs}	2.68 %	2.61 %	2.55 %	2.59 %
wR_{obs}	4.01 %	3.94 %	3.88 %	3.94 %
GOF	2.91	2.87	2.79	2.73
R_{int}	3.54 %	3.58 %	3.63 %	3.67 %
Lu1 Occupation	0.31(3)	0.31(2)	0.28(2)	0.29(2)
Na1 Occupation	0.63(18)	0.61(17)	0.82(17)	0.70(17)
Lu2 Occupation	0.82(3)	0.82(2)	0.85(2)	0.83(2)
Na2 Occupation	slightly negative	0.02(17)	slightly negative	slightly negative
Lu1/Na1 U_{iso} **(Å^2)**	0.0118(13)	0.0123(13)	0.0109(13)	0.0144(13)
Lu2/Na2 U_{iso} **(Å^2)**	0.0176(5)	0.0174(5)	0.0188(5)	0.0192(4)

Table 4.6: The refined twin volumes, agreements factors, site occupancies and isotropic atomic displacement parameters of the metal atoms for the Type B structure of Phase II at four different temperatures.

As with the refinement of the Type A structure we have seen that ADPs are highly correlated with the metal atom composition of the atomic sites, so for a better estimate of the ADPs we have taken an average of the distribution of Lu at the different atomic sites across the four different temperatures and this average composition was used for further refinement (Table 4.7). Occupation of Na is the same at the atomic sites across the different temperatures, as all the Na is present in a single metal atom site. This average value has been used for the isotropic refinement. There is no significant change of the twin volumes or their s.u.s after this refinement (Table 4.7). R_{obs}, wR_{obs} and *GOF* increase slightly from the previous refinement (Table 4.7). The average composition across the different temperatures improves the isotropic ADPs with temperature (Table 4.7). The F1 atom has high isotropic ADP (0.21), which suggests a presence of disorder in the structure. The other fluorine atoms (F2 = 0.013(7) and F3 = 0.022(3)) have much lower U_{iso} values than the F1 atom in the structure for the 100 K dataset.

	100 K	**150 K**	**200 K**	**293 K**
Twin Volume1	0.17(2)	0.17(2)	0.17(2)	0.17(2)
Twin Volume2	0.167(8)	0.167(8)	0.167(8)	0.167(9)
Twin Volume3	0.167(11)	0.167(11)	0.167(11)	0.167(11)
Twin Volume4	0.176(11)	0.175(11)	0.175(11)	0.174(11)
Twin Volume5	0.156(9)	0.157(9)	0.157(9)	0.158(10)
Twin Volume6	0.169(11)	0.168(11)	0.168(11)	0.168(11)
R_{obs}	3.15 %	2.99 %	2.88 %	2.79 %
wR_{obs}	4.12 %	4.03 %	3.96 %	3.99 %
GOF	2.99	2.93	2.84	2.76
Lu1 Occupation	0.30	0.30	0.30	0.30
Na1 Occupation	0.625	0.625	0.625	0.625
Lu2 Occupation	0.83	0.83	0.83	0.83
Na2 Occupation	0	0	0	0
Lu1/Na1 U_{iso} (Å^2)	0.0101(14)	0.0108(14)	0.0119(14)	0.0138(14)
Lu2/Na2 U_{iso} (Å^2)	0.0154(4)	0.0157(4)	0.0165(4)	0.0178(4)

Table 4.7: The refined twin volumes, agreement factors, average used site occupancies and isotropic atomic displacement parameters of the metal atoms for the Type B structure of Phase II at four different temperatures.

After isotropic modelling DF maps were calculated in the same way as was done for the Type A structure. As all the DF maps look consistent across all the temperatures in the generated sections, only the map for the 100 K data have been presented here in Fig. 4.5. The high residual electron density positions have been identified. They are mainly in the z = 0.0, 0.375 and 0.500 layers, and have been marked with open red circle. The heavy atom positions have been marked with red dots in the DF maps. The coordinates of the high residual electron density peaks are approximately

x = 0.247, y = 0, z = 0.5;

x =0.063, y = 0.182, z = 0.365;

x = 0.432, y = 0.186, z = 0.365;

x = 0.252, y = 0.132, z = 0.000.

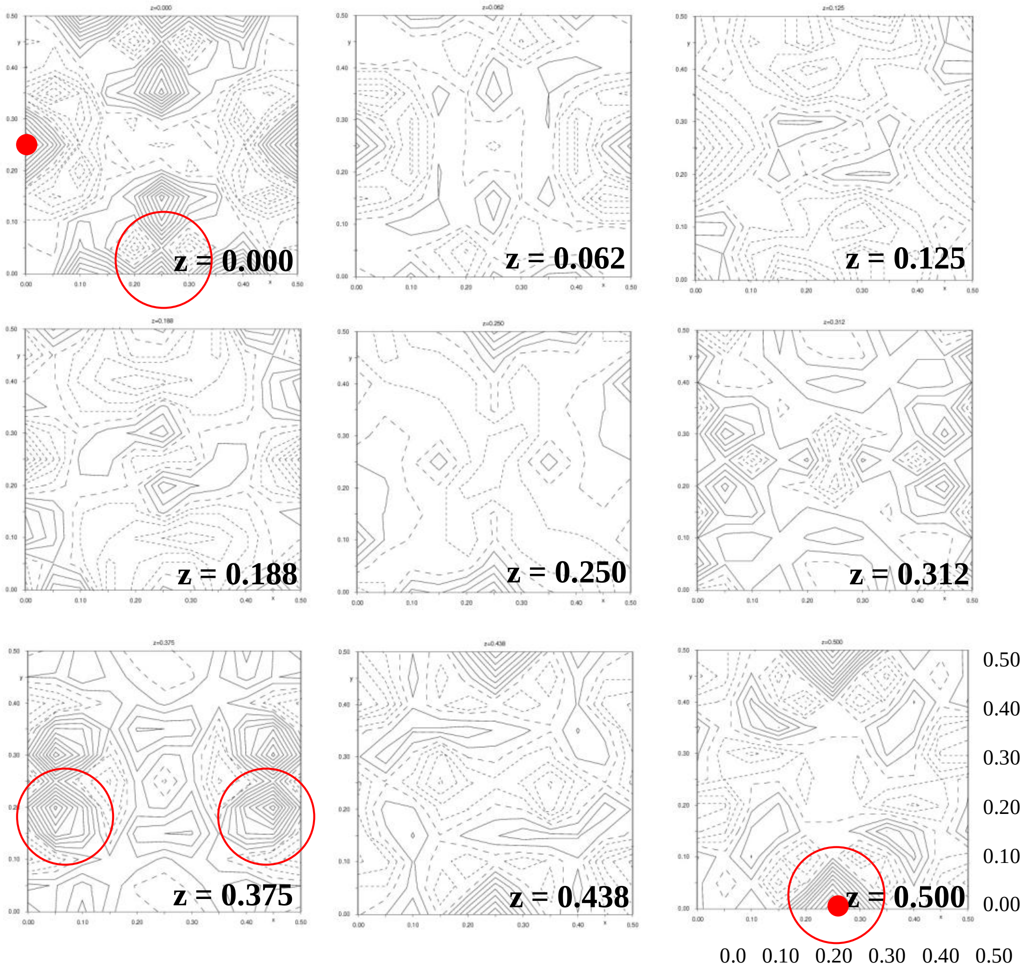

Fig. 4.5: Difference Fourier electron density maps for 100 K dataset for the Type B structure of Phase II.

The positions of the high electron density peaks at z = 0 and 0.375, relative to those of the metal atoms closely resemble Metal-Fluorine distances, so these peaks have been defined as the positions of disordered fluorine atoms namely F4 and F5. The total occupancy of all the fluorine atoms (F1, F2, F3, F4 and F5) was kept sixteen according to the composition of the sample, then the sites of the metal atoms were refined anisotropically and further DF maps were calculated as before. A point is to note that the peak at 0.432, 0.186, 0.365 in the DF map has also been defined as a possible disordered fluorine atom position, but during the refinement occupation of this site becomes negative and so it was deleted in the subsequent refinement. The high electron density peak at z = 0.5 position, may be due to improper absorption correction.

Once we take account of the difference electron densities in the DF map in terms of disordered fluorine atoms and introduce anisotropy in the metal atom sites there is no significant electron density left in the model. The difference electron density maps are consistent across all the temperatures, so DF map for 100 K data set have been plotted in Fig. 4.6. The positions of the metal atoms have been marked with red dots. The scale for the xy section is the same as before.

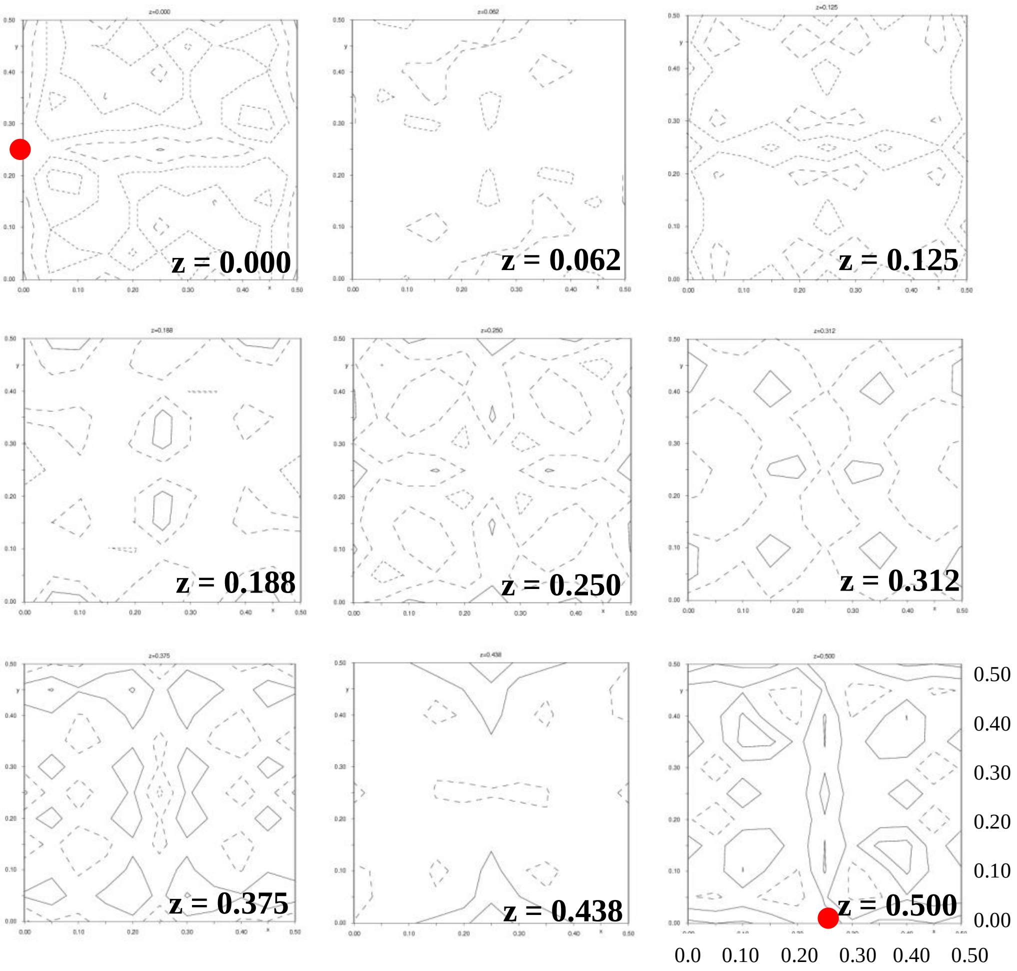

Fig. 4.6: Difference Fourier electron density maps for 100 K dataset for the Type B structure of Phase II.

The refined values of the anisotropic model with the disordered isotropic fluorine atoms have been tabulated in Table 4.8. Twin volumes are consistent across all the temperatures and they have not been influenced by averaging of composition across the different temperatures (Table 4.8). The composition was kept constant at all temperatures to get a better estimate of the anisotropic ADPs (Table 4.8). The agreement factors R_{obs}, wR_{obs} and *GOF* improved significantly from the isotropic refinement (Table 4.8). *GOF* is close to one which suggests that the models have explained the diffraction data properly. The anisotropic ADPs do not change with lowering of temperature from 200 K to 100 K (Table 4.8). A point to note is that Lu1/Na1 has lower anisotropic ADP than the Lu2/Na2 site. The ADPs and their s.u.s were plotted against temperature in Fig. 4.7. The atomic displacement parameters at 293 K data set do not match with 200 K, 150 K and 100 K data set. Most probably the ADPs of the 293 K dataset reach a false minimum which is very close the real minimum. After interpreting the position of the disordered fluorine atoms the isotropic ADPs of the fluorine atoms [U_{iso} = 0.022(3) for 100 K dataset] decrease, but it was not possible to make them anisotropic as they go non-positive definite. The final refined coordinates of the metal atoms across the different temperature are given in Table 4.8. In the Table 4.9, the number of measured reflections, numbers of symmetry independent reflections, numbers of reflections with $I > 3\sigma(I)$ used for the final set of refinements and highest and lowest electron density peak in the model (e/Å^3) across the different temperatures are tabulated.

	100 K	**150 K**	**200 K**	**293 K**
Twin Volume1	0.166(10)	0.166(12)	0.166(11)	0.166(12)
Twin Volume2	0.167(3)	0.167(4)	0.167(4)	0.167(4)
Twin Volume3	0.166(5)	0.166(5)	0.166(5)	0.166(6)
Twin Volume4	0.162(5)	0.157(5)	0.159(5)	0.156(6)
Twin Volume5	0.174(5)	0.178(6)	0.176(5)	0.178(6)
Twin Volume6	0.166(5)	0.167(5)	0.167(5)	0.167(6)
R_{obs}	1.35 %	1.27 %	1.22 %	1.30 %
wR_{obs}	1.53 %	1.54 %	1.51 %	1.55 %
GOF	1.15	1.15	1.11	1.11
Lu1 Occupation	0.30	0.30	0.30	0.30
Na1 Occupation	0.625	0.625	0.625	0.625
Lu2 Occupation	0.83	0.83	0.83	0.83
Na2 Occupation	0	0	0	0
Lu1/Na1 (U_{11}) **Lu2/Na2 (U_{11})** **(Å^2)**	0.003(4) 0.0213(18)	0.004(4) 0.0216(19)	0.005(4) 0.0223(17)	0.013(3) 0.0255(16)
Lu1/Na1 (U_{22}) **Lu2/Na2 (U_{22})** **(Å^2)**	0.005(4) 0.0138(9)	0.006(4) 0.0131(11)	0.007(4) 0.0140(10)	0.0025(18) 0.0123(11)
Lu1/Na1 (U_{33}) **Lu2/Na2 (U_{33})** **(Å^2)**	0.0189(15) 0.0179(10)	0.0209(17) 0.0187(10)	0.0201(17) 0.0194(10)	0.025(2) 0.0215(7)
Lu1/Na1 (x, y, z)	0.2444(9), 0, 0.5	0.2443(10), 0, 0.5	0.2445(10), 0, 0.5	0.2438(10) 0 0.5
Lu2/Na2 (x, y, z)	0, 0.2582(6), 0	0, 0.2575(7), 0	0, 0.2578(6), 0	0 0.2567(6) 0

Table 4.8: The refined twin volumes, agreement factors, average used site occupancies, anisotropic atomic displacement parameters and coordinates of the metal atoms for the Type B structure of Phase II at four different temperatures.

	$2\theta_{(max)}$[°]	Total reflections measured	Symmetry independent reflections	Reflections with I>3σ(I)	Reflections used in the refinement	Δ_{max}/σ	Δρ(max, min) e/Å^3
100 K	55.88	1293	755	755	755	0.0023	0.35, -0.32
150 K	55.84	1308	755	755	755	0.0028	0.29, -0.34
200 K	55.8	1305	755	755	755	0.0023	0.27, -0.30
293 K	56.30	1322	791	791	791	0.0031	0.31, -0.34

Table 4.9: Parameters for final set of refinements for the Type B structure of Phase II.

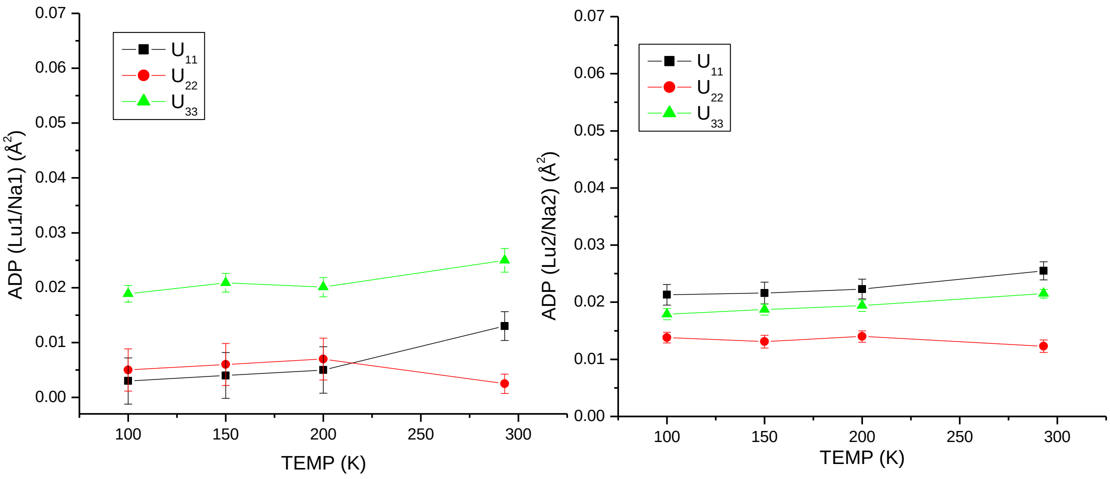

Fig. 4.7: Plot of ADPs (U_{11}, U_{22} and U_{33}) and their s.u.s with change of temperature for the Type B structure of Phase II with uniform composition.

4.3 Comparison of the Type A and Type B Structure of Phase II

The refined model for the Type A and Type B structure have been drawn in Figs. 4.8 and 4.9. Four unit cells were used to draw the structure. Diagrams show only the F1 and F2 atoms for the Type A structure and F1, F2 and F3 for the Type B structure. These fluorine atoms have higher occupancies than the remaining disordered fluorine atoms.

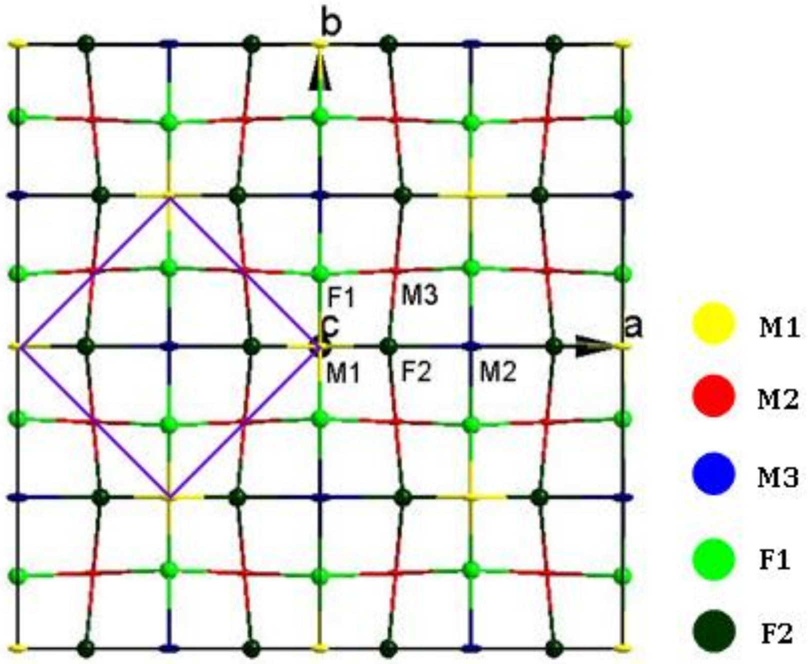

Fig. 4.8: Type A structure of Phase II with 50% ellipsoid probability of metals and fluorine atoms with radius of 0.24 Å based on main reflections. Square box represents the original fluorite cubic cell. The colour codes for all atoms are given on the right hand side of the image.

In the Type A structure each metal atom is coordinated by eight fluorine atoms in a distorted cubic geometry and each fluorine atom is coordinated to four metal centers without considering the fluorine atoms which have much lower occupation (F3 and F4 fluorine atoms). Unlike in the fluorite structure, the fluorine atom positions are shifted from their ideal positions.

From the Inorganic Crystal Structure Database (ICSD) analysis of the lanthanide-fluoride bond distances it is found that on average the Lu-F distance is approximately 2.35 Å for an eight coordinated Lu site and Na-F distance 2.62 Å in an nine coordination and 2.40 in a eight coordination in the sodiumlanthanidefluoride compounds. So if the site is mixed with Na instead of only Lu, then the average metal-fluorine bond distance will increase and if the site has vacancy then the average metal-fluorine distance will be shorter.

This pattern of bond shortening or lengthening can be surmised from the Type A structure (Table 4.10). The M3 metal site is 70% occupied by Na so it will have longer bond distances on average. The M1 metal site is 90% occupied by Lu and the

M2 metal site is occupied by Lu, Na and vacancy so the M1 metal site and M2 metal site will have shorter M-F bond distances on average. The three metal sites have different amount of distribution of metals which makes non-uniform M-F bond distances that ultimately creates a distortion in the structure.

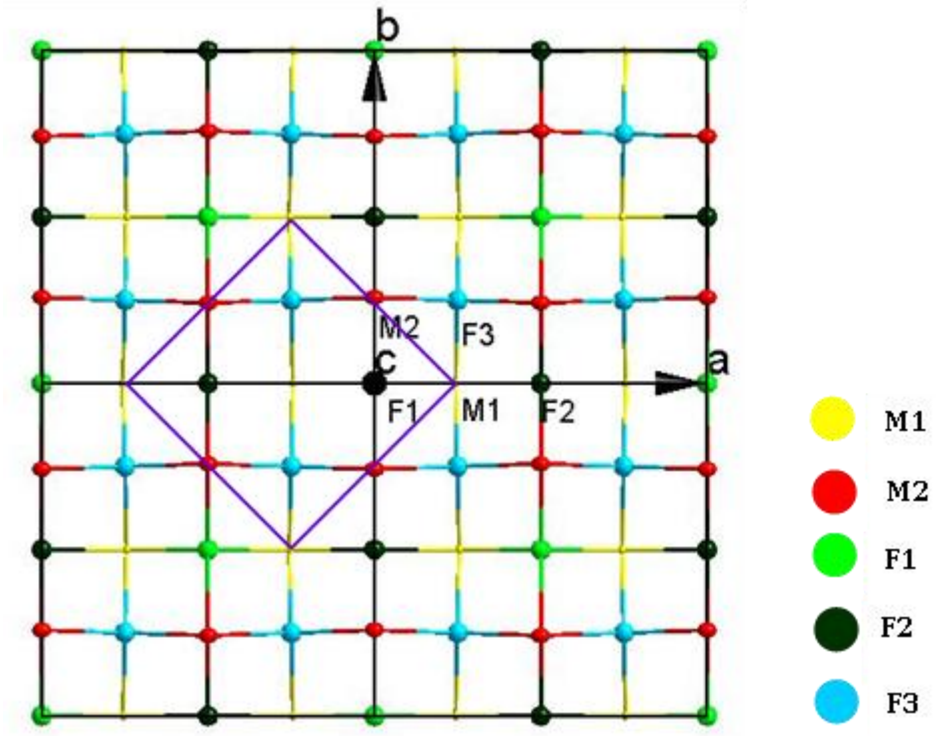

Fig. 4.9: Type B structure of Phase II with 50% ellipsoid probability of metals and fluorine atoms with radius of 0.24 Å based on main reflections. Square box represents the original fluorite cubic cell. The colour codes for all atoms are given on the right hand side of the image.

In the Type B structure we observed a similar pattern of longer or shorter average bond distances (Table 4.11). As the M1 site is mixed with Na it will have longer average M-F distances than the M2 site. The different amount of metal occupation in the atomic sites causes the distortion in the structure and this creates non-uniform metal-fluorine distances around different metal sites.

Although the Type A and Type B structures are different in terms of the distribution of heavy atoms in the asymmetric units, the Type A and Type B structures can be approximately correlated by certain translations in the unit cell.

a) A translation of 0.25 0 0 on the Type A model will convert it to the Type B model and the coordinates of the metal atom sites for the Type A structure after the translation will be

Lu1/Na1 0.25 0 0 with site symmetry 2*mm*

Lu2/Na2 0.50 0.25 0.50 with site symmetry *m*2*m*

Lu3/Na3 0.25 0.50 0 with site symmetry 2*mm*, which is the same as Lu1/Na1, so Lu1/Na1 and Lu3/Na3 atom sites are equivalent after the translation.

These transformed coordinates closely resembles with the coordinates of the metal atoms in the Type B structure.

b) A translation of 0 0.25 0 on the Type A model will also convert it to the Type B model

Lu1/Na1 0 0.25 0 with site symmetry *m*2*m*

Lu2/Na2 0.25 0.50 0.50 with site symmetry 2*mm*

Lu3/Na3 0 0.75 0 with site symmetry *m*2*m*, which is the same as Lu1/Na1 sites, so Lu1/Na1 and Lu3/Na3 atomic site are equivalent after the translation.

As we have mentioned, these two transformations very approximately correlates the two structures as the metal atom position in the Type B structure is at ~ 0.25, 0, 0 and 0, ~ 0.25, 0. Two possible descriptions come from the two unique way of positioning the metal atoms in the unit cell with same space group symmetry *Cmmm* without any distortion of the metal atom positions which will be discussed in § 4.6. The least squares refinement cannot distinguish both the structures, as both of them converge to a reasonable R_{obs}. Are these two structures really different or is just a coordinate transformation? To understand the differences between the Type A and B structures DF maps of both types of structures were examined where metal sites are isotropic and the residual difference electron densities have not interpreted in terms of disordered fluorine atom positions. DF maps were calculated along y for a 100 K dataset with contour ± 0.1 e/$\mathrm{Å}^3$. As we have mentioned that 0 0.25 0 translation transforms the Type A structure to the Type B structure very approximately in the direct space. There are few similarities between the DF maps which are related by the translation of 0 0.25 0, but they are not identical maps, like xz section of Type A at y = 0 resembles with xz section at y = 0.250 of type B model DF and so on, which have been plotted in Fig. 4.10. The DF maps in the left hand side are for the Type A structure and DF maps on the right hand side are for the Type B structure. They have similarities but they are not exactly the same in terms of number of contour lines present. So we can conclude that these two solutions are unique and different in nature, not related with just a coordinate transformation.

TYPE A

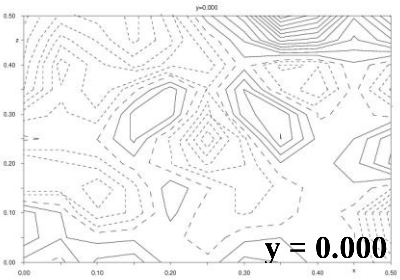
y = 0.000

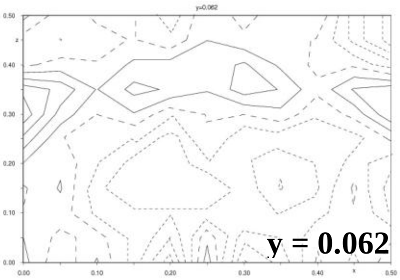
y = 0.062

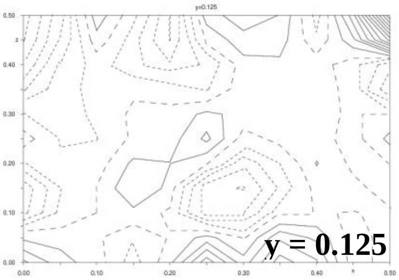
y = 0.125

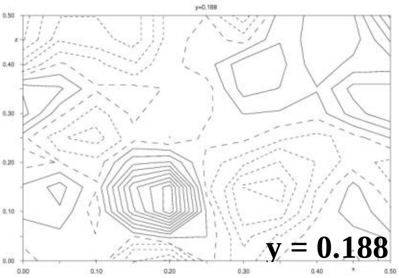
y = 0.188

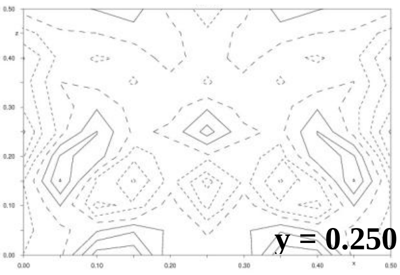
y = 0.250

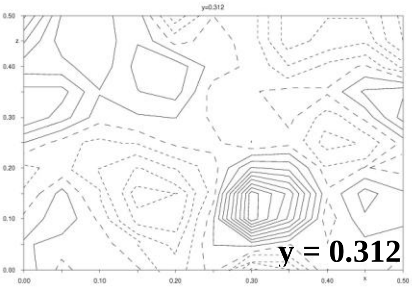
y = 0.312

TYPE B

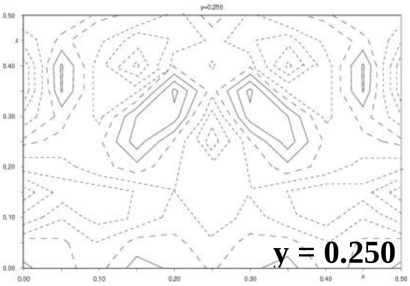
y = 0.250

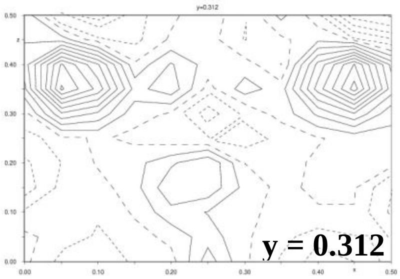
y = 0.312

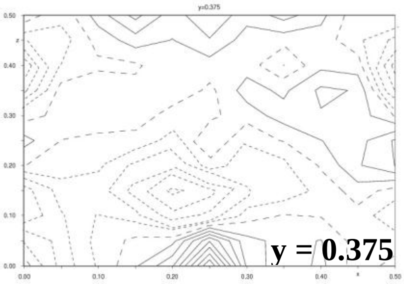
y = 0.375

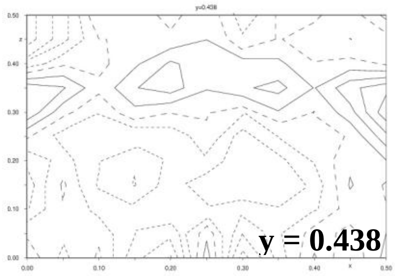
y = 0.438

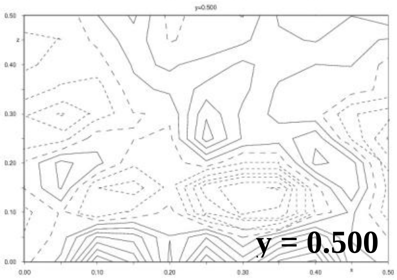
y = 0.500

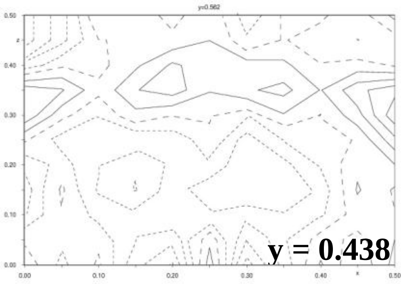
y = 0.438

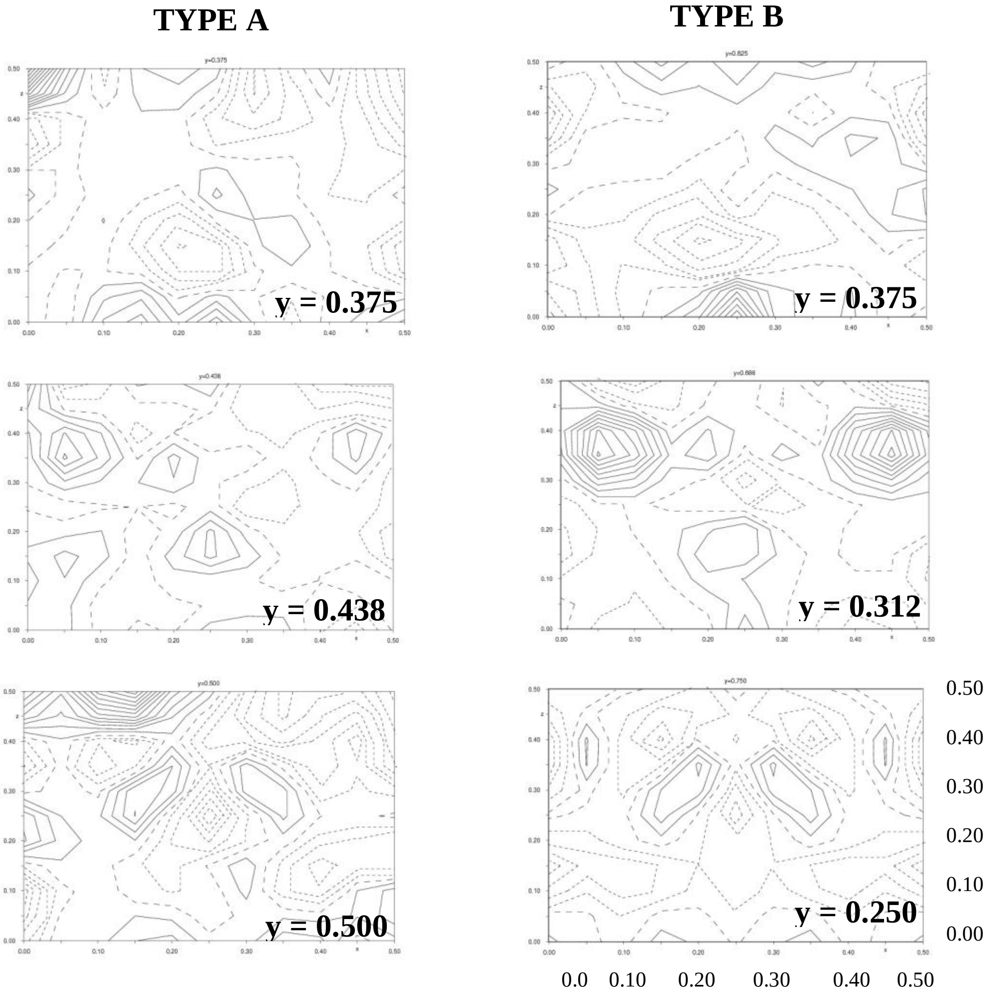

Fig. 4.10: Comparison of DF maps for the Type A and Type B structure of Phase II for isotropic model along y.

4.4 Coordination Geometry of the Metals in Type A and Type B Structure of Phase II

After modelling the Type A and Type B structures and taking account of the residual electron densities in the DF maps in terms of fluorine atoms, we have examined the bond distances around the metal and fluorine atoms. The M-F distances < 3 Å are tabulated in Table 4.10 for the Type A structure and Table 4.11 for the Type B structure. The metals are plotted with 50 % ellipsoidal probability and the fluorine atoms around the metals are plotted with radius of 0.24 Å in Fig. 4.11(a)-(c) for Type A structure and Fig. 4.12(a)-(b) for Type B structure.

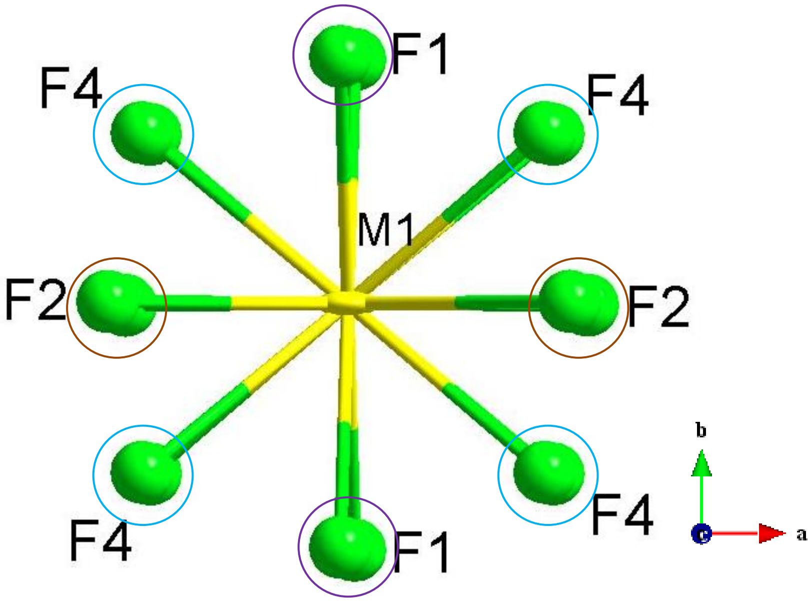

Fig. 4.11(a): The distribution of fluorine atoms around the metal (Lu1/Na1) atoms for the Type A structure. Symmetry related fluorine atoms are marked with the same colour circle. Fluorine atoms above and below the plane of the paper are symmetry related.

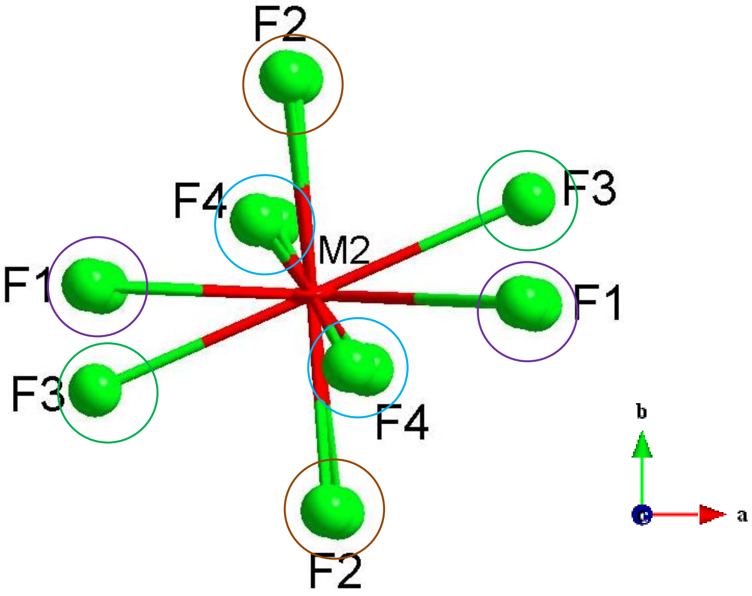

Fig. 4.11(b): The distribution of fluorine atoms around the metal (Lu2/Na2) atoms for the Type A structure of Phase II. Symmetry related fluorine atoms are marked with same colour circle. Fluorine atoms above and below the plane of the paper are symmetry related.

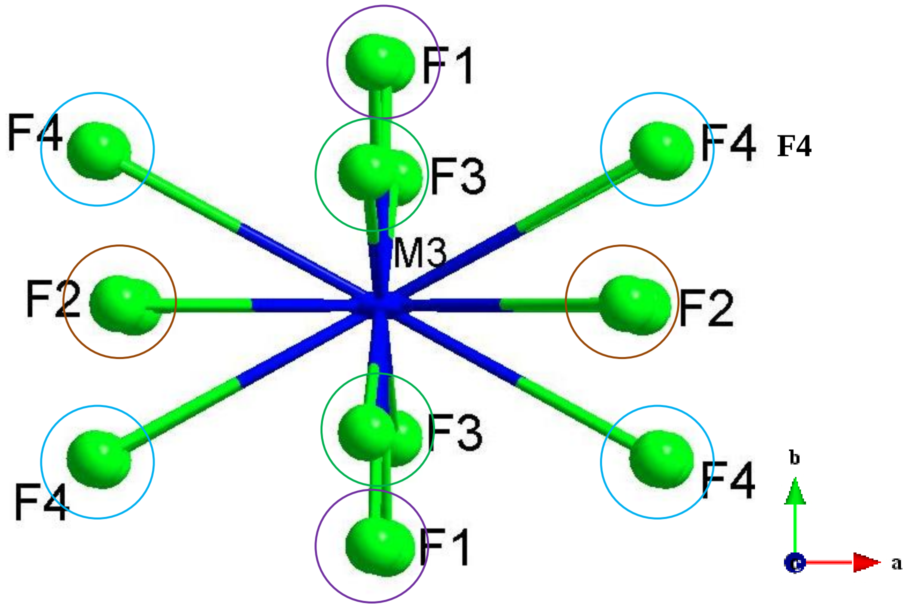

Fig. 4.11(c): The distribution of fluorine atoms around the metal (Lu3/Na3) atoms for the Type A structure of Phase II. Symmetry related fluorine atoms are marked with same colour circle. Fluorine atoms above and below the plane of the paper are symmetry related.

The refined positions for the disordered fluorine atoms are 0 0.2399(19) 0.238(7) for F1 atom, 0.2261(19) 0 0.294(3) for F2 atom, 0.5 0.140(2) 0.5 for F3 atom, 0.197(3) 0.166(2) 0.137(2) for F4 atom. For F1 and F2 atoms it is quite clear that the fluorine atoms have been displaced from the ideal 0 0.25 0.25 and 0.25 0 0.25 positions of a fluorite structure. Taking account of the disordered fluorine atoms there are four symmetry related F1 atoms, four symmetry related F2 atoms and eight symmetry related F4 atoms around the Lu1/Na1 site [Fig. 4.11(a)]. For the Lu2/Na2 site there are four symmetry related F1 atoms, four symmetry related F2 atoms, two symmetry related F3 and four symmetry related F4 atoms [Fig. 4.11(b)]. For the Lu3/Na3 site there are four symmetry related F1 atoms, four symmetry related F2 atoms, four symmetry related F3 atoms and eight symmetry related F4 atoms [Fig. 4.11(c)]. We have tried to find a sensible coordination sphere by combining the disordered metal sites with certain combinations of the disordered fluorine atoms. It was not possible to accommodate some of the fluorine atoms in the coordination sphere due to the short contacts with other disordered fluorine atoms, although they have considerable occupation. Bond distances to the fluorine atoms within 3 Å from the metal atoms are tabulated in Table 4.10. The M-F distances at the different temperatures do not change much so they are presented for the 100 K dataset only.

The number of symmetry related fluorine atoms is given after the respective bond distances and their s.u.s in Table 4.10.

	F1	**F2**	**F3**	**F4**	**Bond Valence Sum**
Bond Distance (Å) M1 (Lu1/Na1)	2.27(2) × 4	2.386(16) × 4	-	2.133(19) × 8	-
Bond Valence Lu1 (v.u.)	0.234903 × 4	0.193759 × 4	-	0.082613 × 8	2.38
Bond Valence Na1 (v.u.)	-	-	-	-	-
Bond Distance (Å) M2 (Lu2/Na2)	2.41(2) × 4	2.252(8) × 4	2.115(6) × 2	2.144(12) × 4	x
Bond Valence Lu2 (v.u.)	0.160902 × 4	0.278321 × 4	0.16887 × 2	0.080193 × 4	2.41
Bond Valence Na2 (v.u.)	0.096544 × 4	0.166997 × 4	0.101325 × 2	0.048117 × 4	1.44
Bond Distance (Å) M3 (Lu3/Na3)	2.40(2) × 4	2.670(15) × 4	2.962(6) × 4	2.78(2) × 4	-
Bond Valence Lu3 (v.u.)	0.16531 × 4	0.089931 × 4	0.017115 × 4	0.014375 × 4	1.15
Bond Valence Na3 (v.u.)	0.099189 × 4	0.05396 × 4	0.010269 × 4	0.008625 × 4	0.69

Table 4.10: The bond distance distribution around the metal atoms, their bond valences and bond valence sum of each of the metal atoms at different atomic sites for the Type A structure of Phase II for the 100 K data. The multipliers refer to the numbers of symmetry equivalent atoms of that type in the coordination sphere.

After examining the M-F distances we have calculated the bond valences at each of the metal centers. Bond valence for M-F distances has been given in valence units (v.u.). Then the bond valence sum for a particular metal site has been calculated by taking account the number of symmetry generated fluorine atoms bonded with the metal site. During the calculation of the bond valence, occupation of the respective fluorine atoms has been taken into account. The occupation of the fluorine atoms will be discussed later (Table 4.12 and 4.13). Table 4.10 shows the bond valences and their sum for the Lu1, Lu2, Na2, Lu3 and Na3 metal atom sites of Type A structure of Phase II for the 100 K data. In the Type A structure Lu1, Lu2 metal sites are slightly under bonded, whereas Lu3 metal site is heavily under bonded. In the M2 atomic site of the Type A structure Na2 metal site is over bonded but Na3 metal site is slightly under bonded in the M3 atomic site. This gives an indication that the Type A structural description may not be the correct one.

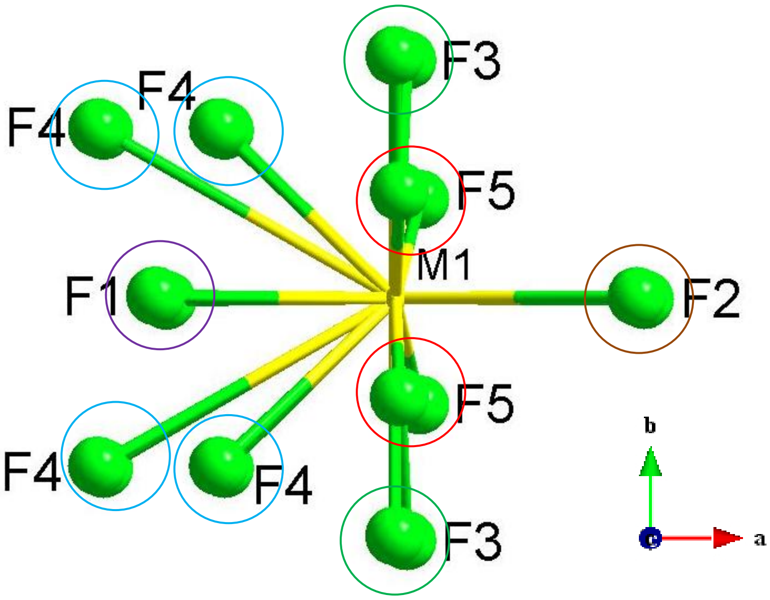

Fig. 4.12(a): The distribution of fluorine atoms around the metal (Lu1/Na1) atoms for the Type B structure of Phase II. Symmetry related fluorine atoms are marked with same colour circle. Fluorine atoms above and below the plane of the paper are symmetry related.

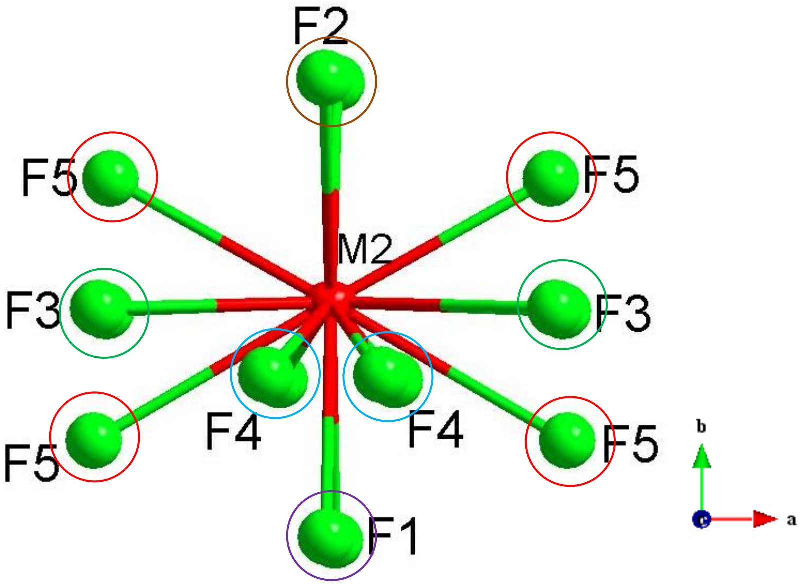

Fig. 4.12(b): The distribution of fluorine atoms around the metal (Lu2/Na2) atoms for the Type B structure of Phase II. Symmetry related fluorine atoms are marked with same colour circle. Fluorine atoms above and below the plane of the paper are symmetry related.

The refined coordinates for the fluorine positions for the Type B structure are 0 0 0.235(7) for F1 atom, 0.5 0 0.322(4) for F2 atom, 0.25 0.25 0.205(4) for F3 atom, 0.063(3) 0.176(2) 0.353(3) for F4 atom, 0.259(3) 0.107(3) 0 for F5 atom. Due to the strain in the structure the fluorine atoms have been displaced from ideal 0 0 0.25 for F1 and 0.5 0 0.25 for F2 in a fluorite structure. Considering the disordered fluorine atoms around the metals, for Lu1/Na1 type of site there are two symmetry related F1 type of atoms, two symmetry related F2 type of atoms, four F3 type of atoms, four symmetry related F4 type of atoms, four symmetry related F5 type of atoms and another four symmetry related F4 type of atoms with a longer distance than the previous F4 type of atom [Fig. 4.12(a)]. These fluorine atoms are within the 3 Å radius of the metal centers. For Lu2/Na2 type of site there are two symmetry related F1 type of atoms, two symmetry related F2 type of atoms, four symmetry related F3 type of atoms, four symmetry related F4 type of atoms, two symmetry related F5 type of atoms and another two symmetry related F5 type of atoms with a larger distance than the previous F5 type of atom within 3 Å from the metal center [Fig. 4.12(b)]. Distance between the metals and the fluorine atoms within 3 Å are tabulated in Table 4.11. An attempt was taken to distribute these disordered fluorine atoms around the metals in a coordination sphere but it was unsuccessful like the Type A structure. The M-F bond distances around the metal sites are tabulated in Table 4.11 for 100 K dataset like before.

Bond valence calculations have been performed for the Type B structure in a similar way. Bond valence sums for Lu1, Na1, Lu2 and Na2 metal sites are given in Table 4.11. In the Type B structure of Phase II, Lu1 metal site is under bonded and Na1 metal site is slightly over bonded. In case of Lu2 metal site, it is slightly under bonded. After examining the bond valence calculation for both the structural Type A and structural Type B, one can say that Type B is a better description of the average structure, as none of the metal sites are highly under bonded unlike Lu3 site for the Type A structure.

	F1	**F2**	**F3**	**F4**	**F5**	**Bond Valence sum**
B. D. (Å) M1 (Lu1/Na1)	2.39(2) × 2	2.207(11) × 2	2.529(14) × 4	2.117(20) × 4 2.86(2) × 4	2.880(7) × 4	-
B. V. Lu1 (v.u.)	0.164986 × 2	0.183019 × 2	0.148311 × 4	0.081696 × 4 0.010967 × 4	0.014197 × 4	1.72
B. V. Na1 (v.u.)	0.098994 × 2	0.109815 × 2	0.088989 × 4	0.049019 × 4 0.006581 × 4	0.008519 × 4	1.03
B. D. (Å) M2 (Lu2/Na2)	2.38(2) × 2	2.576(16) × 2	2.239(11) × 4	2.105(17) × 4	2.32(2) × 2 2.13(2) × 2	-
B. V. Lu2 (v.u.)	0.169506 × 2	0.067511 × 2	0.324764 × 4	0.084389 × 4	0.064495 × 2 0.107781 × 2	2.45
B. V. Na2 (v.u.)	-	-	-	-	-	-

Table 4.11: The bond distance (B. D.) distribution around the metal atoms, their bond valences (B. V.) and bond valence sum of each of the metal atoms at different atomic sites for the Type B structure of Phase II for the 100 K data. The multipliers refer to the numbers of symmetry equivalent atoms of that type in the coordination sphere.

As previously discussed for the coordination of metal atoms by fluorine atoms, M-F distances will be approximately 2.34 Å if only Lu is there in a particular site, the average M-F distances will be less if the site is mixed with vacancy or more if the site is mixed with Na. Now looking the distance distribution of the Type A (Table 4.10) and the Type B (Table 4.11) structures one can see that for the Type A structure in the case of the M3 site except M3-F1 all the bond distances are quite longer than the expected distances. So there are not enough fluorine atoms in the M3 to make a coordination sphere, which will make under-coordinated atomic site. But for the Type B structure in both the atomic sites there are enough number of fluorine atoms with reasonable distances to make coordination sphere. This suggests that the Type B structure may be more correct than the Type A structure.

4.5 Occupation of the Fluorine Atoms in Type A and Type B Structure of Phase II

In the early part of this chapter (Figs. 4.1 and 4.5) it has been discussed that the high electron densities in the DF maps have been interpreted as the position of the disordered fluorine atoms. The occupations of the Fluorine atoms in the Type A and the Type B structures have been tabulated in Table 4.12 and Table 4.13 respectively across all the temperatures.

	F1 Occupation	**F2 Occupation**	**F3 Occupation**	**F4 Occupation**
100 K	0.70(6)	0.79(6)	0.331(19)	0.17(4)
150 K	0.71(6)	0.80(6)	0.32(2)	0.17(4)
200 K	0.69(5)	0.81(5)	0.33(2)	0.17(4)
293 K	0.74(5)	0.78(5)	0.295(16)	0.16(3)

Table 4.12: The population of the disordered fluorine atoms across different temperatures for the Type A structure of Phase II.

For the Type A structure the populations of the fluorine atoms across the different temperatures are consistent. The fluorine populations have high standard uncertainty but the populations itself are consistent. A point to note is that the parent fluorine atoms (F1, F2) have more occupation than the remaining two fluorine atoms obtained from the DF map. There are no two fluorine atoms around any of the metal centers with F…..F distances less than the van der Waals radii and whose occupancy sum is more than one. This suggests there is no problem in the fluorine occupation in the Type A structure. The same thing is valid for the Type B structure.

	F1 Occupation	**F2 Occupation**	**F3 Occupation**	**F4 Occupation**	**F5 Occupation**
100 K	0.68(8)	0.46(7)	0.443(13)	0.161(8)	0.22(6)
150 K	0.71(8)	0.48(7)	0.438(14)	0.159(9)	0.21(6)
200 K	0.70(8)	0.47(7)	0.444(14)	0.159(8)	0.21(6)
293 K	0.82(8)	0.40(8)	0.431(18)	0.163(8)	0.20(7)

Table 4.13: The population of the disordered fluorine atoms across different temperatures for the Type B structure of Phase II.

The populations of the fluorine atoms across different temperature are consistent like in the Type A structure, though some of the s.u.s for the population are quite high. The parent fluorine atoms (F1, F2 and F3) have higher populations than the other two disordered fluorine atoms.

4.6 The Origin of Two Structural Solutions and Relationship of the $NaLuF_4$ Structure to the Fluorite Structure.

The structure of $NaLuF_4$ can be described in two possible ways (Type A structure and Type B structure) which have been discussed in § 4.1 and 4.2. The coordinates of the heavy atoms for the Type A structure in the asymmetric unit of a pseudo-tetragonal unit cell and *Cmmm* space group symmetry are

Heavy atom 1 (M1): x = 0, y = 0, z =0
Heavy atom 2 (M2): x = ¼, y =¼, z = ½
Heavy atom 3 (M3): x = 0, y = ½, z = 0

For the Type B structure the heavy atom positions in a pseudo-tetragonal unit cell with *Cmmm* space group symmetry are

Heavy atom 1(M1): x ~ ¼, y = 0, z = ½
Heavy atom 2 (M2): x = 0, y ~ ¼, z = 0

The possible origin of these two structural descriptions can be understood from the crystallographic orbit theory (Engel *et al.*, 1984). The definitions for the subsequent discussions in this section have been taken from the lecture notes of Massimo Nespolo from the summer Schools on Mathematical Crystallography, which can be accessed from http://www.crystallography.fr/mathcryst/nancy2010.php and from IUCR online Dictionary of Crystallography. A crystallographic orbit is the (infinite) set of atoms obtained from a given atom under the action of the symmetry operations of the space group of the crystal. A crystal structure consists of one or more crystallographic orbits. Each crystallographic orbit possesses an intrinsic symmetry (eigensymmetry) that is equal to or higher than the space group that has generated the orbit. A crystallographic orbit is called characteristic if its intrinsic symmetry (eigensymmetry) is that of the original space group (generating space group). The orbit is called non-characteristic if it displays higher symmetry. If its intrinsic symmetry contains additional translations to that of the original space group, the orbit is called an extraordinary crystallographic orbit. The space group of the crystal structure is the intersection group of the groups that corresponds to the eigensymmetry of each crystallographic orbit occupied by a given type of atom in the crystal structure. The determination of the non-characteristic orbits of the space group and their eigensymmetry groups have been implemented in the computer program NONCHAR available on the Bilbao Crystallographic Server (Aroyo *et al.*, 2006) and available from http://www.cryst.ehu.es/. The program NONCHAR has been used to generate the following description of the eigensymmetries of the orbits in both structural descriptions.

4.6.1 The Eigensymmetries of the Orbits of the Type A Structure

- First, considering the Type A Structure in the space group *Cmmm* with the positions of the heavy atoms only, in an orthorhombic metric with basis vectors 5$\mathbf{a}_\mathbf{T}$, $\mathbf{b}_\mathbf{T}$ and $\mathbf{c}_\mathbf{T}$ ($\mathbf{a}_\mathbf{T} = \mathbf{b}_\mathbf{T} \neq \mathbf{c}_\mathbf{T}$), then

➢ The orbit 2a with an atom at x = 0, y = 0, z =0 will have eigensymmetry *Cmmm*, a characteristic orbit.

➢ The orbit 4f with an atom at x = ¼, y = ¼, z = ½ will have eigensymmetry *Pmmm*, a non-characteristic obit. The following column transformation matrix relates the coordinate system of the eigensymmetry of the orbit to the space group *Cmmm* having basis vectors 5$\mathbf{a}_\mathbf{T}$, $\mathbf{b}_\mathbf{T}$ and $\mathbf{c}_\mathbf{T}$

$$\begin{pmatrix} 0 & 0 & 1 \\ 2 & 0 & 0 \\ 0 & 2 & 0 \end{pmatrix}, \begin{pmatrix} 0 \\ 0 \\ 0 \end{pmatrix}$$

where the first 3X3 matrix describes the rotational part of the transformation of the row of basis vectors to the basis vectors (5$\mathbf{a}_\mathbf{T}$, $\mathbf{b}_\mathbf{T}$ and $\mathbf{c}_\mathbf{T}$) and the second 3x1 column determines the origin shift.

➢ The orbit 2b with an atom at x = 0, y = ½, z = 0 will have eigensymmetry *Cmmm*, a characteristic orbit.

The intersection group of the three orbits with equal population will have *Immm* symmetry with

$5\mathbf{a}_\mathbf{T} = 2 \times 5\mathbf{a'}_\mathbf{T}$

$\mathbf{b}_\mathbf{T} = 2 \times \mathbf{b'}_\mathbf{T}$

$\mathbf{c}_\mathbf{T} = \mathbf{c'}_\mathbf{T}$

where 5$\mathbf{a'}_\mathbf{T}$, $\mathbf{b'}_\mathbf{T}$ and $\mathbf{c'}_\mathbf{T}$ are the basis vectors of the unit cell having symmetry *Immm* and $\mathbf{a'}_\mathbf{T} = \mathbf{b'}_\mathbf{T} \neq \mathbf{c'}_\mathbf{T}$

- Second, considering the Type A structure with space group *Cmmm* in a tetragonal metric with basis vectors $\mathbf{a}_T$, $\mathbf{b}_T$ and $\mathbf{c}_T$ ($\mathbf{a}_T = \mathbf{b}_T \neq \mathbf{c}_T$), then

➢ The orbit 2a with an atom at x = 0, y = 0, z = 0 will have eigensymmetry *P4/mmm*, a non-characteristic orbit and the coordinate system is related to the space group *Cmmm* by the following transformation

$$\begin{pmatrix} 1 & 1 & 0 \\ -1 & 1 & 0 \\ 0 & 0 & 1 \end{pmatrix}, \begin{pmatrix} 0 \\ 0 \\ 0 \end{pmatrix}$$

and the above transformation can be described by Fig. 4.13(a)

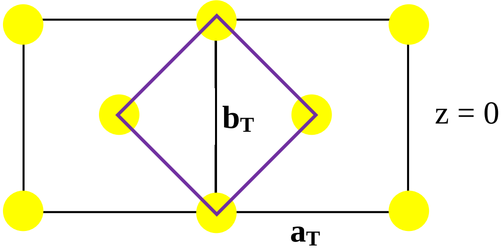

Fig. 4.13(a): The yellow dot indicate the atom positions at z = 0 in two unit cells with basis vectors a_T and b_T which can be transformed from the basis vectors shown in pink by the matrix given above.

➢ The orbit 4f with an atom at x = ¼, y = ¼, z = ½ will have eigensymmetry *P4/mmm*, a non-characteristic orbit and the coordinate system is related to the space group *Cmmm* by the following transformation

$$\begin{pmatrix} 2 & 0 & 0 \\ 0 & 2 & 0 \\ 0 & 0 & 1 \end{pmatrix}, \begin{pmatrix} 0 \\ 0 \\ 0 \end{pmatrix}$$

and the above transformation can be described by Fig. 4.13(b)

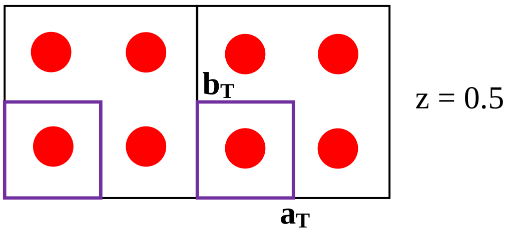

Fig. 4.13(b): The red dots indicate the atom positions at z = 0.5 in two unit cells with basis vectors $\mathbf{a}_T$ and $\mathbf{b}_T$ which can be transformed from the basis vectors shown in pink by the matrix given above.

- The orbit 2b with an atom at x = 0, y = ½, z = 0 will have eigensymmetry *P4/mmm*, a non-characteristic orbit and the coordinate system is related to the space group *Cmmm* by the following transformation

$$\begin{pmatrix} 1 & 1 & 0 \\ -1 & 1 & 0 \\ 0 & 0 & 1 \end{pmatrix}, \begin{pmatrix} 0 \\ 0 \\ 0 \end{pmatrix}$$

and the above transformation can be described by Fig. 4.13(c)

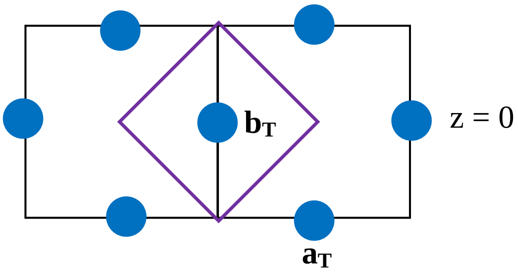

Fig. 4.13(c): The blue dot indicate the atom positions at z = 0 in two unit cells with basis vectors $\mathbf{a}_T$ and $\mathbf{b}_T$ which can be transformed from the basis vectors shown in pink by the matrix given above.

The intersection group of the three orbits, assuming the orbits are equally populated, will have *I4/mmm* symmetry, with

$\mathbf{a}_T = 2 \times \mathbf{a}'_T$

$\mathbf{b}_T = 2 \times \mathbf{b}'_T$

$\mathbf{c}_T = \mathbf{c}'_T$

where $\mathbf{a}'_T$, $\mathbf{b}'_T$ and $\mathbf{c}'_T$ are the basis vectors of the unit cell having symmetry of *I4/mmm*

- Third, considering the Type A structure with space group *Cmmm* and with a cubic metric such that $\mathbf{a}_T = \mathbf{b}_T = \sqrt{2}\mathbf{c}_T$ and defining $\hat{\mathbf{c}}_T = \sqrt{2}\mathbf{c}_T$, then

- The orbit 2a with an atom at x = 0, y = 0, z = 0 will have eigensymmetry $Pm\bar{3}m$, a non-characteristic orbit and the coordinate system is related to the space group *Cmmm* by the following transformation

$$\begin{pmatrix} 1 & 1 & 0 \\ -1 & 1 & 0 \\ 0 & 0 & 1 \end{pmatrix}, \begin{pmatrix} 0 \\ 0 \\ 0 \end{pmatrix}$$

- The orbit 4f with an atom at x = ¼, y = ¼, z = ½ will have eigensymmetry $Pm\bar{3}m$, a non-characteristic orbit and the coordinate system is related to the space group *Cmmm* by the following transformation

$$\begin{pmatrix} 0 & 0 & 1 \\ 2 & 0 & 0 \\ 0 & 2 & 0 \end{pmatrix}, \begin{pmatrix} 0 \\ 0 \\ 0 \end{pmatrix}$$

- The orbit 2b with an atom at x = 0, y = ½, z = 0 will have eigensymmetry $Pm\bar{3}m$, an extraordinary orbit and the coordinate system is related to the space group *Cmmm* by the following transformation

$$\begin{pmatrix} 1 & 1 & 0 \\ -1 & 1 & 0 \\ 0 & 0 & 1 \end{pmatrix}, \begin{pmatrix} 1/2 \\ -1/2 \\ 0 \end{pmatrix}$$

If one takes account of all the three orbits (2a, 4f, 2b) and if the orbits are equally populated, then the intersection group will have $Fm\bar{3}m$ symmetry with

$(\mathbf{a}_T + \mathbf{b}_T)/2 = \mathbf{a}'_C = \mathbf{b}'_C$

$\hat{\mathbf{c}}_T = \mathbf{c}'_C$ and $\mathbf{a}'_C = \mathbf{c}'_C$

where $\mathbf{a}'_C$, $\mathbf{b}'_C$ and $\mathbf{c}'_C$ are the basis vectors of the unit cell having symmetry $Fm\bar{3}m$. Interestingly this space group symmetry is also the eigensymmetry of the metal atom in the fluorite structure. This strongly supports the basis of deriving the $NaLuF_4$ structure from the calcium fluorite structure.

4.6.2 The Eigensymmetries of the Orbits of the Type B Structure

- In the first case of the Type B description (two heavy atom positions in the asymmetric unit) of the structure with space group *Cmmm* and orthorhombic metric unit basis vectors 5$\mathbf{a_T}$, $\mathbf{b_T}$ and $\mathbf{c_T}$ where ($\mathbf{a_T} = \mathbf{b_T} \neq \mathbf{c_T}$)

➢ The orbit 4h with an atom at x = ¼, y = 0, z = ½ will have eigensymmetry *Pmmm*, a non-characteristic orbit and the coordinate system is related to the space group *Cmmm* by the following transformation

$$\begin{pmatrix} 0 & 0 & 1 \\ 2 & 0 & 0 \\ 0 & 2 & 0 \end{pmatrix}, \begin{pmatrix} 0 \\ 0 \\ 0 \end{pmatrix}$$

➢ The orbit 4i with an atom at x = 0, y = ¼, z = 0 will have eigensymmetry *Pmmm*, a non-characteristic orbit and the coordinate system is related to the space group *Cmmm* by the following transformation

$$\begin{pmatrix} 0 & 0 & 1 \\ 2 & 0 & 0 \\ 0 & 2 & 0 \end{pmatrix}, \begin{pmatrix} 0 \\ 0 \\ 0 \end{pmatrix}$$

Now the intersection group of the eigensymmetries of the two equally populated orbits will be *Immm*, with

$5\mathbf{a_T} = 2 \times 5\mathbf{a'_T}$

$\mathbf{b_T} = 2 \times \mathbf{b'_T}$

$\mathbf{c_T} = \mathbf{c'_T}$

where 5$\mathbf{a'_T}$, $\mathbf{b'_T}$ and $\mathbf{c'_T}$ are the basis vectors of the unit cell having *Immm* symmetry and $\mathbf{a'_T} = \mathbf{b'_T} \neq \mathbf{c'_T}$. The intersection group symmetry of the orbits is the same for the Type A and Type B description of the structure with an orthorhombic metric. Conversely, both structural descriptions will have the same diffraction pattern if the atoms are in those specified positions as described above.

- In the second case of the Type B description of the structure with a tetragonal metric defined by the basis vectors $\mathbf{a_T}$, $\mathbf{b_T}$ and $\mathbf{c_T}$ ($\mathbf{a_T} = \mathbf{b_T} \neq \mathbf{c_T}$), then

➢ The orbit 4h with an atom at x = ¼, y = 0, z = ½ will have eigensymmetry *P4/mmm*, an extraordinary orbit and the coordinate system is related to the space group *Cmmm* by the following transformation

$$\begin{pmatrix}2 & 0 & 0\\ 0 & 2 & 0\\ 0 & 0 & 1\end{pmatrix}, \begin{pmatrix}1/2\\ 0\\ 0\end{pmatrix}$$

and the above transformation can be described by Fig. 4.14(a)

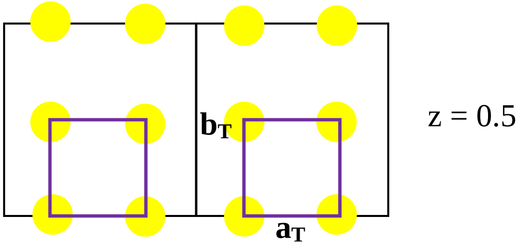

Fig. 4.14(a): The yellow dots indicate the atom positions at z = 0.5 in two unit cells with basis vectors $\mathbf{a}_T$ and $\mathbf{b}_T$ which can be transformed from the basis vectors shown in pink by the matrix given above.

- The orbit 4i with an atom at x = 0, y = ¼, z = 0 will have eigensymmetry *P*4/*mmm*, an extraordinary orbit and the coordinate system is related to the space group *Cmmm* by the following transformation

$$\begin{pmatrix}2 & 0 & 0\\ 0 & 2 & 0\\ 0 & 0 & 1\end{pmatrix}, \begin{pmatrix}1/2\\ 0\\ 0\end{pmatrix}$$

and the above transformation can be described by Fig. 4.14(b)

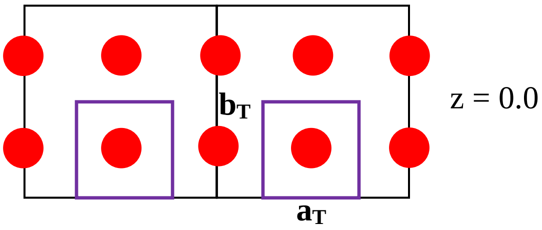

Fig. 4.14(b): The red dots indicate the atom positions at z = 0 in two unit cells with basis vectors $\mathbf{a}_T$ and $\mathbf{b}_T$ which can be transformed from the basis vectors shown in pink by the matrix given above.

The intersection group of the eigensymmetries of the two orbits will be *I*4/*mmm*, with

$\mathbf{a}_T = 2 \times \mathbf{a}'_T$

$\mathbf{b}_T = 2 \times \mathbf{b}'_T$

$\mathbf{c}_T = \mathbf{c}'_T$

where $\mathbf{a'}_T$, $\mathbf{b'}_T$ and $\mathbf{c'}_T$ are the basis vectors of the unit cell having symmetry *I*4/*mmm* and $\mathbf{a'}_T = \mathbf{b'}_T \neq \mathbf{c'}_T$. This suggests that with a tetragonal metric both of the structural description A and B will have the same diffraction pattern and conversely two equally possible structural descriptions of a single diffraction pattern are possible even with a tetragonal metric.

- In the third case, for the Type B description of the structure with a cubic metric, such that the basis vectors $\mathbf{a}_T = \mathbf{b}_T = \sqrt{2}\mathbf{c}_T$ and now one can define $\hat{\mathbf{c}}_T = \sqrt{2}\mathbf{c}_T$, then

- The orbit 4h with an atom at x = ¼, y = 0, z = ½ will have eigensymmetry $Pm\bar{3}m$, an extraordinary orbit and the coordinate system is related to the space group *Cmmm* by the following transformation

$$\begin{pmatrix} 0 & 0 & 1 \\ 2 & 0 & 0 \\ 0 & 2 & 0 \end{pmatrix}, \begin{pmatrix} 0 \\ 0 \\ 1/2 \end{pmatrix}$$

- The orbit 4i with an atom at x = 0, y = ¼, z = 0 will have symmetry eigensymmetry $Pm\bar{3}m$, an extraordinary orbit and the coordinate system is related to the space group *Cmmm* by the following transformation

$$\begin{pmatrix} 0 & 0 & 1 \\ 2 & 0 & 0 \\ 0 & 2 & 0 \end{pmatrix}, \begin{pmatrix} 0 \\ 0 \\ 1/2 \end{pmatrix}$$

If one considers both of the orbits equally populated, then the intersection group of the eigensymmetries of the two orbits will have $Fm\bar{3}m$ symmetry and the new basis vectors $\mathbf{a'}_C$, $\mathbf{b'}_C$, $\mathbf{c'}_C$ can be described by

$(\mathbf{a}_T + \mathbf{b}_T)/2 = \mathbf{a'}_C = \mathbf{b'}_C$

$\hat{\mathbf{c}}_T = \mathbf{c'}_C$ and $\mathbf{a'}_C = \mathbf{c'}_C$

Interestingly $Fm\bar{3}m$ is the eigensymmetry of the metal atom in the fluorite structure which supports the Type B description of the $NaLuF_4$ structure.

4.7 Conclusion

The Phase II diffraction pattern was modeled in a pseudo tetragonal unit cell with *Cmmm* symmetry in two possible ways. Careful data integration of the main reflections gave a good estimate of the twin volumes. The six twin components are roughly equally occupied. It is difficult to distinguish the two structural descriptions A and B in terms of structural refinement. Bond distance spectra and bond valence calculations give a hint structure B is preferable over the other.

4.8 References

Allmann, R. & Hinek, R. (2007). *Acta Cryst. A***63**, 412–417.

Aroyo, M. I., Perez-Mato, J. M., Capillas, C., Kroumova, E., Ivantchev, S., Madariaga, G., Kirov, A. & Wondratschek, H. (2006). *Z Kristallogr* **221**, 15-27.

Behrens, H., Luksch, P. (2006). *Acta Cryst. B***62**, 993–1001.

Belsky, A., Hellenbrandt, M., Karen, V. L. & Luksch, P. (2002). *Acta Cryst. B***58**, 364–369.

Bergerhoff, G. & Brown, I.D. in “Crystallographic Databases”, F.H. Allen *et al.* (Hrsg.) Chester, International Union of Crystallography, (1987).

Engel, P., Matsumotov, T., Steinmann, G. & Wondratschek, H. (1984). *Z. Kristallogr., Suppl. Issue No.1, Oldenbourg, Muenchen.*

Kaduk, J.A. (2002). *Acta Cryst. B***58**, 370–379.

Palatinus, L. & Chapuis, G. (2007). *J. Appl. Cryst.* **40**, 786-790.

Trueblood, K. N., Bürgi, H. B., Burzlaff, H., Dunitz, J. D., Gramaccioli, C. M., Schulz, H. H., Shmueli, U. & Abrahams, S. C. (1996). *Acta Crystallogr A* **52**, 770-781.

Petricek, V., Dusek, M. & Palatinus L. (2006). Jana2006.Structure Determination Software Programs. Institute of Physics, Praha, Czech Republic.

Chapter 5: Understanding the Phase I Structure

The main reflections in the Phase I diffraction pattern are similar to those of Phase II, the difference comes in terms of extra satellite reflections in Phase I and from the nature of diffuse scattering. So we can expect that the average structure of Phase I based on the main reflections will be similar to that of Phase II as they have same the chemical composition as calculated from EDX analysis, and that the Phase I average structure can also be described in two different ways. The modelling of the average structure of Phase I at three different temperatures (100 K, 200 K, 293 K), based on the main reflections only and the similarities and differences to the Phase II structure will be discussed in the first part this chapter.

How can the average structure based on the main reflections be used to understand the fivefold superstructure? The model development and refinement in 3-D space, as well as in Superspace, against the satellite reflections will also be discussed in this chapter. How can the difference electron density map produced by the program SUPERFLIP from satellite reflections be exploited to derive the space group (the *Cmmm* space group used for Phase I and Phase II) in a structure where main reflections are from the overlapping of different twin domains will also be discussed.

5.1 Average Structure Modelling Based on the Main Reflections

Pseudo tetragonal unit cell parameters (**a** = 7.726(2), **b** = 7.743(5), **c** = 5.513(4) Å) have been derived from the indexation of the satellite reflections of Phase I of a room temperature data set as described in § 3.5 and this cell parameter will be used for the refinement of the Phase I average structure based on the main reflections.

5.1.1 Refinement of the Type A Average Structure of Phase I

The initial model in the pseudo-tetragonal unit cell of space group *Cmmm* was set up and refined in an analogous manner to that described in § 4.1 for the Type A structure of Phase II, including the assumptions about the effect of composition on the distribution of the atoms across the sites. In the first refinement, the scale factor, positions of the metal atoms and fluorine atoms, ADPs of the metal atoms and fluorine atoms and occupancies of the metal atoms were refined at the same time. This refinement was unsuccessful as the occupation factors of the Lu^{3+} and Na^{+} ions at different atom sites were unrealistic (exceeded 1.0). To avoid this, the Lu^{3+} and Na^{+} site occupation factors were refined in alternate refinement runs. All the other mentioned parameters were refined in every run. During this refinement the total occupation of the Lu3/Na3 site exceeded one for the 293 K data set. This problem was not encountered for the 100 K and 200 K data sets. So during the isotropic refinement, a 3rd constraint was applied only to the 293 K model so that the site occupation factor of that site does not exceed 0.125, which is the maximum allowed site occupation due to the site multiplicity. A point is to note that the site occupation factor of Na^{+} at the Lu1/Na1 site was constrained to zero, as the Na^{+} occupancy becomes negative during the refinement and the occupancy of Lu^{3+} at the Lu1/Na1 site is high with a low s.u. The remaining amount at the Lu1/Na1 site is a vacancy or may be a small amount of Na, which is not possible to refine with the quality of the data. So the used sets of constraints are

ai[Lu2] = 0.28125-ai[Lu1]-ai[Lu3] [Eq. 5.1]
ai[Na2] = 0.15625-ai[Na1]-ai[Na3] [Eq. 5.2]
ai[Lu3] = 0.125-ai[Na3] [Eq. 5.3] only applied for the 293 K model.

where ai[Lu] and ai[Na] are the site occupation factors of Lu and Na at various atomic sites in the asymmetric unit of the structure.

The refinement values from the different temperature datasets have been tabulated below in Table 5.1. The twin volumes are close to 0.1666 within their s.u. for the 100 K and 200 K refinements (Table 5.1). Twin volume 4 and twin volume 5 for the 293 K refinement does not behave as expected like the 100 K and 200 K refinements. R_{obs} for the 200 K data set are higher than for the other two temperatures (Table 5.1). The reason for this disagreement is most probably due to the high R_{int} of the 200 K dataset. wR_{obs} and *GOF* are similar for the refinements for the three temperatures. The site occupations at the different atomic sites are consistent across the different temperatures (Table 5.1), but the isotropic ADPs are not (Table 5.1), In the isotropic model, the ADPs of the fluorine atoms are large, suggesting there may be disorder in the fluorine atom positions (U_{iso} of F1 = 0.038(7) and F2 = 0.099(17) for 293 K dataset).

	100 K	**200 K**	**293 K**
Twin Volume1	0.17(4)	0.17(5)	0.17(14)
Twin Volume2	0.167(16)	0.17(2)	0.17(5)
Twin Volume3	0.17(2)	0.17(2)	0.18(7)
Twin Volume4	0.156(17)	0.14(2)	0.05(6)
Twin Volume5	0.172(17)	0.18(2)	0.26(6)
Twin Volume6	0.17(2)	0.17(2)	0.18(7)
R_{obs}	2.67 %	3.57 %	3.10 %
wR_{obs}	4.46 %	4.67 %	4.70 %
GOF	3.47	3.03	3.72
R_{int}	5.18 %	7.29 %	4.08 %
Lu1 Occupation	0.8361	0.8659	0.897
Na1 Occupation	000000	000000	000000
Lu2 Occupation	0.5953	0.575	0.5211
Na2 Occupation	0.27(3)	0.26(4)	0.280(8)
Lu3 Occupation	0.2234	0.2341	0.311(16)
Na3 Occupation	0.70(7)	0.74(9)	0.689(16)
Lu1/Na1 U_{iso} (Å^2)	0145(10)	0.0165(16)	0.0238(14)
Lu2/Na2 U_{iso} (Å^2)	0.0190(18)	0.019(5)	0.0143(12)
Lu3/Na3 U_{iso} (Å^2)	0.016(3)	0.019(5)	0.036(3)

Table 5.1: The refined twin volumes, agreement factors, site occupancies and isotropic atomic displacement parameters of the metals for the Type A structure of Phase I at three different temperatures.

After isotropic modelling, DF maps were calculated in a similar way as described in § 4.1. The DF maps for the 100 K, 200 K and 293 K data look consistent if one considers only the stronger features. There are some additional features present in the map for the 200 K model. These additional strong features were considered as noise, as they are absent in the maps for the 100 K and 293 K datasets. The noise may come from poor data integration or poor absorption corrections, which is indicated by a higher R_{int} for the 200 K dataset. Only the DF maps from the 293 K data set are presented in Fig. 5.1.

The largest peaks of electron density are mainly in the z = 0.5 and z = 0.125 layers as for the Type A DF maps of Phase II. These features have been marked with open red circles in the DF maps in Fig. 5.1. The coordinates of the electron density peaks are

x = 0.50, y = 0.140, z = 0.5;

x = 0.180, y = 0.179, z = 0.138;

x = 0.141, y = 0.5, z = 0.5.

These positions are consistent across all temperatures as well. The peaks are also broad, as seen previously. The scaling for the DF maps is as described in § 4.1.

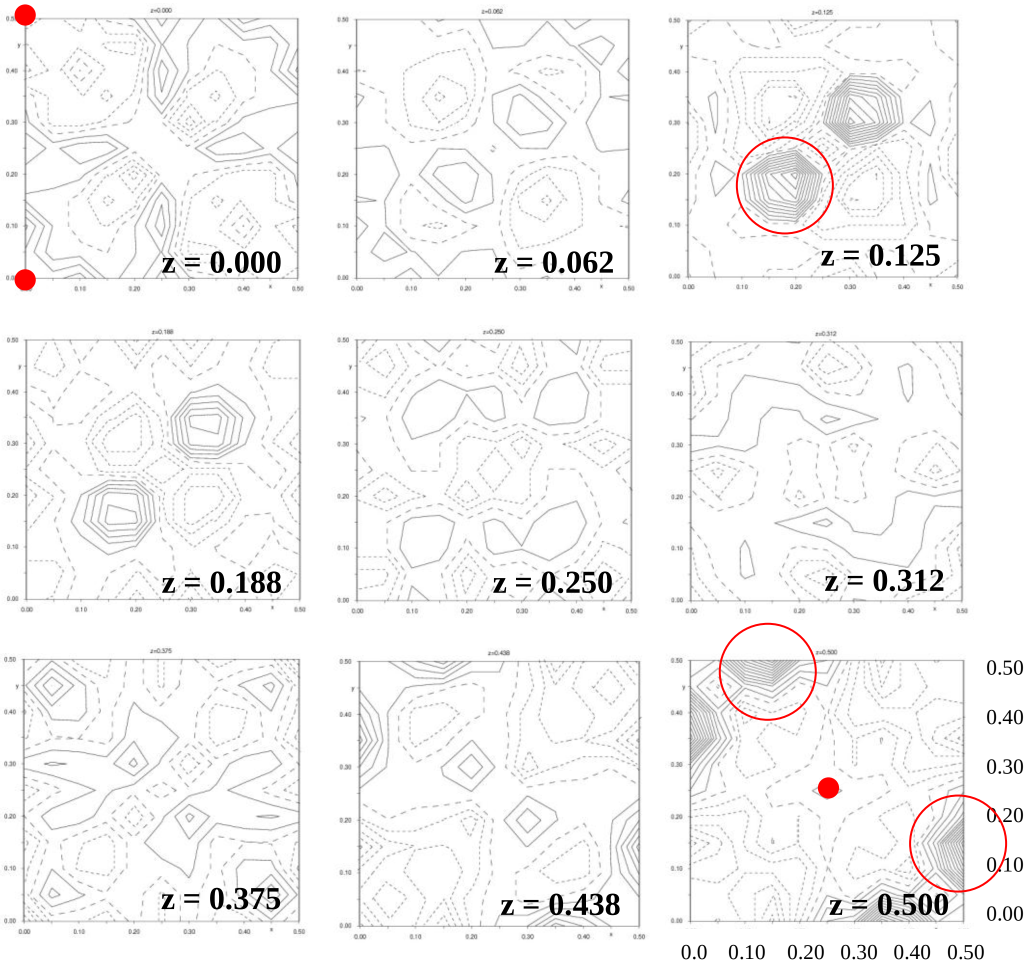

Fig. 5.1: Difference Fourier electron density maps for the 293 K dataset after isotropic modelling for the Type A structure of Phase I.

The positions of the electron density peaks relative to those of the metal atoms closely resemble metal-fluorine distances, so these peaks have been defined as additional positions of disordered fluorine atoms, namely F3 and F4. The total occupancy of the fluorine atoms F1, F2, F3 and F4 was kept to 16 according to the composition of the sample. After refining the occupancies of the disordered fluorine atoms, the sites of the metal atoms were refined anisotropically and further DF maps were calculated analogously to the procedure described in § 4.1. A point to note is that the third peak (0.141, 0.5, 0.5) in the DF map has also been defined as a possible disordered fluorine atom position, but during the refinement occupation of this site becomes negative and so it was deleted in the subsequent refinement.

Once we take account of the electron densities in the DF map in terms of disordered fluorine atoms and introduce anisotropy for the metal sites, there is no significant residual electron density left in the maps for the 100 K and 293 K data set. The noise in the DF maps of the 200 K data set remains visible. The DF maps at this stage are consistent across all the temperatures except the noisy features in the 200 K DF maps and only the maps for the 293 K data set have been presented in Fig. 5.2. After introducing disorder at the fluorine atom positions, the isotropic ADPs of the fluorine atoms produces a more reasonable value for the fluorine atoms, although only a single common ADP value was refined for all fluorine atoms (U_{iso} = 0.0385(15) for 293 K dataset). It was not possible to make the fluorine atoms anisotropic, as the ADPs go non-positive definite during the refinement. This is may be due to poor absorption corrections or there is not enough information in the data set to allow the fluorine atoms to be refined anisotropically.

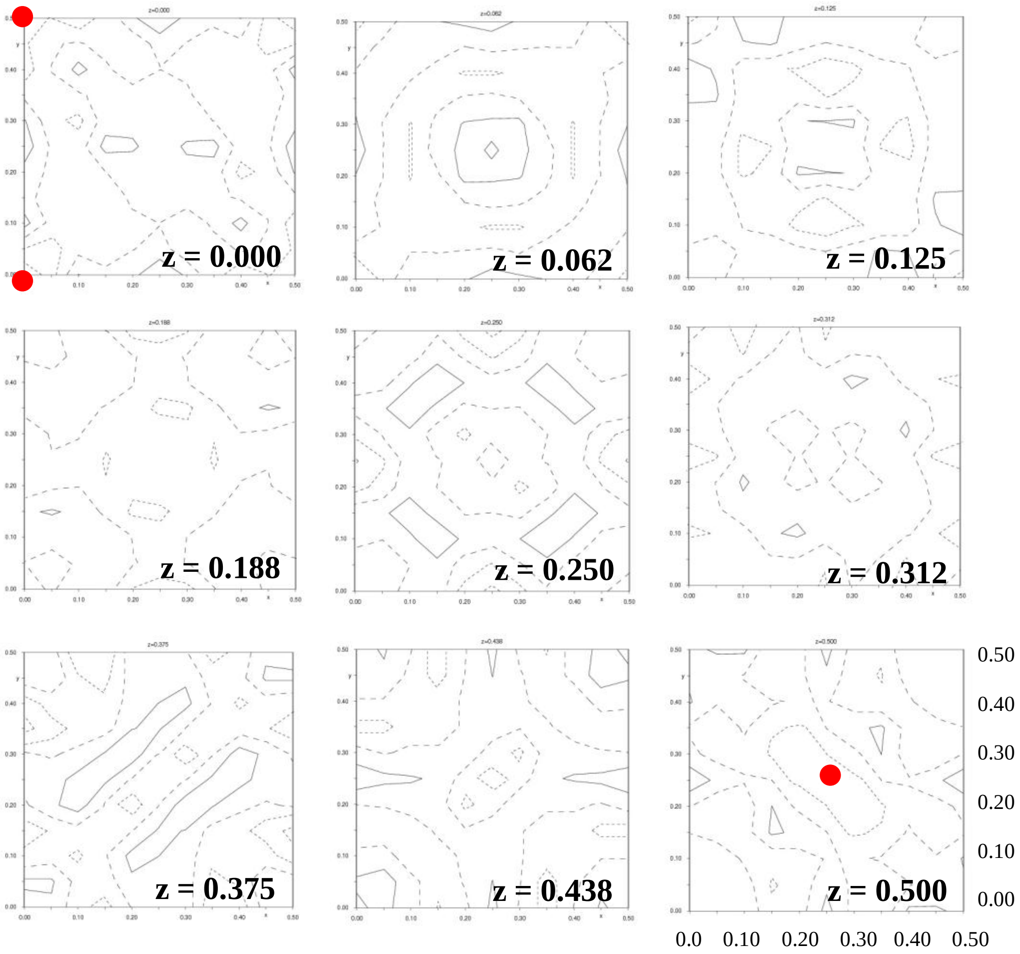

Fig. 5.2: Difference Fourier electron density maps for the 293 K dataset for the anisotropic model for the Type A structure of Phase I.

During the anisotropic refinement, the occupation of the heavy atoms at the Lu3/Na3 site exceeded the maximum possible physical occupation of one for the 100 K and the 200 K data sets, so during the anisotropic refinement an additional constraint was used so that the site occupation factor of that site does not exceed 0.125 which is the maximum allowed site occupation factor due to the site multiplicity. This additional constraint was already present for the 293 K data set in the isotropic refinement. Anisotropic refinement values are tabulated in Table 5.2(a)-(b). The s.u.s for the twin volumes have improved with the anisotropic refinement [Table 5.2(a)]. The twin volumes are now close to 1/6 for the 293 K refinement with anisotropic metal atoms and taking account of the disorder in the fluorine atom positions. R_{obs}, wR_{obs} and *GOF* reduce significantly once the disorder in the fluorine atoms has been introduced [Table 5.2(a)]. The occupancies of the metals at the different atomic sites is similar at all temperatures [Table 5.2(a)]. During the anisotropic refinement, U_{11} is always smaller than U_{22} and U_{33} and the values are not consistent across the temperatures [Table 5.2(a)]. The number of measured reflections, number of symmetry independent reflections, number of reflections with I > 3σ(I) and number of reflections used during the refinement are given in [Table 5.2(b)]. There are still some difference density peaks present in the 200 K DF maps after the anisotropic refinement of the metal atoms and accounting for the disorder in the fluorine atom positions. We have tried to further optimize the data integration of the 200 K data set, but there was no significant improvement. The anisotropic ADPs and their s.u.s for the different metal sites have been plotted against temperature in Fig. 5.3.

	100 K	**200 K**	**293 K**
Twin Volume1	0.167(8)	0.166(11)	0.168(9)
Twin Volume2	0.166(3)	0.165(4)	0.167(3)
Twin Volume3	0.167(3)	0.167(4)	0.167(4)
Twin Volume4	0.173(5)	0.169(8)	0.162(6)
Twin Volume5	0.160(4)	0.168(5)	0.171(4)
Twin Volume6	0.167(3)	0.166(4)	0.166(4)
R_{obs}	1.10 %	1.16 %	0.93 %
wR_{obs}	2.25 %	1.77 %	1.18 %
GOF	1.00	1.24	1.02
Lu1 Occupation	0.9279	0.9011	0.9034
Na1 Occupation	0.00000	0.00000	0.0000
Lu2 Occupation	0.4911	0.5329	0.5021
Na2 Occupation	0.295(2)	0.267(4)	0.296(4)
Lu3 Occupation	0.340(4)	0.283(7)	0.342(7)
Na3 Occupation	0.660(4)	0.717(7)	0.658(7)
Lu1/Na1 (U_{11}) **Lu2/Na2** (U_{11}) **Lu3/Na3** (U_{11}) **(Å^2)**	0.0110(9) 0.0030(14) 0.015(3)	0.0127(9) 0.0052(9) 0.0184(16)	0.0120(10) 0.0075(13) 0.024(3)
Lu1/Na1 (U_{22}) **Lu2/Na2** (U_{22}) **Lu3/Na3** (U_{22}) **(Å^2)**	0.0317(12) 0.0214(15) 0.022(3)	0.042(2) 0.069(4) 0.039(8)	0.042(2) 0.045(4) 0.043(7)
Lu1/Na1 (U_{33}) **Lu2/Na2** (U_{33}) **Lu3/Na3** (U_{33}) **(Å^2)**	0.0140(4) 0.019(2) 0.043(3)	0.0110(6) 0.0020(7) 0.0172(18)	0.0153(11) 0.013(2) 0.025(4)

Table 5.2 (a): The refined twin volumes, agreement factors, site occupancies and anisotropic atomic displacement parameters of the metals for the Type A structure of Phase I at the three temperatures.

	$2\theta_{(\max)}$[°]	Total reflections measured	Symmetry independent reflections	Reflections with $I>3\sigma(I)$	Reflections used in the refinement	$\Delta_{\max}/\sigma$	$\Delta\rho$(max, min) e/Å^3
100 K	55.6	1422	810	810	810	0.0039	0.32,-0.37
200 K	55.6	1412	808	808	808	0.0032	1.65,-1.84
293 K	56.1	1183	681	681	681	0.0034	0.19,-0.21

Table 5.2(b): Some parameters for the final set of refinements for the Type A structure of Phase I

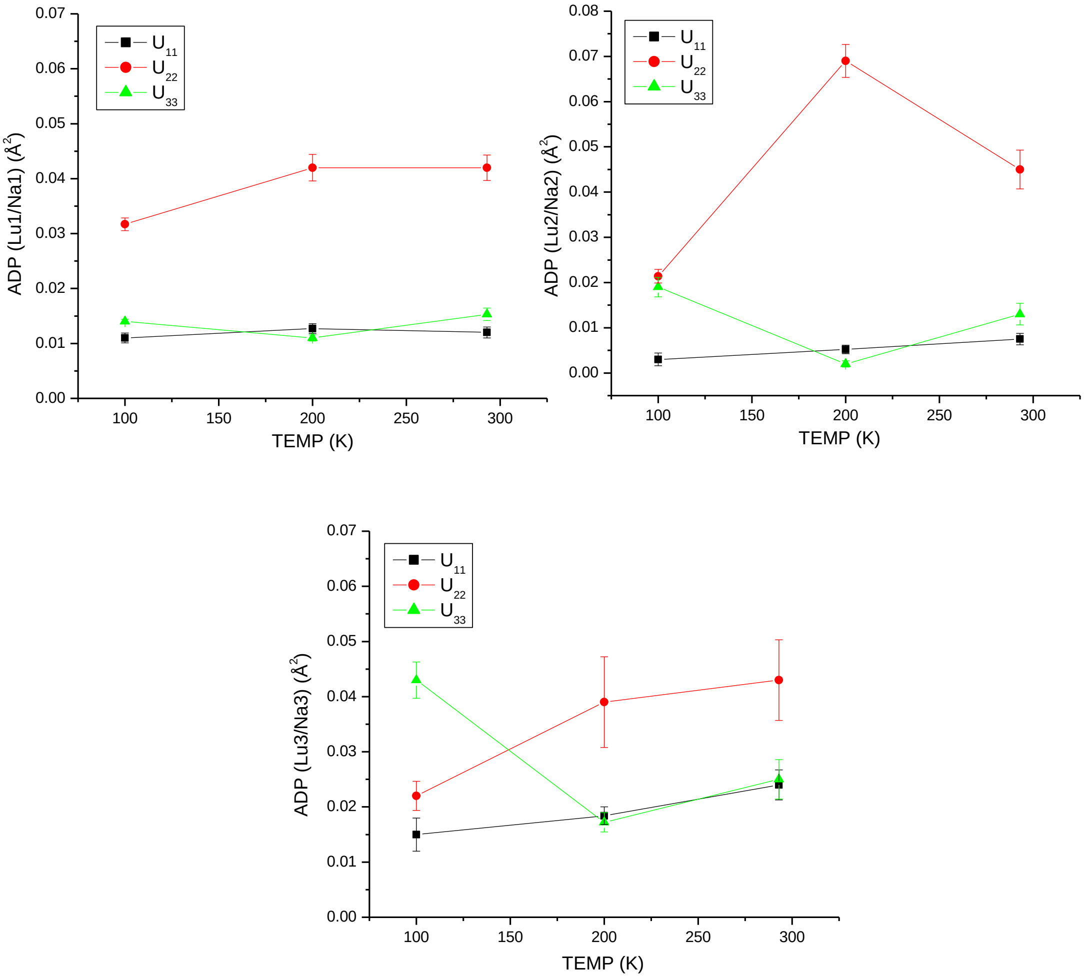

Fig. 5.3: Plots of the ADPs (U_{11}, U_{22} and U_{33}) and their s.u. of the metals against temperature for the Type A structure of Phase I.

5.1.2 Description of the Type A Average Structure of Phase I

The Type A refined structure based on the main reflections of Phase I is shown in Fig. 5.4. The diagram shows only the highly occupied F1 and F2 atoms. A projection of four unit cells is shown.

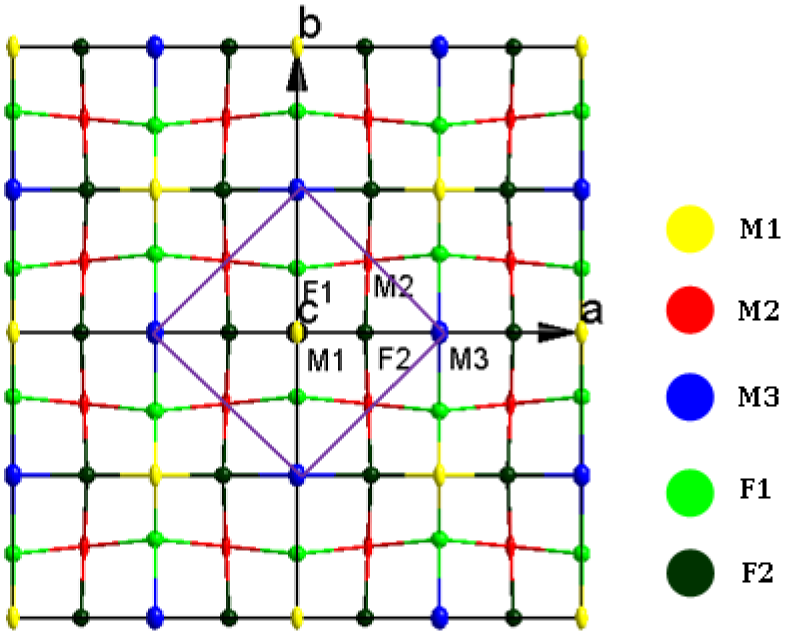

Fig. 5.4: The Type A structure of Phase I, with 50% probability ellipsoids for the metals and fluorine atoms with a radius of 0.24 Å, based on the main reflections, the square box represent the original fluorite cubic cell. The colour codes for all atoms are given on the right hand side of the image.

The Type A structure of the Phase I sample is distorted. The fluorine atoms are shifted from the ideal positions of 0 0.25 0.25 and 0.25 0 0.25 for atoms F1 and F2 respectively. The refined positions of the fluorines are F1 = 0 0.2248(19) 0.297(3), F2 = 0.2396(14) 0 0.254(3), F3 = 0.5 0.147(2) 0.5, F4 = 0.1867(18) 0.1552(19) 0.141(2). The distortion in the structure is due to the different occupancies of the metals at different sites, which will cause uneven M-F distances around the metal centers. Considering only the F1 and F2 atoms in the structure, each metal site has distorted cubic coordination geometry and the fluorine atoms have distorted tetrahedral coordination geometry. The positions of the fluorine atoms (F1, F2, F3 and F4) are similar at all three temperatures, the M-F bond distances shorter than 3 Å are tabulated in Table 5.3 for the RT data se only. The numbers of symmetry related fluorine atoms connected with a particular metal center are given after the respective bond distances in Table 5.3. So the occupancies of the various fluorine atom sites at the different temperatures are also similar within 3σ, the occupancies of the fluorine atoms are given only for the RT structure in Table 5.3 As the metal positions are the same for the Type A structure for both Phase I and Phase II and the position of the residual peaks in the DF maps are similar in both cases, the disordered fluorine distributions around the metal atoms are expected to be similar in both Type A structures of Phase I and Phase II. The distributions of the fluorine atoms around the different metal centers have been discussed in § 4.3. A point to note is that the directions of distortion in the Type A structure of both phases are not same. The distortions of the F atoms are along the crystallographic **b** axis for the Type A structure of Phase I (Fig. 5.4) but for the Type A structure of Phase II it is along the crystallographic **a** axis (Fig. 4.8 of § 4). From the M-F bond distances (Table 5.3 for the Type A of Phase I & Table 4.10 for the Type A of Phase II) of the Type A structure of Phase I and Phase II, it appears that the M-F1 bond distances of the Type A structure of Phase I is similar with the M-F2 bond distances of the Type A structure of Phase II within 3σ and similarly for the M-F2 bond distance of the Type A structure of Phase I.

The distribution of Lu and Na in the different atomic sites is similar in the Type A structures of Phase I and Phase II.

Once we have the information of the M-F bond distances (< 3 Å) and the occupancies of the fluorine atoms, bond valence calculations (Brown, 1996) were performed. All the bond valences for a particular M-F bond needs to be multiplied by the occupations of the respective fluorine atoms. The Lu1 atom at the M1 site is underbonded (Table 5.3). The Lu2 atom at the M2 site is also underbonded and the Na2 atom at the M2 site is slightly overbonded (Table 5.3). The Lu3 atom at the M3 site is highly underbonded and the Na3 atom at the same site is also underbonded (Table 5.3).

	F1	**F2**	**F3**	**F4**	**Bond Valence sum**
Bond Distance (Å) M1(Lu1/Na1)	2.39(2) × 4	2.321(13) × 4	-	2.03(1) × 8	-
Bond Valence Lu1 (v.u.)	0.160133 × 4	0.236817 × 4	-	0.115549 × 8	2.51
Bond Valence Na1 (v.u.)	-	-	-	-	-
Bond Distance (Å) M2(Lu2/Na2)	2.241(8) × 4	2.36(1) × 4	2.090(6) × 2	2.17 (1) × 4	-
Bond Valence Lu2 (v.u.)	0.239538 × 4	0.213126 × 4	0.188316 × 2	0.079148 × 4	2.50
Bond Valence Na2 (v.u.)	0.143727 × 4	0.12788 × 4	0.112993 × 2	0.04749 × 4	1.50
Bond Distance (Å) M3(Lu3/Na3)	2.69(2) × 4	2.45(1) × 4	2.982(6) × 4	2.812(14) × 8	-
Bond Valence Lu3 (v.u.)	0.071179 × 4	0.167108 × 4	0.0169 × 4	0.01396 × 8	1.13
Bond Valence Na3 (v.u.)	0.042709 × 4	0.100267 × 4	0.01014 × 4	0.008376 × 8	0.68
Occupation(F)	0.66(3)	0.81 (3)	0.345(14)	0.18(2)	-

Table 5.3: The bond distance distribution around the metal atoms, their bond valances, bond valence sum of each of the metal atoms at different atomic sites and fluorine atom occupancies for the Type A structure of Phase I at RT. The multipliers refer to the numbers of symmetry equivalent fluorine atoms of that type in the coordination sphere.

5.1.3 Refinement of the Type B Average Structure of Phase I

After the necessary coordinate transformation as described in § 4.2 the Type B structure of Phase I was refined in a pseudo tetragonal metric unit cell with space group *Cmmm*. At first, all the parameters (scale factor, occupancies of the metal atoms, positions of the metal atoms and fluorine atoms, isotropic atomic displacement parameters) have been refined with the use of compositional constraints on the metal site occupation

ai[Lu1] = 0.28125-ai[Lu2] [Eq. 5.4]

ai[Na1] = 0.15625-ai[Na2] [Eq. 5.5]

where ai[Lu] and ai[Na] are the site occupation factors of the metals in the asymmetric unit of the structure.

During the refinement it was observed that the site occupation at Lu2/Na2 exceeded the maximum physical occupation of one. So a new constraint for the Lu2/Na2 was used so that it does not exceed the site occupation factor of 0.25, which is the maxima allowed by the site symmetry.

The new set of constraints is

ai[Lu1] = 0.28125-ai[Lu2] [Eq. 5.4]
ai[Na1] = 0.15625-ai[Na2] [Eq. 5.5]
ai[Na2] = 0.25-ai[Lu2] [Eq. 5.6]

but in Eq. 5.6 the site occupation factor of Na2 is an independent variable, whereas in Eq. 5.5 it is a dependent variable. So ai[Na2] in Eq. 5.5 is replaced by Eq. 5.6, the new set of constraints is

ai[Lu1] = 0.28125-ai[Lu2] [Eq. 5.4]
ai[Na1] = ai[Lu2]-.09375 [Eq. 5.5a]
ai[Na2] = 0.25-ai[Lu2] [Eq. 5.6]

Then an isotropic refinement was performed with the data sets from the three temperatures, refining all the parameters at the same time and the values from the refinement are tabulated in the Table 5.4. The twin volumes are close to 1/6 for the 100 K refinement (Table 5.4), but for the 200 K and 293 K dataset twin volume 4 and twin volume 5 did not behave well. R_{obs} for the 200 K dataset is higher than for the 100 K and 293 K datasets as well (Table 5.4). The occupancies of the metals at different atomic sites are consistent across the different temperatures (Table 5.4). The isotropic ADPs of the metals do not change with lowering of the temperature (Table 5.4). The isotropic ADPs of the fluorine atoms, especially for the F2 and F3 atoms are high (U_{iso} for F1 = 0.027(6), F2 = 0.13(4), F3 = 0.065(8) for the 293 K data set).

	100 K	**200 K**	**293 K**
Twin Volume1	0.17(2)	0.16(10)	0.16(9)
Twin Volume2	0.166(9)	0.16(2)	0.17(3)
Twin Volume3	0.166(12)	0.17(4)	0.17(4)
Twin Volume4	0.189(11)	0.31(5)	0.25(5)
Twin Volume5	0.145(11)	0.03(5)	0.09(5)
Twin Volume6	0.167(12)	0.17(4)	0.17(4)
R_{obs}	2.73 %	3.52 %	3.06 %
wR_{obs}	4.62 %	4.72 %	5.00 %
GOF	3.59 %	3.07 %	3.97 %
R_{int}	5.18 %	7.29 %	4.08 %
Lu1 Occupation	0.373(5)	0.364(5)	0.373(6)
Na1 Occupation	0.377(5)	0.386(5)	0.377(6)
Lu2 Occupation	0.752(5)	0.761(5)	0.752(6)
Na2 Occupation	0.248(5)	0.239(5)	0.248(6)
Lu1/Na1 U_{iso} (Å^2)	0.0164(18)	0.0178(14)	0.020(2)
Lu2/Na2 U_{iso} (Å^2)	0.0163(6)	0.0173(6)	0.0190(9)

Table 5.4: The refined twin volumes, agreement factors, occupancies and isotropic atomic displacement parameters of the metals for the Type B structure of Phase I at the three temperatures.

After isotropic modelling, DF maps were calculated in a similar way to that described in § 4.1. Strong features in the DF maps across all the temperatures are consistent in the calculated layers, so map for the 293 K data set is given as a representative example in Fig. 5.5. For the 200 K dataset, extra electron density peaks were observed, possibly as a result of the data quality, as already indicated. The largest peaks of residual electron density are mainly in the z = 0.0 and z = 0.375 layers similar to the DF maps of the Type B structure of Phase II. These peaks are marked with open red circles, the heavy atom positions are marked with red dots in the DF maps. The coordinates of the largest residual electron density peaks are approximately

x = 0.069, y = 0.178, z = 0.361;

x = 0.428, y = 0.179, z = 0.360;

x = 0.250, y = 0.137, z = 0.000.

The scale for the plots along the x and y direction is shown for the layer z = 0.500. and to the entire DF map.

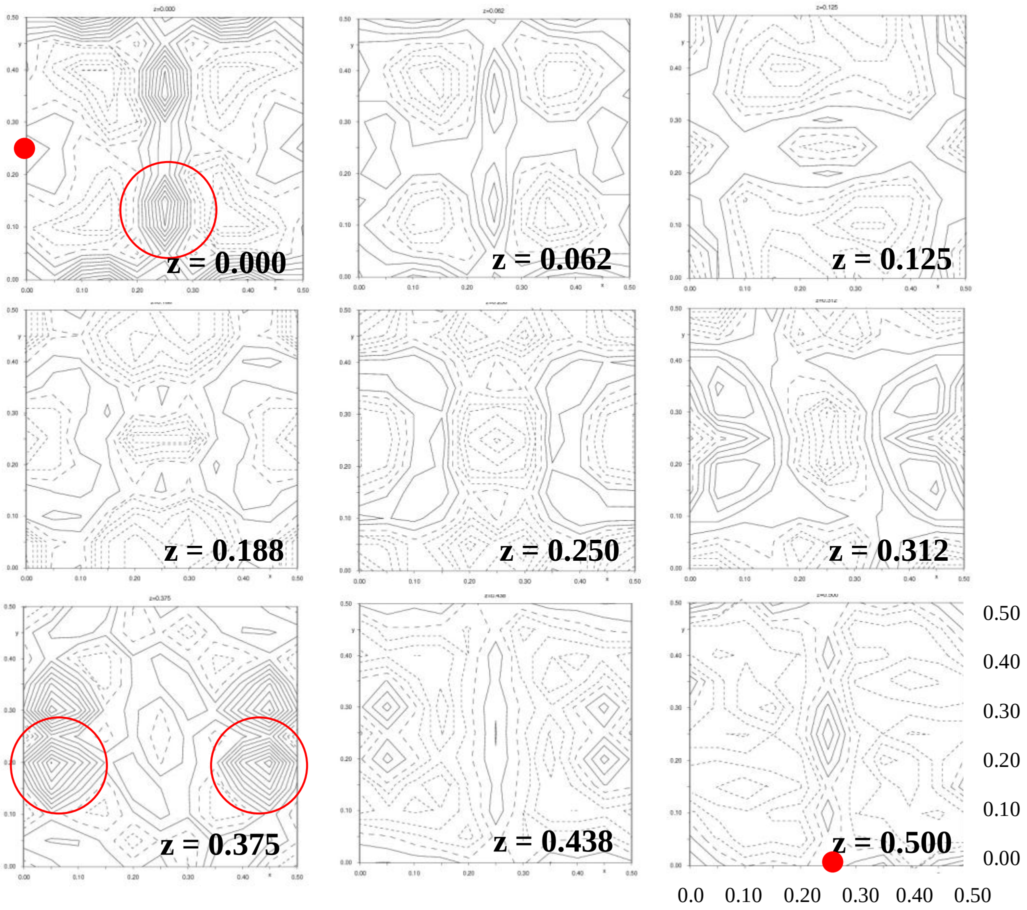

Fig. 5.5: Difference Fourier electron density maps for the 293 K dataset after isotropic modelling for the Type B structure of Phase I.

The positions of the residual electron density peaks relative to the metal atoms closely resemble metal-fluorine distances, so these peaks have been defined as the positions of disordered fluorine atoms namely F4 and F5. After refining the occupancies of the fluorine atoms (F1, F2, F3, F4 and F5) keeping a total occupancy of 16 according to the composition of the sample, further DF maps were calculated in a similar way to that described in § 4.1. A point to note is that the difference electron density peak at 0.428, 0.179, 0.360 was treated as a possible position of a disordered fluorine atom, but during the refinement the occupation of this atom goes negative, so it was removed from the subsequent refinement.

Once we take account of the electron densities in terms of disordered fluorine there is no significant electron density left in the calculated DF maps. The DF maps are consistent across all the temperatures. The DF maps for the 293K data set are presented as a representative example in Fig. 5.6. The positions of the metals are marked with red dots. The scale for the DF map along the x and y directions is shown for the z = 0.50 layer. The same scale has been used for the other DF sections.

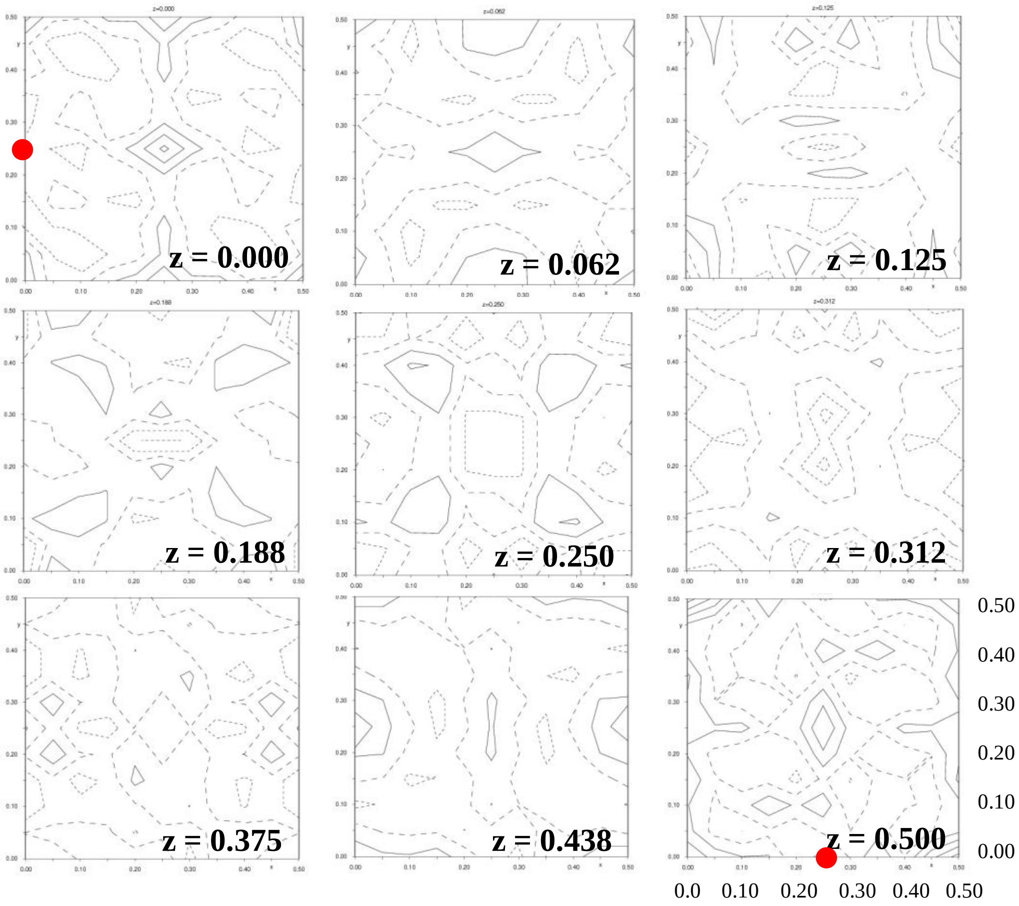

Fig. 5.6: Difference Fourier electron density maps for the 293 K dataset for the Type B structure of Phase I after modelling the disordered fluorine atoms.

Once the difference electron density was interpreted in terms of disordered fluorine atoms, further attempts were made to refine the metal atoms anisotropically, but this was not possible for Lu1/Na1, as U_{22} goes slightly negative during the refinement for the 293 K data set. But the other metal site, Lu2/Na2 could be refined anisotropically. For the 100 K and 200 K data sets all the metal sites were refined anisotropically. All the fluorine atoms in the structure were refined with a common isotropic U value (U_{iso} = 0.0399(11) for the 293 K dataset with all metal atoms anisotropic). The isotropic APDs improve once we interpret the disorder in the fluorine atom positions. The refined values for the anisotropic model are tabulated in Table 5.5(a). The twin volumes do not change for the 100 K data set. But the previously inconsistent twin volumes for the 200 K and 293 K data sets approach 1/6 in the anisotropic refinement [5.5(a)]. R_{obs}, wR_{obs} and *GOF* improve significantly from the earlier isotropic refinement [5.5(a)]. R_{obs} for the 200 K data set is still higher than for the 100 K and 293 K data sets. The occupation factors of the metals across the different temperatures are consistent [5.5(a)]. The U_{22} of the metal sites are lower than U_{11} and U_{33} in the anisotropic refinement. There is a sudden increase in the U_{11} and U_{33} values with change of temperature from 100 K and 200 K to 293 K [5.5(a)]. The final refined coordinates for the metal atom positions are given in Table 5.5(a). The number of measured reflections, number of symmetry independent reflections, number of reflections with $I > 3\sigma(I)$ and number of reflections used during the refinement have been given in Table [5.5(b)].

	100 K	**200 K**	**293 K**
Twin Volume1	0.166(8)	0.167(15)	0.166(10)
Twin Volume2	0.167(3)	0.168(5)	0.167(3)
Twin Volume3	0.165(3)	0.168(7)	0.166(4)
Twin Volume4	0.167(4)	0.158(6)	0.158(5)
Twin Volume5	0.170(4)	0.171(7)	0.177(6)
Twin Volume6	0.166(3)	0.168(7)	0.167(4)
R_{obs}	1.18	2.57	1.22
wR_{obs}	1.30	2.37	1.49
GOF	1.04	1.58	1.22
Lu1 Occupation	0.3660(19)	0.359(3)	0.386(3)
Na1 Occupation	0.3840(19)	0.391(3)	0.364(3)
Lu2 Occupation	0.7590(19)	0.766(3)	0.739(3)
Na2 Occupation	0.2410(19)	0.234(3)	0.261(3)
Lu1/Na1 (U_{11}) **Lu2/Na2 (U_{11})** **(Å^2)**	0.020(2) 0.0233(12)	0.018(4) 0.0227(14)	0.039(3) 0.0353(11)
Lu1/Na1 (U_{22}) **Lu2/Na2 (U_{22})** **(Å^2)**	0.0005(11) 0.0103(7)	0.0015(19) 0.0095(11)	-0.0027(12) 0.0022(10)
Lu1/Na1 (U_{33}) **Lu2/Na2 (U_{33})** **(Å^2)**	0.0244(10) 0.0198(5)	0.028(3) 0.0249(13)	0.047(3) 0.0320(13)
Lu1/Na1 (x, y, z)	0.2436(6) 0 0.5	0.2545(8) 0 0.5	0.2459(2) 0 0.5
Lu2/Na2 (x, y, z)	0 0.2565(3) 0	0 0.2432(5) 0	0 0.2558(8) 0

Table 5.5(a): The refined twin volumes, agreement factors, occupancies, anisotropic atomic displacement parameters and atomic coordinates of the metals for the Type B structure of Phase I at the three temperatures.

	$2\theta_{(max)}$[°]	Total reflections measured	Symmetry independent reflections	Reflections with I>3σ(I)	Reflections used in the refinement	Δ_{max}/σ	Δρ(max, mean) e/Å^3
100 K	55.6	1422	810	810	810	0.0006	0.27,-0.34
200 K	55.6	1412	808	808	808	0.0018	1.40,-1.51
293 K	56.1	1183	681	681	681	0.0025	0.26,-0.25

Table 5.5(b): Some parameters for final set of refinements for the Type B structure of Phase I.

The anisotropic ADPs and their s.u.s at different metal sites are plotted against temperature in Fig. 5.7. The sudden change of U values for the RT refinement may be due to non-optimized data integration or poor absorption correction.

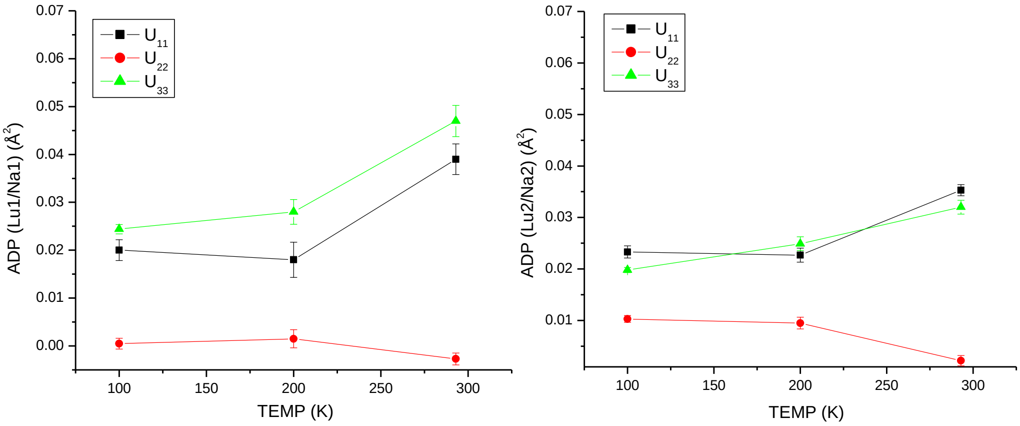

Fig. 5.7: Plot of ADPs (U_{11}, U_{22}, U_{33}) of the metals against temperature for the Type B structure of Phase I.

5.1.4 Description of the Type B Structure of Phase I

During the anisotropic refinement of the metals for the RT dataset, we have seen that U_{11} goes slightly negative, so for the further calculation and description of the average structure we have made the entire model isotropic with the five disordered fluorine atom positions (U_{iso} = 0.037(3) for the 293 K dataset when all the metal atoms isotropic and disorder in the fluorine atom positions are interpreted). During this change there is no significant change in the occupation of the metals at different atomic sites for the refinement of the RT dataset (Lu1/Na1 occupation 0.374(4)/0.376(4), Lu2/Na2 occupation 0.751(4)/0.249(4) with metal atom isotropic and disordered fluorine atom positions interpreted). The Type B structure of Phase I for the RT data set is plotted in Fig. 5.8 after the disorder in the fluorine positions was introduced with the metal atoms isotropic. In the diagram, only the F1, F2 and F3 fluorine atoms are plotted. Four unit cells are shown.

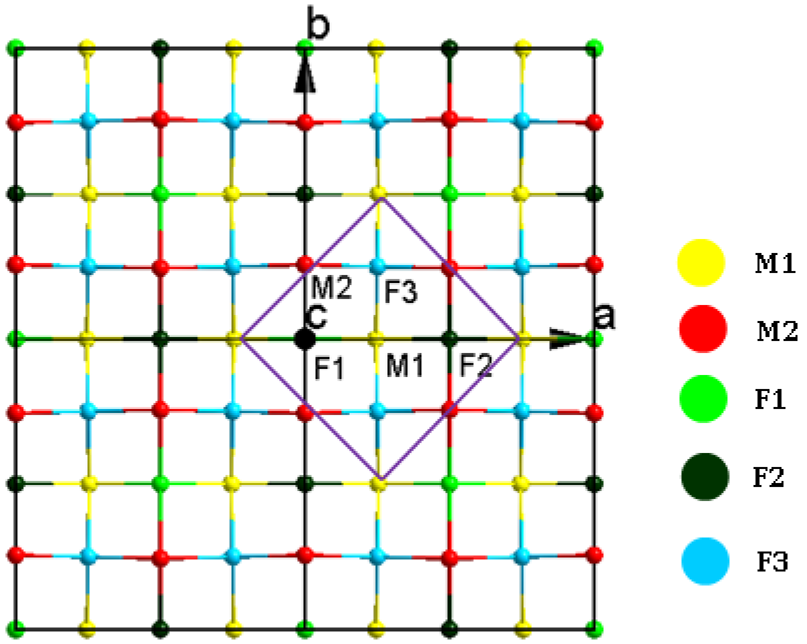

Fig. 5.8: The Type B structure of Phase I with isotropic metal atoms and fluorine atoms with a radius of 0.24 Å based on the main reflections, the square box represents the original fluorite cubic cell. The colour codes for all atoms are given on the right hand side of the image.

The refined coordinates for the fluorine atom positions are 0 0 0.222(11) for atom F1, 0.5 0 0.329(9) for atom F2, 0.25 0.25 0.216(10) for atom F3, 0.068(4) 0.179(3) 0.346(3) for atom F4, 0.254(7) 0.119(5) 0 for atom F5 when all the metal atoms are isotropic. The metal sites are mixed with Lu^{3+}/Na^{+}/Vacancy and the proportion of these constituents varies at the different atom sites. This makes an uneven distribution of M-F distances and distorts the structure. The fluorine atoms have been displaced from the ideal 0 0 0.25 position for F1, 0.5 0 .25 for atom F2 and 0.25 0.25 0.25 for atom F3. The refined coordinates for the disordered fluorine atoms are comparable with those of the Type B structure of Phase II. The distributions of the disordered fluorine atoms have been discussed in § 4.3 for the Type B structure of the Phase II sample. The M-F bond distances less than 3 Å are tabulated in Table 5.6. The number of symmetry generated F atoms connected with a metal site is given after the respective bond distances in Table 5.6. As the occupancies of the disordered fluorine atoms are similar at the different temperature within 3σ, only the occupancies of the fluorine atoms at room temperature with all the metal atoms isotropic are given in Table 5.6. A point to note is that the M2 site of the Type B structure of Phase II is 83% occupied by Lu^{3+} and 27% empty, but in the Type B structure of Phase I, the M2 site is 74% occupied by Lu^{3+} as well as 26 % occupied by Na^{+} without any vacancy.

	F1	**F2**	**F3**	**F4**	**F5**	**Bond Valence Sum**
B. D. (Å) M1 (Lu1/Na1)	2.44(4) × 2	2.18(2) × 2	2.49(3) × 4	2.13(3) × 4 2.92(3) × 4	2.907(12) × 4	-
B. V. Lu1 (v.u.)	0.171686 × 2	0.184034 × 2	0.090731 × 4	0.093573 × 4 0.011063 × 4	0.010799 × 4	1.54
B. V. Na1 (v.u.)	0.103015 × 2	0.110424 × 2	0.045552 × 4	0.056146 × 4 0.006638 × 4	0.006479 × 4	0.89
B. D. (Å) M2 (Lu2/Na2)	2.33(3) × 2	2.62(3) × 2	2.27(3) × 4	2.07(2) × 4	2.23(5) × 2 2.13(5) × 2	-
B. V. Lu2 (v.u.)	0.231126 × 2	0.056032 × 2	0.137586 × 4	0.110047 × 4	0.0673 × 2 0.088184 × 2	2.31
B. V. Na2 (v.u.)	0.13868 × 2	0.03362 × 2	0.082554 × 4	0.06603 × 4	0.040381 × 2 0.052912 × 2	1.13
Occupation (F)	0.81(12)	0.43(12)	0.41(2)	0.191(12)	0.18(10)	-

Table 5.6: The bond distance (B. D.) distribution around the metal atoms, their bond valences (B. V.), bond valence sum of each of the metal atoms at different atomic sites and the fluorine atom occupancies for the Type B structure of Phase I at RT. The multipliers refer to the numbers of symmetry equivalent fluorine atoms of that type in the coordination sphere.

Bond valance calculations were performed for the metal atoms taking account of the occupancy of the fluorine atoms which are within 3 Å distances from the metal sites. The Lu1 atom at the M1 site is under bonded and the Na1 atom in the M1 site is slightly under bonded (Table 5.6). The Lu2 atom at the M2 site is under bonded and the Na1 atom at the M2 site is slightly over bonded (Table 5.6).

As both the Type A and Type B structures of Phase I refine with a similar agreement factor, one way to distinguish the two solutions is to look at the metal-fluorine distances, as discussed in § 4.3 (Table 5.3 for Type A and Table 5.6 for Type B of Phase I). There are long metal-fluorine bond distances around the M3 site of the

Type A structure, which result in an under-coordinated M3 metal site. This is not the situation for any of the metal sites of the Type B structure of Phase I. This suggests that the Type B structure of Phase I is chemically more reasonable than the Type A structure.

Once the average structure based on the main reflections is ready, it can be used to understand the modulation present in structure, which will be discussed in the subsequent part of this chapter. The satellite data set was collected only at room temperature, so all the treatments and refinements based on the satellite reflections are at RT only.

5.2 Understanding the Superstructure

After modelling the average structure in the small pseudo-tetragonal unit cell, now one can proceed to understand the modulation present in the structure, which is the cause of the satellite reflections. Standard structure solution methods can solve a structure from X-ray or neutron scattering data. But the presence of pseudo-translation effects or a so-called superstructure complicates the structure solution. The problem of solving the superstructure from the satellite reflections is non-trivial due to very small differences between the subcells and weak intensities of the superstructure reflections (satellite reflections). Due to the pseudo-translation the atoms in the unit cell are no longer randomly distributed, as a result direct methods does not work for superstructure solutions (Woolfson, 1971). Palatinus *et al.* proposed a method for solving modulated structures by constructing difference densities based on satellite reflections only (Palatinus *et al.*, 2011). This method is based on the charge-flipping algorithm (Oszlányi & Süto, 2004, 2005, 2008) in its band-flipping variant (Oszlányi & Süto, 2004, 2007), which allows *ab initio* reconstructions of scattering densities with both positive and negative regions. In this description the main reflections have the information on the average structure and the satellite reflections have the information about the differences between the true structure and the average structure. In the absence of main reflections, information about the true structure can be obtained by the constructing difference electron density from the superstructure reflections. It may be possible that the main reflections are unavailable from a single measurement of a modulated structure for two reasons. First, a modulated structure often shows twinning when the modulated structures result from phase transitions (Rae *et al.*, 1992) and the twin domains are present in such a way that the main reflections have contributions from different twin domains, but the satellite reflections are completely separated. In α-$NaLuF_4$ the main reflections are overlaps from six twin domains, whereas the satellite reflections are completely separated. In addition the overlaps of the main reflections are not perfect, which complicates the integration of the main and satellite reflections simultaneously. This ultimately hinders the use of the main reflections during the refinement of a modulated structure. Secondly, the intensities of the main reflections are usually much stronger than those of the satellite reflections. It may be possible that during the data collection process to collect accurate intensities for the satellite reflections, most of the main reflections become saturated on the detector, leading to incorrect intensities for the latter. It may be possible to collect a separate dataset where accurate intensities for the main reflections were measured, but as the main reflections and satellite reflections come from two separate measurements there is always a chance that there is very little information about the relative scaling of the main and satellite reflections. In the case of the data collection for α-$NaLuF_4$, the intensities of the satellite reflections and the main reflections were collected separately, as the satellite reflections are much weaker than the main reflections. It may be possible to find the scale factor between the two data sets by using the intensities of the visible satellite reflections which were measured during the main reflection data collection and those of the corresponding satellite reflections from the satellite data collection, but the main reflections are composed of overlaps from the twinning and the compound of interest has a high absorption coefficient. A small error in the absorption correction will influence the relative scale factor between the main and satellite reflections.

One of the main properties of the charge-flipping algorithm is the fact that it does not require any prior knowledge of space group symmetry. Initially, the electron density is reconstructed in space group $P1$, then one can derive the symmetry from the electron density peak positions. The same is true for difference densities. By constructing a difference density map one can eliminate the higher symmetry due to twining which is present in the superstructure and then analyze the symmetries in the difference density to give the symmetry present in the modulated structure. In the case of α-$NaLuF_4$, as the main reflections are composed from the overlap of orthorhombic twin domains, it is always complicated to find the true space group symmetry of the structure from the main reflections. So we have used the difference density from the satellite reflections for the analysis of the symmetry present in the structure.

The iteration using the band-flipping algorithm converged to two stable solutions with two types of difference density maps. These two maps are different in terms of the type of modulation. The two solutions have been called Type I (Fig. 5.9) and Type II difference density (Fig. 5.10).

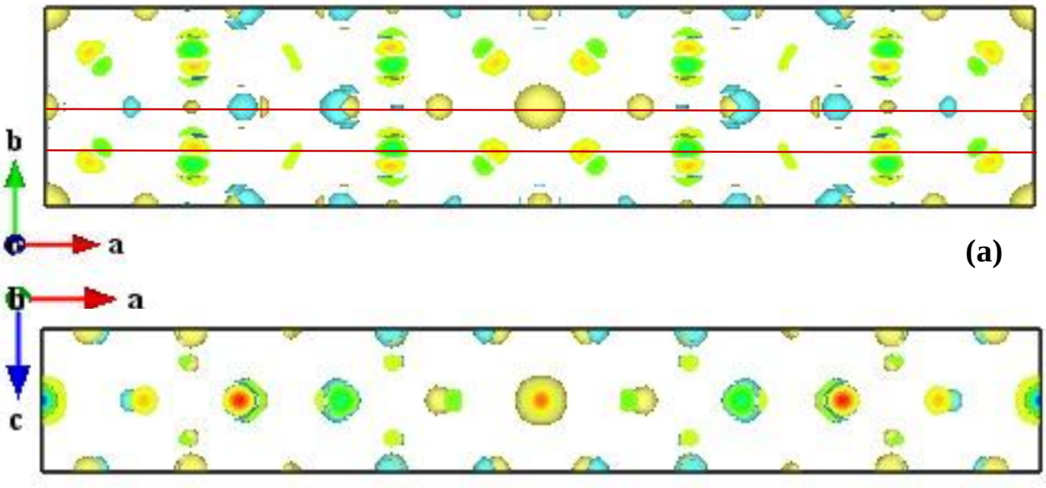

(a)

(b)

Fig. 5.9: (a) Difference electron density maps of Type I projected along c. The rows of different difference density (modulation) are marked with red lines. (b) Difference electron density maps of Type I projected along b - positive density shown in yellow, negative in turquoise.

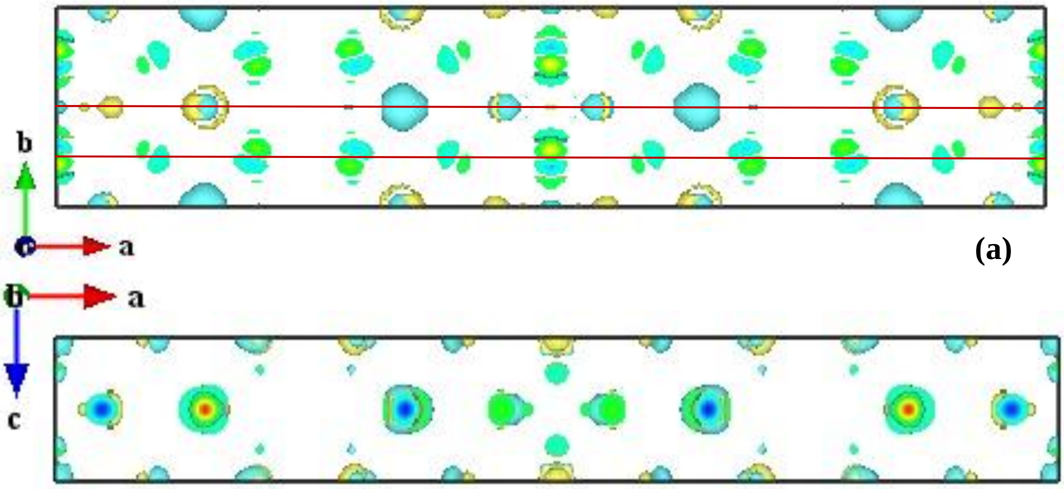

(a)

(b)

Fig. 5.10: (a) Difference electron density maps of Type II projected along c. The rows of different difference density (modulation) are marked with red lines. (b) Difference electron density maps of Type II projected along b - positive density shown in yellow, negative in turquoise.

The recently published algorithm (Palatinus & van der Lee, 2008) has been used to understand the symmetry. It does not depend upon the systematic absences, but analyses the symmetry of the electron densities or difference electron densities for the presence of symmetry operations compatible with the lattice parameters. Each symmetry element is assigned with a symmetry agreement factor ϕ_{sym}. The space group is derived from the list of symmetry operations with low $\phi_{\mathrm{sym.}}$ The algorithm yielded unambiguously and reproducibly space group *Cmmm*. The ϕ_{sym} values of symmetry operations belongs to *Cmmm* was less than 10% indicating a very good match, while the other symmetry operations have $\phi_{\mathrm{sym}} \cong 15\%$ or more.

As we have seen, there are two types of difference density map obtained after running SUPERFLIP (Palatinus & Chapuis, 2007) on the satellite reflections. To understand the similarities and differences between these two difference densities, we have performed some tests where in one case the Type I difference density has been used as a reference density to compare with the difference density coming from 100 runs of SUPERFLIP on satellite reflections, and in the other case the Type II difference density has been used as a reference to compare with the difference density coming from another 100 runs of SUPERFLIP on satellite reflections.

We have used iterations using the band flipping algorithm of converged solution for this analysis. In the first test, where the difference density of Type I is used as a reference density, 52 runs converged after a mean of 161 cycles. Out of 100 runs, 68 runs produce mmm symmetry with an overall agreement factor of 14%, while 19 runs produce 2*mm* or *m*2*m* symmetry and the remaining 13 yield a different symmetry. Out of 68 runs, the difference density of Type I is obtained 31 times and the difference density of Type II is obtained 37 times with a reference match of 16% on average with a shift approximately 0.85 0 0 or 0.15 0 0 relative to the Type I difference density. The lower reference match indicates a good match of the difference densities obtained from SUPERFLIP with the reference difference density (Type I difference density) with the difference being a shift only. A point to note is that the overall agreement factor is slightly higher than 10% because some unconverged solutions were taken into account during the calculation of the mean of the overall agreement factor.

In another test, the Type II difference density is used as reference density, out of 100 runs, 59 runs converged after a mean of 172 cycles. Out of 100 runs 70 runs produce mmm symmetry with an average overall agreement factor of 14%, while 23 runs produce 2*mm* or *m*2*m* symmetry and 7 runs produce a symmetry other than mmm, 2*mm* or *m*2*m*. Out of 70 runs, the difference density of Type I is obtained 32 times with a reference match of 14% on average with a shift of approximately 0.85 0 0 or 0.15 0 0 relative to the Type II difference density, while the difference density of Type II is obtained 38 times.

The above two tests suggest that there is an equal probability of obtaining a difference electron density of either kind. The only way to distinguish the solutions is to perform a refinement starting from each of the difference electron density maps and compare how the refinements proceed and the models they converge to. Although the average structures based on the main reflections were distinguished on the basis of the metal-fluorine bond distances (see § 5.1.4), can we reach the same conclusion if we refine the modulated structure based on the satellite reflections?

In Fig. 5.9(a) we can see two rows of visually different difference electron density. These two rows of difference density have been marked with red lines. In one case, the difference densities are separated, positive to one side, negative to the other side of the mean position. This represents positional disorder. In the other case, in some places there are more positive densities and some places more negative densities, which represents occupational modulation. We see a similar pattern of difference electron density in Fig. 5.10(a), which suggests positional modulation along one line and occupational modulation along another line parallel to the a axis. A point to note is that the position along the **a**-axis of the difference electron density is entirely different in the Type I difference density compared to the Type II difference density, with the shift between the two patterns being 0.85 0 0 or 0.15 0 0.

5.3 Refinement of the Superstructure in 3-D Space

After reconstructing the difference density from the satellite reflections, positive and negative densities were interpreted to obtain qualitatively the distortion in the fivefold superstructure. However, the peak height cannot be used for quantitative analysis of occupational modulation and, at the same time, the amplitude of displacement cannot be inferred from the position of the difference density peaks formed due to the displacement of the atom from its average position. A point to note is that there is an ambiguity in the signs of the peaks, the negative value in the solution can be positive in reality. So both possibilities need to be tested for the Type

I and Type II difference densities to find the correct solution. Interestingly, the Type I difference density map describes the modulation in the fivefold Type A structure of Phase I and the Type II difference density map describes the modulation in the fivefold Type B structure of Phase I. The two unique ways of describing the small cell average structure and two unique ways of describing the modulation in the two difference densities converge to the same point as the two difference densities describe the modulation in the fivefold expanded super structure of Type A and Type B of Phase I. The following protocols were followed to refine the fivefold superstructure.

a) The Type A and Type B structures of Phase I have been extended to the fivefold orthorhombic supercell and this is called the ideal fivefold superstructure.
b) Deviations in the ideal super structure (Type A and Type B superstructure) have been added from the difference density map.
c) In each superstructure there are two possible ways to add the deviation depending upon which features will be treated as positive and which feature will be treated as negative.
d) For the Type A superstructure, in the first case the yellow features were taken as representing positive density and the turquoise features were defined as negative density [Fig. 5.9 (a)-(b)]. This is defined as the Type A Direction 1 superstructure for the refinement and in the second case the yellow features were taken as representing negative density and the turquoise features were defined as positive density. This was defined as the Type A Direction 2 superstructure. In terms of the deformation which has been added initially in the ideal superstructure, they are just opposite in direction.
e) For the Type B superstructure, the same procedure was followed and two refinements were defined as the Type B Direction 1 superstructure and Type B Direction 2 superstructure.
f) The Lu and Na atoms present at the same atomic position were refined by using a common U value.
g) First an isoptropic model was refined. The atoms in the fivefold superstructure generated by an expansion from the atomic coordinates of the atoms in the smaller unit cell average structure were assigned the same isotropic U value initially and then they have been refined with different isotropic U values.

After that, the metal positions were refined anisotropically if possible and the anisotropicity was introduced starting with the highest occupied Lu metal center and then proceeding stepwise to the lowest occupied Lu metal center.

h) All the models were refined against only the satellite reflections and the satellite reflections used are from that twin domain which has the best R_{int} from the independent integration of the six satellite directions. The satellite reflections used for the refinement have an R_{int} of 4.25 % after the empirical absorption correction in SADABS.

i) It was not possible to refine the Lu and Na occupation at the same time, so of each element the occupations were in alternate refinement runs.

5.3.1 Refinement of the Type A Superstructure

The small cell average structure has been expanded to a fivefold superstructure. The atom positions Lu1/Na1, Lu1a/Na1a and Lu1b/Na1b in the superstructure were derived from the position of Lu1/Na1 in the small cell average structure (Fig 5.4) and similarly Lu2/Na2, Lu2a/Na2a, Lu2b/Na2b were derived from the Lu2/Na2 (Fig. 5.4) and Lu3/Na3, Lu3a/Na3a, Lu3b/Na3b from Lu3/Na3 (Fig. 5.4). The positions of the metal atoms before the refinement in the fivefold superstructure are shown in Fig. 5.11. The difference density around the metal positions is shown in Fig. 5.11. The sites Lu1/Na1, Lu1a/Na1a, Lu2a/Na2a will be termed as a Lu1/Na1 Type of site, Lu2/Na2, Lu2a/Na2a. Lu2b/Na2b will be termed as a Lu2/Na2 Type of site and Lu3/Na3, Lu3a/Na3a, Lu3b/Na3b will be termed as a Lu3/Na3 Type of site.

Compositional constraints were used on each metal site based on the site occupation obtained for each of the Lu1/Na1, Lu2/Na2 and Lu3/Na3 sites in the small cell average structure. The numerical values used in the occupational constrained are: the occupations of the metal in a metal site in the small cell average structure without the site symmetry multiplied by five due to fivefold superstructure. The occupations for the fivefold superstructure refinement have been taken from the Table 5.2(a) of the RT refinement. So the set of constraints in the fivefold Type A superstructure is

ai[Lu1] = 0.564655-ai[Lu1a]-ai[Lu1b] [Eq. 5.7]

ai[Lu2b] = 0.627675-ai[Lu2]-ai[Lu2a] [Eq. 5.8]

ai[Lu3] = 0.21392-ai[Lu3a]-ai[Lu3b] [Eq. 5.9]

ai[Na1] = 0-ai[Na1a]-ai[Na1b] [Eq. 5.10]

ai[Na2b] = 0.37017-ai[Na2]-ai[Na2a] [Eq. 5.11] ai[Na3] = 0.41108-ai[Na3a]-ai[Na3b] [Eq. 5.12]

where ai[Lu], ai[Na] are the site occupation factors of Lu and Na at different atomic sites in the asymmetric unit of the fivefold superstructure. The same compositional constraints have been used for the Type A Direction 1 refinement and the Type 2 Direction 2 refinement. Once we add the deviation in the Type A ideal superstructure according to the difference density map, subsequent refinement was performed for both the directions.

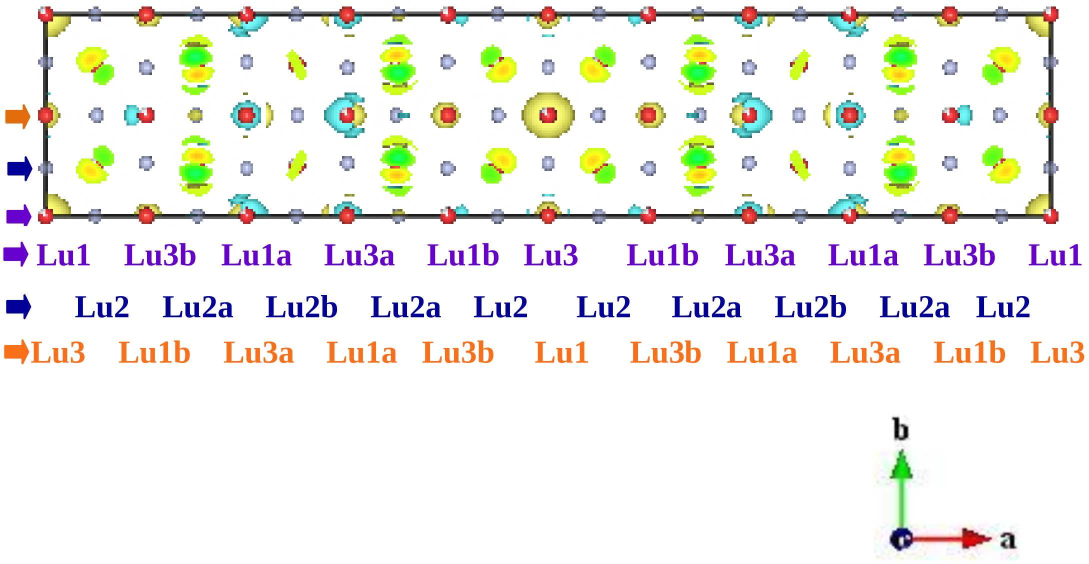

Fig. 5.11: The expanded fivefold superstructure from the Type A small cell structure of Phase I. The metal positions are shown by red dots. The difference densities around the metal atom positions are also shown. The fluorine atom positions have been omitted for clarity. The three parallel rows of cations are marked with coloured arrows and the atom names are given in the below of the image. For clarity the atom name Na has been omitted in each metal site.

5.3.1.1 Refinement of the Type A Direction 1 Superstructure

During the refinement it was necessary to add an additional constraint to the Lu2a/Na2a site so that the site occupation does not exceed the maximum possible physical occupation. It was not possible to refine Lu1/Na1 sites anisotropically, so these sites were refined with a common isotropic U [U_{iso} = 0.0137(12)]. Only the highly occupied fluorine atoms in the small cell average structure have been used for the refinement of the fivefold superstructure and they have been treated as fully occupied fluorine atoms in the superstructure. F1, F1a and F1b in the superstructure come from atom F1 of the small structure and the F2, F2a, F2b, F2c, F2d set of atoms in the superstructure comes from atom F2 in the small cell structure. The fluorine atoms were refined isotropically and it was not possible to refine them anisotropically as the U values go non-positive definite during the refinement [U_{iso} for F1 = 0.07(3), F1a = 0.07(2)), F1b = 0.07(3), F2, F2a, F2b, F2c, F2d = 0.058(13)]. It was not possible to refine the isotropic U values of the F2 set of atoms individually, as the U_{iso} goes very high during the refinement. The refinement converges with a R_{obs} of 15.80 % and wR_{obs} of 14.78 %. After the refinement it is interesting to examine the arrangement of the atoms as a function of their occupancies. A nice rendering of occupancies is produced by the program VESTA (Momma & Izumi, 2008). In the following image (Fig. 5.12) the “pie charts” show the proportion of Lu (red), Na (yellow) and vacancies (grey) at each site and the fluorine positions are shown in green. The Lu/Na families of atoms in three different rows are marked with three differently coloured arrows at the left of the image and the names of the atoms are given below of the images. The same colours are used for atom numbering; Na atom names have been removed for better clarity.

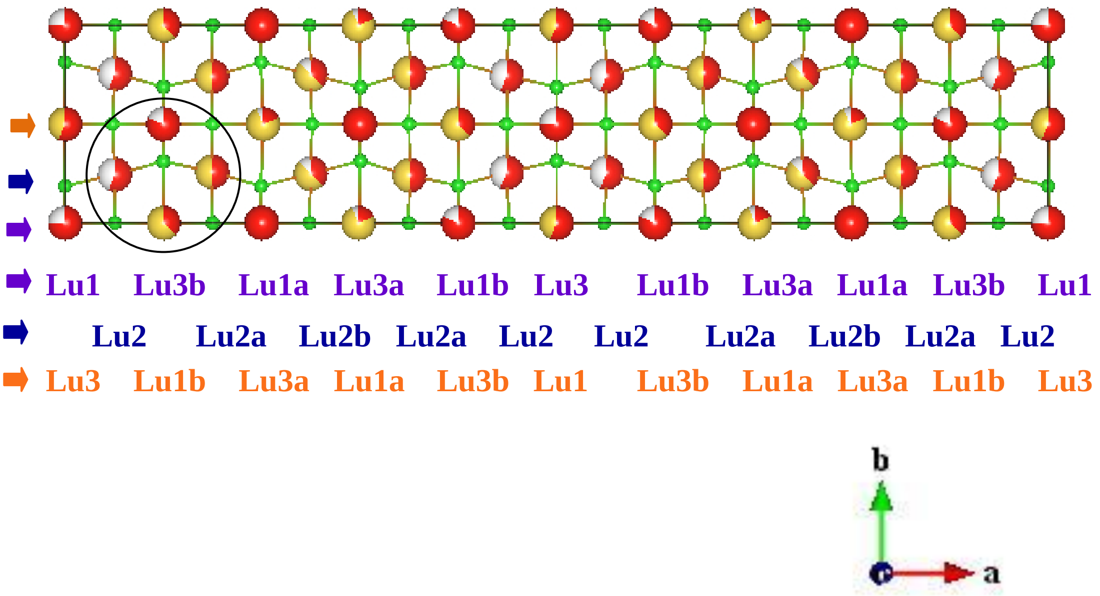

Fig. 5.12: The variation of the occupation of the metal sites (Lu, Na) and vacancy in the Type A Direction 1 superstructure (Lu : red, Na : yellow, Vacancy : grey). The three parallel rows of cations are marked with coloured arrows and the atom names are given below the image. For clarity the atom name Na has been omitted in each metal site.

Although a critical examination of the metal-fluorine bond distances in the superstructure indicated some of the M-F distances in the structure are chemically unrealistic. For example, we have examined the bond distances around the F1b atoms marked with a black circle in the Fig. 5.12; Lu2/Na2-F1b ~ 2.11Å, Lu2a/Na2a-F1b ~ 2.13Å, Lu1b/Na1b-F1b ~ 3.82Å and Lu3b/Na3b-F1b ~ 4.27Å, where last two of them are high compared to the average M-F distances. As the result is chemically unrealistic it was discarded.

5.3.1.2 Refinement of the Type A Direction 2 Superstructure

During the refinement of this structure R_{obs} stays at a very high value (R_{obs} ~ 25%) and some of the isotropic ADPs goes negative (Lu1/Na1 family of sites) at the initial stage. The refinement does not converge, not even with increased damping (damp value of 0.1, the damp value in the Jana program can be varied from 0 to 1 and a value of 1 suggests there is no damping in the refinement).

This suggests either that the starting model is far away from the real description of the fivefold superstructure or that the initial description of the modulations added from the difference density map in the Type A direction 2 superstructure is unrealistic. So this result was also discarded.

The refinements of the Type A superstructure does not converge to a chemically sensible solution in either of the refinements (Type A Direction 1 and Type A direction 2). The same observation was made during the refinement of the Type A structure in the small cell. Next, the refinement of the Type B superstructure was attempted.

5.3.2 Refinement of the Type B Superstructure

The small cell Type B average structure of Phase I consists of Lu1/Na1 and Lu2/Na2 sites of metal atoms, which have been expanded to the fivefold superstructure and the positions of the unique atoms in the superstructure, Lu1/Na1, Lu1a/Na1a, Lu1b/Na1b, Lu1c/Na1c and Lu1d/Na1d originate from the Lu1/Na1 site of the small cell structure. Similarly the positions of the Lu2/Na2, Lu2a/Na2a, Lu2b/Na2b sites are derived from the Lu2/Na2 site of the small cell average structure. The set of sites Lu1/Na1, Lu1a/Na1a, Lu1b/Na1b, Lu1c/Na1c, Lu1d/Na1d will be termed as the Lu1/Na1 type of sites and, similarly, the other set of sites will be termed as the Lu2/Na2 type of sites. The following image (Fig. 5.13) shows the positions of the metals in the fivefold superstructure before the refinement as red dots.

Fig. 5.13: The expanded fivefold superstructure from the Type B small cell structure. The metal positions are shown by red dots and the difference density around the metal atoms is shown. The fluorine atom positions have been omitted for clarity. The two parallel rows of cations are marked with coloured arrows and the atom names are given in the below the image. For clarity the atom name Na has been omitted in each metal site.

Compositional constraints have been used for each type of metal site. The constraints are based on the refinement of the small cell average Type B structure at RT where the metal atoms are isotropic and the possible disorder in the fluorine positions have been interpreted (§ 5.1.4) The occupation (without the site symmetry) needs to be multiplied by five to be usable in the following occupational constraints. So the constraints are

ai[Lu1] = 0.467705-ai[Lu1a]-ai[Lu1b]-ai[Lu1c]-ai[Lu1d] [Eq. 5.13]

ai[Na1] = 0.469795-ai[Na1a]-ai[Na1b]-ai[Na1c]-ai[Na1d] [Eq. 5.14]

ai[Lu2] = 0.938545-ai[Lu2a]-ai[Lu2b] [Eq. 5.15]

ai[Na2] = 0.311455-ai[Na2a]-ai[Na2b] [Eq. 5.16]

The occupation ai[Lu] and ai[Na] are the site occupation factors of Lu and Na at different atomic sites in the asymmetric unit of the fivefold Type B superstructure. Once the initial model is set up by adding the deviation from the Type II difference density map, subsequent refinements were performed on the two initial models. The two initial models depend on which feature is chosen as positive density and which feature is chosen as negative density. The most highly occupied fluorine atoms (F1, F2, F3) in the small cell average structure have been used for this refinement and the occupation factors of the fluorine atoms were not refined. These fluorine atoms are treated as fully occupied fluorine atoms.

5.3.2.1 Refinement of the Type B Direction 1 Superstructure

For this refinement, the yellow features in Fig. 5.13 have been chosen as positive density and turquoise features as negative density. The refinement of the fivefold superstructure was performed according to the protocol mentioned in 5.3. During the refinement, it was necessary to add an additional constraint for the Lu2/Na2 and Lu2a/Na2a sites so that the site occupation does not exceed the maximum possible physical occupation. All the metal positions were refined anisotropically, only the heavy atom site Lu1a/Na1a atomic site has a low U_{33} value close to zero. The fluorine atoms were refined isotropically and then a common U value was refined for the fluorine atoms [U_{iso} for F1 set of atoms 0.063(14), F2 set of atoms 0.10(2), F3 set of atoms 0.03(4)]. It was not possible to refine the fluorine atoms anistropically as their ADPs become non-positive definite. The refinement converges with a R_{obs} of 13.72 % and wR_{obs} of 19.64 %. The following image (Fig. 5.14) shows the displacement ellipsoid plot for the fivefold superstructure with 50% probability ellipsoids for the heavy atoms except Lu1a/Na1a (radius of 0.34 Å) and fluorine atoms with a radius of 0.34 Å. The parallel rows of Lu/Na family of atoms are marked with coloured arrows on the left of the image and the atom names are given below the image. The same colour code for naming the rows of heavy atom sites have been used for all the figures of Type B refinement.

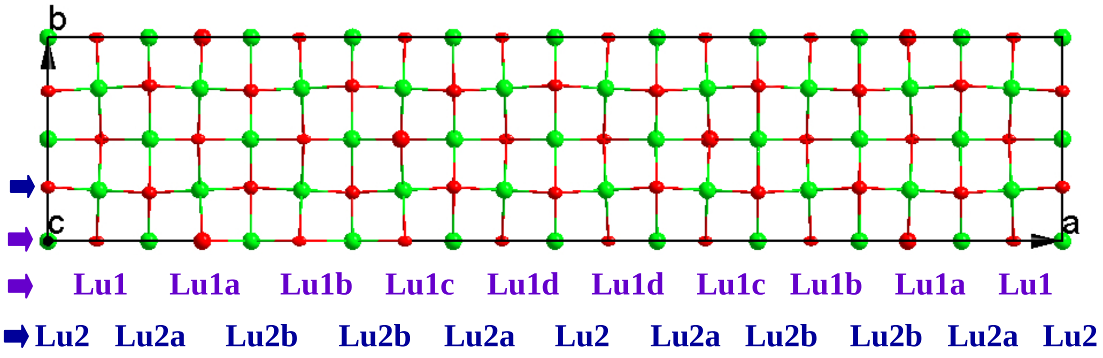

Fig. 5.14: Plot of the displacement ellipsoids for the fivefold superstructure of Type B Direction 1 after the refinement in 3-D space. The two parallel rows of cations are marked with coloured arrows and the atom names given below the image. For clarity the atom name Na has been omitted in each metal site.

Now it is more interesting to check the occupancies of the atomic sites. The following figure (Fig. 5.15) shows the proportions of Lu (red), Na (yellow) and vacancies (grey) on each site and the fluorine atoms have been marked with green dots.

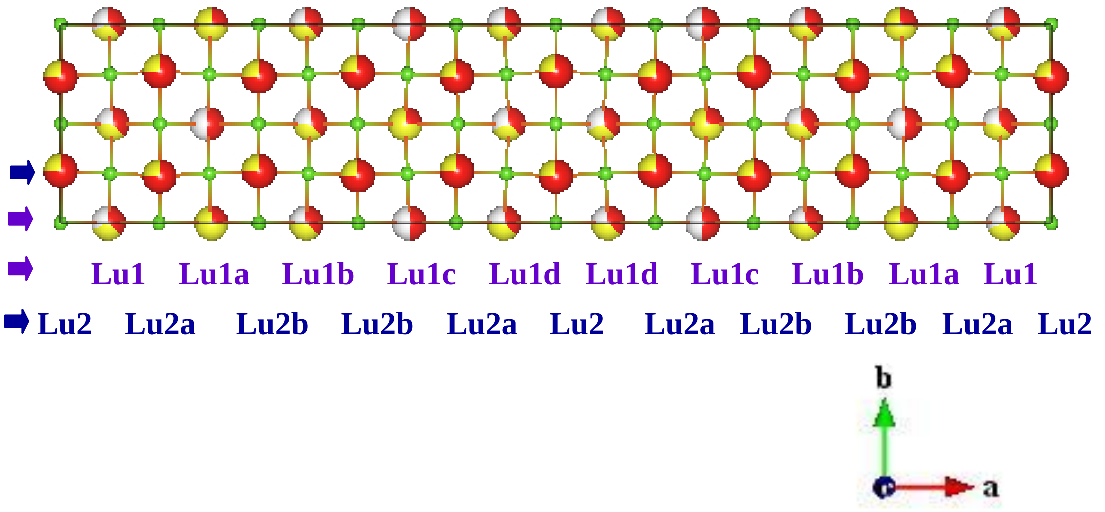

Fig. 5.15: The variation of the occupation of the metal sites (Lu, Na) and vacancy in the Type B Direction 1 superstructure (Lu: red; Na: yellow; Vacancy: grey). The positions of the fluorine atoms are shown by green dots. The two parallel rows of cations are marked with coloured arrows and the atom names are given below the image. For clarity the atom name Na has been omitted in each metal site.

The Lu1/Na1 set of atoms show occupational modulation and the Lu2/Na2 set of atoms shows positional modulation, as expected from the Type II difference density maps. There are eight fluorine atoms around each metal site making a distorted cubic coordination geometry and the fluorine atoms are surrounded by four metal sites in tetrahedral geometry. Now, it would be interesting to see whether we can improve the refinement result if we start our initial model from the other direction and whether we reach the same positions and occupations for the atoms.

5.3.2.2 Refinement of the Type B Direction 2 Superstructure

The refinement was performed according to the mentioned protocol in 5.3 for the Type B direction 2 superstructure, after adding the necessary deviations in terms of the positions and occupations of the different metal sites from the Type II difference density map. All the metal atom positions were successfully refined anisotropically, which was not the case for the Type A superstructure. This indicates that the Type B superstructure is a better description than the Type A superstructure. The fluorine atoms were refined isotropically [U_{iso} for the F1 set of atoms 0.078(16), F2 set of atoms 0.082(16), F3 set of atoms 0.04(2)] as in the previous refinement of the Type B Direction 1 superstructure. Interestingly, the Type B Direction 1 superstructure and Type B Direction 2 superstructure do not converge to the same positions and occupations for the heavy atoms. The refinement converges with a R_{obs} of 12.80 % and wR_{obs} of 18.58 %. The R_{obs} value for this refinement is better than in the Type B Direction 1 superstructure refinement and also better than for the Type A superstructure refinement, which gives an additional indication that this particular refinement describes the modulation in the structure in a superior way. The following image (Fig. 5.16) shows the displacement ellipsoid plot of the fivefold superstructure with 50% probability ellipsoids for of the metal atoms and the fluorine atoms with a radius of 0.34 Å. The fluorine atoms have high U_{iso} which suggests that the fluorine positions are disordered.

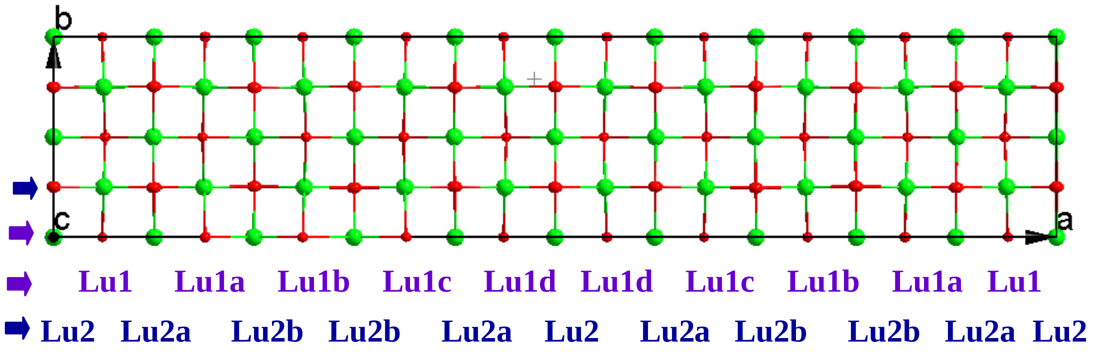

Fig. 5.16: Plot of the displacement ellipsoids for the fivefold superstructure of Type B Direction 2 after the refinement in 3-D space. The two parallel rows of cations are marked with coloured arrows and the atom names given below the image. For clarity the atom name Na has been omitted in each metal site.

Now it will be interesting to look the occupancies of the atomic sites with the improve description of the modulation in the fivefold superstructure. The following image (Fig. 5.17) the “pie charts” show the proportion of Lu (red), Na (yellow) and vacancies at different atomic sites.

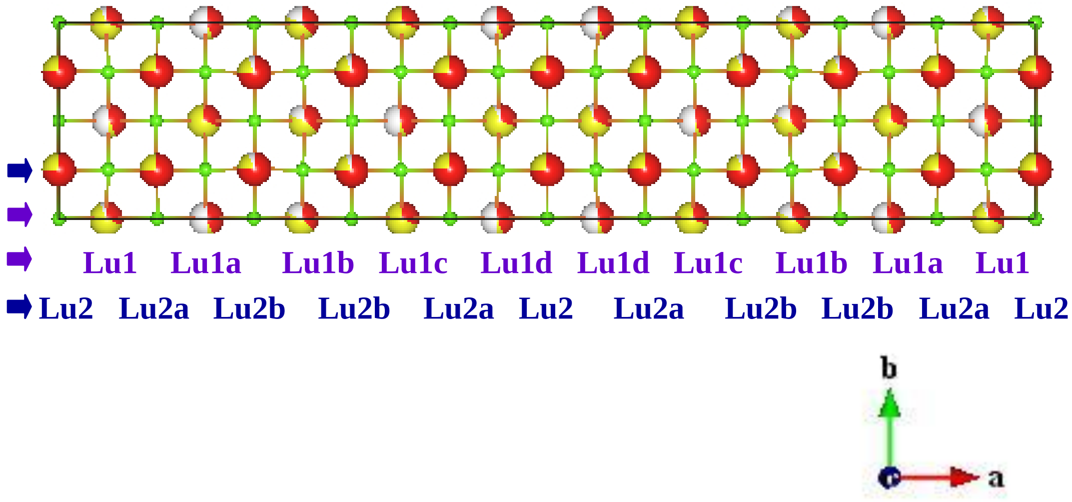

Fig. 5.17: ***The variation of the occupation of the metal sites (Lu, Na) and vacancy in the Type B Direction 2 superstructure (Lu: red; Na: yellow; Vacancy: grey). The positions of the fluorine atoms are shown by green dots. The two parallel rows of cations are marked with coloured arrows and the atom names are given below the image. For clarity the atom name Na has been omitted in each metal site.***

There is occupational modulation of the Lu1/Na1 set of atoms and there is positional modulation of the Lu2/Na2 set of atoms, though the positional modulation is not as strong as observed in the Type II difference density map. It seems that there is a clear correlation between how close the fluorine atoms are to the metal sites and the occupancy of Lu in those sites. This can be quantified by listing the occupancies, average M-F distances and bond valences (Table 5.7). There are no s.u.s in the occupations in the Lu1c/Na1c and Lu2a/Na2a sites in Table 5.17, as in these two atomic sites additional occupational constraints (Eq. 5.17 & 5.18) were used during the refinement and in the last cycles of refinement only the Na occupations were refined in each site.

ai[Na1c] = 0.25-ai[Lu1c] [Eq. 5.17]
ai[Na2a] = 0.50-ai[Lu2a] [Eq. 5.18]

Site	Occ(Lu), Occ(Na)	Bond valence sum (Lu,Na)	Average distance (Å)
Lu1/Na1	0.3131, 0.646(6)	1.09, 0.65	2.61
Lu1a/Na1a	0.4544, 0.051(4)	1.11, 0.67	2.60
Lu1b/Na1b	0.3538, 0.446(3)	1.09, 0.66	2.61
Lu1c/Na1c	0.3031, 0.6969	1.08, 0.65	2.61
Lu1d/Na1d	0.4459, 0.039(3)	1.11, 0.66	2.60
Lu2/Na2	0.7436, 0.339(3)	3.44, 2.06	2.18
Lu2a/Na2a	0.7411, 2589	3.44, 2.07	2.18
Lu2b/Na2b	0.7644, 0.1945(15)	2.72, 2.05	2.18

Table 5.7: The occupation of different atomic sites with Lu and Na, and their calculated bond valences for each type of atom for the Type B Direction 2 superstructure refinement. The average metal-fluorine distances are also tabulated.

It appears from Table 5.7 that the Lu2/Na2 type of site which has higher Lu occupation than the Lu1/Na1 type of site, has a shorter metal-fluorine distance. But the Lu1/Na1 type of site, which is occupationally modulated, does not show much variation in the average metal-fluorine bond distances and their bond valences, which is unexpected. Although the refinement looks robust, the modulation in the fluorine positions is not optimized enough. Each metal atom has eight neighbors. The bond distances around each of the metal atom sites is given in (Table 5.8)

	Bond distances (Å)
Lu1	2.49(3) F1 × 2, 2.65(3) F2 × 2, 2.65(4) F3 × 4
Lu1a	2.50(3) F1a × 2, 2.61(3) F2 × 2, 2.65(4) F3a × 4
Lu1b	2.51(3) F1a × 2, 2.62(3) F2a × 2, 2.65(4) F3b × 4
Lu1c	2.51(3) F1b × 2, 2.64(3) F2a × 2, 2.65(4) F3a × 4
Lu1d	2.48(3) F1b × 2, 2.64(3) F2b × 2, 2.65(4) F3 × 4
Lu2	2.24(3) F1 × 2, 2.15(3) F3 × 4, 2.18(2) F2b × 2
Lu2a	2.15(3) F3a × 2, 2.17 (2) F2 × 2, 2.15 (3) F3 × 2,2.25 (2) F1b × 2
Lu2b	2.25(2) F1a × 2, 2.16(3) F3a × 2, 2.15(3) F3b × 2, 2.17(2) F2a × 2

Table 5.8: The metal-fluorine bond distances around each of the metal sites in the refinement of the Type B Direction 2 superstructure. The multipliers refer to the numbers of symmetry equivalent fluorine atoms of that type in the coordination sphere.

5.4 Refinement in Superspace

The standard tool for handling modulated structure is to use a superspace approach (de Wolff *et al.*, 1981; Janssen *et al.*, 1992; van Smaalen, 1995). In this approach, in the first step a reciprocal unit cell is established using the main reflections. In the next step the systematic distribution of satellite reflections in the reciprocal space are used to define the fourth vector, so-called modulation vector **q**. This addition of one vector **q** (**q** = 0.4, 0, 0 in our case) with maximum satellite index two will index all the satellite reflections belonging to one orthorhombic twin domain, and introduces no redundant “empty” lattice nodes. This implies a transition into four-dimensional space. This higher dimensional concept affects all the steps of structure analysis which has been discussed briefly in § 1. The complexity of higher dimensional space can be reduced by use of projections in reciprocal space or sections in direct space of the higher dimensional space. Instead of a detailed discussion on the treatment of superspace in understanding modulated structure, we will show how refinement in superspace approach can be used to understand such a complex structure.

During the refinement of the fivefold superstructure in 3-D space which has been discussed, the main problem arising is due to the heavy correlations between the atomic positions which are caused by the weak positional modulation of the Lu2/Na2 set of atom sites in the Type B superstructure. Prof. Lukas Palatinus from the Department of Structure Analysis, Prague, offered to refine the structure in superspace. In principle, the structure modeled in 3-D space as a fivefold superstructure should be equivalent to that obtained from a superspace refinement. The solution of the Type B direction 2 superstructure should be comparable, as it has the lowest R-values and it makes the most chemical sense in terms of M-F bond lengths.

The key advantages of refining the structure in the superspace are

a) The refinement of the small cell average structure against main reflections and modulation against satellite reflections can be done simultaneously, and also one has a permanent control over the match of the average structure to the main reflections.
b) The parameters of modulation (i.e. the deviation of the individual atom positions, ADPs and occupancy) from the average structure can easily be controlled, and they can be switched on/off without complicated restrictions.
c) It turns out in the subsequent superspace refinement that two solutions came out from SUPERFLIP result naturally from the superspace solution, and the correct one can be chosen easily in superspace refinement without complicated refinement of fivefold modulated structure in 3-D space.

5.4.1 Solution

The solution in superspace produces a similar picture as the solution in the fivefold supercell from the band flipping of satellite reflections. One position is predominantly positionally modulated, while the other one has strong occupational modulation. The initial model was built by choosing a positional modulation wave for the Lu2/Na2 site and an occupational wave for Lu1/Na1 site. Separate scale factors were refined for the main reflections and the satellite reflections during the refinement. The refinement is stable, although large correlations are always present.

5.4.2 Refinement

In superspace, the refinement consist of adding modulation of various parameters so that R-values against the satellite reflections drop and at the same time R-values against the main reflections do not rise too much. By doing all this, the structure should make chemical sense as well.

Starting from the small cell average structure as derived in § 5.1.4, the atomic sites which are mixed with Lu and Na were constrained to identical positions and they share the same ADP for the isotropic and anisotropic refinement. At first, positional modulation and occupational modulation was added to the Lu2/Na2 site and Lu1/Na1 site and the occupational constraints given in Eq. 5.4-5.6 were used. During the refinement, it is necessary to include the variation of ADP parameters as it can also be modulated. After refining only the heavy atoms and keeping the fluorine atoms at their non-modulated positions, the following R factors were obtained: $R_{(\mathrm{main,\ obs})}$ ~ 3 %, $R_{(\mathrm{1st\ order\ satellite,\ obs})}$ ~ 13.5 %, $R_{(\mathrm{2nd\ order\ satellite,\ obs})}$ ~ 18%. The combined R-value for all the satellites in this stage is $R_{(\mathrm{all\ satellites,\ obs})}$ ~ 15%.

During the refinement, it turns out that the amplitude of the modulation is highly correlated with the scale factor of the satellite reflections, so the refinement was performed with several values of satellite scale factors and R-values were compared (Table 5.9).

Scale Factor	$R_{(\mathrm{main,\ obs})}$	$R_{(\mathrm{1st\ order\ sats,\ obs})}$	$R_{(\mathrm{2nd\ order\ sats,\ obs})}$
30.0	3.33 %	13.52 %	17.92 %
25.00	3.31 %	13.54 %	17.95 %
20.00	3.26 %	13.58 %	17.98 %
15.00	3.18 %	13.55 %	17.99 %
10.00	2.93 %	13.66 %	17.97 %

Table 5.9: The variation of R-values with change of scale factor for the satellite reflections.

From the table it appears that the R-values for the satellite reflections essentially do not change with a change of scale factor and only the R-value on the main reflections increases somewhat with increasing scale factor of the satellite reflections. However, the underlying models are different with different scale factors as the amplitude of modulation changes.

There is no unique way of finding a scale factor solely based on the refinement. Some other argument needs to be applied to obtain the scale factor for the satellite reflections. The scale factor 15 was chosen because it is the lowest scale factor and does not yield atomic occupancies outside the physical range of 0-1.

As the next step, the modulation of the fluorine atoms was taken into account. At first modulation in the fluorine atom positions was introduced, resulting in the following R-values

$R_{\text{main, obs}} = 4.02\%$, $R_{\text{1st order satellites, obs}} = 10.52\%$, $R_{\text{2nd order satellites, obs}} = 15.24\%$.

The next step is to refine the fluorine atoms anisotropically and to add the positional modulation, resulting in the following R-values

$R_{\text{main, obs}} = 3.76\%$, $R_{\text{1st order satellites, obs}} = 9.39\%$, $R_{\text{2nd order satellites, obs}} = 14.25\%$.

At this point the fluorine atoms which have been added from the DF maps of the small cell structure (the F4 and F5 atoms) were too unstable to be kept in the refinement, so they were removed and the following R-values were obtained

$R_{\text{main, obs}} = 3.73\%$, $R_{\text{1st order satellites, obs}} = 11.04\%$, $R_{\text{2nd order satellites, obs}} = 17.57\%$.

In the final step, modulation of the ADP parameters was added to the three types of fluorine atoms (the F1, F2 and F3 atoms). The ADP parameters also have the “power” to emulate the modulation of the occupancy. During this refinement improvement of R-values for the 1st order and 2nd order satellites is significant.

$R_{\text{main, obs}} = 4.02\%$, $R_{\text{1st order satellites, obs}} = 9.40\%$, $R_{\text{2nd order satellites, obs}} = 15.66\%$.

Apart from the correlation of scale factors there is also strong correlation with the twin volumes. This correlation can be removed by including all six independently integrated dataset for the satellite reflections from the six twin directions. However, for the purpose of this refinement and comparison with the 3-D space refinement, the twin volumes were fixed to 1/6. The resulting R-values are

$R_{\text{main, obs}} = 4.21\%$, $R_{\text{1st order satellites, obs}} = 9.03\%$, $R_{\text{2nd order satellites}} = 15.14\%$, $R_{\text{all satellites, obs}} = 11.01\%$.

Looking at the statistics of the combined R-values of the main and satellite reflections as a function of resolution, we find a surprising trend (Table 5.10):

sinθ/λ limits	**0.310844**	**0.387518**	**0.446958**	**0.489943**	**0.527708**	**0.562184**	**0.590167**	**0.640089**
R_{obs}	11.00 %	9.53 %	6.21 %	5.76 %	6.26 %	4.83 %	5.80 %	6.37 %

Table 5.10: The change of combined R-values of the main and satellite reflections with resolution of the data.

It is interesting to note that the combined R-factors of main and satellite reflections at low-resolution are much larger than at the higher resolution. This might be related to various problems, one of them being improper absorption correction, another being the presence of additional, undescribed disorder from the strong diffuse scattering intensity, which influences mainly low-resolution reflections. We have observed additional strong features in the DF maps of the small cell average structure, which have been interpreted as the positions of disordered fluorine atoms, but those fluorine atoms have been discarded during the refinement of the modulated structure and moreover, the light atoms contribute relatively more to the low angle reflections. If the badly matching 243 low angle reflections out of a total of 1353 reflections are removed from the refined structure, the *R*-values for the refinement with $\sin(\theta)/\lambda > 0.35$ Å^{-1} are :

$R_{\text{main, obs}} = 3.61\%$, $R_{\text{1st order satellites, obs}} = 6.93\%$, $R_{\text{2nd order satellites, obs}} = 11.82\%$, $R_{\text{all satellites, obs}} = 8.46\%$.

It seems that this refinement is better behaved than the refinement with all the reflections, not only because of the lower *R*-values, but also the atomic displacement parameters behave better than in the previous refinement.

Until this moment the refinement proceeds as if the structure is incommensurately modulated, that is as if the modulation vector is an irrational number. In reality the modulation vector (**q**) is 0.4, 0, 0 which is a rational number. The single incommensurate solution splits into two commensurate solutions, depending on the choice of the parameter t. The t values are the phases of the atomic modulation function which has a period of 1 and this wave function runs parallel to the superspace vector (see § 1.3.2) with a range of 0 (origin of the cell) to 1 (origin of the next cell). A different value of t will lead to different set of points in three-dimensional space, which are related to the one obtained for t = 0 by a simple origin shift. In general varying t for a certain geometric parameter from t = 0 to 1 provides all values of this parameter occurring anywhere in the three-dimensional crystal structure (Smaalen, 2007). In general the *R*-values of the incommensurate refinement and different commensurate refinements are very close to each other. This is also the reason SUPERFILP found two different difference density maps from the satellite reflections of the fivefold supercell. These two solutions correspond to two possible commensurate choices. The two possible choices of t, lead to two different structures and the *R*-values (Table 5.11).

t	$R_{\text{main, obs}}$	$R_{\text{1st order satellites, obs}}$	$R_{\text{2nd order satellites, obs}}$	$R_{\text{all satellites, obs}}$
0.0	3.58 %	7.35 %	12.43 %	8.94 %
0.1	3.58 %	6.87 %	11.00 %	8.17 %

Table 5.11: The change of R-values with different choices of t values.

It seems that the solution with t = 0.1 is better than that with t = 0.0. By taking the solution at t = 0.1 and performing a zero refinement cycle against all the reflections, the following *R*-values were obtained:

$R_{\text{main, obs}} = 4.11\%$, $R_{\text{1st order satellites, obs}} = 8.79\%$, $R_{\text{2nd order satellites, obs}} = 15.82\%$.

Interestingly, this choice of t = 0.1 corresponds to the Type B superstructure and more precisely Type B Direction 2 superstructure in terms of the occupation and positional details of the heavy atoms in three-dimensional space.

5.4.3 Validation and Interpretation of the Structure from the Superspace Refinement

The refinement results in superspace have a number of large correlation coefficients, some of them as large as 0.97. A point to note is that this number is much less in superspace refinement than the number of correlations coefficient in the 3-D space refinement. This is the list of largest correlations

-0.975 correlation : x[Lu1]/xsin1[Lu1]

-0.972 correlation : y[Lu2]/U22cos1[Lu2]

-0.966 correlation : U33cos1[F2]/U33cos2[F2]

-0.940 correlation : U33[Lu1]/U33sin1[Lu1]

-0.931 correlation : y[Lu2]/ycos2[Lu2]

0.909 correlation : ycos2[Lu2]/U22cos1[Lu2]

The above sin and cos values are the part of the modulation function for a particular parameter which has been used during the refinement, *e.g.* y ycos2[Lu2] means the second harmonic modulation of y coordinate of Lu. The correlations are mainly between the positions and their modulations. It may be possible to remove these positional correlations by fixing the coordinates of the atoms to the positions refined against the small cell average structure only.

The structure refined in superspace converted to the corresponding fivefold supercell and plotted in Fig. 5.18 with 50% displacement ellipsoidal probability of all atoms. The high ADPs of the fluorine atoms suggests possible disorder in the fluorine positions. The F1a fluorine atom has high U_{11} (0.106 Å^2), F2b fluorine atom has high U_{33} (0.40 Å^2), F3 has high U_{22} (0.104 Å^2) and U_{33} (0.142 Å^2) and F3a atom has high U_{22} (0.150 Å^2) value in the refinement.

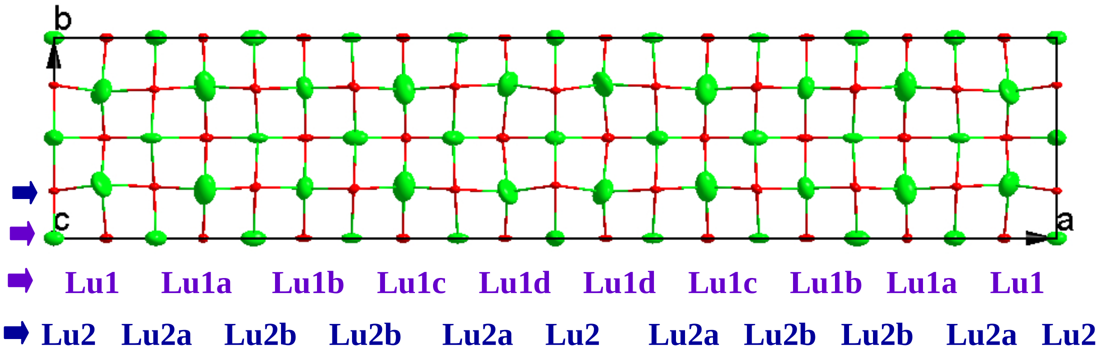

Fig. 5.18: Plot of the displacement ellipsoids for the fivefold structure derived from the Superspace refinement. The two parallel rows of cations are marked with coloured arrows and the atom names given the below the image. For clarity the atom name Na has been omitted in each metal site.

Now it is more interesting to check the occupancies of the atomic sites. The following figure (Fig. 5.19) the “pie charts” show the proportion of Lu (red) and Na (yellow) and vacancies (grey) on each site:

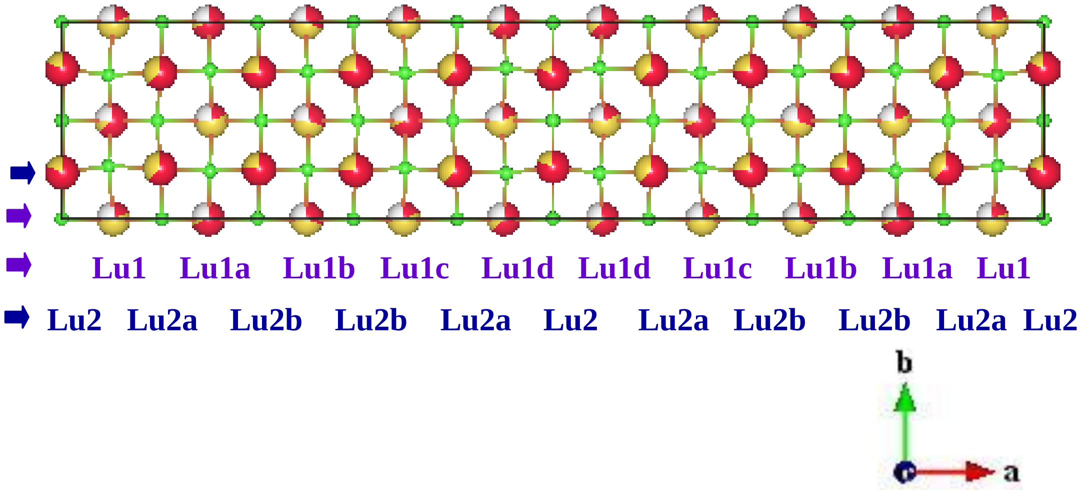

Fig. 5.19: The Variation of the occupation of the metal sites (Lu, Na) and vacancy of the fivefold superstructure derived from the superspace refinement (Lu: red; Na: yellow; Vacancy: grey). The positions of the fluorine atoms are shown by green dots. The two parallel rows of cations are marked with coloured arrows and the atom names are given below the image. For clarity the atom name Na has been omitted in each metal site.

In the fivefold superstructure constructed from the superspace model (Fig. 5.19) the fluorine atoms are “breathing” around the heavy atoms. It seems that there is a clear correlation between how close the fluorine atoms are to the metal sites, and the occupancy of Lu on that metal site. This is quantifiable by listing the average metal-fluorine distances for each metal site. The occupancies, average M-F distances and the bond valences are tabulated in Table 5.12 and all the M-F distances around each of the metal atom site are given in Table 5.13.

Site	**Occ(Lu), Occ(Na)**	**Bond valence (Lu,Na)**	**Average distance (Å)**
Lu1/Na1	0.2022, 0.5478	1.49,0.90	2.4914
Lu1a/Na1a	0.6936, 0.0564	1.99, 1.19	2.3845
Lu1b/Na1b	0.2909, 0.4591	1.87, 1.12	2.4065
Lu1c/Na1c	0.1914, 0.5586	1.50, 0.90	2.4895
Lu1d/Na1d	0.6083, 0.1417	2.21, 1.33	2.3507
Lu2/Na2	0.7836, 0.2164	2.60, 1.56	2.2862
Lu2a/Na2a	0.6486, 0.3514	2.10, 1.26	2.3652
Lu2b/Na2b	0.779, 0.221	1.84, 1.41	2.3205

Table 5.12: The occupancies of Lu and Na at different atomic sites and their calculated bond valences for each type of atom in the fivefold superstructure derived from the superspace model. The average metal-fluorine distances are also shown.

	Bond distances (Å)
Lu1/Na1	2.3985 F2 × 2, 2.5216 F3 × 4, 2.5238 F1 × 2
Lu1a/Na1a	2.3251 F2 × 2, 2.3704 F3a × 4, 2.4722 F1a × 2
Lu1b/Na1b	2.3484 F2a × 2, 2.4077 F3b × 4, 2.4624 F1a × 2
Lu1c/Na1c	2.4579 F2a × 2, 2.4611 F3a × 4, 2.5779 F1b × 2
Lu1d/Na1d	2.2875 F3 × 4, 2.3332 F1b × 2, 2.4948 F2b × 2
Lu2/Na2	2.2137 F1 × 2, 2.2842 F3 × 4, 2.3627 F2b × 2
Lu2a/Na2a	2.2820 F1b × 2, 2.3649 F3a × 2, 2.3822 F2 × 2, 2.4317 F3 × 2
Lu2b/Na2b	2.3065 F2a × 2, 2.3145 F3b × 2, 2.3196 F1a × 2, 2.3414 F3a × 2

Table 5.13: The metal-fluorine bond distances around each of the metal sites in the Superspace refinement. The multipliers refer to the numbers of symmetry equivalent fluorine atoms of that type in the coordination sphere.

Looking at the table (Table 5.12) we can see a correlation between the occupancy of Lu/Na and the bond valences (relative to the values for the average small cell structure). The bond valence for Lu is high if the metal site is highly occupied by Lu and similarly it is low if the metal site is less occupied by Lu, and hence the bond valence of Lu varies across the atomic site. The only exception is Lu1b/Na1b, as the site is less occupied by Lu but it has higher bond valance for Lu compared to the other sites. Similarly there is a negative correlation between the Lu occupancy and the average distances to the fluorine atoms as expected, except for the Lu1b/Na1b site. It seems there is some anomaly for the bond distances around the Lu1b/Na1b site.

In general, the bond distances and bond valences correlate with the Lu occupation in the atomic sites. But a very careful examination reveals that the bond valences do not match extremely well with the expected numbers (like if a metal site is fully occupied by Lu only and bonded with the fluorine atoms which are fully occupied, then we expect a bond valence close to 3 for the Lu), but one has to bear in mind that the fluorine atoms are still some sort of average positions between the optimized positions with respect to the Lu atoms and the Na atoms. Some sort of average is thus expected and it will affect the bond valences. The fluorine atoms are also disordered, which have not been taken under consideration during the 3-D space or superspace refinement, so proper account of the occupancy of the fluorine atoms may improve the bond valence calculation.

5.4.4 Conclusion for the Superspace Refinement

The principal feature of the fivefold superstructure from the superspace refinement is the occupational modulation of the heavy atoms. The refinement is robust in terms of refinement and chemically logical, but the structure can be improved by considering the following points:

a) Inclusion of the satellite reflections from the other twin domains may stabilize the refinement further and hopefully it will remove the correlation between the twin domains.
b) The scale factor for the satellite reflections needs to be varied again against the final model to search for an optimum scale factor, because with a decrease in the scale factor, the modulation amplitude will increase. With increasing modulation the bond valence sums may become more reasonable.

c) Some severe positional correlation can be removed by fixing the coordinates of the atoms to the positions refined against the small cell average structure.

d) It was not possible to refine the Lu and Na occupancies independently. Refinement of the Lu and Na occupation simultaneously may improve the model.

e) It was not possible to model the disorder in the fluorine positions. By refining the disorder in the fluorine atom positions, the poor match between the low-angle reflections might be removed.

5.5 Comparison of the Refinement in the 3-D Space and Superspace

The refinements in 3-D space and superspace give similar trends in terms of the site occupations and the positions of the heavy atoms. As it is difficult to calculate the s.u. from the superspace refinement, we have compared the values of occupations from both the refinements in Table 5.14 without s.u.s. For the comparison we have used the values from the refinement of the Type B Direction 2 superstructre in 3-D space, not only because it has the lowest R-values, but the ADPs and geometry are also more sensible. The occupation of the different atomic sites in an ideal fivefold structure without the modulation are also given in Table 5.14.

	Occupation without modulation	**3-D refinement Occupation**	**Superspace refinement Occupation**
Lu1/Na1	0.374, 0.376	0.3131 (-.06), 0.646 (+0.27)	0.2022 (-0.17), 0.5478 (+0.17)
Lu1a/Na1a	0.374, 0.376	0.4544 (+0.08), 0.051 (-0.32)	0.6936 (+0.32), 0.0564 (-0.32)
Lu1b/Na1b	0.374, 0.376	0.3538 (-0.02), 0.446 (+0.07)	0.2909 (-0.08), 0.4591 (+0.08)
Lu1c/Na1c	0.374, 0.376	0.3031 (-0.07), 0.6969 (+0.32)	0.1914 (-0.18), 0.5586 (+0.18)
Lu1d/Na1d	0.374, 0.376	0.4459 (+0.07), 0.039 (-0.34)	0.6083 (+0.23), 0.1417 (-0.23)
Lu2/Na2	0.751, 0.249	0.7436 (-0.01), 0.339 (+0.09)	0.7836 (+0.03), 0.2164 (-0.03)
Lu2a/Na2a	0.751, 0.249	0.7411 (-0.01), 2589 (+0.01)	0.6486 (-0.10), 0.3514 (+0.10)
Lu2b/Na2b	0.751, 0.249	0.7644 (+0.01), 0.1945 (-0.05)	0.779 (+0.03), 0.221 (-0.03)

Table 5.14: A comparison of the occupancies of Lu and Na at different atomic sites for the 3-D space refinement and the superspace refinement. The values in the parenthesis give the change of occupation of Lu and Na at different atomic sites from the ideal site occupation.

The trends in terms of occupation of Lu and Na at different atomic sites are similar but in some cases the values differ significantly in the two refinements. In the Lu1/Na1 type of site the occupancies of Na are very close in both refinements but those of Lu do not match very well. Overall the direction of the change of Lu and Na occupation at different atomic site in 3-D space and superspace refinement from the ideal occupation is same, the difference is essentially a difference in the modulation amplitude. A point to note is that during the refinement in 3-D space the sum of the occupancies of Lu and Na are fixed according to the small cell average structure, so a mismatch in one site will influence the occupation of the other site. For the Lu2/Na2 type of site the occupancies of Lu match quite well in both refinements, but the Na occupancies matches less well.

The atomic positions of the metals from both refinements are tabulated in Table 5.15. The ideal positions of the atoms are also given in the table.

	Ideal position (without modulation)	**3-D refinement**	**Superspace refinement**
Lu1/Na1	0.04918 0.0 0.5	0.0486 0.0 0.5 (<)	0.05235 0.0 0.5
Lu1a/Na1a	0.1508 0.0 0.5	0.1511 0.0 0.5 (>)	0.14888 0.0 0.5
Lu1b/Na1b	0.2492 0.0 0.5	0.2484 0.0 0.5 (~)	0.24908 0.0 0.5
Lu1c/Na1c	0.3508 0.0 0.5	0.3515 0.0 0.5 (>)	0.34800 0.0 0.5
Lu1d/Na1d	0.4492 0.0 0.5	0.4485 0.0 0.5 (~)	0.44976 0.0 0.5
Lu2/Na2	0.0 0.2558 0.0	0.0 0.2512 0.0 (>)	0.0 0.23629 0.0
Lu2a/Na2a	0.1 0.2558 0.0	0.100007 0.2476 0.0 (~)	0.09991 0.242951 0.0
Lu2b/Na2b	0.2 0.2558 0.0	0.200110 0.2540 0.0 (~)	0.20080 0.25415 0.0

Table 5.15: A comparison of the positions of the metals in the 3-D space refinement and superspace refinement (<, >, ~ symbols in the parenthesis indicate the coordinates of the atomics sites in 3-D space refinement are smaller, greater and similar compared to the positions of the same atomic site in the superspace refinement respectively).

It appears that the positions of the metal atoms derived from both types of refinements have converged to similar places. The average M-F distances are not similar, however, although the metal-fluorine bond distances around the Lu2/Na2 family of atoms are shorter than for the Lu1/Na1 family of atoms in both models, but the bond distances do not match very well (Tables 5.7, 5.8 for the 3-D space refinement and Tables 5.12, 5.13 for the superspace refinement). The bond distances are more evenly distributed in the superspace model than in the 3-D space model. The modulations in the fluorine atom positions are more prominent in the superspace model. The uneven distribution of the metal-fluorine distances is expected because the metal sites have different amounts of Lu and Na and so the fluorine atoms will expect more or less attraction depending upon the Lu occupancy in a particular site and secondly fluorine atom will lie close to Lu^{3+} due to smaller ionic radii of Lu^{3+} than Na^{+} (Pauling, 1940). In terms of the fluorine atom positions, the superspace refinement gives much better positions because of allowed modulation of fluorine atom positions and ADPs.

In the 3-D refinement, the initial starting model should be as close as possible to the correct solution, so that during the refinement, the model converges to the correct minima, instead of going to a false minimum, which has very similar *R*-value. The estimated deviation from the difference density is a random guess in this case and the choice of the positive and negative nature of the electron density in the difference electron density maps also has an effect on the refinement results. They do not converge to a single right solution as the correct solution is starting point dependent. In the 3-D refinement there is no easy way to choose the correct sign of the difference electron density without any subsequent refinement. The refinement in superspace gives more control on the structure during the refinement process. But it is interesting to note that the best solution obtained from each method lead to approximately the same structure.

In the small cell structure refinement, Type B of the Phase I structure was more favorable than Type A of the Phase I structure and we reach the same conclusion in the refinement of the structure both in the 3-D space and in the superspace refinement.

5.6 Conclusion

The average structure was described in two unique ways; there was an indication from the bond distances that that Type B structure makes more chemical sense than the Type A structure. The positional and occupational modulation in the structure was successfully refined in both spaces and we reach the same conclusion from the refinement of the modulated structure that one model is preferable to the other. To distinguish the refinements it becomes essential to use chemical sense and not just the *R*-values. It also can be concluded that in the small cell average structure the Lu atoms are underbonded and Na atoms are overbonded (Table 5.6), but in the modulated structure the fluorine atoms have a chance to better adopt their position, this makes the driving force for the modulation.

5.7 References

Brown, I. D. (1996). *J Appl Crystallogr* **29**, 479-480.

Momma, K. & Izumi, F. (2008). *Journal of Applied Crystallography* **41**, 653-658.

Palatinus, L., Fleischer, F., Pattison, P., Weber, T. & Steurer, W. (2011). *Acta Crystallogr A* **67**, 9-20.

Pauling, L. (1940). *The nature of the chemical bond*. New York: Cornell University Press.

Rae, A. D., Thompson, J. G. & Withers, R. L. (1992). *Acta Crystallogr B* **48**, 418-428.

Smaalen, S. v. (2007). *Incommensurate crystallography*. Oxford: Oxford University Press.

Woolfson, M. M. (1971). *REP. PROG. PHYS.* **34**, 369-433.

Wolff, P. M. de, Janssen, T. & Janner, A. (1981). Acta Cryst. A**37**, 625-636.

van Smaalen, S. (1995). *Crystallogr. Rev.* **4**, 79-202.

Chapter 6: Conclusions and Outlook

The diffraction pattern of $NaLuF_4$ with apparently "cubic" symmetry arises from six independent orthorhombic twin domains or maybe three independent tetragonal twin domains, although both of the phases have been treated as a sixfold orthorhombic twin structure. The twinning is a natural property of the compound. The sample of $NaLuF_4$ was prepared in a very slow process by the Bridgman method with a cooling time of 3-4 weeks, but the twinning in the samples was still present. The sample of $NaLuF_4$ was prepared in three batches at three different times, but a crystal exhibiting the Phase II diffraction pattern (no satellite reflections) was only ever found in the sample from the first preparation. The observation contradicts the fact that in all three preparations of the sample the same synthetic procedure was followed and Energy-Dispersive X-ray spectroscopy (EDX) analysis performed by Dr. Karl Krämer in Bern on both phases gave the same chemical composition of $Na_5Lu_9F_{32}$. The high angle main reflections from both phases appear to be split because of overlap from the twin domains and this causes difficulties with determining accurate unit cell parameters. The best estimation of the unit cell parameters can be obtained from the integration of the satellite reflections alone which are not effected by overlaps. A further experiment with higher angular resolution may allow the twin overlaps to be resolved at higher angles, which may improve the estimation of cell parameters.

Data integration of main and satellite reflections have a critical role in such a complex structure analysis. Use of higher mask size to integrate the main reflections had an influence on the refinement of twin volumes and ADPs of metal atoms. The use of a non-crystallographic absence condition for integrating the satellite reflections from a diffraction pattern of main and satellite reflections was also important for the refinement of the modulated structure. Further use of such non-crystallographic conditions in similar complex diffraction pattern may prove vital in modelling the structure.

The two phases differ mainly in the occupancies of Lu^{3+}, Na^{+} and vacancy in the heavy atom sites of the average structure. The diffraction pattern of each phase was explained in terms of two different structural models, which can be understood from the crystallographic orbit theory and after structure refinement one of the descriptions is chemically more meaningful in both of the phases. Although the *R*-values are very close for the two descriptions of the structure, a critical examination of the metal-fluorine bond distances indicated which model was more likely to be correct. The refinement of each model employed compositional constraints and additional constraints were required for one single mixed atomic site during the refinement.

The average structure of Phase I is distorted from the ideal positions of a fluorite structure due to the uneven distribution of metal-fluorine distances around the metal sites which mainly arises from the sites being variously occupied by Lu^{3+}, Na^{+} or vacancy. In the small cell average structure (Fig. 6.1) of the Phase I sample, the Lu atoms are underbonded and the Na atoms are overbonded and this leads to a modulated superstructure, in which the fluorine atoms can better position themselves around the metal atoms. In the fivefold superstructure of Phase I (Fig. 6.2) strong occupational and positional modulation in the metal sites are observed. While the disorder in the fluorine atom positions could be interpreted in the small cell average structure, it was unsuccessful in the fivefold superstructure due to insufficient information about the fluorine atom positions in the satellite reflection data, as the fluorine atom is a weak scatterer. The modulation in the structure obtained from the 3-D space refinement and from a (3+1) D superspace refinement is similar, but superspace refinement gives less correlation of the refined parameters. However, during the superspace refinement, obtaining the scale factor between the main and satellite reflections was not straightforward, as the two sets of reflections were integrated from two different measurements and there were no common reflections. The fivefold superstructure model developed during this work can be used as a starting point for understanding the origin of the diffuse scattering. However, it is highly probable that the diffuse scattering is also influenced by the twinning, which needs to be deconvoluted before one can start to understand the diffuse scattering qualitatively and then quantitatively. Electron diffraction on micro-grains of the sample may help to deconvolute the diffuse scattering if the twin domains are separable in these micro-grains. The diffuse lines present along $\mathbf{a}^*_T$, $\mathbf{b}^*_T$ and $\mathbf{c}^*_T$ in the Phase I diffraction pattern suggest a stacking fault along these directions in the structure, but the squares formed in two dimension by the intersection of these diffuse lines needs to be deconvoluted to understand whether it is consequence of twining or if they are really present in all the directions of a single domain? The atomic sites are occupied with different amounts of Lu atoms in the fivefold superstructure, but at the local level how these atoms are really arranged and the short range interactions between them can only be understood from an analysis of the diffuse scattering. From the preliminary analysis, there is an indication that the Lu and Na metal sites have different coordination geometries. How these coordination spheres look at the local level cannot be explained from the sharp Bragg reflections in the diffraction pattern. Another source of the diffuse scattering may be strain in the twin boundaries.

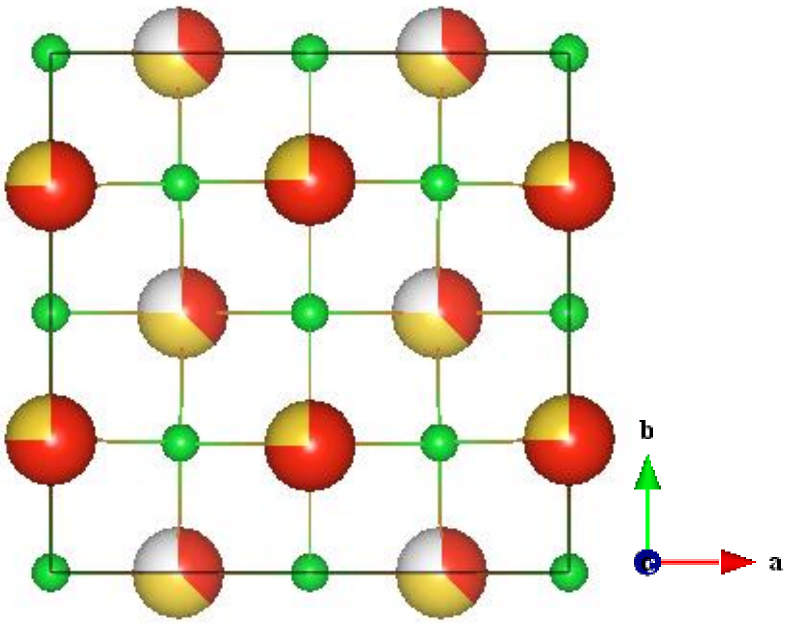

Fig. 6.1: The average structure of the Phase I sample based on the main reflections. The positions of the fluorine atoms are shown in green and the occupancies of the heavy metals are shown in red (Lu), yellow (Na) and grey (vacancy).

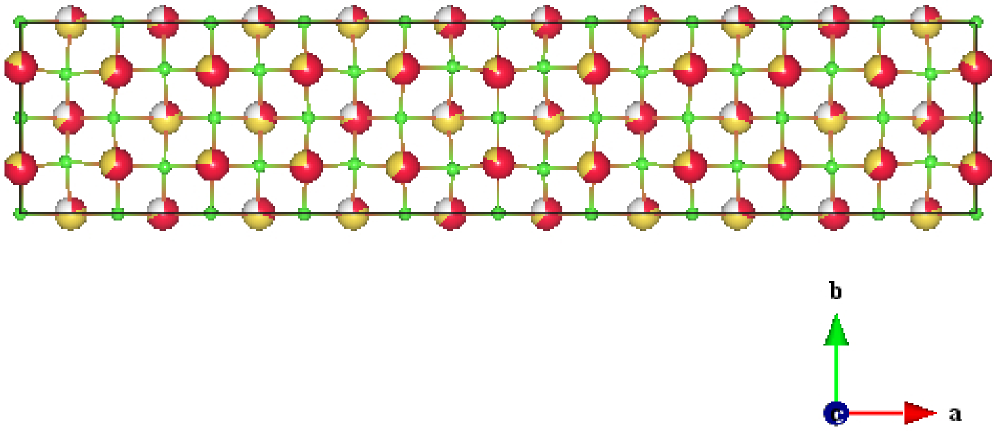

Fig. 6.2: The fivefold modulated structure derived from the superspace refinement of the Phase I sample. The positions of the fluorine atoms are shown in green and the occupancies of the heavy metals in red (Lu), yellow (Na) and grey (vacancy).

The use of difference electron density maps in understanding the fivefold modulation was important and was used as a basis to refine the fivefold superstructure. The refinement was difficult, but the structure refined in 3-D space closely matches structure refined in (3+1) D superspace and will be a basis to model the diffuse scattering.

The Phase II structure (Fig. 6.3) is also distorted but there are no positional or occupational modulations of the metal atoms. In the average structure Lu atoms are underbonded and the fluorine positions are also disordered between several sites with possibly different coordination geometries around the metal sites like in the Phase I structure. The diffuse scattering intensities need to be deconvoluted for a better understanding of their origin The average structure which has been developed based on the Bragg reflections can be used as a starting point to understand the relative arrangement of the Lu and Na atoms locally.

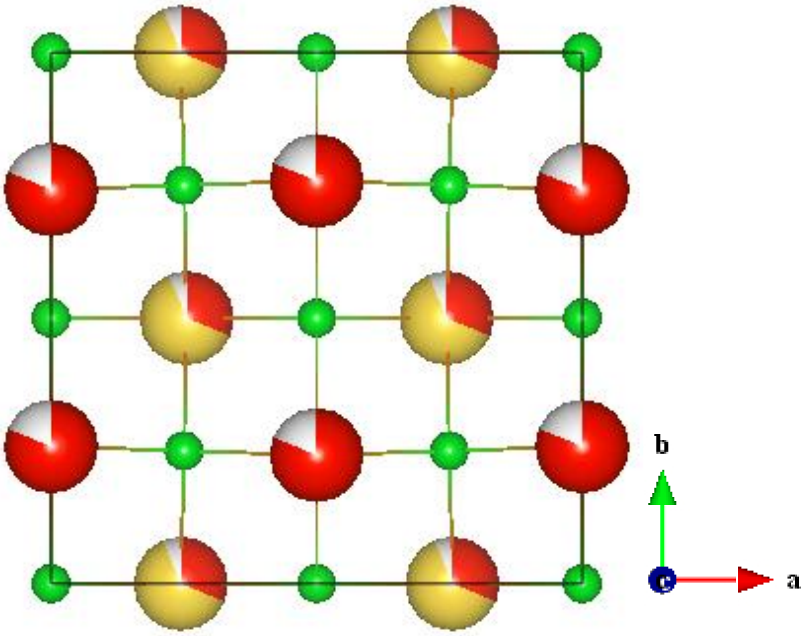

Fig. 6.3: The average structure of the Phase II sample based on the main reflections. The positions of fluorine atoms are shown in green and the occupancies of the heavy metals are shown in red (Lu), yellow (Na) and grey (vacancy).

Appendix A

A.1 Crystallographic Data for the Final Set of Refinements for the Phase I and Phase II Structure of Chapter 4 and Chapter 5

Crystallization method	Bridgman Synthesis	Bridgman Synthesis	Bridgman Synthesis	Bridgman Synthesis
Chemical formula	$Na_5Lu_9F_{32}$	$Na_5Lu_9F_{32}$	$Na_5Lu_9F_{32}$	$Na_5Lu_9F_{32}$
Formula weight (g mol^{-1})	71.8	71.8	71.8	71.8
Crystal colour, habit	colourless, irregular cube	colourless, irregular cubic	colourless, irregular cubic	colourless, irregular cubic
Crystal dimensions (mm)	0.1 × 0.1 × 0.1	0.1 × 0.1 × 0.1	0.1 × 0.1 × 0.1	0.1 × 0.1 × 0.1
Temperature (K)	100	150	200	293
Cell setting	orthorhombic	orthorhombic	orthorhombic	orthorhombic
Space group	*Cmmm*	*Cmmm*	*Cmmm*	*Cmmm*
Unit cell parameters				
***a* (Å)**	7.746(2)	7.746(2)	7.746(2)	7.746(2)
***b* (Å)**	7.743(5)	7.743(5)	7.743(5)	7.743(5)
***c* (Å)**	5.513(4)	5.513(4)	5.513(4)	5.513(4)
V (Å^3)	330.7(3)	330.7(3)	330.7(3)	330.7(3)
F(000)	491	491	491	491
Z	16	16	16	16
Radiation Type	synchrotron	synchrotron	synchrotron	synchrotron
Wavelength (Å)	0.70826	0.70826	0.70826	0.70826
μ (mm^{-1})	33.354	33.354	33.354	33.354
Detector	Mar345 IP	Mar345 IP	Mar345 IP	Mar345 IP
Method of measurement	ϕ scan	ϕ scan	ϕ scan	ϕ scan
Scan Width (°)	1.0	1.0	1.0	1.0
Absorption correction	multi scan (*SADABS*)	multi scan (*SADABS*)	multi scan (*SADABS*)	multi scan (*SADABS*)
Transmission factors (min; max)	0.510; 1	0.509; 1	0.519; 1	0.493; 1
$2\theta_{(max)}$ [°]	55.88	55.84	55.80	56.30
Total reflections measured	1293	1308	1305	1322
Symmetry independent reflections	755	755	755	791
R_{int}	3.54	3.58	3.63	3.67
Criteria for observed reflections	I > 3σ(I)	I > 3σ(I)	I > 3σ(I)	I > 3σ(I)
Redundancy	10.275	10.395	10.371	10.028
Range of *hkl*	$-10 \leq h \geq 10$ $-10 \leq k \geq 10$ $-7 \leq l \geq 7$	$-10 \leq h \leq 10$ $-10 \leq k \leq 10$ $-7 \leq l \leq 7$	$-10 \leq h \leq 10$ $-10 \leq k \leq 10$ $-7 \leq l \leq 7$	$-10 \leq h \leq 10$ $-10 \leq k \leq 10$ $-7 \leq l \leq 7$
Refinement on	F	F	F	F
Weighting scheme	$w=1/[\sigma^2(F) + 0.0001F^2]$	$w=1/[\sigma^2(F) + 0.0001F^2]$	$w=1/[\sigma^2(F) + 0.0001F^2]$	$w=1/[\sigma^2(F) + 0.0001F^2]$
R_{obs}/wR_{all} (Main reflections)	1.18/1.47	1.26/1.53	1.28/1.53	1.04/1.29
Goodness-of-fit (obs/all)	1.10/1.10	1.15/1.15	1.13/1.13	0.92/0.92
No of parameters	28	28	28	28
Final Δ_{max}/σ	0.0033	0.0034	0.0035	0.0033
Δρ (max; min) (e Å^{-3})	0.20, -0.32	0.21,-0.35	0.23,-0.32	0.18, -0.23
Refinement software	*JANA2006*	*JANA2006*	*JANA2006*	*JANA2006*
Source of atomic scattering factor	*International Tables for X-ray Crystallography* (Vol. C)	*International Tables for X-ray Crystallography* (Vol. C)	*International Tables for X-ray Crystallography* (Vol. C)	*International Tables for X-ray Crystallography* (Vol. C)

Table A.1: The crystallographic data for the final set of refinements based on main reflections of the Type A structure of Phase II at four temperatures.

Crystallization method	Bridgman Synthesis	Bridgman Synthesis	Bridgman Synthesis	Bridgman Synthesis
Chemical formula	$Na_5Lu_9F_{32}$	$Na_5Lu_9F_{32}$	$Na_5Lu_9F_{32}$	$Na_5Lu_9F_{32}$
Formula weight (g mol^{-1})	71.8	71.8	71.8	71.8
Crystal colour, habit	colourless, irregular cubic	colourless, irregular cubic	colourless, irregular cubic	colourless, irregular cubic
Crystal dimensions (mm)	0.1 × 0.1 × 0.1	0.1 × 0.1 × 0.1	0.1 × 0.1 × 0.1	0.1 × 0.1 × 0.1
Temperature (K)	100	150	200	293
Cell setting	orthorhombic	orthorhombic	orthorhombic	orthorhombic
Space group	*Cmmm*	*Cmmm*	*Cmmm*	*Cmmm*
Unit cell parameters **a(Å)** **b (Å)** **c (Å)** **V (Å^3)**	 7.746(2) 7.743(5) 5.513(4) 330.7(3)	 7.746(2) 7.743(5) 5.513(4) 330.7(3)	 7.746(2) 7.743(5) 5.513(4) 330.7(3)	 7.746(2) 7.743(5) 5.513(4) 330.7(3)
F(000)	491	491	491	491
Z	16	16	16	16
Radiation Type	synchrotron	synchrotron	synchrotron	synchrotron
Wavelength (Å)	0.70826	0.70826	0.70826	0.70826
μ (mm^{-1})	33.354	33.354	33.354	33.354
Detector	Mar345 IP	Mar345 IP	Mar345 IP	Mar345 IP
Method of measurement	ϕ scan	ϕ scan	ϕ scan	ϕ scan
Scan Width (°)	1.0	1.0	1.0	1.0
Absorption correction	multi scan (*SADABS*)	multi scan (*SADABS*)	multi scan (*SADABS*)	multi scan (*SADABS*)
Transmission factors (min; max)	0.510; 1	0.509; 1	0.519; 1	0.493; 1
$2\theta_{(max)}$ [°]	55.88	55.84	55.80	56.30
Total reflections measured	1293	1308	1305	1322
Symmetry independent reflections	755	7556	755	755
R_{int}	3.54	3.58	3.63	3.67
Criteria for observed reflections	$I > 3\sigma(I)$	$I > 3\sigma(I)$	$I > 3\sigma(I)$	$I > 3\sigma(I)$
Redundancy	10.275	10.395	10.371	10.028
Range of *hkl*	$-10 \leq h \geq 10$ $-10 \leq k \geq 10$ $-7 \leq l \geq 7$	$-10 \leq h \leq 10$ $-10 \leq k \leq 10$ $-7 \leq l \leq 7$	$-10 \leq h \leq 10$ $-10 \leq k \leq 10$ $-7 \leq l \leq 7$	$-10 \leq h \leq 10$ $-10 \leq k \leq 10$ $-7 \leq l \leq 7$
Refinement on	F	F	F	F
Weighting scheme	$w=1/[\sigma^2(F) + 0.0001F^2]$	$w=1/[\sigma^2(F) + 0.0001F^2]$	$w=1/[\sigma^2(F) + 0.0001F^2]$	$w=1/[\sigma^2(F) + 0.0001F^2]$
R_{obs}/wR_{all} (Main reflections)	1.35/1.53	1.27/1.54	1.22/1.51	1.30/1.55
Goodness-of-fit (obs/all)	1.15/1.15	1.15/1.15	1.11/1.11	1.11/1.11
No of parameters	27	27	27	27
Final Δ_{max}/σ	0.0023	0.0028	0.0023	0.0031
$\Delta\rho$ (max; min) (e Å^{-3})	0.35,-0.32	0.29,-0.34	0.27,-0.30	0.31,-0.34
Refinement software	*JANA2006*	*JANA2006*	*JANA2006*	*JANA2006*
Source of atomic scattering factor	*International Tables for X-ray Crystallography* (Vol. C)	*International Tables for X-ray Crystallography* (Vol. C)	*International Tables for X-ray Crystallography* (Vol. C)	*International Tables for X-ray Crystallography* (Vol. C)

Table A.2: The crystallographic data for the final set of refinements based on main reflections of the Type B structure of Phase II at four temperatures.

Crystallization method	Bridgman Synthesis	Bridgman Synthesis	Bridgman Synthesis
Chemical formula	$Na_5Lu_9F_{32}$	$Na_5Lu_9F_{32}$	$Na_5Lu_9F_{32}$
Formula weight (g mol^{-1})	71.8	71.8	71.8
Crystal colour, habit	colourless, irregular cubic	colourless, irregular cubic	colourless, tablet
Crystal dimensions (mm)	0.1 × 0.1 × 0.1	0.1 × 0.1 × 0.1	0.1 × 0.075 × 0.05
Temperature (K)	100	200	293
Cell setting	orthorhombic	orthorhombic	orthorhombic
Space group	*Cmmm*	*Cmmm*	*Cmmm*
Unit cell parameters ***a*** **(Å)** ***b*** **(Å)** ***c*** **(Å)** ***V*** **(Å^3)**	7.746(2) 7.743(5) 5.513(4) 330.7(3)	7.746(2) 7.743(5) 5.513(4) 330.7(3)	7.746(2) 7.743(5) 5.513(4) 330.7(3)
***F*(000)**	491	491	491
Z	16	16	16
Radiation Type	synchrotron	synchrotron	synchrotron
Wavelength (Å)	0.70150	0.70150	0.73550
μ (mm^{-1})	32.615	32.615	36.907
Detector	Mar345 IP	Mar345 IP	Mar345 IP
Method of measurement	ϕ scan	ϕ scan	ϕ scan
Scan Width (°)	1.0	1.0	1.0
Absorption correction	multi scan (*SADABS*)	multi scan (*SADABS*)	multi scan (*SADABS*)
Transmission factors (min; max)	0.260; 1	0.298; 1	0.275; 1
$2\theta_{(max)}$ [°]	55.6	55.6	56.1
Total reflections measured	1422	1412	1183
Symmetry independent reflections	810	808	681
R_{int}	5.18	7.29	4.08
Criteria for observed reflections	$I > 3\sigma(I)$	$I > 3\sigma(I)$	$I > 3\sigma(I)$
Redundancy	10.533	10.485	10.423
Range of *hkl*	$-10 \leq h \leq 10$ $-10 \leq k \leq 10$ $-7 \leq l \leq 7$	$-10 \leq h \leq 10$ $-10 \leq k \leq 10$ $-7 \leq l \leq 7$	$-9 \leq h \leq 9$ $-9 \leq k \leq 9$ $-7 \leq l \leq 7$
Refinement on	F	F	F
Weighting scheme	$w=1/[\sigma^2(F) + 0.0001F^2]$	$w=1/[\sigma^2(F) + 0.0001F^2]$	$w=1/[\sigma^2(F) + 0.0001F^2]$
R_{obs}/wR_{all} (Main reflections)	1.10/1.16	2.25/1.77	1.00/1.24
Goodness-of-fit (obs/all)	0.93/0.93	1.18/1.18	1.02/1.02
No of parameters	29	29	29
Final Δ_{max}/σ	0.0039	0.0032	0.0034
$\Delta\rho$ (max; min) (e Å^{-3})	0.32,-0.37	1.65,-1.84	0.19,-0.21
Refinement software	*JANA2006*	*JANA2006*	*JANA2006*
Source of atomic scattering factor	*International Tables for X-ray Crystallography* (Vol. C)	*International Tables for X-ray Crystallography* (Vol. C)	*International Tables for X-ray Crystallography* (Vol. C)

Table A.3: The crystallographic data for the final set of refinements based on main reflections of the Type A structure of Phase I at four temperatures.

Crystallization method	Bridgman Synthesis	Bridgman Synthesis	Bridgman Synthesis
Chemical formula	$Na_5Lu_9F_{32}$	$Na_5Lu_9F_{32}$	$Na_5Lu_9F_{32}$
Formula weight (g mol^{-1})	71.8	71.8	71.8
Crystal colour, habit	colourless, irregular cubic	colourless, irregular cubic	colourless, tablet
Crystal dimensions (mm)	0.1 × 0.1 × 0.1	0.1 × 0.1 × 0.1	0.1 × 0.075 × 0.05
Temperature (K)	100	200	293
Cell setting	orthorhombic	orthorhombic	orthorhombic
Space group	*Cmmm*	*Cmmm*	*Cmmm*
Unit cell parameters			
a **(Å)**	7.746(2)	7.746(2)	7.746(2)
b **(Å)**	7.743(5)	7.743(5)	7.743(5)
c **(Å)**	5.513(4)	5.513(4)	5.513(4)
V **(Å^3)**	330.7(3)	330.7(3)	330.7(3)
***F*(000)**	491	491	491
Z	16	16	16
Radiation Type	synchrotron	synchrotron	synchrotron
Wavelength (Å)	0.70150	0.70150	0.73550
μ (mm^{-1})	32.615	32.615	36.907
Detector	Mar345 IP	Mar345 IP	Mar345 IP
Method of measurement	ϕ scan	ϕ scan	ϕ scan
Scan Width (°)	1.0	1.0	1.0
Absorption correction	multi scan (*SADABS*)	multi scan (*SADABS*)	multi scan (*SADABS*)
Transmission factors (min; max)	0.260; 1	0.298; 1	0.275; 1
$2\theta_{(max)}$ [°]	55.6	55.6	56.1
Total reflections measured	1422	1412	1183
Symmetry independent reflections	810	808	681
R_{int}	5.18	7.29	4.08
Criteria for observed reflections	$I > 3\sigma(I)$	$I > 3\sigma(I)$	$I > 3\sigma(I)$
Redundancy	10.533	10.485	10.423
Range of *hkl*	$-10 \leq h \leq 10$ $-10 \leq k \leq 10$ $-7 \leq l \leq 7$	$-10 \leq h \leq 10$ $-10 \leq k \leq 10$ $-7 \leq l \leq 7$	$-9 \leq h \leq 9$ $-9 \leq k \leq 9$ $-7 \leq l \leq 7$
Refinement on	F	F	F
Weighting scheme	$w=1/[\sigma^2(F) + 0.0001F^2]$	$w=1/[\sigma^2(F) + 0.0001F^2]$	$w=1/[\sigma^2(F) + 0.0001F^2]$
R_{obs}/wR_{all} (Main reflections)	1.18/1.30	2.57/2.37	1.22/1.49
Goodness-of-fit (obs/all)	1.04/1.04	1.58/1.58	1.22/1.22
No of parameters	28	28	28
Final Δ_{max}/σ	0.0006	0.0018	0.0025
$\Delta\rho$ (max; min) (e Å^{-3})	0.27,-0.34	1.40,-1.51	0.26,-0.25
Refinement software	*JANA2006*	*JANA2006*	*JANA2006*
Source of atomic scattering factor	*International Tables for X-ray Crystallography* (Vol. C)	*International Tables for X-ray Crystallography* (Vol. C)	*International Tables for X-ray Crystallography* (Vol. C)

Table A.4: The crystallographic data for the final set of refinements based on main reflections of the Type B structure of Phase I at four temperatures.

Crystallization method	Bridgman Synthesis
Chemical formula	$Na_5Lu_9F_{32}$
Formula weight (g mol^{-1})	1148.8
Crystal colour, habit	colourless, tablet
Crystal dimensions (mm)	0.1 × 0.075 × 0.05
Temperature (K)	293
Cell setting	orthorhombic
Space group	*Cmmm*
Unit cell parameters ***a*** **(Å)** ***b*** **(Å)** ***c*** **(Å)** ***V*** **(Å^3)**	38.628(12) 7.743(5) 5.513(4) 1648.9(17)
***F*(000)**	2455
Z	5
Radiation Type	synchrotron
Wavelength (Å)	0.73550
μ (mm^{-1})	36.908
Detector	Mar345 IP
Method of measurement	ϕ scan
Scan Width (°)	0.5
Absorption correction	multi scan (*SADABS*)
Transmission factors (min; max)	0.0918; 1
$2\theta_{(max)}$ [°]	52.88
Total reflections measured	4378
Symmetry independent reflections (all)	731
R_{int}	4.25
Criteria for observed reflections	$I > 3\sigma(I)$
Redundancy	5.989
Range of *hkl*	$-46 \leq h \leq 46$ $-9 \leq k \leq 9$ $-6 \leq l \leq 6$
Refinement on	F
Weighting scheme	$w=1/[\sigma^2(F) + 0.0001F^2]$
R_{obs}/wR_{all} (Satellite reflections)	12.80/18.97
Goodness-of-fit (obs/all)	7.64/7.35
No of parameters	61
Final Δ_{max}/σ	0.0048
$\Delta\rho$ (max; min) (e Å^{-3})	0.26,-0.24
Refinement software	*JANA2006*
Source of atomic scattering factor	*International Tables for X-ray Crystallography* (Vol. C)

Table A.5: The crystallographic data for the 3-D space refinement based on satellite reflections of the fivefold superstructure of Phase I at RT.

Crystallization method	Bridgman Synthesis
Chemical formula	$Na_5Lu_9F_{32}$
Formula weight (g mol^{-1})	71.8
Crystal colour, habit	colourless, tablet
Crystal dimensions (mm)	0.1 × 0.075 × 0.05
Temperature (K)	293
t_0	0.1
q vector	0.4 0 0
Cell setting	orthorhombic
Super space group	*Cmmm(a00)000*
Unit cell parameters ***a*** **(Å)** ***b*** **(Å)** ***c*** **(Å)** ***V*** **(Å^3)**	 7.7256 7.743 5.513 329.7839
Z	16
Radiation Type	synchrotron
Wavelength (Å)	0.73550
μ (mm^{-1})	36.908
Detector	Mar345 IP
Method of measurement	ϕ scan
Scan Width (°)	1.0 (mains) &0.5 (satellites)
Absorption correction	multi scan (*SADABS*)
$2\theta_{(max)}$ [°]	56.1
No of independent reflections (all/obs)	1353/1274
No of independent main reflections (all/obs)	622/620
No of independent first-order satellite reflections (all/obs)	366/338
No of independent second-order satellite reflections (all/obs)	365/316
Criteria for observed reflections	$I > 3\sigma(I)$
Redundancy	4.11
Range of *hkl*	$-10 \leq h \leq 10$ $-9 \leq k \leq 9$ $-6 \leq l \leq 7$ $-2 \leq m \leq 2$
Refinement on	F
Weighting scheme	$w=1/[\sigma^2(F) + 0.0001F^2]$
R_{obs}/wR_{all} **All reflections**	5.22/9.25
R_{obs}/wR_{all} **Main reflections**	3.58/5.43
R_{obs}/wR_{all} **First-order satellite reflections**	6.87/9.34
R_{obs}/wR_{all} **Second-order satellite reflections**	11.00/14.11
Goodness-of-fit (obs/all)	3.21/3.15
No of parameters	99
Refinement software	*JANA2006*
Source of atomic scattering factor	*International Tables for X-ray Crystallography* (Vol. C)

Table A.6: The crystallographic data for the superspace refinement of Phase I at RT.

Type A Structure of Phase II							
		x, y, z	**Occupation**	**U_{11} (Å^2)**	**U_{22} (Å^2)**	**U_{33} (Å^2)**	**U_{12} (Å^2)**
100 K	**Lu1/Na1**	0 0 0	0.9444	0.0250(12)	0.0044(12)	0.0251(17)	0
	Lu2/Na2	-0.25 0.25 0.5	0.5007, 0.2771	0.0236(19)	0.0032(15)	0.034(2)	0.0012(4)
	Lu3/Na3	0 0.5 0	0.3042, 0.6958	0.035(4)	0.006(3)	0.028(4)	0
	F1	0 0.2399(18) 0.238(7)	0.70(6)	**U_{iso}** = 0.0276(19)			
	F2	0.2261(19) 0 0.294(3)	0.79(6)	**U_{iso}** = 0.0276(19)			
	F3	0.5 0.140(2) 0.5	0.331(19)	**U_{iso}** = 0.0276(19)			
	F4	0.197(3) 0.166(2) 0.137(2)	0.17(4)	**U_{iso}** = 0.0276(19)			
150 K	**Lu1/Na1**	0 0 0	0.9444	0.0261(13)	0.0043(12)	0.0258(18)	0
	Lu2/Na2	-0.25 0.25 0.5	0.5007, 0.2771	0.025(2)	0.0019(14)	0.037(2)	0.0013(4)
	Lu3/Na3	0 0.5 0	0.3042, 0.6958	0.035(4)	0.005(3)	0.032(4)	0
	F1	0 0.241(2) 0.236(7)	0.71(6)	**U_{iso}** = 0.028(2)			
	F2	0.226(2) 0 0.292(3)	0.80(6)	**U_{iso}** = 0.028(2)			
	F3	0.5 0.142(2) 0.5	0.32(2)	**U_{iso}** = 0.028(2)			
	F4	0.195(3) 0.167(2) 0.136(3)	0.17(4)	**U_{iso}** = 0.028(2)			
200 K	**Lu1/Na1**	0 0 0	0.9444	0.0265(12)	0.0048(12)	0.0263(17)	0
	Lu2/Na2	-0.25 0.25 0.5	0.5007, 0.2771	0.027(2)	0.0023(14)	0.042(2)	0.0016(4)
	Lu3/Na3	0 0.5 0	0.3042, 0.6958	0.034(4)	0.001(2)	0.032(3)	0
	F1	0 0.243(2) 0.226(8)	0.69(5)	**U_{iso}** = 0.027(2)			
	F2	0.226(2) 0 0.293(3)	0.81(5)	**U_{iso}** = 0.027(2)			
	F3	0.5 0.143(2) 0.5	0.33(2)	**U_{iso}** = 0.027(2)			
	F4	0.194(3) 0.167(2) 0.136(2)	0.17(4)	**U_{iso}** = 0.027(2)			
293 K	**Lu1/Na1**	0 0 0	0.9444	0.0133(11)	0.0403(14)	0.0128(6)	0
	Lu2/Na2	-0.25 0.25 0.5	0.5007, 0.2771	0.0077(13)	0.056(2)	0.0061(10)	-0.0031(3)
	Lu3/Na3	0 0.5 0	0.3042, 0.6958	0.022(3)	0.063(5)	0.014(2)	0
	F1	0 0.224(3) 0.287(3)	0.74(5)	**U_{iso}** = 0.0360(13)			
	F2	0.2416(18) 0 0.257(5)	0.78(5)	**U_{iso}** = 0.0360(13)			
	F3	0.5 0.147(3) 0.5	0.295(16)	**U_{iso}** = 0.0360(13)			
	F4	0.194(2) 0.161(2) 0.141(2)	0.16(3)	**U_{iso}** = 0.0360(13)			

Table A.7: The positions and ADPs of the atoms in the final set of refinements in the Type A structure of Phase II.

Type B Structure of Phase II						
		x, y, z	**Occupation**	**U_{11} (Å^2)**	**U_{22} (Å^2)**	**U_{33} (Å^2)**
100 K	**Lu1/Na1**	0.2444(9) 0 0.5	0.2967, 0.625	0.003(4)	0.005(4)	0.0189(15)
	Lu2/Na2	0 0.2582(6) 0	0.8283	0.0213(18)	0.0138(9)	0.0179(10)
	F1	0 0 0.235(7)	0.68(8)	U_{iso} = 0.022(3)		
	F2	0.5 0 0.321(4)	0.46(7)	U_{iso} = 0.022(3)		
	F3	0.25 0.25 0.205(4)	0.89(3)	U_{iso} = 0.022(3)		
	F4	0.063(3) 0.176(2) 0.353(3)	0.161(8)	U_{iso} = 0.022(3)		
	F5	0.259(3) 0.107(3) 0	0.22(6)	U_{iso} = 0.022(3)		
150 K	**Lu1/Na1**	0.2443(10) 0 0.5	0.2967, 0.625	0.004(4)	0.006(4)	0.0209(17)
	Lu2/Na2	0 0.2575(7) 0	0.8283	0.0216(19)	0.0131(11)	0.0187(10)
	F1	0 0 0.235(7)	0.72(8)	U_{iso} = 0.024(3)		
	F2	0.5 0 0.321(4)	0.48(7)	U_{iso} = 0.024(3)		
	F3	0.25 0.25 0.206(5)	0.88(3)	U_{iso} = 0.024(3)		
	F4	0.065(3) 0.178(2) 0.352(3)	0.159(8)	U_{iso} = 0.024(3)		
	F5	0.241(3) 0.392(3) 0	0.21(6)	U_{iso} = 0.024(3)		
200 K	**Lu1/Na1**	0.2445(10) 0 0.5	0.2967, 0.625	0.005(4)	0.007(4)	0.0201(17)
	Lu2/Na2	0 0.2578(6) 0	0.8283	0.0223(17)	0.0140(10)	0.0194(10)
	F1	0 0 0.235(7)	0.70(8)	U_{iso} = 0.024(3)		
	F2	0.5 0 0.322(4)	0.47(7)	U_{iso} = 0.024(3)		
	F3	0.25 0.25 0.206(4)	0.89(3)	U_{iso} = 0.024(3)		
	F4	0.065(3) 0.177(3) 0.351(3)	0.159(8)	U_{iso} = 0.024(3)		
	F5	0.259(3) 0.108(3) 0	0.21(6)	U_{iso} = 0.024(3)		
293 K	**Lu1/Na1**	0.2438(10) 0 0.5	0.2967, 0.625	0.013(3)	0.0025(18)	0.025(2)
	Lu2/Na2	0 0.2567(6) 0	0.8283	0.0255(16)	0.0123(11)	0.0215(7)
	F1	0 0 0.229(7)	0.82(8)	U_{iso} = 0.031(2)		
	F2	0.5 0 0.321(5)	0.40(8)	U_{iso} = 0.031(2)		
	F3	0.25 0.25 0.212(6)	0.86(3)	U_{iso} = 0.031(2)		
	F4	0.065(4) 0.175(3)	0.163(8)	U_{iso} = 0.031(2)		
	F5	0.243(4) 0.386(3) 0	0.20(7)	U_{iso} = 0.031(2)		

Table A.8: The positions and ADPs of the atoms in the final set of refinements in the Type B structure of Phase II.

Type A Structure of Phase I

		x, y, z	Occupation	U_{11} (Å^2)	U_{22} (Å^2)	U_{33} (Å^2)	U_{12} (Å^2)
100 K	**Lu1/Na1**	0 0 0	0.9279	0.0110(9)	0.0317(12)	0.0140(4)	0
	Lu2/Na2	-0.25 0.25 0.5	0.4911, 0.295(2)	0.0030(14)	0.0214(15)	0.019(2)	-0.0035(3)
	Lu3/Na3	0 0.5 0	0.340(4), 0.660(4)	0.015(3)	0.022(3)	0.043(3)	0
	F1	0 0.2213(16) 0.296(2)	0.68(3)	U_{iso} = 0.0336(11)			
	F2	0.2410(11) 0 0.245(3)	0.76(3)	U_{iso} = 0.0336(11)			
	F3	0.5 0.137(2) 0.5	0.324(12)	U_{iso} = 0.0336(11)			
	F4	0.1868(14) 0.1560(15) 0.1364(13)	0.201(19)	U_{iso} = 0.0336(11)			
200 K	**Lu1/Na1**	0 0 0	0.9011	0.0127(9)	0.042(2)	0.0110(6)	0
	Lu2/Na2	-0.25 0.25 0.5	0.5329, 0.267(4)	0.0052(9)	0.069(4)	0.0020(7)	-0.0041(6)
	Lu3/Na3	0 0.5 0	0.283(7), 0.717(7)	0.0184(16)	0.039(8)	0.0172(18)	0
	F1	0 0.2316(11) 0.282(2)	0.97(3)	U_{iso} = 0.0335(16)			
	F2	0.2487(10) 0 0.201(4)	0.58(4)	U_{iso} = 0.0335(16)			
	F3	0.5 0.146(4) 0.5	0.258(19)	U_{iso} = 0.0335(16)			
	F4	0.200(3) 0.157(2) 0.137(3)	0.16(2)	U_{iso} = 0.0335(16)			
293 K	**Lu1/Na1**	0 0 0	0.9034	0.0120(10)	0.042(2)	0.0153(11)	0
	Lu2/Na2	-0.25 0.25 0.5	0.5021, 0.296(4)	0.0075(13)	0.045(4)	0.013(2)	-0.0005(4)
	Lu3/Na3	0 0.5 0	0.342(7), 0.658(7)	0.024(3)	0.043(7)	0.025(4)	0
	F1	0 0.2248(19) 0.297(3)	0.66(3)	U_{iso} = 0.0385(15)			
	F2	0.2396(14) 0 0.254(3)	0.81(3)	U_{iso} = 0.0385(15)			
	F3	0.5 0.147(2) 0.5	0.345(14)	U_{iso} = 0.0385(15)			
	F4	0.1867(18) 0.1552(19) 0.141(2)	0.18(2)	U_{iso} = 0.0385(15)			

Table A.9: The positions and ADPs of the atoms in the final set of refinements in the Type A structure of Phase I.

Type B Structure of Phase I

		x, y, z	Occupation	**U_{11} (Å^2)**	**U_{22} (Å^2)**	**U_{33} (Å^2)**
100 K	**Lu1/Na1**	0.2436(6) 0 0.5	0.3660(19), 0.3840(19)	0.020(2)	0.0005(11)	0.0244(10)
	Lu2/Na2	0 0.2565(3) 0	0.7590(19), 0.2410(19)	0.0233(12)	0.0103(7)	0.0198(5)
	F1	0 0 0.220(7)	0.66(7)	**U_{iso}** = 0.0342(16)		
	F2	0.5 0 0.328(7)	0.37(8)	**U_{iso}** = 0.0342(16)		
	F3	0.25 0.25 0.217(5)	0.87(2)	**U_{iso}** = 0.0342(16)		
	F4	0.065(2) 0.1799(18) 0.3466(19)	0.188(8)	**U_{iso}** = 0.0342(16)		
	F5	0.261(2) 0.114(2) 0	0.24(6)	**U_{iso}** = 0.0342(16)		
200 K	**Lu1/Na1**	0.2545(8) 0 0.5	0.359(3), 0.391(3)	0.018(4)	0.0015(19)	0.028(3)
	Lu2/Na2	0 0.2432(5) 0	0.766(3), 0.234(3)	0.0227(14)	0.0095(11)	0.0249(13)
	F1	0 0 0.324(5)	0.56(12)	**U_{iso}** = 0.032(3)		
	F2	0.5 0 0.229(10)	0.62(10)	**U_{iso}** = 0.032(3)		
	F3	0.25 0.25 0.209(6)	0.90(4)	**U_{iso}** = 0.032(3)		
	F4	0.072(4) 0.185(4) 0.367(4)	0.164(11)	**U_{iso}** = 0.032(3)		
	F5	0.243(6) 0.150(4) 0	0.18(9)	**U_{iso}** = 0.032(3)		
293 K	**Lu1/Na1**	0.2450(9) 0 0.5	0.386(3), 0.364(3)	0.039(3)	-0.0027(12)	0.047(3)
	Lu2/Na2	0 0.2539(3) 0	0.739(3), 0.261(3)	0.0353(11)	0.0022(10)	0.0320(13)
	F1	0 0 0.210(4)	1.04(8)	**U_{iso}** = 0.0399(11)		
	F2	0.5 0 0.332(8)	0.40(5)	**U_{iso}** = 0.0399(11)		
	F3	0.25 0.25 0.229(4)	0.73(4)	**U_{iso}** = 0.0399(11)		
	F4	0.071(2) 0.1861(19) 0.351(2)	0.201(6)	**U_{iso}** = 0.0399(11)		
	F5	0.246(7) 0.123(4) 0	0.15(7)	**U_{iso}** = 0.0399(11)		
293 K	**Lu1/Na1**	0.2459(2) 0 0.5	0.374(4), 0.376(4)	**U_{iso}** = 0.0193(11)		
	Lu2/Na2	0 0.2558(8) 0	0.751(4), 0.249(4)	**U_{iso}** = 0.0195(4)		
	F1	0 0 0.222(11)	0.81(12)	**U_{iso}** = 0.037(3)		
	F2	0.5 0 0.329(9)	0.43(12)	**U_{iso}** = 0.037(3)		
	F3	0.25 0.25 0.216(10)	0.82(5)	**U_{iso}** = 0.037(3)		
	F4	0.068(4) 0.179(3) 0.346(3)	0.191(12)	**U_{iso}** = 0.037(3)		
	F5	0.254(7) 0.119(5) 0	0.18(10)	**U_{iso}** = 0.037(3)		

Table A.10: The positions and ADPs of the atoms in the final set of refinements in the Type B structure of Phase I.

	3-D space refinement						**Superspace refinement**					
	x, y, z	**occupation**	**U_{11} (Å^2)**	**U_{22} (Å^2)**	**U_{33} (Å^2)**	**U_{12} (Å^2)**	**x, y, z**	**occupation**	**U_{11} (Å^2)**	**U_{22} (Å^2)**	**U_{33} (Å^2)**	**U_{12} (Å^2)**
Lu1/Na1	0.0486(5) 0 0.5	0.3131, 0.646(6)	0.017(3)	0.015(5)	0.017(5)	0	0.05235 0.0 0.5	0.2022, 0.5478	0.029934	0.015256	0.047767	0
Lu1a/Na1a	0.1511(4) 0 0.5	0.4544, 0.051(4)	0.020(3)	0.018(4)	0.020(4)	0	0.14888 0.0 0.5	0.6936, 0.0564	0.018066	0.015618	0.026194	0
Lu1b/Nab	0.2484(5) 0 0.5	0.3538, 0.446(3)	0.018(3)	0.016(4)	0.018(5)	0	0.24908 0.0 0.5	0.2909, 0.4591	0.047396	0.01023	0.049136	0
Lu1c/Na1c	0.3515(5) 0 0.55	0.3031, 0.6969	0.017(3)	0.015(5)	0.017(5)	0	0.34800 0.0 0.5	0.1914, 0.5586	0.034243	0.014269	0.050916	0
Lu1d/Na1d	0.4485(5) 0 0.5	0.4459, 0.039(3)	0.020(3)	0.016(4)	0.020(4)	0	0.44976 0.0 0.5	0.6083, 0.1417	0.034621	0.008368	0.032068	0
Lu2/Na2	0 0.2512(18) 0	0.7436, 0.339(3)	0.034(3)	0.022(2)	0.037(3)	0	0.0 0.23629 0.0	0.7836, 0.2164	0.020485	0.008608	0.033903	0
Lu2a/Na2a	0.100007(3) 0.2476(18) 0	0.7411, 2589	0.036(3)	0.021(2)	0.037(3)	0.00006(8)	0.09991 0.242951 0.0	0.6486, 0.3514	0.02041	0.009968	0.025503	0.000864
Lu2b/Na2b	0.200110(5) 0.2540(18) 0	0.7644, 0.1945(15)	0.035(3)	0.021(2)	0.035(3)	0.00081(9)	0.20080 0.25415 0.0	0.779, 0.221	0.022904	0.015594	0.022106	-0.004849

Table A.11: The positions, occupations and anisotropic ADPs of the heavy metal atoms in the fivefold structure of 3-D space refinement and in the fivefold superstructure derived from superspace refinement at RT.

	3-D space refinement		**Superspace refinement**						
	x, y, z	**U_{iso} (Å^2)**	**x, y, z**	**U_{11} (Å^2)**	**U_{22} (Å^2)**	**U_{33} (Å^2)**	**U_{12} (Å^2)**	**U_{13} (Å^2)**	**U_{23} (Å^2)**
F1	0 0 0.202(8)	0.078(16)	0 0 0.22606	0.067277	0.032463	0.02359	0	0	0
F1a	0.19966(8) 0 0.199(8)	0.078(16)	0.19914 0 0.22243	0.105375	0.040752	0.037434	0	-0.011209	0
F1b	0.40050(10) 0 0.202(8)	0.078(16)	0.40284 0 0.23351	0.077708	0.018361	0.03918	0	-0.010076	0
F2	0.10046(10) 0 0.186(7)	0.082(16)	0.10182 0 0.23706	0.078238	0.038935	0.126052	0	0.022591	0
F2a	0.29965(8) 0 0.189(7)	0.082(16)	0.29676 0 0.23566	0.071056	0.017121	0.067571	0	0.005038	0
F2b	0.5 0 0.184(7)	0.082(16)	0.50000 0 0.21561	0.060625	0.041857	0.398903	0	0	0
F3	0.05000(2) 0.2508(3)	0.04(2)	0.04744 0.26837 0.24319	0.07083	0.104726	0.141827	-0.023653	-0.031319	-0.027456
F3a	0.15001(2) 0.2500(2) 0.172(11)	0.04(2)	0.15075 0.24264 0.23815	0.078918	0.150286	0.093665	-0.010031	-0.011145	0.033758
F3b	0.25 0.25 0.172(11)	0.04(2)	0.25 0.25 0.24038	0.049286	0.085877	0.069708	0.008667	0	0

Table A.12: The positions and ADPs of the fluorine atoms in the fivefold structure of 3-D space refinement and in the fivefold superstructure derived from superspace refinement at RT.

A.2 Computer Programs Used

CryAlis PRO RED (*CrysAlis* PRO; Aglilent, 2010)

Jana2006 (Petricek *et al.*, 2006)

SUPERFLIP (Palatinus *et al.*, 2007)

DIAMOND (Brandenburg *et al.*, 1999)

VESTA 3 (Momma *et. al.*, 2011)

NONCHAR (Aroyo *et al.*,2006)

A.3 Supporting Materials

All the supporting information regarding the refinement of Phase I and Phase II structure and the lecture notes of Massimo Nespolo in School on Mathematical Crystallography, Nancy, France, 2010 are given.

a) Jana2006 refinement files and the cif files for the final set of refinements for the Phase I structures of Type A and B at 100 K, 200 K and 293 K. For the Type B structure at 293 K two models are there: one with heavy metal atoms is isotropic and the other one where the heavy metal atoms are anisotropic.

b) Jana2006 refinement files and the cif files for the final set of refinements of the fivefold superstructure in 3-D space and the fivefold model derived from the superspace refinement.

c) Jana2006 refinement files and the cif files for the final set of refinements for the Phase II structures of Type A and B at 100 K, 150 K, 200 K and 293 K.

d) Intensity files for the main reflections of both phases and the satellite reflections of Phase I for six twin components. The twin1 satellite reflections were used for the modulated structure refinement.

Curriculum Vitae

Family name: DAS
First name: Partha Pratim
Date of Birth: 03.03.1983
Nationality: Indian

1993-1999	West Bengal Secondary Examination, Ramakrishna Mission Vidyapith, Purulia, WestBengal, India.
1999-2001	West Bengal Higher Secondary Examination, (Science stream), Ramakrishna Mission Residential college Narendrapur, Calcutta, WestBengal, India.
2001-2004	B.Sc. (Chemistry Hon.) Ramakrishna Mission Residential College Narendrapur, Calcutta, WestBengal, India.
2004-2007	M.S. (Chemical Sc.) (3 Year Degree Course), Indian Institute Of Science, Bangalore, India.
2007-2011	Ph.D. Thesis, Organic chemistry institute, University of Zürich, Zürich, Switzerland.

2007	M.S. thesis “Supramolecular Assembly of C-methyl resocin[4]arene: a structural approach via x-ray diffraction technique” at solid state structural chemistry unit under supervision of Prof. T. N. Guru Row, Indian Institute of Science, Bangalore, India.
2011	Ph.D. thesis “α-“NaLuF$_4$”: a Structure with Sixfold Twinning, Modulation and Diffuse Scattering. Structure Determination and Disorder Modelling.” at organic chemistry institute under supervision of Dr. Anthony Linden and collaboration with Prof. Hans-Beat Bürgi, University of Zürich, Zürich, Switzerland.

Acknowledgements

It is a pleasure to thank many people who made this thesis possible.

First and foremost I offer my sincerest gratitude to my supervisor, PD. Dr. Anthony Linden and my collaborator Prof. Dr. Hans-Beat Bürgi who have supported me throughout my thesis with their patience and knowledge whilst allowing me to work in my own way. I offer my sincere thanks to them for their great contribution to my scientific formation.

I wish to thank Prof. Dr. Lukas Palatinus of Department of Structure Analysis, Prague for his helpful introduction into the mysteries of modulated structure, the refinements conducted in 4-D space and for many constructive scientific discussions.

I wish to thank the members of my Ph.D. examination committee: Prof. Dr. Jay Sigel and Prof. Dr. Greta R. Patzke of University of Zürich, Switzerland.

I wish to thank Dr. Phil Pattison, Dr. Dmitry Chernyshov, Dr. Yaroslav Filinchuk and all the SNBL staff for their kind support during the measurements conducted at the SNBL, ESRF, Grenoble.

I wish to thank Dr. Karl Krämer of University of Bern, Switzerland for recording the powder diffraction patterns and the EDX measurement for the sample.

I wish to thank Daniel Biner of the University of Bern, Switzerland for the synthesis of the samples.

I wish to express my sincere gratitude to the Swiss National Foundation for financial support for this work.

I am grateful to my friends, colleagues and secretaries in the Organic Chemistry Institute, Zurich, Switzerland for assisting me in different ways.

I would like to thank the many people who taught me chemistry and crystallography: my school teachers, my undergraduate teachers and graduate teachers, especially Prof. T. N. Guru Row of Indian Institute of Science, Bangalore.

I am deeply indebted to my former and present colleagues (especially Rangana Warshamanaga and Peter Uebelhart) for their support in all the matters, scientific and beyond. They have always provided a warm and friendly environment.

My friends, you are an important part in my life. I am very grateful for your help in getting me through the difficult times, and for all the emotional support and caring you have provided.

Lastly, and most importantly, I wish to thank my parents and sister. They have provided unconditional support and love through all the years. To them I dedicate this thesis.